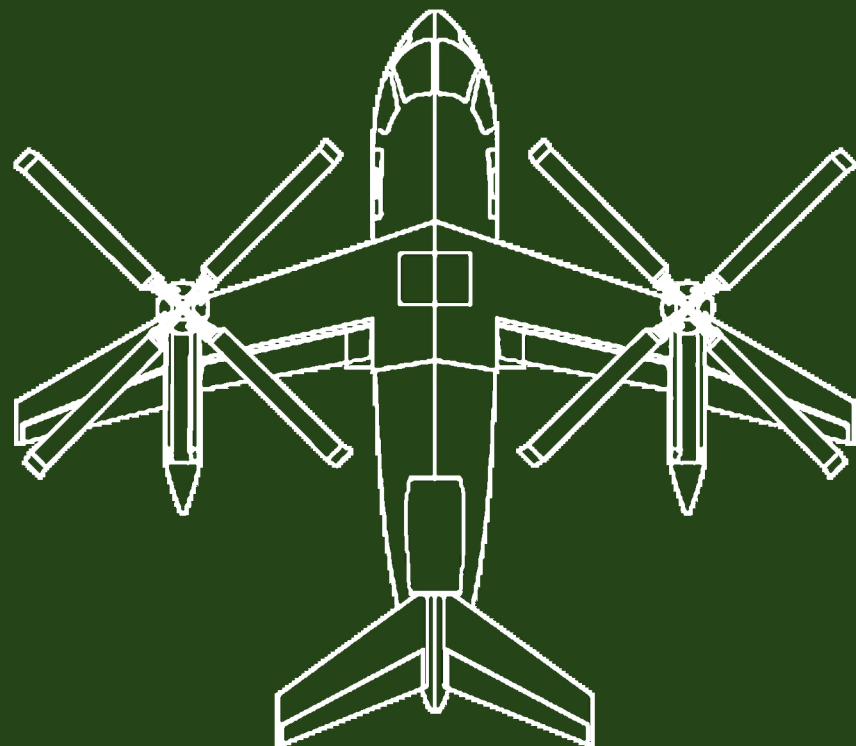


RAVEN 4



High-Speed Vertical Take-Off
and Landing Aircraft



POLITECNICO
MILANO 1863

Project Raven 4

High-Speed Vertical Takeoff and Landing Aircraft



**Beatriz Del Villano - Lorenzo Germinario
Giovanni Maria Maneschi - Matteo Mazzoleni**

Aircraft Design Course
Academic Year 2022/2023

Politecnico di Milano
DAER - Aerospace department
Milan, Italy
10/10/2023

Team members



Beatriz Del Villano
beatriz.delvillano@mail.polimi.it
Graduate student

Beatriz Del Villano



Lorenzo Germinario
lorenzo.germinario@mail.polimi.it
Graduate student

Lorenzo Germinario



Giovanni Maria Maneschi
giovannimaria.maneschi@mail.polimi.it
Graduate student

Giovanni Maria Maneschi



Matteo Mazzoleni
matteo1.mazzoleni@mail.polimi.it
Graduate student

Matteo Mazzoleni

Team advisors



Lorenzo Trainelli
lorenzo.trainelli@polimi.it

Lorenzo Trainelli



Carlo E. D. Riboldi
carlo.riboldi@polimi.it

Carlo E. D. Riboldi

Abstract

The *Raven 4* is an innovative jet-propelled fixed-wing aircraft equipped with two folding rotors mounted on the wings to enable vertical flight capability. It has been developed in response to the challenge posed by the Vertical Flight Society in requesting a High Speed Vertical Take-off and Landing vehicle capable of overcoming the limitations of current VTOL technology.

The most significant innovations implemented pertain to a dual power plant available on board for high-speed flight in both rotorcraft and airplane modes. Additionally, an innovative mechanism called *Multirail Technology* has been developed to facilitate the folding of the rotors around dedicated nacelles on the wings, ensuring the attainment of high-speed objectives.

Contents

Abstract	i
Contents	iii
1 Executive summary	1
2 Theme description	3
2.1 Operating concept	3
2.2 RFP aircraft requirements	4
2.3 RFP mission profile	5
3 Work organization within the group	7
4 Table of correspondence	11
5 Market analysis	13
5.1 Functional needs of military airlift	13
5.2 Operational scenarios	15
5.3 Operational missions	16
5.4 Competitors	17
5.5 Cargo utilization	21
5.6 MIL-STD certification framework	21
6 Technological analysis	23
6.1 Historical background	23
6.2 Downwash consideration	26
6.3 Nibbio - <i>Ragno technology</i>	28
6.4 Telescopic blades	30
6.5 Tilting mechanism	30

7 Conceptual design trade studies	33
7.1 Possible configurations	34
7.2 Analytic Hierarchy Process	35
7.3 Selection of the propulsion system	39
7.4 Selection of the final configuration	40
8 Emission of requirements	43
9 Preliminary sizing	45
9.1 Aircraft weight estimation	45
9.1.1 Statistical regression for empty weight fraction	45
9.1.2 Fuel fraction method	46
9.1.3 Weight estimation results	48
9.2 Jet-mode sizing matrix plot	50
9.3 Rotorcraft-mode	52
9.3.1 Momentum theory	54
9.3.2 Blade element theory	57
9.3.3 Sizing procedure	59
9.3.4 Power loading	68
9.3.5 Summary of preliminary sizing results	71
9.3.6 Results analysis	71
9.3.7 Code validation	73
10 Rotor design	75
10.1 Rotor configuration	75
10.2 Blade structure	78
10.3 Blade aeroelasticity	79
10.4 Folding mechanism: the <i>Multirail Technology</i>	83
10.5 Folding mechanism preliminary sizing	87
10.5.1 Kinematics	87
10.5.2 Quasi-static force and moments	90
10.5.3 Quasi-static power and time-to-fold	92
10.5.4 Folding mechanism preliminary sizing results	94
10.6 Blade Airfoil Section	94
11 Wing Design	99
11.1 Introduction	99
11.2 Airfoil section	100

11.3 Finite wing parameters	108
11.3.1 Wing incidence	108
11.3.2 Aspect ratio	109
11.3.3 Taper ratio	109
11.3.4 Sweep angle	110
11.3.5 Twist angle	113
11.3.6 Dihedral angle	114
11.3.7 Lift and load distribution	115
11.4 High Lift Device	116
11.5 Analysis on XFLR5	117
12 Tail design	119
12.1 Tail configuration	119
12.1.1 Tail location	119
12.1.2 Aft tail configuration	120
12.2 Tail volume coefficient	122
12.3 Optimum tail arm	124
12.4 Horizontal and vertical tail surface	125
12.5 V-tail parameters	126
12.5.1 Tail desired lift coefficient in cruise trim condition	126
12.5.2 Airfoil section	127
12.5.3 Sweep angle	127
12.5.4 Aspect ratio and taper ratio	128
12.5.5 Incidence	128
12.5.6 Summary of tail parameters	129
12.6 Final Results for wing and tail together	129
13 Fuselage design	133
13.1 Design requirements	133
13.1.1 Cargo section	134
13.1.2 Flight deck	134
13.1.3 Fuel tanks	135
13.1.4 Landing gear	136
13.2 External design	141
13.2.1 Length-to-Diameter ratio	142
13.3 Internal arrangement	143
14 Propulsion and onboard systems	145

14.1 Jet engine	145
14.1.1 Choice of the engine	145
14.1.2 Position of the engine	149
14.1.3 Safety consideration	150
14.2 Turboshaft engines for rotors	150
14.3 Drive system	153
14.4 Fuel system	153
14.4.1 In-flight refueling	155
14.5 Electrical system	156
14.6 Instrumentation and avionics	156
15 Structural sizing and weight analysis	159
15.1 Preliminary mass breakdown	159
15.2 Material selection and properties	159
15.3 Structural sizing	161
15.3.1 V-n diagram	162
15.3.2 Sizing maneuvers	163
15.3.3 Mass configurations	164
15.3.4 Component design loads	165
15.3.5 Trim and modal analysis	169
15.3.6 Flutter analysis	171
15.4 Final mass breakdown	173
15.5 Center of gravity range analysis	175
15.5.1 Rotorcraft mode	176
15.5.2 Jet mode	177
15.5.3 CG variation during Primary Mission	178
15.5.4 CG location and landing gear	181
16 Controls	183
16.1 Jet-mode	183
16.1.1 Aileron design	185
16.1.2 Rudder design	188
16.1.3 Elevator design	189
16.2 Rotorcraft-mode	190
16.3 Conversion phase	191
17 Aerodynamic characteristics	195
17.1 Drag build-up approach	195

17.1.1 Drag due to the wing	196
17.1.2 Drag due to the fuselage	199
17.1.3 Drag due to the jet engine	200
17.1.4 Drag due to the nacelles on the wing	202
17.1.5 Drag due to the empennage	204
17.1.6 Drag due to the flap	206
17.1.7 Drag due to the trim	207
17.1.8 Drag due to the landing gear	208
17.1.9 Drag due to the rotor hub and unfolded rotors	208
17.1.10 Final results for drag estimation	209
18 Performance	213
18.1 Jet mode	213
18.1.1 Take-Off performance	218
18.1.2 Landing performance	222
18.1.3 Climb performance	228
18.1.4 Range performance and operational flight envelope	230
18.2 Rotorcraft mode	233
18.2.1 Hover performance	233
18.2.2 Rotor download	235
18.2.3 Edgewise forward flight	237
18.2.4 Summary of rotorcraft performance	242
18.2.5 Conversion and jet thrust	243
18.3 Mission performance data	243
19 Equilibrium, control and static stability	247
19.1 Longitudinal equilibrium, control and static stability in jet-mode	247
19.1.1 Two surface model	248
19.1.2 Borri's formulation	248
19.1.3 Crocco's diagram	253
19.1.4 Maneuvering stability	258
19.2 Trimmed lift and polar for Take-off, Conversion, Cruise, and Landing configurations in jet-mode	260
19.2.1 Trim in cruise	260
19.2.2 Trim in conversion	261
19.2.3 Trim in take-off and landing	262
19.3 Equilibrium and control in rotorcraft-mode	265
19.3.1 Hover condition	265

19.3.2 Edgewise forward flight condition	267
19.3.3 Conclusions about trim in edgewise forward flight	270
20 Dynamic stability and flying qualities	271
20.1 Aircraft dynamics linearized framework	271
20.1.1 Longitudinal dynamics model	272
20.1.2 Lateral-directional dynamics model	273
20.2 Stability and control derivatives	274
20.3 Free dynamic response	275
20.3.1 Free longitudinal response and eigenanalysis	276
20.3.2 Free Lateral-directional response and eigenanalysis	279
20.4 Flying qualities	282
20.4.1 Phugoid	283
20.4.2 Short period	283
20.4.3 Roll	284
20.4.4 Spiral	285
20.4.5 Dutch roll	285
21 Simulation and flight control laws development, handling qualities	287
21.1 Simulation framework	287
21.2 SAS, CAS, Autopilot	290
21.2.1 General considerations	290
21.2.2 SAS and CAS implementation	291
21.3 Visual interface	292
22 Manufacturing and cost analysis	295
22.1 Market analysis	295
22.2 Aircraft Development and Procurement Cost	296
22.2.1 Analytical approach and Database	298
22.2.2 Cost estimation	298
22.2.3 Correction to the model and influence of material	300
22.2.4 Price estimation	301
22.2.5 Sensitivity analysis	302
22.2.6 Operating cost	305
23 Aircraft drawings	309
24 Risk assessment	321

25 Conclusions and critical evaluation	325
Bibliography	329
List of Figures	333
List of Tables	341
List of Tools	345
Acronyms	347
Acknowledgements	349

1 | Executive summary

The *Raven 4* is capable of operating in two distinct modes: during the cruise and penetration phases it operates as a classic jet-propelled fixed-wing aircraft. Two folding rotors are mounted on the wings, providing it with vertical flight capability. The peculiarity of this machine is its extremely high cruising speed. To achieve this characteristic, the rotor is not only closed but also rotated in a direction parallel to the flow to reduce aerodynamic drag. These extraordinary capabilities are achieved through the *Multirail Technology*, which makes it possible to perform an extremely complex operation, namely, the in-flight opening and closing of a rotor with a simple approach, ensuring reliability and robustness. The machine is equipped with 2 turboshafts on the wings and a tail-mounted turbojet. During the entire operational time, all three engines remain on: the propulsion system not engaged in the specific flight phase is kept idle or at the power necessary to power the on-board systems.

Jet-mode In jet-mode the aircraft behaves in all aspects as a fixed-wing aircraft, including runway take-off and landing capability.

Rotorcraft-mode In rotorcraft-mode, the aircraft behaves like a compound helicopter in a side-by-side configuration: the thrust of the jet is appropriately modulated by the flight management system to optimally satisfy the different phases of flight; however, in hover, the presence of the cyclic on both rotors allows it to perform all the maneuvers of a classic helicopter.

A drive shaft joins the two rotors so as to ensure the stability of the machine even if one of the two engines fails.

Unlike tiltrotors, rotors cannot operate unless fixed in vertical position. Rotation of the rotors to position themselves parallel to the flow, in order to switch to jet-mode, is carried out when they are turned off. This choice, in addition to simplifying the mechanics of flight and the folding mechanism, allows for maximum optimization of the rotorcraft-mode.

Conversion Conversion from one mode to the other can be carried out in both directions and in flight, at a speed between 110 and 130 knots.

When in rotorcraft-mode, reached the speed range described above and with the flaps

in extended configuration, the angle of attack of the wing is increased and the rotor simultaneously slowed down; thrust is provided by the jet. Once locked, through the *Multirail Technology* the blades close "in a flower fashioned way" and simultaneously the mast rotates by exploiting a hinge. Once the rotor is locked in a position parallel to the wing, it is possible to increase the speed and retract the flaps. The same operation can be performed in the opposite direction to change from jet-mode to rotorcraft-mode.

The whole design phase was driven by the awareness that complicated ideas only work on paper: the real world requires simple solutions to complex problems. Simplicity and mature technologies make this project the winning choice. The only real innovation, the *Multirail Technology* was developed with the same mindset. In the following paragraphs its ingenious simplicity based on mature technologies will come out in full force.

This project is a simple solution to a complex problem: an aircraft, feasible with current technologies, that can combine the capabilities of a fixed-wing aircraft with a rotary-wing aircraft.



2 | Theme description

The project topic that will be explored for the conduct of the "Aircraft Design" course of the Politecnico di Milano is set and demanded by the request for proposal of the Vertical Flight Society student design competition 2022-2023, sponsored by Sikorsky, a Lockheed Company.

The Request for Proposal (RFP) is seeking air vehicle concepts which incorporate technologies and design features enabling threat avoidance to meet critical military needs in highly-contested environments.

The vehicle shall be capable of carrying a payload of 5,000 lb (2,268 kg) within an internal cargo bay with dimensions of 6.5 ft (1.98 m) high, 8 ft (2.43 m) wide, 30 ft (9.14 m) long at a mission Radius of Action of 500 nm (926 km). The vehicle shall have a cruise speed of no less than 450 kn (833 km/hr) at a threat- avoidance altitude greater than 20,000 ft (6,096 m) mean sea level (MSL). In addition to the speed, altitude, payload and range requirements, the vehicle design shall also include features to mitigate the severity of the outwash/downwash environment on ground personnel as well as minimize the susceptibility of the propulsion system to Foreign Object Debris (FOD) ingestion during vertical take-off and landing (VTOL) operations.

2.1. Operating concept

A vehicle capable of efficient hover and extended VTOL operations tends to require large open rotor systems, which make it difficult to achieve the speed requirement of greater than 450 kn true airspeed (KTAS) (833 km/h) at 20,000 ft (6,096 m) MSL. Similarly, a vehicle capable of high-speed tends to require smaller open or covered rotor systems, which make operations difficult from unprepared surfaces and place ground personnel and equipment in severe downwash/outwash environments. To satisfy these diametrically opposed requirements and to meet the System Objectives, fundamental research and application of advanced technologies is necessary to enable transformational capability beyond the current state-of-the-art VTOL aircraft.

The proposed theme encouraged to explore a broad spectrum of technologies as new

propulsion systems for power/energy management, structural improvements, novel air vehicle configurations and any others.

While meeting the speed and altitude requirements, the terminal operations requirement of downwash/outwash severity mitigation for ground crew and equipment must also be met. Generally, the ability to sustain hover operations near the ground is directly tied to the rotor disk loading. A high disk loading results in high rotor outwash velocity fields that can significantly impact ground personnel and erode unprepared surfaces in the landing zone. That's why we would want to avoid a high disk loading in the project.

2.2. RFP aircraft requirements

As the operational environment, the competition's request for proposal (RFP) goes to clarify the requirements that the vehicle shall meet:

1. The aircraft shall be manned with a crew of three at 250 lb (113 kg) each.
2. Structural Design Gross Weight (SDGW) shall be defined as the Takeoff Gross Weight (TOGW) of the Primary Mission illustrated in (title of the chapter....) while carrying 5,000 lb (2,258 kg) of Payload and a Mission Equipment Package (MEP) of 1,000 lb (454 kg).
3. Airframe limit load factor shall be 3.5g at SDGW.
4. A weight contingency of 5% shall be applied to the sum of the component weights.
5. Landing Gear shall be designed for a sink speed of 10 ft/s (3.0 m/s) at SDGW with 2/3 rotor lift.
6. The aircraft shall be able to fly 450 KTAS (833 km/h) at 20,000 ft (6,096 m) MSL international standard atmosphere (ISA) conditions using no more than 100% Maximum Continuous Power (MCP) or 100% maximum continuous torque from the primary propulsion system at SDGW.
7. The aircraft shall have a mission Radius of Action (ROA) of 500 nm (926 km) while carrying 5,000 lb (2,268 kg) payload and 1,000 lb (454 kg) MEP, comprised of 450 nm (833 km) of cruise speed greater than 450 KTAS (833 km/h) at no less than 20,000 ft (6,096 m) MSL ISA and 50 nm (92.6 km) of cruise speed at the propulsion system's MCP at an ambient condition of 2,000 ft MSL 85°F.
8. The aircraft shall be capable of executing a Hover Out of Ground Effect (HOGE) at the mid-mission segment of the Primary Mission illustrated in Figure 2.1 using



no more than 90% of the engine Maximum Rated Power (MRP) or 100% of the gearbox and/or motor torque at an ambient condition of 2,000 ft (609.6 m) MSL and 85°F (24°C).

2.3. RFP mission profile

The Primary Mission profile and takeoff criteria give by the competition are illustrated in Figure 2.1. The takeoff condition shall be 2,000 ft (609.6 m) pressure altitude and 85°F (24°C) outside air temperature (2k/85°F). The mission profile shall include:

1. 10 minute flight idle
2. 2-min Hover In Ground Effect (HIGE) takeoff
3. Cruise-climb at best climb speed (VBROC) where range credit may be taken for the total Radius of Action (ROA) in Segments 4 and 6
4. Cruise 450 nm (833 km/h) at be no less than 20,000 ft (6,096 m) ISA conditions or best cruise altitude at the best range speed (VBR) or no less than 450 KTAS (833 km/hr)
5. Descend to 2,000 ft MSL 85°F (no range credit may be taken)
6. 50 nm (92.6 km) of low-altitude, high-speed penetration
7. 2-min mid-mission Landing Zone (LZ) Hover Out of Ground Effect (HOGE) at Mid-Mission Gross Weight (MMGW). Segments 3-6 are repeated, followed by a 2 min HOGE landing segment. Fuel/Energy reserves shall be 20 min at VBR and 2k/85°F.

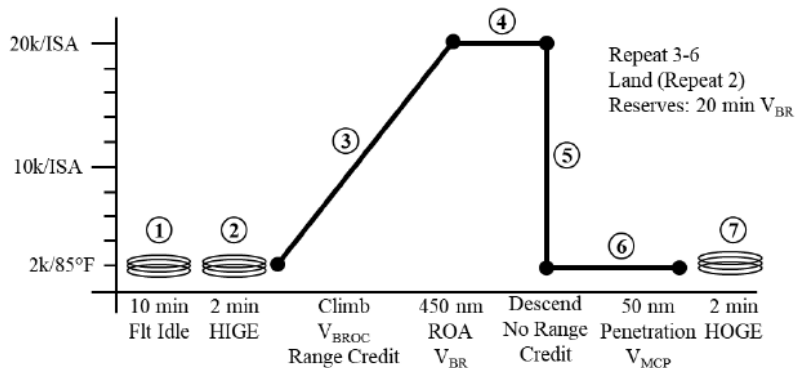


Figure 2.1: Primary mission profile given by the RFP of the Vertical Flight Society

3 | Work organization within the group

To accomplish the success of a project, achieving its goals in terms of results, time and cost, a proper planning and scheduling of the activities to be carried out is strictly necessary. In this regard in the initial phase the team met to define how the project would be organized. Having defined the team leader, the work breakdown structure was defined (Figure 3.1) along with the Logical Framework of the sequence of activities.

Ultimately, it was possible to produce a Gantt chart (Figure 3.2) that took into account the available resources, the needs of each team member, and carefully consider the winter break to take university examinations and any holidays relevant to the time cadence of the conduct of activities. A possible lengthening of the timelines in the early stages was taken into account in the calculation being the first time the group members worked together on such a large project in terms of knowledge, timing and decision making problems. Although this forming and norming phase was taken into consideration, the initial timeline trend turned out to be longer than expected, forcing the group to work with more effort in the last weeks of the project.

The Gantt chart shown in Figure 3.2 refers to the work done starting October 17, 2022 and delivered for the Vertical Flight Society competition on May 31, 2023. Subsequent to the delivery time, after the summer break, in September the project was then closed including some updates for the completeness of the work so that all the sustained work could be delivered to the Aerospace Department of Politecnico di Milano by reporting it without restriction on the final total number of pages, exemplifying in detail each step and results achieved.

3| Work organization within the group

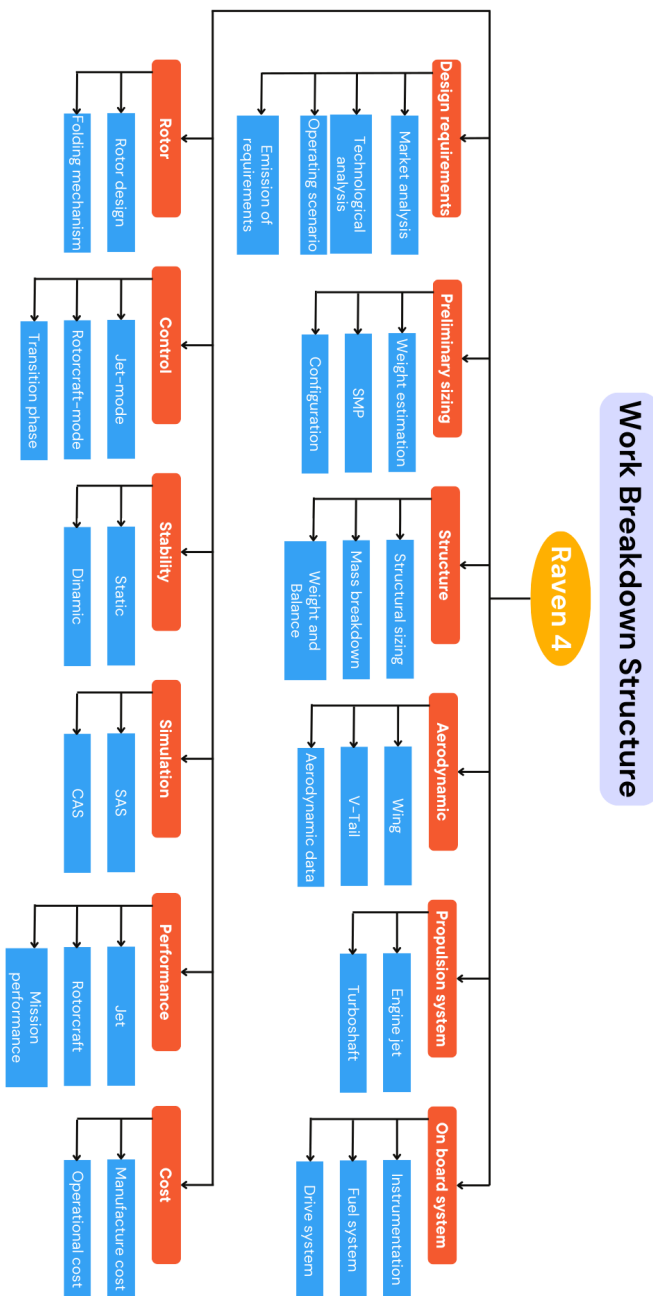


Figure 3.1: Work breakdown structure



3| Work organization within the group

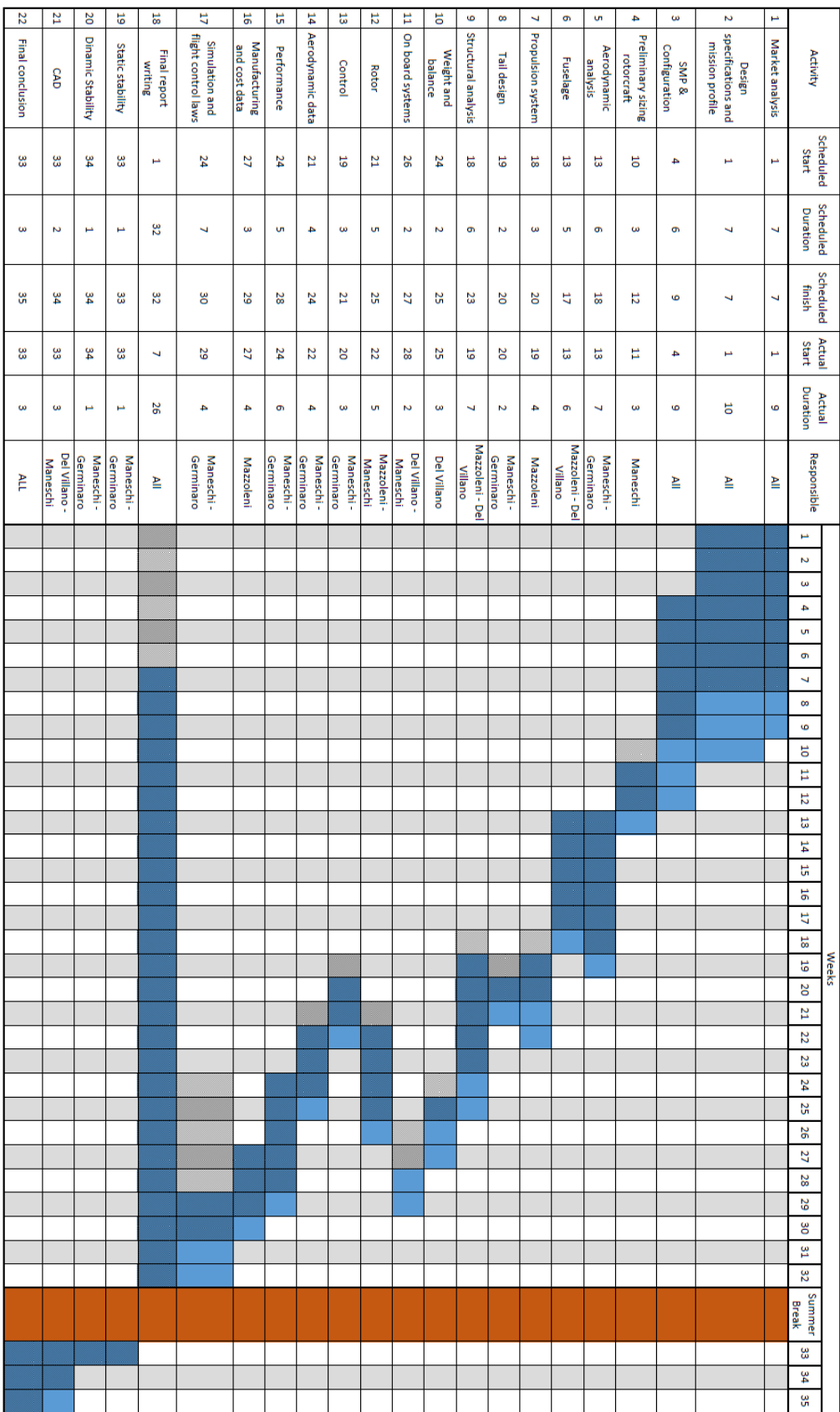


Figure 3.2: Gantt chart and work organization

4 | Table of correspondence

Content	Chapter
Theme description	2
Work organization within the group	3
Analysis of the theme, market study, state of the art, certification framework	5, 2, 6
Emission of requirements, design specifications, mission profiles, technological and economical constraints, etc.	2, 5, 7, 8
Initial sizing of weight, thrust-to-weight/power-to-weight, wind loading and disk loading	9
Comparative analysis of possible candidate configurations	7
Selection and motivation of a configuration	7
Design of the fuselage	13
Design of the wing (including high-lift devices), tail, control surfaces, trim, etc.	11, 12, 16, 19
Rotor design	9, 10
Selection and integration of propulsion	14
Onboard systems	14
Structural sizing	15
Analysis of weight performance, center-of-gravity travel	15
Performance analysis	18, 17
Static stability and control (including Crocco's diagram), in level and maneuvering flight, for all configurations	19

Table 4.1: Table of correspondence between report chapters and contents (continuation on next page)

Content	Chapter
Dynamic stability and flying qualities, for all configurations	20
Simulation, flight control laws development and handling qualities	21
Cost analysis	22
Drawings (3-view, internal arrangements, etc.)	23
Conclusions, comparison of results with existing products, critical evaluation in reference to initial goals	24, 25
Bibliography and sitography	25

Table 4.2: Continuation of table of correspondence between report chapters and contents



5 | Market analysis

The Request For Proposal seeks air vehicle concepts which incorporate technologies and design features enabling threat avoidance to meet critical military needs in highly-contested environments. Therefore, the aim of this market analysis is to understand what are the characteristics of the military environment in which the aircraft should be able to operate, what kind of missions it could perform and what is the current state of the art, in order to develop a product that brings innovation in the current market and is competitive with respect to the existing aircraft.

5.1. Functional needs of military airlift

On the basis of the Aircraft Requirements (Chapter 2) it can be assumed that the aircraft will be a high speed military cargo for light payload; therefore in this section the demands of military airlift will be analyzed. Military airlift, the organized delivery of supplies or personnel via transport aircraft, can be divided in two types of operations: strategical airlift and tactical airlift. Strategical airlift consists in the operations of transport of materiel over long distances outside the country or the theater of operations. While tactical airlift is the airborne transportation of supplies and equipment within a theatre of operations. From the mission radius of action demanded by the RFP, it may be supposed that the vehicle should be able to perform operations of tactical airlift.

A study of the RAND corporation [5] identified three broad operational missions that tactical airlift must be able to provide:

1. ROUTINE SUSTAINMENT: defined as the steady state delivery of required supplies and personnel to units. The required routine sustainment can be identified and planned well in advance. These items may consist of water, food, and other items needed to conduct planned operations.
2. TIME SENSITIVE/MISSION CRITICAL RESUPPLY (TS/MC): defined as the delivery of supplies and personnel on short notice outside the steady state demands. The requirement for this capability is driven by the need for items with unpredictable

consumption rates and the need for items that are not kept on hand at every operational location. TS/MC resupply may also include delivery of key personnel with specific skills.

3. MANEUVERS: defined as the transport of combat teams around the battlefield using the intra-theater airlift system. The maneuver task is associated with the initial deployment, redeployment and extraction of these teams as required. Maneuver missions may include:

- Transport to mission locations
- Transport to mission in progress
- Transport to one mission area to another
- Transport following completion of a mission to include moving the mission team as well as any materiel or personnel acquired during operations

Some important conditions that can affect the success of the mission must be taken into account in the analysis of intra-theater operations:

- Adverse weather
- Multiple, simultaneous, distributed decentralized battles and campaigns
- Anti-access environment
- In support of forces operating in and from austere or unimproved locations
- Degraded environment
- Multinational environment
- Absence of preexisting arrangement
- Consistent with sea basing

At the same time some positive attributes and conditions can be considered:

- Smallest logistical footprint
- Speed, accuracy and efficiency
- Distribution to the point of requirement
- Basing flexibility (the ability to operate across strategic and operational distances)

The tasks identified above should be accomplished with the following standards:



- Ability to meet force and materiel movement demand
- Ability to deliver optimized movement of forces and materiel throughout theater from a cycle time perspective
- Capability to provide materiel support for the current and planned operations

Air Force planners have identified an increased demand for air cargo delivery to dispersed, austere locations in response to enemy attacks on ground lines of communication.

5.2. Operational scenarios

In order to understand what are the characteristics of the highly-contested environments in which the aircraft shall be able to operate, the military actions conducted by the U.S. military forces in the last 30 years have been analyzed.

An analysis of the number and types of operations was carried out from 1990 and 2019; it led to the conclusion that military operations are conducted in very different operational scenarios all over the world, each of which with various characteristics in terms of climate, infrastructure and distance from U.S. bases. Considering these features in the design process will lead to the development of a very versatile aircraft, that can be used in several types of operations.

In figure 5.1 it is possible to recognize 10 country in which U.S. military force has started the most military operations.



Figure 5.1: U.S. military operations country

More than 60 operations have been conducted in very different operational scenarios all over the world, each of which with various characteristics in terms of climate, infrastructure and distance from U.S. bases. Considering these features in the design process will lead to the development of a very versatile aircraft, that can be used in several types of operations.

Among the various operations carried out by U.S. military forces we can identify: civilian evacuations, human relief, deployment of military personnel, security passage, hostage rescue, military exercise, offensive/raid, missile attack/air attack, bombing campaign.

Two countries have been considered as examples, Afghanistan and Iraq. Afghanistan is a highly mountainous region, very far from bases in the continental United States and those overseas with permanent U.S. forces, landlocked and rugged, with limited and greatly deteriorated transportation infrastructure. While Iraq is characterized by a desert environment, flat and bald terrain and dozen very well-prepared bases.

5.3. Operational missions

From the previous paragraphs it is possible to draw up a list of missions that the aircraft will be capable of execute:

- (Combat) search and rescue, CSAR



Raven 4

- Emergency transport of personnel
- War zone extractions
- Rapid military penetrations
- Air support
- VIP transport
- Transport of light supplies

5.4. Competitors

Starting from the considerations in the previous sections regarding the RFP requirements and the broad operational and logistical needs in military contexts, some existing aircraft that can best meet the needs and requirements corresponding to the defined mission profile have been identified. Nowadays does not exist an aircraft that can satisfy all the requirements set by the RFP, therefore several vehicles have been taken into account, each of which meets at least one of the payload, internal cargo dimension, range and cruise speed demand.

The aircraft that currently can both perform hover and flight in cruise at relatively high speed are tiltrotors. They take off and land vertically by means of two or more rotors located at the tips of the wing, that in the cruise phase are tilted in a horizontal position and used as propellers. This type of vehicle combines the capability of an helicopter and a propeller-driven aircraft, overcoming the limits of both of them. The dimension of the rotor needed to sustain the aircraft during the hover phase represents a problem during the cruise phase due to the aerodynamic performance, therefore these aircraft can't reach speeds comparable with jets, which are the only ones that can achieve the speeds required by the request for proposal.

Tiltrotors that have been considered are:

- Bell XV-15: experimental VTOL aircraft that flew for the first time in 1977.
- Bell Boeing V-22 Osprey: V/STOL military transport aircraft. It was the first tiltrotor for military service: it flew for the first time in 1989 and entered in service in 2007.
- AgustaWestland AW609: VTOL aircraft aimed at the civil aviation market. It flew for the first time in 2003.

- Bell V-280 Valor: it's the newest among the considered tiltrotors and it's still under development, in the phase of flight testing.



(a) Bell XV-15



(b) Bell Boeing V-22 Osprey



(c) AgustaWestland AW609



(d) Bell V-280 Valor

Figure 5.2: Tiltrotors

There is also an example of VTOL aircraft jet-propelled, the Dornier Do 31, that remained in prototype status.



Figure 5.3: Dornier Do 31



In addition, three tactical airlifters have been analyzed:

- Boeing CH-47 Chinook: heavy-lift helicopter characterized by a tandem rotor configuration. The dimensions of its internal cargo are the same of the dimensions demanded in the RFP.
- Alenia C-27J Spartan: propeller-driven military transport aircraft that reaches the highest speed among the considered vehicles.
- Lockheed C-130 Hercules: that is currently used by U.S. Air Force for intra-theater operations [8].



(a) Boeing CH-47 Chinook



(b) Alenia C-27J Spartan



(c) Lockheed C-130 Hercules

Figure 5.4: Tactical airlifters

In Table 5.1 are summarized all the competitors that have been considered and their main characteristics.

	Gross weight	Empty weight	Payload	Cruise speed	Range	Internal cargo
V-22 (VTO)	52,600 lb (23,859 kg)	33,460 lb (15,177 kg)	20,000 lb (9,072 kg)	257 kn (476 km/h)	350 nm (648 km)	24.18x6x6 ft (7.37x1.83x1.83 m)
V-280	3,865 lb (14,000 kg)	18,078 lb (8,200 kg)	12,000 lb (5,443 kg)	280 kn (519 km/h)	800 nm (1,481 km)	- -
AW-609 (VTO)	16,800 lb (7,620 kg)	10,441 lb (4,736 kg)	6,000 lb (2,721 kg)	270 kn (500 km/h)	270 nm (500 km)	- -
Do-31 (VTO)	49,500 lb (22,453 kg)	30,574 lb (13,868 kg)	7,715 lb (3,500 kg)	350 kn (650 km/h)	972 nm (1,800 km)	- -
CH-47	50,000 lb (22,680 kg)	25,350 lb (11,500 kg)	28,220 lb (12,800 kg)	140 kn (259 km/h)	505 nm (935 km)	30x8.2x6.5 ft (9.19x2.5x1.98 m)
C27-j	71,650 lb (32,500 kg)	37,480 lb (17,000 kg)	25,350 lb (11,500 kg)	315 kn (583 km/h)	1,080 nm (2,000 km)	28.15x8x7.38 ft (8.58x2.45x2.25 m)
C-130H	153,772 lb (69,750 kg)	76,780 lb (34,827 kg)	42,085 lb (19,090 kg)	292 kn (540 km/h)	1,050 nm (1,945 km)	40.4x10x9 ft (12.31x3.05x2.74 m)

Table 5.1: Characteristics of the competitors



5.5. Cargo utilization

In the current historical period, it is possible to observe an ever-increasing demand for airlifting operation due to ever-increasing attacks on land links and because of the dispersed nature of the global wars, which translates to multiple, simultaneous, decentralized operations scattered across huge areas.

Because of these multiple and decentralized operations, it is not always possible and convenient to prepare near the areas of interest adequate runways for resupply of materials and supplies needed for the mission. In fact, the runways are either not present or hardly able to be long enough and prepared to accommodate heavy military cargo. Here then is where an aircraft like the Raven 4 shows itself in its versatility by being able to land and take off vertically and being able to move quickly within the areas of interest.

Therefore, the usefulness of the available cargo compartment shows itself to be very versatile and usable for a wide range of operations such as:

- Equipped for search and rescue operations
- VIP transport
- Troop transportation
- 463L Master Pallet (a standardized pallet used for transporting military air cargo)

For the available size, it is also possible to include some light transport vehicles such as the Land Rover Wolf. For transporting such vehicles however the Raven 4 would not show itself as the best candidate because of its low available payload. In this regard, an increase in the payload can be taken into account in the design phase to ensure greater flexibility of executable operations and thus also optimize the use of the large cargo compartment required. In fact, the cargo dimensions request in the RFP appear to be very large compared to the payload which is capable of carrying.

5.6. MIL-STD certification framework

The development of a new military HSVTOL aircraft must meet a rigorous set of certification requirements. These requirements are mainly defined by the United States military in a series of MIL-STD documents. The indications of the certifications available from MIL-STD documents have been followed wherever possible in this work to ensure the consistency of the project with the appropriate safety measures, required mission standards, operational condition and military standards. These are requirements to ensure that the

aircraft can withstand the harsh conditions of military operations.



6 | Technological analysis

The aim of this analysis is to investigate the technological limitations and potential issues that may be of concern in the preliminary phase of the project. A first observation of these issues allows for an exploration of the current state of the art and the possible existing solutions to be taken into consideration in the project's development.

6.1. Historical background

In human history, the possibility of developing an aircraft with VTOL capabilities has driven research to explore various configurations that could prove convenient and feasible, as shown in Figure 6.1.

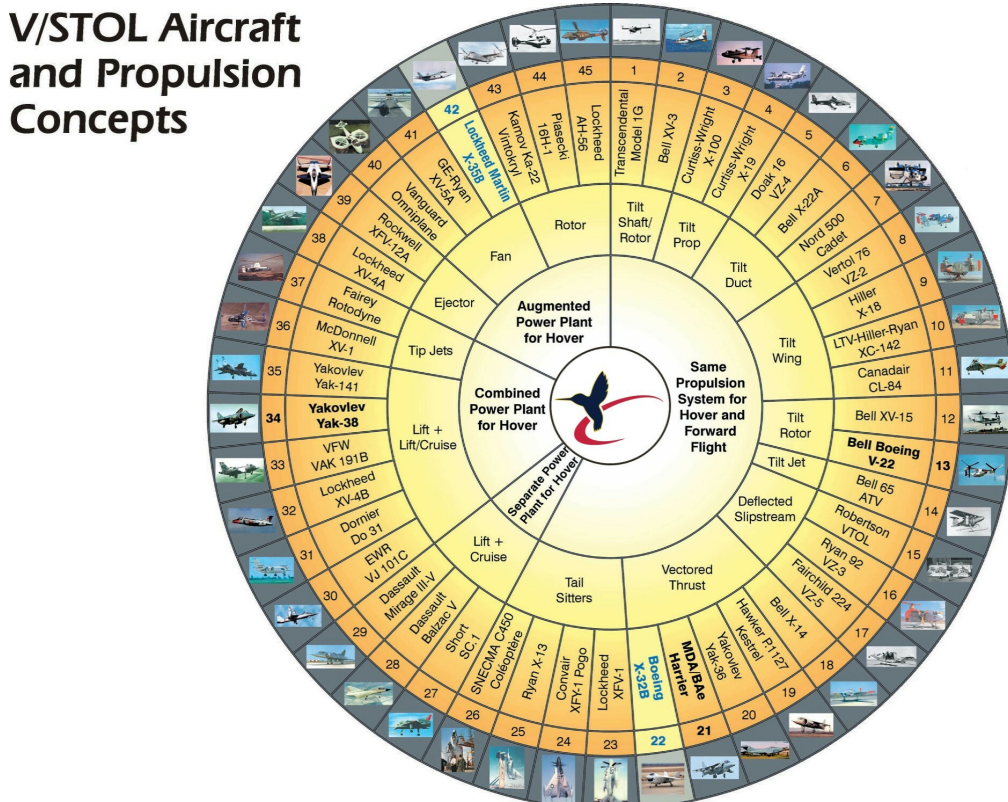


Figure 6.1: Illustration of vertical and short take-off and landing [32].

From the beginning, a fundamental parameter known as disk loading has been defined. Therefore, if the thrust for vertical take-off is generated over a small area, such as the exhaust nozzle of a direct-lift jet engine, the lifting device is referred to as high disk loading type. In this regard, systems with low disk loading have proven to be more efficient, capable of producing more thrust per horsepower.

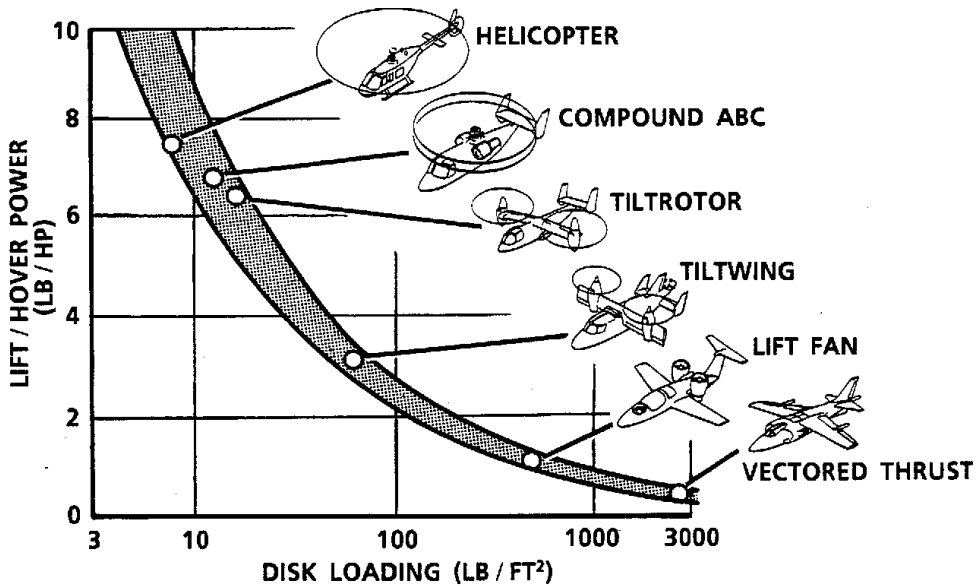


Figure 6.2: Dependence on disk loading of hover efficiency

The initial steps towards a feasible aircraft capable of both cruising like an airplane and sustaining vertical flight were undertaken through the XV-3 program by the Army and Air Force.

The test program began in 1955 by Bell company. Early on, challenges regarding hover stability were observed and had to be addressed through an extensive campaign of experimental tests. Ultimately, the program was evaluated as "The XV-3 demonstrated that the fixed-wing prop-rotor concept is operationally practical with safety and complexity comparable to helicopters".





Figure 6.3: XV-3

The studies continued with parallel projects until February 1972 when Bell developed an initial folding version. The stop/fold tiltrotor eliminated the aeroelastic instability by stopping the rotor while in the airplane configuration. The aerodynamic drag of the stopped rotor blades was then reduced by folding them back along the nacelle, while a convertible engine was used to produce the jet thrust required for airplane-mode flight.

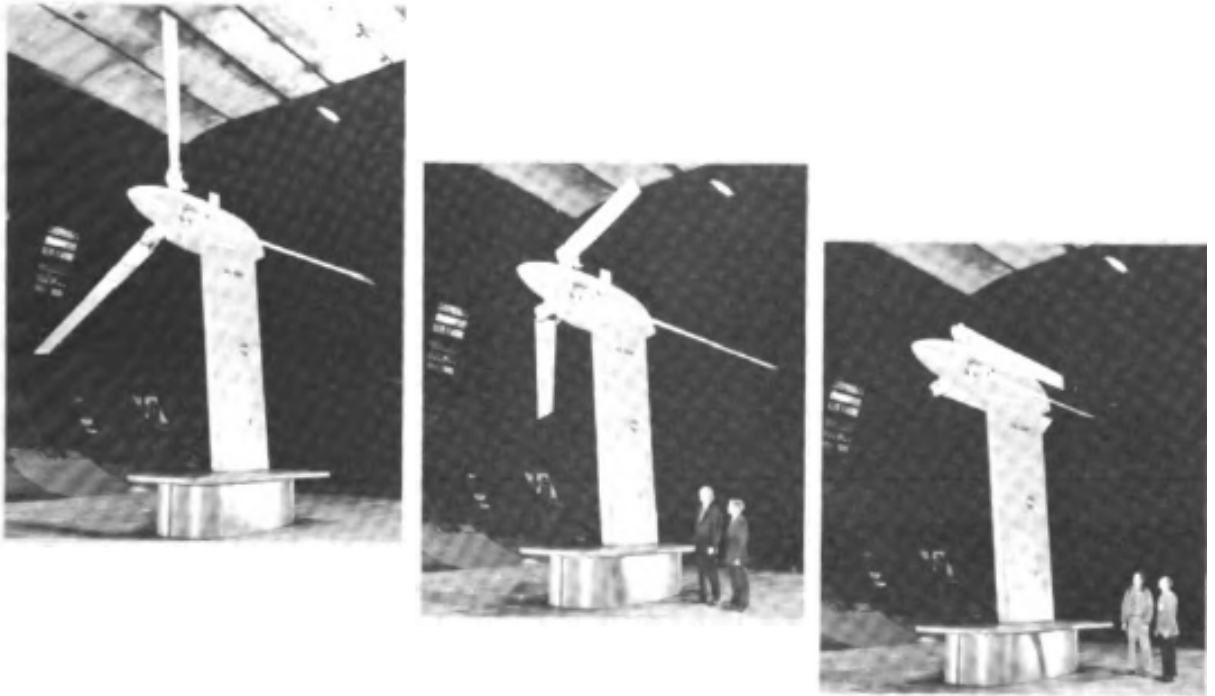


Figure 6.4: The Bell stop/fold tilt rotor in the wind tunnel [12].

However, the stop/fold tilt rotor had the additional penalties of the increased complexity and weight with the lack of the convertible engine TRL. For these reason, it was put aside

because it would require further advancements to be an effective contender.

Another weakness identified in the XV-3 program was the inefficiency of the rotor in airplane mode. For this reason, extensive wind tunnel testing was dedicated to studying the best possible configuration for the rotor blades.

6.2. Downwash consideration

In the development of an aircraft with multiple rotors as in a side-by-side configuration, such as that of the V-22 and V-280, there are aerodynamic losses from the interference between the main rotors and between the rotors and fuselage. These losses reduce the overall efficiency of twin main rotor configurations to about the same level as for the single main and tail rotor configuration.

In a configuration as the tandem rotor helicopter one, there are two contra-rotating main rotors with longitudinal separation; the main rotor disks are usually overlapped, typically by 30% to 50% (the shaft separation is around $1.7R$ to $1.5R$). To minimize the aerodynamic interference created by the operation of the rear rotor in the wake of the front rotor, the rear rotor is elevated on a pylon above the front rotor.

As well as the tandem rotor helicopter, the side-by-side configuration has two contra-rotating main rotors with lateral separation and the rotors are mounted on the tips of wings with usually no overlap (so the shaft separation is at least $2R$).

One of the challenges associated with the modeling, simulation and performance prediction of these aircraft is the complex interactional aerodynamic flow fields of multiple rotors operating in close proximity. Several recent studies have used high-fidelity computations to represent these flows resulting in good physical insights as well as an understanding of beneficial geometries/configurations. During take-off and landing operations around vertiports, however, these multi-copters will be close to the ground, and rotor-rotor-ground aerodynamic interactions can be expected to strongly influence the performance and loads.

The publication "A Computational Investigation of Side-by-Side Rotors in Ground Effect" [6] investigates just the interactional aerodynamics of hovering side-by-side rotors in ground effect. They analyze the performance of side-by-side rotors in ground effect compared to isolated rotors out of ground effect; and analyze the highly turbulent mixing region identified where the wakes of each rotor collide between the side-by-side rotors in ground effect.

It explores the hovering phase in ground effect and out of ground effect for the case where



the side-by-side rotor are positioned at a distance equal to 2.5 the radius of the rotors. It looks to use high fidelity blade resolved CFD to further investigate the aerodynamics of multiple close proximity rotors in ground effect.

As the result of the work it can be see, in compare with a single rotor, a decrease in performance due to the highly turbulent mixing region identified where the wakes of each rotor collide, which moreover carry a substantial vibratory loading for both rotors as blades pass through the center mixing region. In Figure 6.5 can be see a side-by-side configuration in hover in ground effect at an eight equal to the half of the diameter of the rotor in which the vorticity magnitude is highlighted.

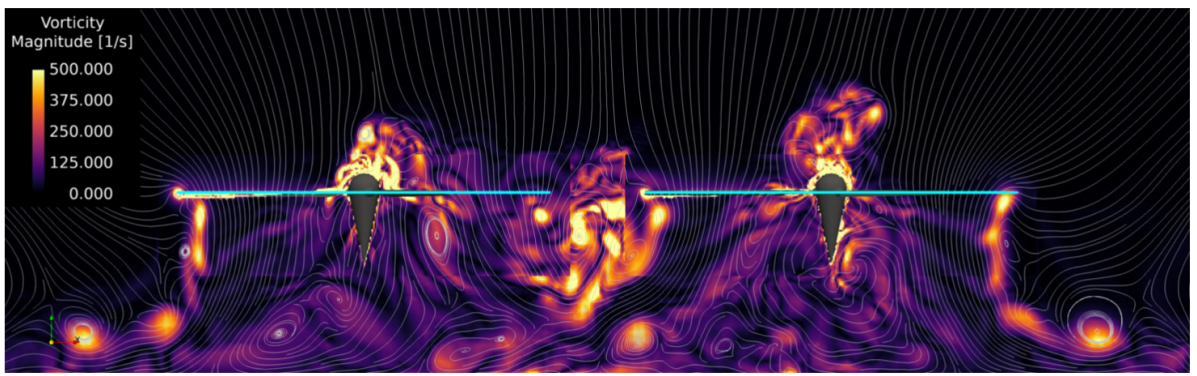


Figure 6.5: Slice cutting through side-by-side $H/D = 0.5$ $2.5R$ separation IGE rotor hubs colored by vorticity magnitude

In the end, it is possible to say that for a configuration side by side with a 2.5 radius separation between rotors, at a high $H/D = 1$ or $H/D = 0.5$ it is necessary just a 2% of thrust extra in respect to a single engine rotor in hover in ground effect, as it can be seen from the [6] results in Figure 6.6.

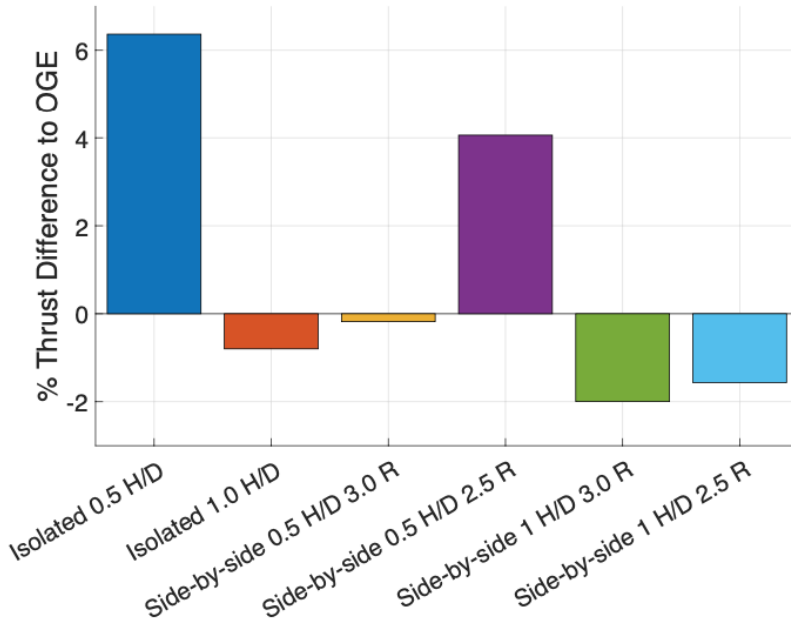


Figure 6.6: Relative thrust difference between six IGE rotor cases and an isolated OGE rotor (IGE minus OGE)

Another critical study is related to the relative flow that impacts the fuselage and wing from the rotor, worsening hover performance and increasing vibrations and structural loads. However, this kind of analysis and insights, due to their complexity and unpredictability requires accurate and precise models of the considered system: materials, geometries, loads, etc. For this reason within this work will not be addressed these issues being a preliminary project.

6.3. Nibbio - *Ragno* technology

The Nibbio project (Figure 6.7), developed by students in the aircraft design course at Politecnico di Milano, proposes an clever solution to the rotor folding problem called *Ragno*. In fact, through a single rotary mechanism contained within the rotor shaft it manages through kinematic linkages to fold the blades onto the nacelle, as shown in Figures 6.8 and 6.9. Certainly the actuation of all the blades simultaneously makes the folding mechanism efficient and well integrated. However, from the available documents [30], it appears that when the rotor is in operation the mechanism prevents its blades from flapping. This in itself for the Nibbio might not be a problem, or even an advantage, since the rotor remains operational during the shaft rotation to the horizontal. This though would certainly be a factor in generating high time-repetitive loads on the kinematic



mechanism if the mechanism were used in edgewise flight at high speeds. The possibility of leaving the mechanism free to rotate however would not solve the problem, since the flapping of the blades would not be independent.



Figure 6.7: Nibbio

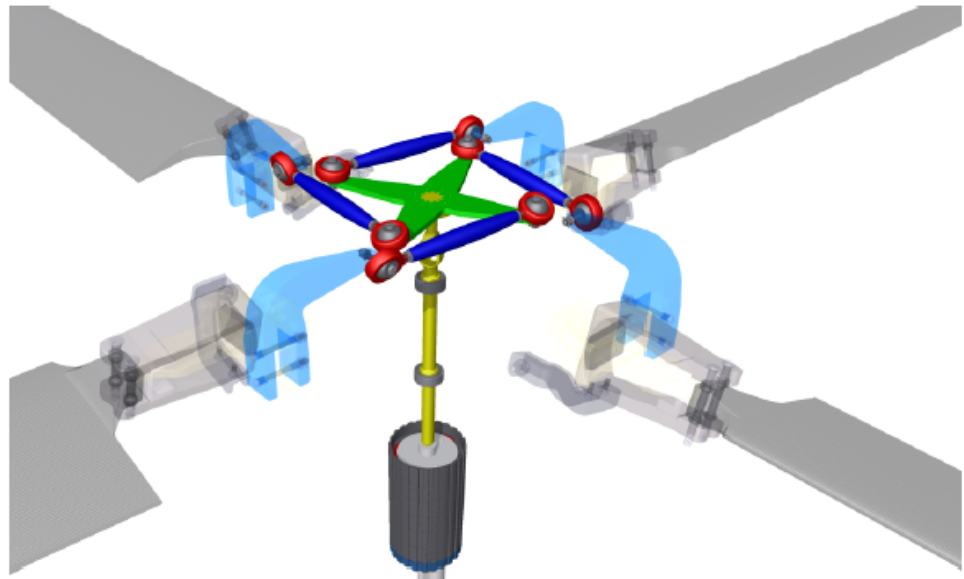


Figure 6.8: Ragnor

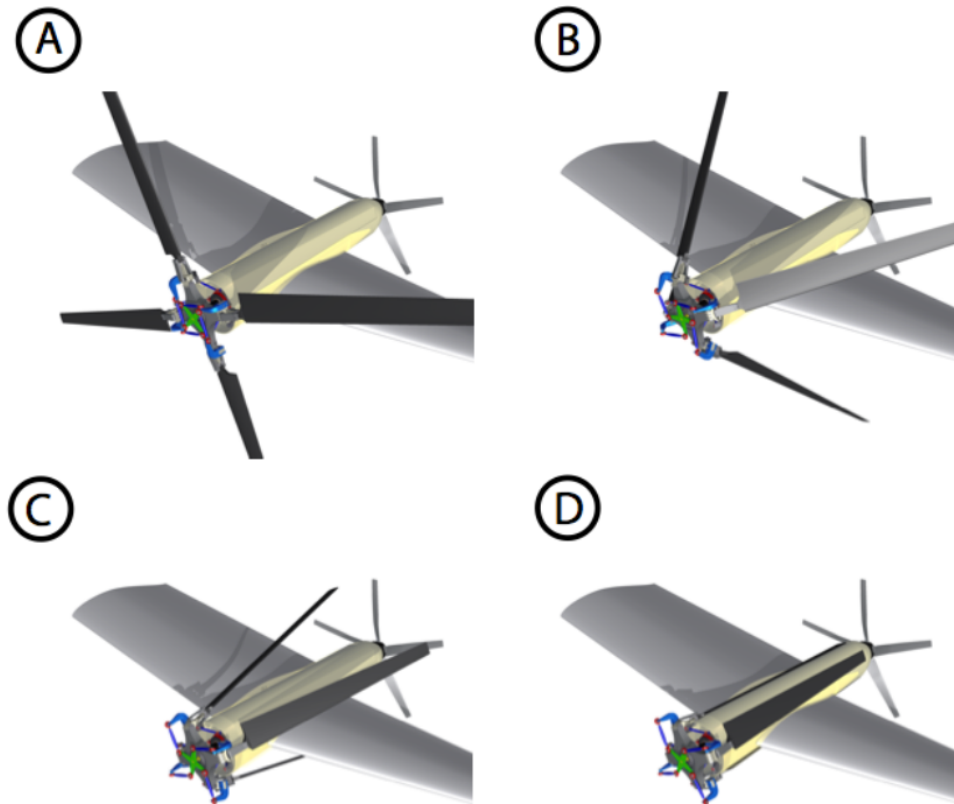


Figure 6.9: *Ragno* folding steps

6.4. Telescopic blades

One of the main challenges in the design of this aircraft is the difference between the rotor dimensions required for vertical takeoff and landing and those allowed for high-speed flight. In fact, the longer the rotor blades, the greater the thrust they generate. However, at high speeds, large rotor blades represent an issue in terms of aerodynamic performance. For this reason, have been analyzed telescopic blades, i.e. blades that have the ability to change their length during flight, allowing the helicopter to adapt to different situations and workloads.

However, this technology exists only at a theoretical level and has not yet found any practical real-world applications.

6.5. Tilting mechanism

Through the examination of the tiltrotors discussed in the Chapter 5, it can be seen that there exist several rotor tilting mechanisms.



The V-22 Osprey rotates the entire nacelles in the conversion phase from helicopter to airplane mode, while the V-280 has a innovative tilting gearbox design where the output shaft is connected to the drive system through a spiral bevel gearbox that transfers power to the fixed gearbox and proprotor gearbox, which rotates on two big spherical bearings driven by a conversion actuator mechanism. In this way, the gearbox is the only thing that rotates whereas the engines do not.

The difference between the 2 mechanisms can be seen in Figure 6.10.



(a) V-22 tilting mechanism



(b) V-280 tilting mechanism

Figure 6.10: Two different tilting mechanism

The V-280 fixed engine configuration provides both operational and maintainability features across the spectrum of FVL multi-service mission sets. This configuration allows maintainers the ability to remove an engine, drive shaft or gearbox independent of each other, reducing time required for maintenance procedures, and increasing aircraft availability to the operator. Having a non-rotating nacelle affords troops easy access entering and exiting the side doors and allows the aircraft to deploy self-protection weapons while conducting low-speed flight approaching, departing and in landing zones [20].

7 | Conceptual design trade studies

In this chapter some possible configurations will be analyzed in order to choose the one able to best satisfy the requirements. The selection of a configuration consists in the choice of aerodynamic and control surfaces, shape of the fuselage and propulsive system.

The study of the best possible configuration in each aspect was carried out in conjunction with the preliminary sizing in order to get quantitative feedback on it especially in terms of the propulsion system chosen.

First of all, from the RFP the required performance to be achieved were analyzed so that they would guide the choices to be made. A great deal of attention was paid to the propulsion system capable of providing the required speeds and altitudes as well as the ability to VTOL. In fact, as mentioned before in Chapter 5, the tiltrotors currently in the market capable of sustaining a vertical landing and takeoff while in cruise flight behaving like a conventional aircraft, exploit a propulsive system with propellers positioned on the wingtips equipped with a mechanism to rotate the shaft and thus the thrust axis. Such aircraft thus exploit propeller propulsion in cruise flight, which is insufficient for the performance required by the Vertical Flight Society. In fact such aircraft can reach for reasons of aerodynamic performance of the propellers speeds up to 280 kn (519 km/h). For this reason, it is immediate to have to rely on the use of one or more jet engine in cruise.

From this consideration, attention was then turned to the critical issues addressed to the sustainment of vertical flight, taking into consideration both jet, rotors and propellers.

This chapter will explore their advantages and disadvantages, along with their operations and possible arrangements in the aircraft design.

7.1. Possible configurations

Starting by considering an aircraft that possesses a jet propulsion system as its only propulsion system, it is possible to immediately assume its implications. First of all, the advantage of carrying on board a single propulsion system that can be used both in the vertical take-off and landing phases and in the cruise phase is evident. This option would be convenient from a point of view of the complications involved in controlling and managing two different power plants. A conventional wisdom says that it is undesirable to "mix" different types of power plants in one airplane due to the difference mode of piloting and the conversion phase that would be required to change from one configuration to the other. Although, therefore, this solution would be convenient because it is the only one that can meet the requirement of carrying a single power plant on board, it must be discarded because of the high complications associated with the use of jet engines in the vertical take-off and landing phases. In fact, special attention is required in the RFP to include features to mitigate the severity of the outwash/downwash environment on ground personnel. Therefore, the possibility of sustaining a possible vertical or hover flight with a jet propulsion system would be unthinkable due to the speed and heat of the jet exhaust.

The only existing aircraft that possesses the ability to also use its jet engine for vertical take-off and landing is the F-35B, which in fact fills a totally different role from that required by the Raven 4.

For hover and vertical flight phases, therefore, it is necessary to turn to a propulsion system such as a rotor or propeller. In order not to incur in too high drag or structural problems related to the blades (whether these rotor or proprotor) it will be necessary to develop an innovative technology that allows the blades to close on properly sized nacelles. So as to ensure higher efficiency, lower drag, lower power consumption, and a cleaner aircraft design.

So now, in this analysis, several configurations have been considered, that can be divided in two large groups on the basis of the type of blades used in the propulsive system:

- Rotor blades: in this type of configurations the rotors can be used only in the hover phase.
- Proprotor blades: in this type of configurations the rotors can be used both in hover phase and propeller mode.



Furthermore, have been considered configurations with different number of rotors, different number of wings, swept both backward and forward, and different location of the rotor engines. All these configurations are characterized by a jet engine mounted on the rear fuselage, necessary to satisfy the requirement of high speed in cruise phase.

They are described below:

1. Two rotors with rotor blades located at wing tips and one engine for each rotor.
2. Two rotors with rotor blades located at wing tips and one engine for both rotors placed in the fuselage.
3. Four rotors with rotor blades located at wing tips and at horizontal tail tips; one engine for each rotor.
4. X-wing four rotors configuration with rotor blades located at wing tips and one engine for each rotor.
5. Two rotors with proprotor blades located at wing tips and one engine for each rotor.
6. Two rotors with proprotor blades located at wing tips, one engine for each rotor and tilting wings.
7. Two rotors with proprotor blades located at wing tips and one engine for both rotors placed in the fuselage.
8. Four rotors with proprotor blades, two on each of the two swept back wings.
9. Four rotors with proprotor blades located at wing tips and one engine for each rotor.
10. X-wing four rotors configuration with proprotor blades located at wing tips and one engine for each rotor.

7.2. Analytic Hierarchy Process

In order to choose the best configuration between the ten listed previously, the Analytical Hierarchy Process (AHP), an analytical process used to make complex decisions, has been applied.

This method consists in:

1. Selection of criteria that each configuration has to satisfy.
2. Ordering the criteria from most to least desirable. This order is obtained through pairwise comparison of criteria, giving a relative weight to each one with respect to

the others.

3. Numerical weights are calculated for each configuration. These weights represent the alternatives' relative ability to achieve the goal.

In order to avoid bias in decisions and have more reliable results, the team was divided into two group who worked independently. Only in a second moment the group was reunited to compare the result of the Analytical Hierarchy process and to establish the final criteria ranking.

Criteria that have been considered are drag, downwash mitigation, hover performance, maneuverability, best rate of climb, weight, technical maturity, conversion phase, safety, cost, damage resistance, complexity of the engine, size, fuel consumption, maintainability, versatility, foldability and stealthiness.

The obtained weights for each criteria have then been scaled in percentile from the most important to the last. Obtaining the following order of importance for the criteria to be considered most when choosing the configuration:

Criteria			
1	Downwash	11	Damage resistance
2	Drag	12	Versatility
3	Conversion phase	13	Cost
4	Hover performance	14	Stealthiness
5	Best rate of climb	15	Maintainability
6	Technical maturity	16	Size
7	Maneuverability	17	Fuel consumption
8	Complexity of the engine	18	Foldability
9	Safety	19	Manufacturability
10	Weight		

Table 7.1: Criteria order for the configuration choice

1. Downwash: turns out to be the most important criterion when choosing the configuration since it ensures the fulfillment of a specific requirement of the RFP and an adequacy to the operations to be performed in terms of search and rescue and troop transportation. In fact, without good mitigation of this phenomenon the designed aircraft would not be suitable for the type of mission to which it would be dedicated.
2. Drag: a critical factor for an aircraft that must fly at high speed.



3. Conversion phase: turns out to be the most critical phase for an aircraft of this type. The conversion from rotorcraft-mode to jet-mode and vice versa, in addition to never being experienced, also requires special attention to both the mechanics of flight and the mix of controls that pilots will have to watch out for.
4. Hover performance: operations and stability in hover turn out to be of considerable importance to be suitable for the missions of interest.
5. Best rate of climb: Operating in a hostile environment, the ability to move quickly away from any ground threats, such as shoulder-fired missiles, may be a determining factor
6. Technical maturity: given the high technological challenge in developing an aircraft that is capable of both high-speed operation and hover and vertical flight, we need to proceed in steps without projecting to technological frontiers that are still too far away and still not very feasible such that a TRL 9 level is reached in 2036 as required by the RFP.
7. Maneuverability: high maneuverability can make a difference for handling qualities especially when the Raven 4 will need to operate close to the ground in penetration or rotorcraft-mode phases.
8. Complexity of the propulsion system: similarly to the technical maturity discussion, the complexity of the propulsion system turns out to be a crucial point for the TRL of an aircraft as this.
9. Safety: given the technological challenge to be faced, safety becomes a key factor to refer to in order to ensure a possible investment in the development and production of such an aircraft. It should be noted that such an aircraft would meet MIL-STD military certifications that allow much less controlled production and use than a civilian use aircraft. Using the Raven 4 in military contexts helps to be able to take higher design risks than the assurance that a civilian aircraft would have instead.
10. Weight: weight is not among the most important characteristics but still a decisive factor for an aircraft capable of sustaining vertical thrust.
11. Damage resistance: operating in a military context it is necessary to take into consideration the possibility of possible firefighting; although this is a factor to be taken into consideration it is necessary to remember what roles Raven 4 is primarily dedicated to.
12. Versatility: in developing such an aircraft, offer the ability to fulfill multiple roles

of search and rescue, light supply, troop transportation and infiltration may prove to be of considerable importance in the current market.

13. Cost: considering such a project means being aware of a considerable engineering and testing effort to ensure its success. Thus, while cost remains a major benchmark for the validity of a program, it is necessary not to be guided primarily by this factor in order not to incur an impossible goal to achieve.
14. Stealthiness: Always an important factor in military context. Intended as aural, thermal and radar.
15. Maintainability: in military programs there is a downward trend in the cost of maintaining the assets. So it is right to pay attention to it but because of the technological complexity involved, maintenance will need to be done consistently and meticulously.
16. Size: given the large size of the cargo area, this becomes a secondary factor to look at for successful design.
17. Fuel consumption: to ensure the success of the project and contextualizing its use in the military, no attention was paid to fuel consumption if not for weight issues.
18. Foldability: shipborne capabilities can be crucial for operations in remote areas, as well as for the ease of machine transport and parking. However, to ensure the initial success of the project design, attention was paid to other key factors, leaving the possibility of such consideration in the future.
19. Manufacturability: In an aircraft of this complexity this does not seem to be a determining parameter. Consider also that the number of examples that would be built would be very limited.

Therefore, assigning for each criteria a grade from 1 to 5 for each selected configuration, a final score was obtained for each configuration, where those with the highest scores will turn out to be the most interesting for the project.

Configuration	1	2	3	4	5	6	7	8	9	10
Weight	133.86	131.29	80.43	85.29	123.29	115.57	122	91.43	85	81.29

Table 7.2: Configuration weights

As can be seen in Table 7.2 the winning configuration is the first one: two rotors, with rotor blades, located at wing tips and one engine for each rotor. The second emerging



configuration turns out to be the same as the first but with proprotor instead of rotors. The comparison of these two propulsion systems for flight in the rotorcraft-mode required quantitative analyses to investigate which of the two was the most convenient configuration.

7.3. Selection of the propulsion system

The main guidelines in the choice of propulsive system for vertical and hover flight are given below.

Rotor:

- Forward flight capabilities limited to edgewise flight.
- Regarding the mechanism for closing the blades around the nacelle, it is possible to exploit a technology already acquired presented with the Nibbio project during the Vertical Flight Society competition in 2016.
- Engines require less power needed to sustain vertical flight than proprotor.
- Ability to perform autorotation.
- Lower disk loading and thus reduced downwash.

Proprotor:

- Climb phase can be done with propellers (more efficient than jet). In addition, the engine jet and the proprotor propulsion system can combine in climb phase to achieve better performance in terms of climb rate and climb gradient.
- Higher power requirements w.r.t rotors.
- Folding method yet to be developed. Technology not yet existing.
- There is a limited possibility of autorotation.
- For the same vertical thrust, the disk loading is greater and so the downwash.

From these observations together with the information obtained from the SMP presented in the Preliminary sizing Chapter [9], the choice of rotors was chosen.

In choosing the propulsion system configuration, the possibility of equipping the rotors with telescopic blades to sharpen the folding mechanism of the blades around the nacelles present on the wingtips was explored. This technology also presented in Chapter 6 was

found to be discarded because of the additional complexity it would add to the design and its very low TRL.

7.4. Selection of the final configuration

Once the propulsive system has been chosen, the other aspects that define the configuration have to be analyzed.

- **Wing**

An high wing configuration has been chosen, because it allows the aircraft's fuselage to be closer to the ground during the operations of loading and unloading. Allowing operations executable from the side doors. The choice therefore of a high wing configuration turns out to be quite unequivocal.

- **Tail**

Among the tail configurations analyzed we have: traditional tail, T-tail, H-tail and V-tail.

Taking into account the presence of one jet engine on the top of the rear fuselage, the possibility of having a traditional tail or a T-tail has to be discarded. In fact only if the jet engine was integrated into the tail (Figure 7.1) or if two jet engines were mounted as in Figure 7.2 this configuration would be possible.



Figure 7.1: Engine tail integration



Figure 7.2: Two engines at the tail

This configuration was later discarded because a single mid-engine is found to be more protected from ingestion of debris as well as being a lighter and more fuel-efficient solution. The integrated jet engine solution was instead discarded due to the



structural complexity related also to the presence of the rear cargo ramp, combined with a greater cross section radar.

An H-tail, on the other hand, was discarded to facilitate access to the rear ramp while maintaining an aerodynamic fuselage profile. A V-tail was found to be favorable so that it could with its surface area shield the hot gases coming out of the jet engine, thus bringing greater thermal shielding, which in a military environment can result in greater stealthiness. Furthermore, V-tail reduces the number of right angles on the aircraft, improving its stealthiness.



(a) Traditional tail



(b) T-tail



(c) V-tail



(d) H-tail

Figure 7.3: Tail configurations

- **Fuselage** An aerodynamic profile was chosen for the fuselage that would optimize performance at high speed. Side doors will be taken into account in its design for easy access and mission performance in case of search and rescue. Along with these there will also be a rear ramp for more convenient access in the case of cargo transport: this choice will involve additional attention to the corners of the tail cone to avoid separation flows that can increase drag at high speeds.

A pressurization of the cabin and cockpit is be taken into account to guarantee to ensure greater safety and operational capability of pilots and passengers.

- **Position of engine-jet** Taking into account the possibility of debris ingestion and the operational capability of the aircraft, the only place where it was possible to

put a jet engine was on the top of the rear part of the fuselage.

- **Landing gear** The choice of a high wing will require the addition of pods for the landing gear bay, due to the limited space available in the fuselage. A forward tricycle configuration was chosen to ensure at a preliminary stage the support of an undercarriage that could apply not only to a vertical landing or takeoff, but also to a conventional landing.

In Figure 7.4 it's possible to see a sketch of the preliminary configuration.

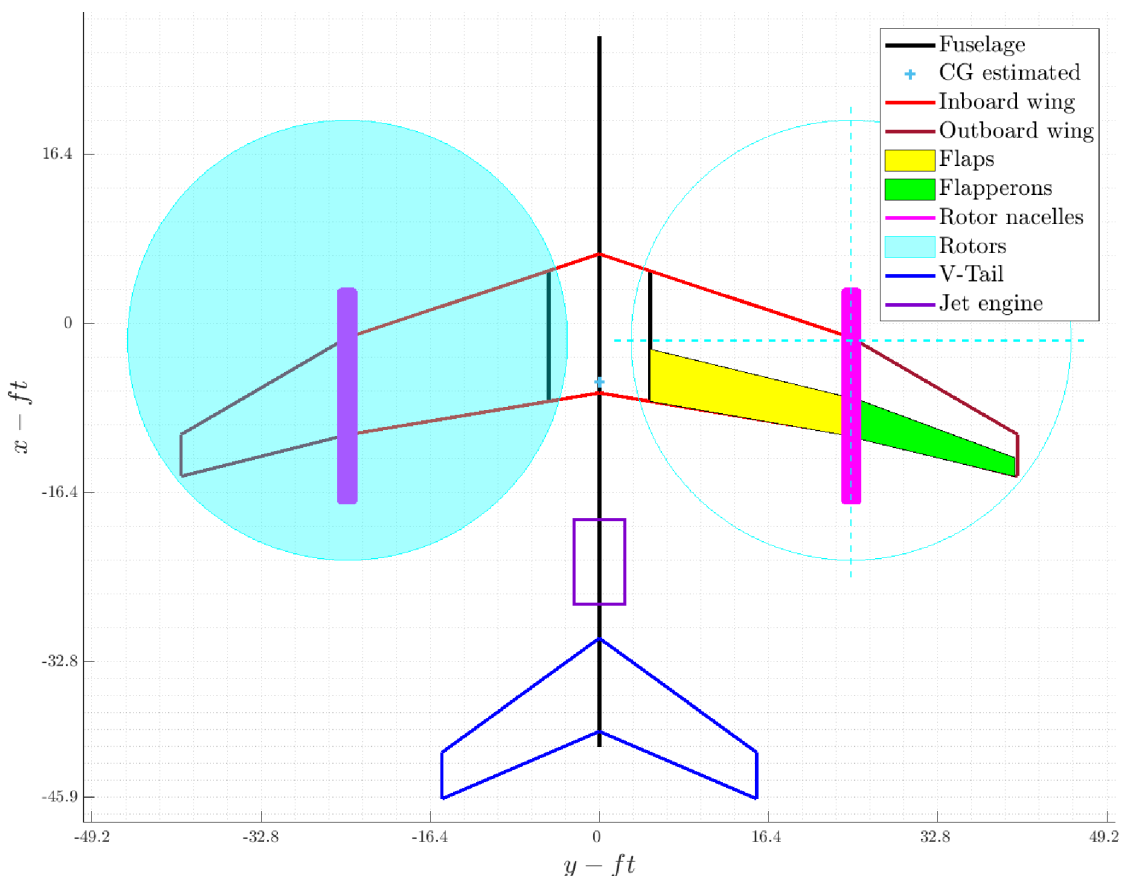


Figure 7.4: Top view of the preliminary aircraft



8 | Emission of requirements

To initiate the design of the aircraft, a list of requirements to be adhered to and achieved was developed through market analysis and an iterative process throughout the preliminary design to best express the potential of the aircraft presented here.

These requirements are summarized in Table 8.1.

	Value	Selection
Crew	3 member	RFP
Range	1,000 nm (1852 km)	RFP
Payload	7300 lb (3310 kg)	Team
Cruise altitude	20,000 ft (6,096 m) ISA or higher	RFP
Cruise speed	450 KTAS (833 km/h)	RFP
Penetration speed	500 KTAS (926 km/h) @sea level ISA	Team
Rate of climb	3700 ft/min (18.8 m/s) @sea level ISA	Team
Time to climb at cruise altitude	6.6 min (396 s)	Team
Stall speed in conversion config.	100 KTAS (185 km/h) @2,000ft ISA	Team
Cruise ceiling	Cruise altitude or higher	Team
Service ceiling	50,000 ft (15,240 m) ISA	Team
Takeoff distance	3,280 ft (1,000 m)	Team
Landing distance	3,280 ft (1,000 m)	Team
Sustained turn	2.5g @450 KTAS, sea level ISA	Team
Instantaneous turn	3g @230 KTAS, sea level ISA	Team

Table 8.1: Emission of jet-mode requirements

As an example of this mainline we can check at the choice to add the payload weight available with respect to the request for proposal [31], which was only of 5,000 *lb*. This choice was, in fact, made as a conclusion of an iterative approach, with further studies conducted in the project to enhance the aircraft's performance and optimize operational capabilities, thereby making the best use of the ample cargo space required by the client.

As for the aircraft requirements mentioned in Table 8.1, that have both general and specific relevance to the flight as a traditional jet-propelled aircraft, the following are the design requirements for the rotorcraft-mode phase defined from the Vertical Flight Society's RFP and by the team from the market and/or sensitivity analysis.

	Value	Selection by
Disk loading @MTOW	lower than 23 psf (1100 N/m^2)	Team
HOGE	MMGW @ 2000 ft ISA + 13°C , MCP	RFP
HIGE	MTOW @ 2000 ft ISA + 13°C , MCP	RFP
Vertical climb	6 ft/s (20 m/s) @ 2000 ft ISA + 13°C , MCP	Team
V_H	130 KTAS (67 m/s) @ 2000 ft ISA + 13°C , MCP	Team

Table 8.2: Emission of rotorcraft-mode requirements



9 | Preliminary sizing

9.1. Aircraft weight estimation

The purpose of this chapter is to obtain a preliminary estimate of the Maximum Take-Off Weight through an analytical-statistical method described in reference [23], presented below.

The weight of the aircraft can be broken down as follows:

$$W_{MTOW} = W_E + W_C + W_L + W_F \quad (9.1)$$

Now, from mission requirements the crew weight W_C as well as the payload W_L are known. Hence the unknowns remain W_E and W_F .

The purpose of the next sections is to get them as a function of MTOW.

9.1.1. Statistical regression for empty weight fraction

This relationship between empty weight and MTOW can be obtained through statistical data for categories of aircraft or can be created ad hoc for the case study by collecting categories of aircraft that match the aircraft being designed.

Each category of aircraft has a ratio of empty weight to MTOW that vary in a way that can be described by a regular function. Supposed that the aircraft in size, purpose and characteristics regarding empty weight fraction might behave similarly to jet transports, twin turboprops and military cargo, a potential similarity for the empty weight fraction related to the Maximum Take-Off Weight can be assumed as an initial assumption. In fact, by considering as reference aircraft the existing modern tiltrotors that are emerging in the international scenario, especially in the military scenario, it's possible to see that they cover the same region in the graph going to indicate a structural and propulsive similarity as shown in Figure 9.2. As previously mentioned in the market analysis, tiltrotors considered are: V-22 Osprey, V-280, AW-609, XV-15 and the Do-31. Before arriving at a final choice for the regression, other military aircraft have been considered, including helicopters such as the CH-47 and jet aircraft such as the C27-j and the C-130H, which

have weight, payload, and speed characteristics in common with the design of the Raven 4. Ultimately, given the particularity of the goal to be achieved, we opted to consider only the tiltrotors currently on the international scene because of the greatest similarity in terms of configuration and role to be played.

However, in order to close the technology gap with our design, for which a jet engine will need to be installed, an increased payload equal to the additional propulsion system was considered in the iterative calculation for maximum takeoff weight. In other words in this phase the jet engine has been considered as an increased payload of 1500 kg.

The regression was also compared with other types of regression considered at the conceptual stage to be less reliable and less conservative for our aircraft. In fact, different regressions led to a final weight assumption that was too conservative or unbalanced so that the final result could not be reliable.

9.1.2. Fuel fraction method

Now it's time to consider fuel. The primary mission can be broken down into sub phases, and for each of them the fraction of fuel to total can be obtained through statistical data obtained from [23] selecting the categories of aircraft that could most closely resemble our aircraft. Business jets, Military Patrol Bomb, Transport Jet and Regional Turboprop. Results are reported in table 9.1.

$$\frac{W_F}{W_{MTOW}} = 1 - \frac{W_N}{W_{MTOW}} = 1 - \left(\frac{W_N}{W_{N-1}} \frac{W_{N-1}}{W_{N-2}} \dots \frac{1}{W_{MTOW}} \right) \quad (9.2)$$

1 st Part	Idle	HIGE	Climb	Cruise	Descent	Penetration	HOGE
	0.9900	0.9930	0.9700	0.9580	0.9876	0.9957	0.9900
2 nd Part	Climb	Cruise	Descent	Penetration	HOGE	Landing	Reserve
	0.9700	0.9580	0.9876	0.9957	0.9900	0.9980	0.9809

Table 9.1: Fuel fraction for each part of the mission.

As can be seen in the Table (9.1) in the equal flight phases, lower fuel consumption in the later phases, due to the lower weight, was not considered in order to ensure a wider safety margin. In fact, the information necessary for accurate calculation of the fractions of fuel needed is not yet available.

In truth, not all fuel fraction has been statistically estimated. In fact, Breguet's formulas have been used for the cruise phases. However, these formulas depend, among other



things, on the lift to drag ratio so it is necessary to get an estimate of the polar. To construct the polar model, two distinct methods have been followed. The first method is an empirical approach based on a possible classical geometry of the aircraft to obtain the wetted surface, while the second one is a historical-statistical method based once again on reference values taken from [23]. In order to proceed with an univocal choice, greater confidence was placed in the polar derived from the Roskam's work, since it is more conservative and has already been verified in other aircraft design. Both methods were fed with initial statistical guesses consistent with the aircraft being developed, as well as direct competitors. Results for the two different approaches are reported in Figure 9.1.

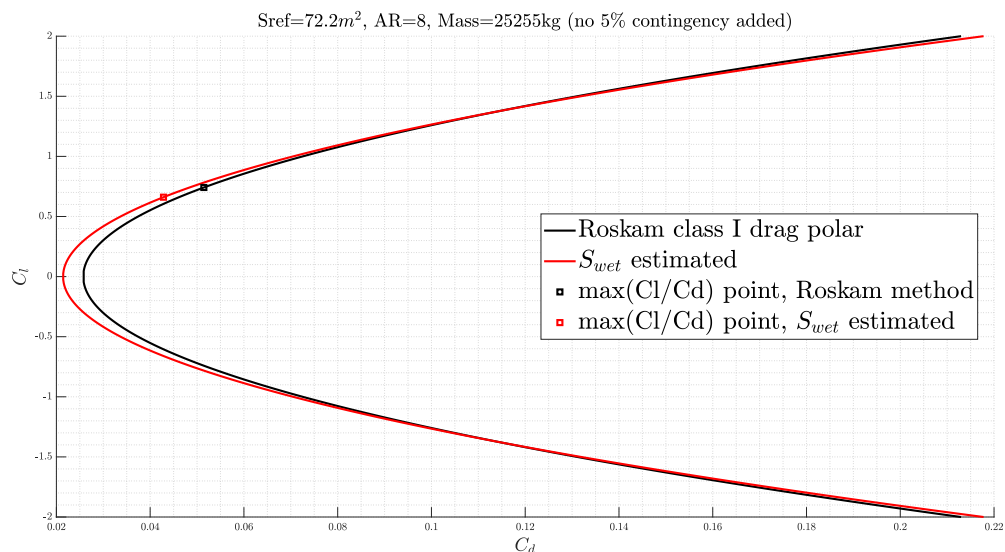


Figure 9.1: Different polar estimation methods

It is important that, among other things, the polar estimate depends on the chosen surface. However, we will see that the next section, the sizing matrix plot section, also depends on the surface. So it's important to keep in mind that this is an iterative process and that all the values given in these tables refer to the last iteration.

Aerodynamic parameters used and obtained are reported in 9.2

S_{ref}	777.2 ft^2 (72.2 m^2)
AR	8
Cf_e	0.004
e	0.85
K_e	$\frac{1}{(\pi \cdot AR \cdot e)}$

Table 9.2: Aerodynamics parameters

9.1.3. Weight estimation results

At this point:

$$W_E = W_E(W_{MTOW}) \quad (9.3)$$

$$W_F = W_F(W_{MTOW}) \quad (9.4)$$

Hence the following equation 9.5 can be solved for W_{MTOW} , using some algorithm, e.g. Newton-Raphson.

$$W_{MTOW} = \frac{W_C + W_L}{1 - \frac{W_F}{W_{MTOW}} - \frac{W_E}{W_{MTOW}}} \quad (9.5)$$

Graphical solution is shown in 9.2.

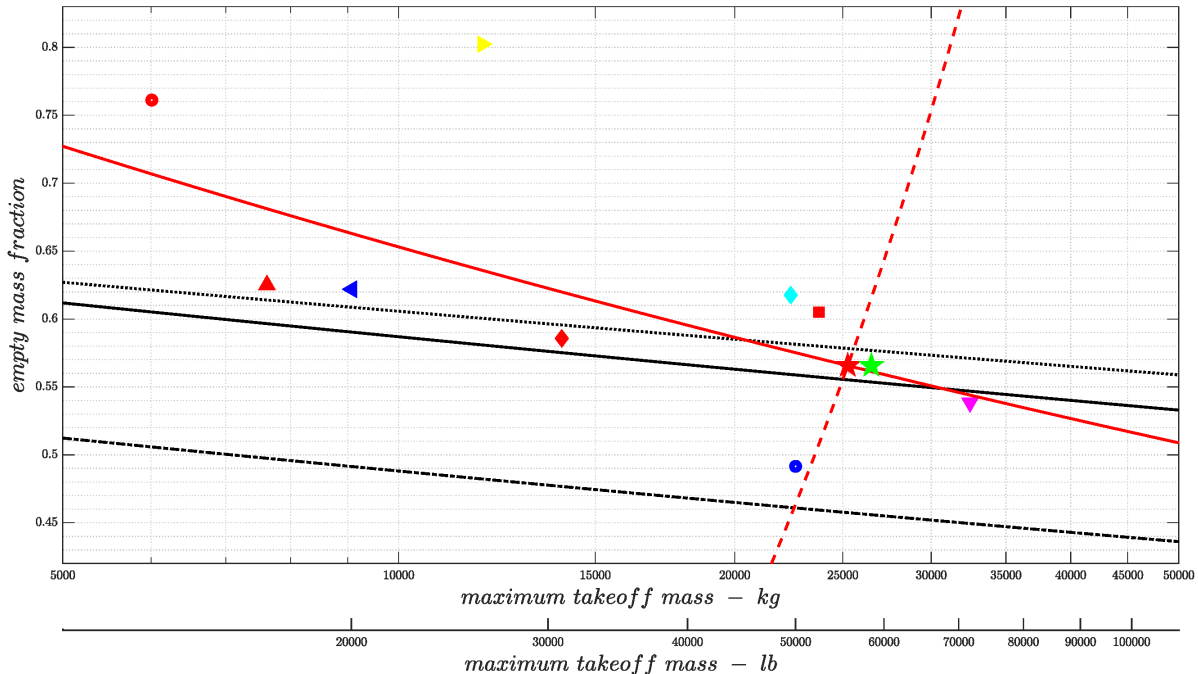


Figure 9.2: Graphical solution of the implicit equation (9.5)



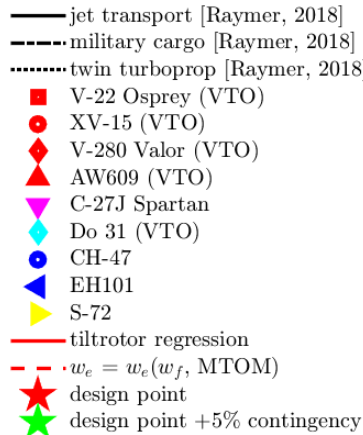


Figure 9.3: Legend of Figure 9.2

The design point is in the area of V-22, while achieving a slightly lower empty mass fraction, consistent with technological progress over the V-22 design period.

A weight contingency of 5% was added as a margin of safety.

Finally note that in the results below, Figure 9.4 and Table 9.3, the jet engine weight was shifted back from payload to empty weight.

Payload	MEP	Crew	Fuel	Empty weight	Total weight
7,321lb (3,321kg)	1,049lb (476kg)	784lb (356kg)	12,760lb (5,788kg)	36,541lb (16,575kg)	58,462lb (26,518kg)

Table 9.3: Weight fractions obtained at the initial iteration

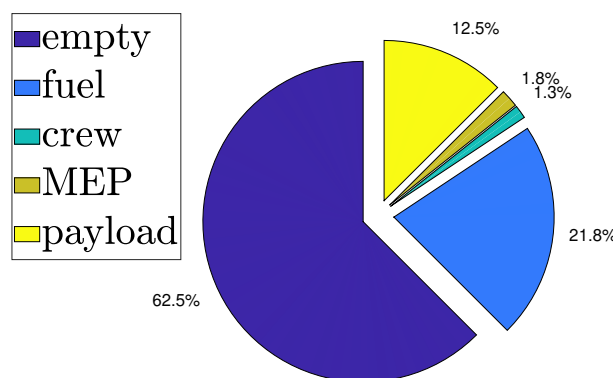


Figure 9.4: Preliminary weight breakdown

9.2. Jet-mode sizing matrix plot

The sizing matrix plot for the jet-mode aims to obtain an estimated thrust-to-weight ratio (in terms of Maximum Continuous Thrust) and weight-to-wing area ratio, also called wing loading. Establishing these quantities is extremely effective at the preliminary stage since a large number of aircraft performance can be related to them.

Starting from the requirements issued in the Chapter 8, and using both analytical and statistical formulas provided by reference [19] and [23], it is possible to generate the following graphs, figures 9.5, 9.7.

It is important to note that the results are dependent on the weight and reference surface, which are used to generate the drag polar. However, the same weight obtained during weight estimation is dependent on the reference surface, for the same reason. By choosing the design point in the sizing matrix plot it is then possible to update the reference surface, which then entered into the weight estimation will generate an updated weight. This iterative process must be continued until convergence is achieved. For the sake of brevity, the results below are the final results, i.e. after convergence has occurred.

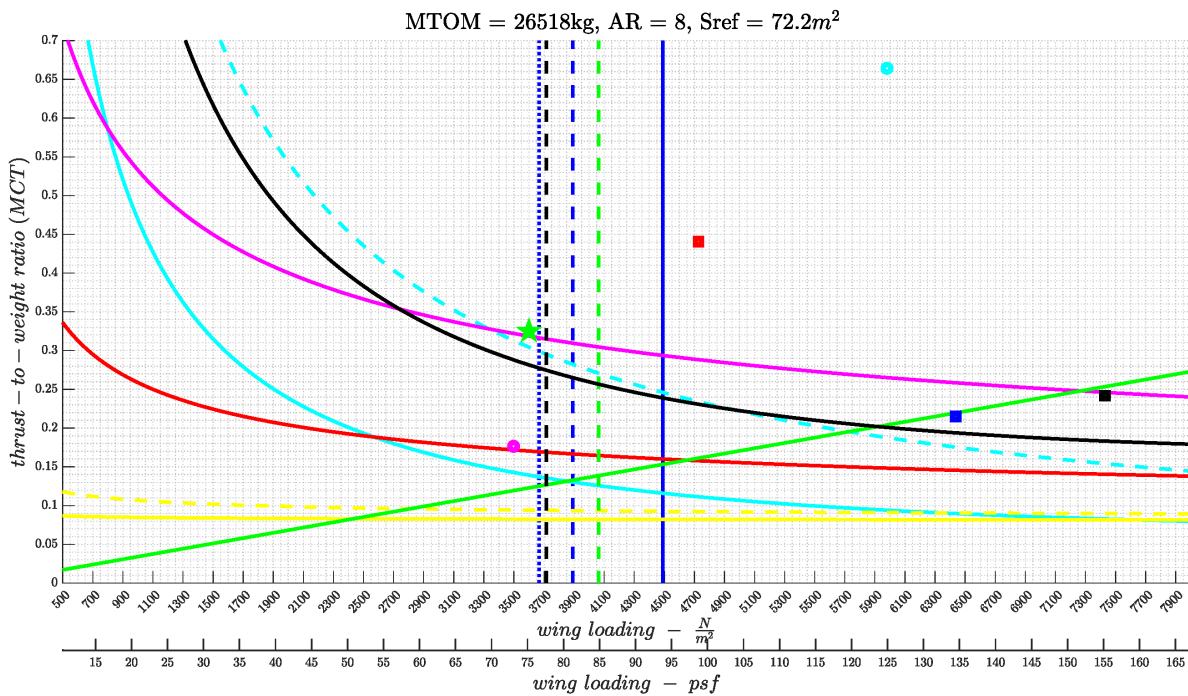


Figure 9.5: Jet-mode sizing matrix plot



- stall clean config. @20000ft ISA, @Cl=1.3, 200KTAS
- - - stall conversion config. @sea level ISA, @Cl=2.4, 100KTAS
- · · stall conversion config. @2000ft ISA, @Cl=2.4, 100KTAS
- cruise speed @20000ft ISA, cruise weight, 450KTAS
- penetration @sea level ISA, cruise weight, 500KTAS
- climb rate @max(L/D) clean config. @sea level ISA, 3700fpm
- time to climb clean config. @20000ft ISA, 6.6min
- cruise ceiling 20000ft
- service ceiling 50000ft
- takeoff distance 1000m
- landing distance 1000m, @110KIAS Vapproach
- sustained turn @sea level, R=2500m, 450KIAS, 65deg (n=2.4), clean config.
- instantaneous turn @sea level, n=3, 230KIAS, clean config.
- C-17 Globemaster III
- C-5 Galaxy
- B-2 Spirit
- Do-31 (STO)
- Harrier GR3
- ★ design point

Figure 9.6: Legend Figure 9.5 and Figure 9.7

For the purpose of clarity, the same graph is shown in the figure 9.7, with only the performances that are constraining or that are particularly important because they are set by the RFP.

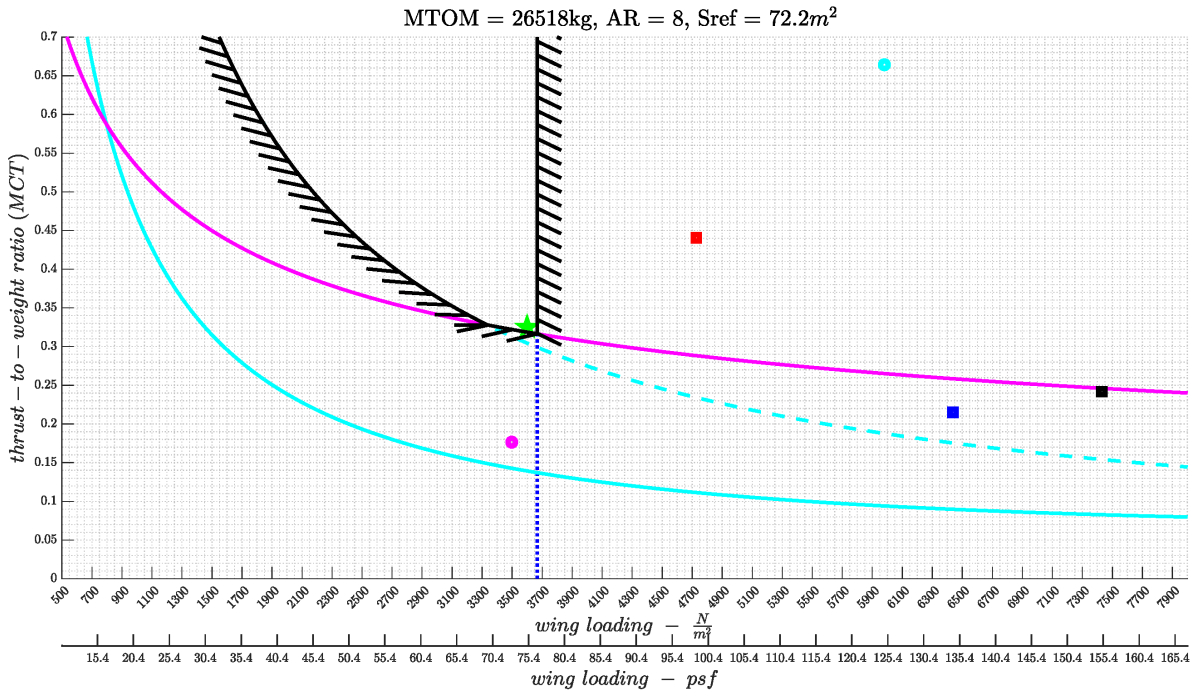


Figure 9.7: Jet-mode sizing matrix plot decluttered

From the design point, it can be seen that the aircraft should have a design wing surface of 775 ft^2 (72 m^2) and a turbojet capable of delivering in MCT a thrust of $18,097 \text{ lb}_f$

(80.5 kN).

Before moving on, it seems opportune to elaborate on the chosen stall speed in conversion configuration, which is the one that in SMP has the greatest impact on the design point and is a key characteristic of the aircraft as it affects conversion phase. Figure 9.8 shows a sensitivity study regarding this:

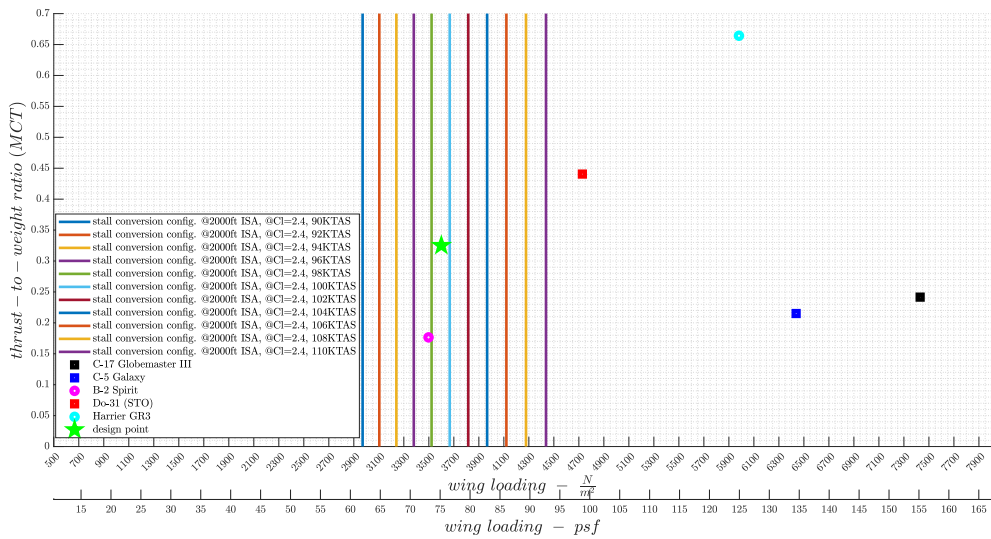


Figure 9.8: Stall speed sensitivity analysis

Surely this is one of those parameters that analysis needs to be careful about in subsequent design iterations, even evaluating a higher maximum lift coefficient, exploiting for example a more complex flaps system, with respect to the maximum lift coefficient chosen here.

9.3. Rotorcraft-mode

Similarly to the previous paragraphs, the sizing matrix plot for the rotorcraft-mode aims to obtain an estimated weight-to-power ratio (in terms of MCP) and weight-to-rotor area ratio, also called disk loading.

This second parameter is particularly critical in the design of the rotor as it is directly tied to the downwash/outwash effects of the rotor. As will be detailed in the next chapter, the lift is obtained from momentum conservation, hence accelerating the air through the rotor. This generates a downwash. Consider now a situation close to the ground, due to the terrain boundary condition, the momentum changes direction, becoming parallel to the ground in a radial-symmetric fashioned way, Figure 9.9. On the other hand, the



ground generates an increment of pressure underside the rotor, enhancing the thrust (or reducing the power required for a given thrust): this is known as the ground effect.

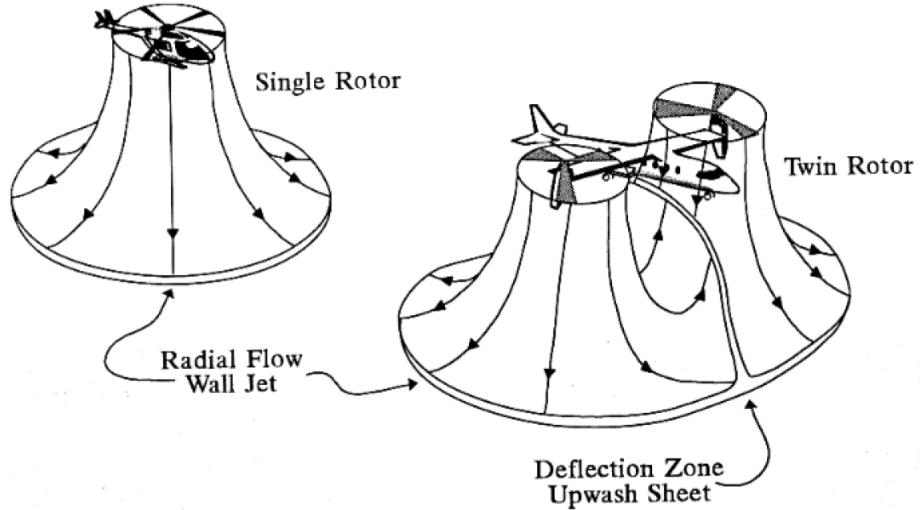


Figure 9.9: Downwash/outwash effect of single and twin rotors [16]

These phenomena heavily affect the operational capabilities of the vehicle: ground personnel difficulties, and surface degradation may prevent the success of the mission. In particular, the degradation of the surface could generate high-speed debris, dangerous for humans but also for the aircraft itself, e.g. foreign object ingestion in engines. In this sense, it is important not only to consider the rotor design but also specific operational surfaces. Detailed information about rotor wash modeling can be found in [16]. In this preliminary phase, the mitigation of these effects is treated as an upper limit to the disk loading value.

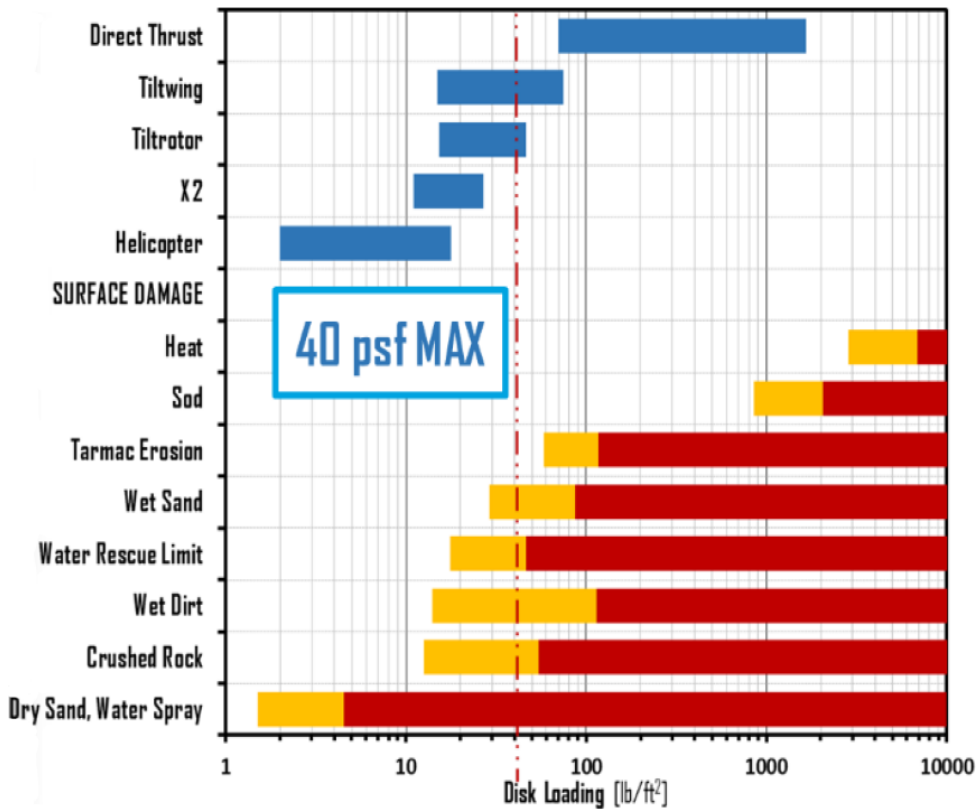


Figure 9.10: Onset of surface failure [31]

Figure 9.10 shows disk loading data for the main rotorcraft designs and its effect on different types of surfaces: in terms of operational capabilities the limit is set at 40 psi (1915.21 Pa) by the RFP. It is clear why a direct thrust design has been avoided, even without considering the high temperatures coming out of the turbines for such a solution. The most critical surface is, as expected, the dry sand/water spray that imposes a significant limit on the disk loading. For this purpose, the lower, the better. However, this implies a greater rotor radius, which could become critical, especially if the rotor must be in-flight foldable.

The problem of preliminary sizing is approached first with a very simple approach, and then goes on to complicate the model to better capture different physical phenomena.

9.3.1. Momentum theory

Momentum theory applies the basic conservation laws of fluid mechanics (conservation of mass, momentum, and energy) to the rotor and the flow as a whole to estimate the rotor performance. The theory is a global analysis, relating the overall flow velocities to the total rotor thrust and power.

In momentum theory the rotor is modeled as an actuator disk, which is a circular surface



of zero thickness that can support a pressure difference (but no velocity change) and thus accelerate the air through the disk. The loading is assumed to be steady, but in general can vary over the surface of the disk. The actuator disk can also support a torque, which imparts angular momentum to the fluid that passes through the disk. The task of the analysis is to determine the influence of the actuator disk on the flow and, in particular, to find the induced velocity and power for a given thrust. The actuator disk model is only an approximation to the actual rotor. Distributing the rotor blade loading over a disk is equivalent to considering an infinite number of blades. The detailed flow of the actuator disk is thus very different from that of a real rotor with a small number of blades. The real flow field is actually unsteady, with a wake of discrete vorticity corresponding to the discrete loading. The actual induced power is therefore larger than the momentum theory result because of the nonuniform and unsteady induced velocity. For analytic details refer to [9].

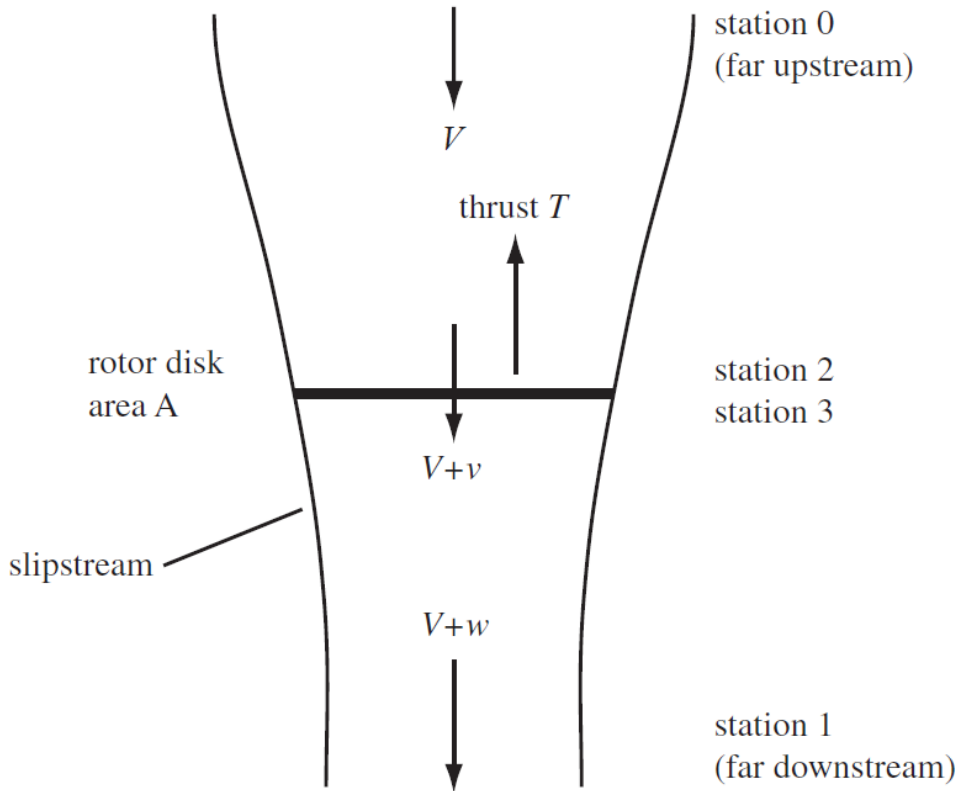


Figure 9.11: Momentum theory model

With reference to the figure 9.11, power and disk loading can be related in vertical flight

as follows:

$$P = T(V + v) = T \left(\frac{V}{2} + \sqrt{\left(\frac{V}{2}\right)^2 + v_h^2} \right) \quad (9.6)$$

$$v_h = \sqrt{\frac{T}{2\rho A}} = \sqrt{\frac{W}{2\rho A}} \quad (9.7)$$

Note that $\frac{W}{A}$ is the disk loading. If the vertical velocity V is zero, the equation goes back to the classic hover condition, i.e. $P = Tv = Tv_h$.

This framework considers only the inescapable induced power, but neither the power required to actuate the rotor, nor all real losses. For this reason, a figure of merit is introduced as follows:

$$M = \frac{P}{P_{req}} = 0.7 \quad (9.8)$$

the figure of merit value is obtained from statistics of well-designed rotors (typical values from 0.74 to 0.78), 0.7 is a conservative starting guess.

In particular, three different conditions have been considered and will be maintained throughout the chapter:

- Hover, unless otherwise specified intended as HOGE
- Vertical Climb at $V_v=19.68\text{ft/s}$ (6m/s) (to mark the performance of the V22 Osprey)
- Forward Flight at $V_{fw}=100\text{kn}$ (51.4m/s), that is the rotorcraft-to-aircraft ideal conversion speed

Each condition has been evaluated, as requested by the RFP [31] at:

- Sea Level ISA, corresponding to a density of $\rho = 1.225\text{kg/m}^3$ (0.076lb/ft^3)
- 2000ft ISA + 55.33°F (12.96°C), corresponding to a density of $\rho = 1.105\text{kg/m}^3$ (0.068lb/ft^3)

For the sake of brevity the equations for forward flight are not reported, since this conditions turns out not to be critical. For details refer to [9].



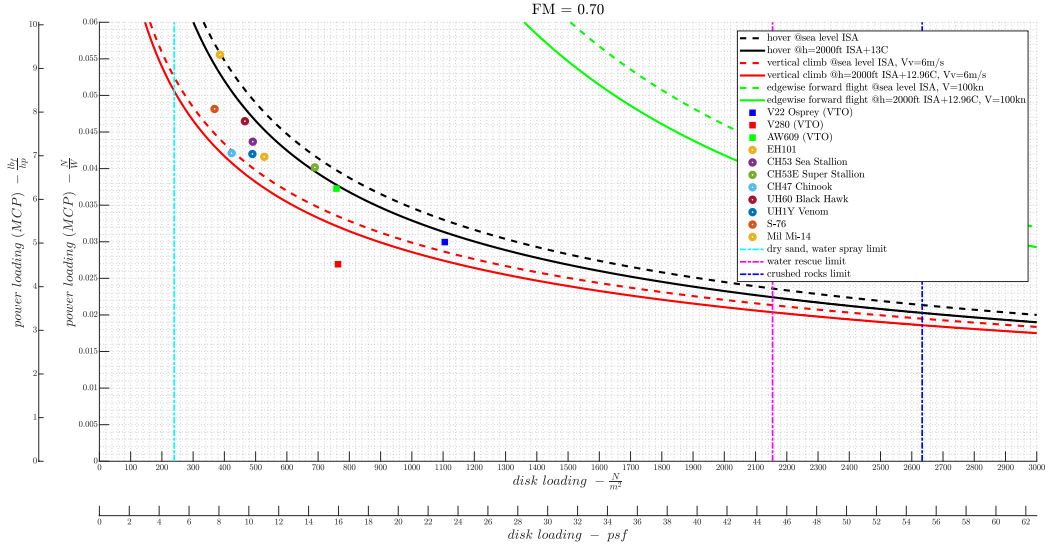


Figure 9.12: Momentum theory results

Results are shown in Figure 9.12. The available design area is under the curves. The most critical condition results in the vertical climb: note that the power required increases with V , but the climb power increment is reduced by the induced power decrease. In addition, the increase in altitude causes an increase in the power required.

Furthermore, design points of several existing rotorcrafts are reported; note two well-defined different areas: one for classic helicopters, with a lower disk loading and a higher weight-to-power ratio, and one for tiltrotors, where the higher disk loading imposed by the geometric constraint and the horizontal thrust requirement cause an increased induced power (specifically they are prop-rotors instead of rotors, this implies a completely different design of the blades, see chapter 5 for details). For completeness, there are also reported the limits for degradation of the two most critical surfaces: note that for water spray and dry sand the requirement is particularly stringent, such that no competitor is able to meet (the two vertical lines are a limitation on the right side).

However, both classes are indeed coherent with the model.

9.3.2. Blade element theory

After an initial more general analysis, blade element theory was introduced to obtain a more realistic model. Indeed, momentum theory is not concerned with the details of the rotor airloads or flow, and hence is not sufficient for designing the blades.

Blade element theory calculates the forces on the blade caused by its motion through the air, and hence the forces and performance of the entire rotor. Blade element theory is

lifting-line theory applied to the rotating wing. Each blade section is assumed to act as a two-dimensional airfoil to produce aerodynamic forces, with the influence of the wake and the rest of the rotor contained entirely in an induced angle-of-attack at the section. The solution thus requires an estimate of the wake-induced velocity at the rotor disk, which is provided by momentum theory, vortex theory, or nonuniform inflow calculations. For a detailed discussion see reference [9].

Ignoring for the moment the forward flight condition, which has been shown to be non-critical, and consider the hover condition. The rotor power breakdown can be done as follows:

$$P = P_i + P_o + P_c \quad (9.9)$$

where:

- P_i : inescapable induced power, the one considered in momentum theory
- P_o : profile power, necessary to move the blades through the air
- P_c : climb power, as seen in the previous paragraph

So the new thing introduced is profile power, estimated through blade element theory. From this time, the presence of two rotors on the aircraft will be approached as an equivalent aircraft with one rotor and weight halved; losses caused by the interaction between the rotors will be considered through efficiency coefficients.

Equation (9.9) can be developed as follows, expanding the three terms under the reasonable assumption in vertical climb that $V = V_v \ll v_h$:

$$P = \frac{kT^{3/2}}{\sqrt{2\rho A}} + \rho A(\Omega R)^3 \frac{\sigma c_{do}}{8} + \frac{VT}{2} = \frac{kW^{3/2}}{\sqrt{2\rho A}} + \rho A(\Omega R)^3 \frac{\sigma c_{do}}{8} + \frac{VW}{2} \quad (9.10)$$

$$\sigma = \frac{Nc}{\pi R} \quad (9.11)$$

where k is an empirical coefficient accounting for losses (mainly due to nonuniform inflow), chosen from statistic 1.17; Ω is the rotation speed of the rotor; the solidity ratio σ accounts for blades number N , chord c , radius R ; a mean drag coefficient $c_{do}=0.0140$ is used for the profile power.

Finally, a coefficient is used to consider all real losses, from transmission-related losses to aerodynamic interactions, such as with the fuselage and, in this specific case, the wings:

$$P_{req} = \frac{1}{\eta} P = \frac{1}{0.85} P \quad (9.12)$$



From blade element theory it is also possible to get an expression for the thrust generated by the rotor, in the case of constant chord, linear twist, and assuming uniform inflow:

$$T = \rho A (\Omega R)^2 \frac{\sigma a}{2} \left(\theta_0 \frac{B^3}{3} + \theta_{tw} \frac{B^4}{4} - \lambda \frac{B^2}{2} \right) = W \quad (9.13)$$

where $B=0.97$ accounts for tip losses that are particularly impactful on rotorcraft since the dynamic pressure is proportional to the square of the radius, a is the blade section two-dimensional lift-curve slope, θ_0 is the collective pitch angle and θ_{tw} is the linear twist rate. Details of the computation of inflow ratio λ can be found in [9].

9.3.3. Sizing procedure

Now that the necessary tools have been presented, it is possible to proceed with the sizing process.

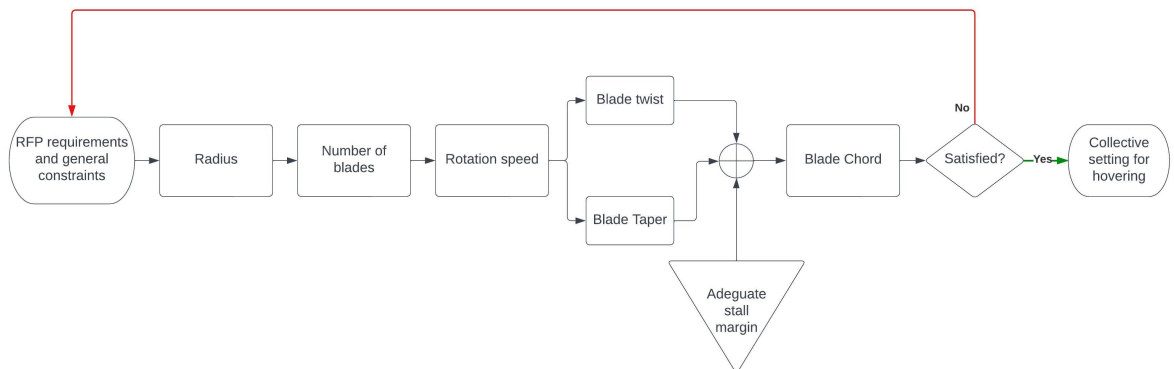


Figure 9.13: Sizing procedure breakdown

Figure 9.13 presents the breakdown of the procedure detailed in the next paragraphs. The airfoil currently used is a NACA23012. The final choice will be discussed later. The sizing weight is the MTOW which currently coincides with the SDGW.

9.3.3.1. Radius

Ideally, increasing the radius it's possible to reduce the induced power, in addition to the obvious general physical limitations, in the present case there are additional considerations, mainly due to the side-by-side configuration and the need to have to fold the blades:

- Since the rotor thrust is applied on its axis, an excessive distance of the same from

the plane of symmetry of the sail would generate a major bending moment at the root of the wing.

By not considering inter-meshing solutions (since interference with the fuselage could be critical during folding, as well as rotor synchronization and mutual interference issues), an excessively long radius would lead to excessive bending moments. Figure 9.14 shows a comparison with aircraft of similar configuration; the black line represent the raven 4 wing root bending moment as a function of the distance between wing root and rotor axis.

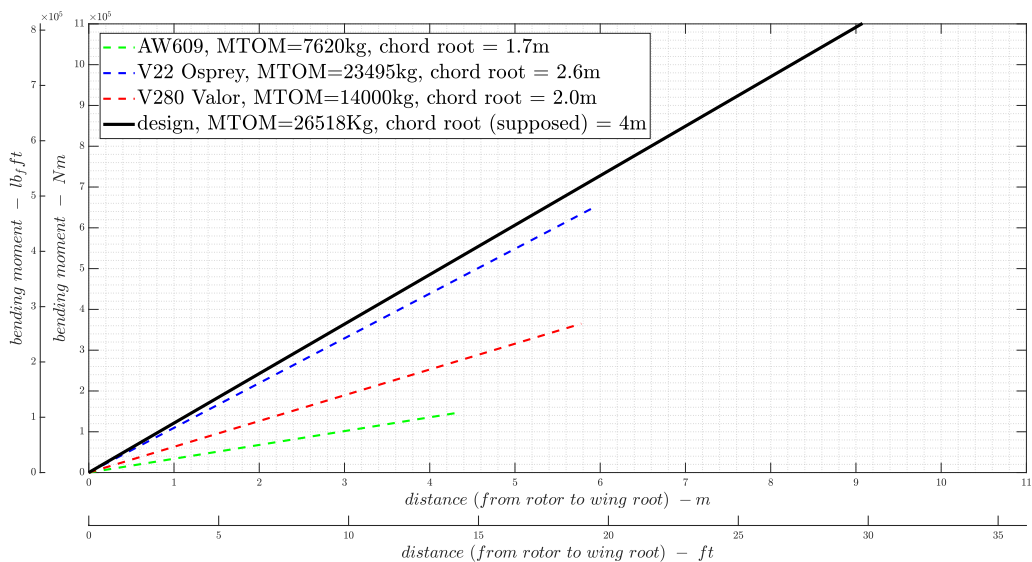


Figure 9.14: Wing root bending moment

- Normally helicopter blades are stiffened by centrifugal force. Unfortunately, during the conversion phase the rotor is stopped and the stiffening is lost. Therefore, it is important to consider the effect of deflection of the blade stopped and exposed to the wind. Figures 9.15 and 9.16 report a study of the deflection of the blade tip as blade stiffness and blade pitch vary, imagining that it behaves like a flat plate exposed frontally to the wind and acting on the collective to reduce its frontal section. Details of the conditions analyzed are given in the title of the figure; of course it's also worth keeping an eye on the stresses in the section, which will be reported later. The condition analyzed sees the open rotor exposed against the wind: in reality this condition does not occur since the closure already begins during the rotation of the mast. However, in this way, a conservative approach is guaranteed. Results are obtained exploiting the elastic line differential equation.



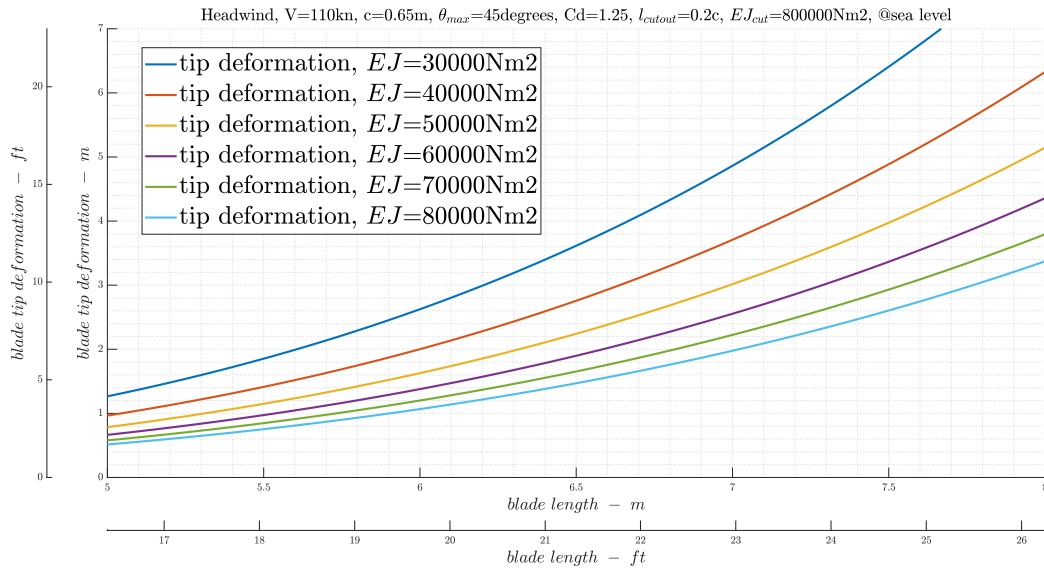


Figure 9.15: Blade tip deflection, varying EJ

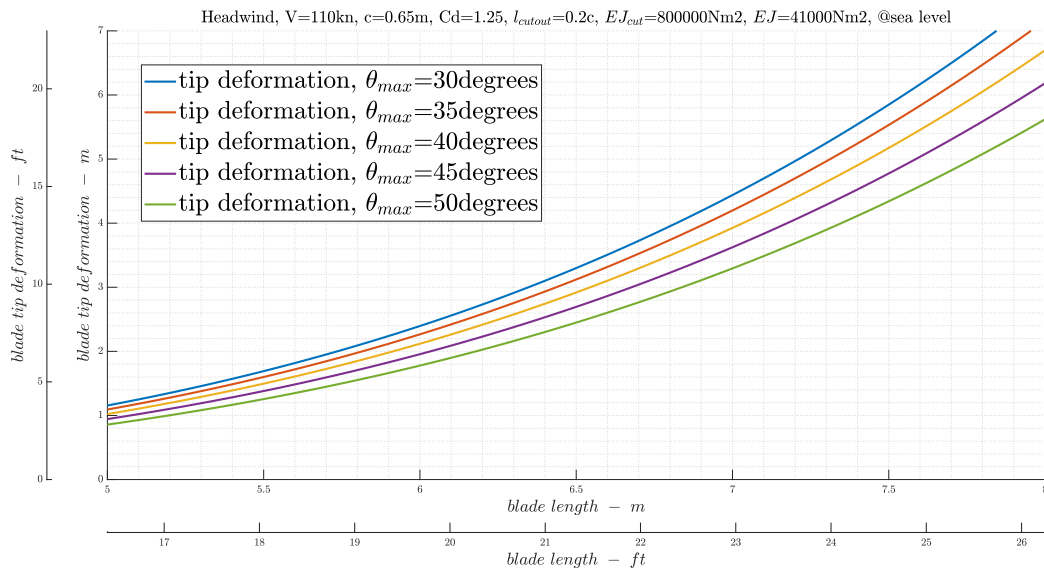


Figure 9.16: Blade tip deflection, varying blade pitch

- A blade that is too long could also create clutter complications, especially when folding the rotor. To this end, a clever way to optimize the folding could be to position before closure, controlling the position of the shaft with an angular encoder, so that the distance between blades and fuselage is as large as possible: consider a 4-blade rotor, with the blades rotated 45 degrees with respect to the straight rotor-fuselage line, the effective encumbrance during closure, and thus forward rotation of the shaft, can be reduced by a factor $\cos(\frac{\pi}{4})$

- On the other hand, a particularly small radius requires, as already seen, more power because of the high induced velocity and, again because of the latter generates an increase in downwash, which as discussed before can be directly related to disk loading. Figure 9.17 shows a sensitivity analysis concerning disk loading vs radius.

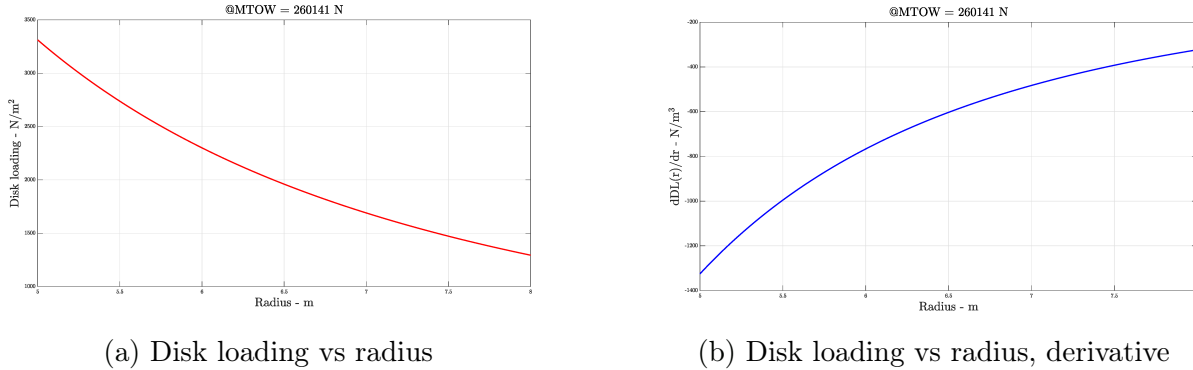


Figure 9.17: Disk loading vs radius sensitivity analysis

As a first guess, considering these factors, a radius of 6.5 meters seems reasonable.

For completeness in Figure 9.18 is given the blade deformation for the chosen radius, under the same conditions as described above.

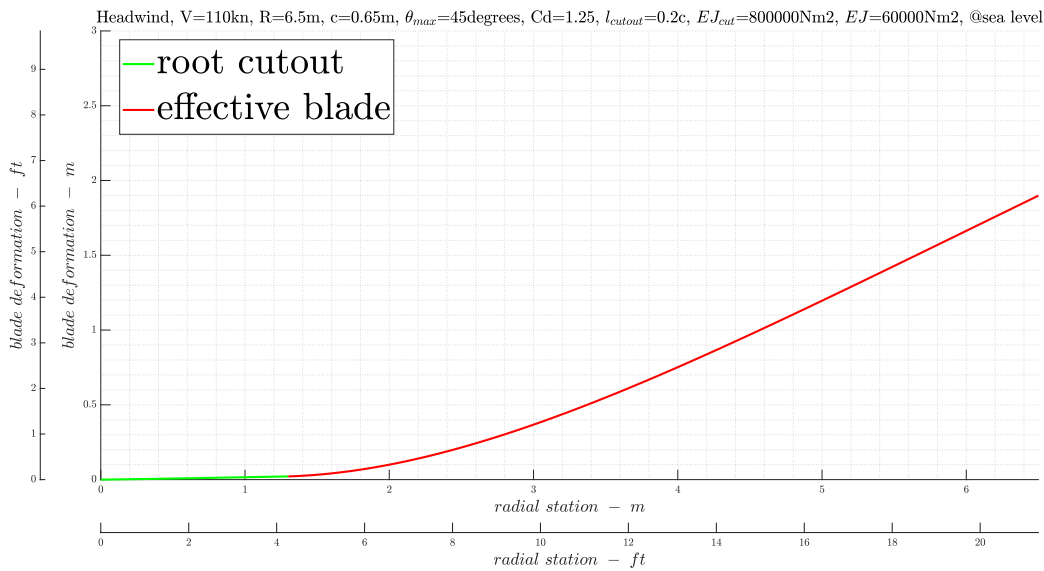


Figure 9.18: Blade deflection for the chosen radius

Under these loads, approximating the root of the blade as rectangular, a stress of 45Mpa is obtained, which seems entirely manageable. On the other hand, the dynamic stability of the blade in the free stream must be further assessed.



9.3.3.2. Number of blades

From a study of competitors with similar weight, it was found that the number of blades that could be considered is three, four, or five. For the three configuration, for no change on the power required, there would be a larger chord (inconvenient when folding) and greater loads on the blade. The five-blade configuration, on the other hand, would require an overly complicated locking mechanism with countless components. The four-blade configuration was found to be particularly smooth in folding geometry.

9.3.3.3. Rotation Speed

The choice of rotational speed is mainly a matter of avoiding compressibility problems in tip, while maintaining sufficient speed to ensure centrifugal stiffening. Having fixed the blade radius, it was possible to perform a study observing the main competitors, as reported in figure 9.19. Note that tiltrotors have a much higher tip speed, since the rotor does not have to operate in forward flight but only in hover (for forward flight the rotor is tilted and the rotation speed properly reduced).

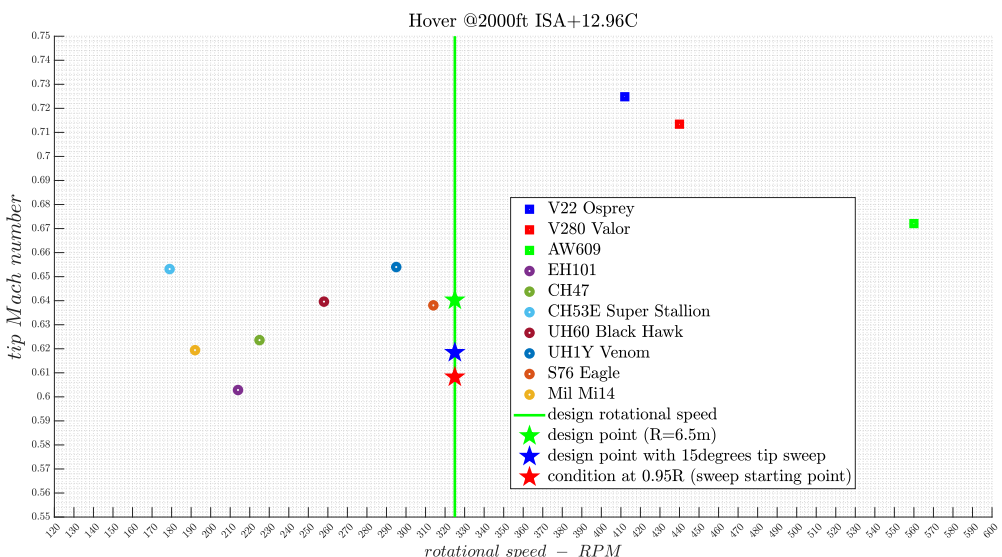


Figure 9.19: Tip speed analysis

The most critical situation occurs in forward flight when the forward blade rotation speed is added to the forward speed. In this aspect, conversion to jet mode at 110 knots limits the forward speed to be operated, making the problem less severe. Furthermore, rotor unloading as speed increases caused by the wing might reduce the average rotor thrust coefficient, further alleviating compressibility problems. To be conservative, it is still

possible to add a small tip sweep: the amount of sweep is usually kept low enough ($< 20^\circ$) so that there are no inertial couplings introduced into the blade dynamics by an aft centre of gravity or by aerodynamic couplings caused by a more rearward centre of pressure. A constant sweep angle offers simplicity in design and construction, but may result in higher than desirable aerodynamic torsional couplings because of the rearward location of the local centre of lift.

9.3.3.4. Blade twist and taper ratio

The optimum rotor requires both induced and profile power to be minimized at the same time: minimum induced power requires uniform inflow (ideal rotor), minimum profile power requires that each blade section operate at its optimum condition, i.e. maximum lift-to-drag ratio. It is therefore obvious that the optimum rotor, fixed an airfoil, will have to have both taper and twist.

However, according to the reference [9], the effect of the taper is limited and can be neglected initially. Negative twist improves rotor hover performance, but also tends to increase hover download and reduce hover in-ground-effect thrust augmentation. Moderate values of negative twist improve rotor performance in forward flight, since unloading the tips delays stall on the retreating blade and compressibility effects on the advancing blade. Large values of negative twist, although beneficial for hover performance, contribute to the appearance of negative loading on the advancing side in forward flight. Thus twist reduces forward flight maximum lift-to-drag ratio and increases hub vibratory loads and blade alternating loads at maximum speed.

Since in the present case the hover is particularly important, not having to sustain high speeds in helicopter mode, a moderately high twist is chosen, i.e. -16°

9.3.3.5. Blade chord

The blade chord is chosen to close the problem equations with the previously chosen parameters, taking care to ensure an adequate margin on the stall, chosen to be 4° . The blade angle of attack as a function of the radius is known since inflow ratio and rotor speed are known.

As a first guess, the result of 0.64 meters seems acceptable. It is a parameter to be monitored carefully since it heavily influences the design of the rotor nacelle, which must accommodate the closed blades.



9.3.3.6. Sizing results

Below are the results obtained with the procedure and tools presented earlier. The code was validated by entering data from the AgustaWestland EH101, yielding excellent results. The validation results are reported in section 9.3.7.

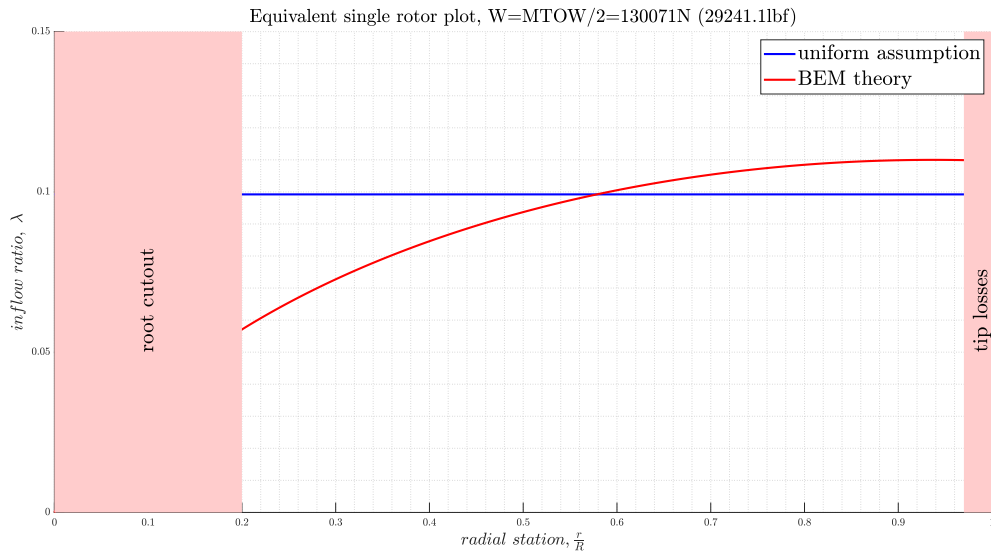


Figure 9.20: Induced velocity results

Figure 9.20 reports the results for induced velocity obtained with combined Blade Element and Momentum theory BEM and the relative linear approximation used. As notable, in the blade operational zone the error committed is small.

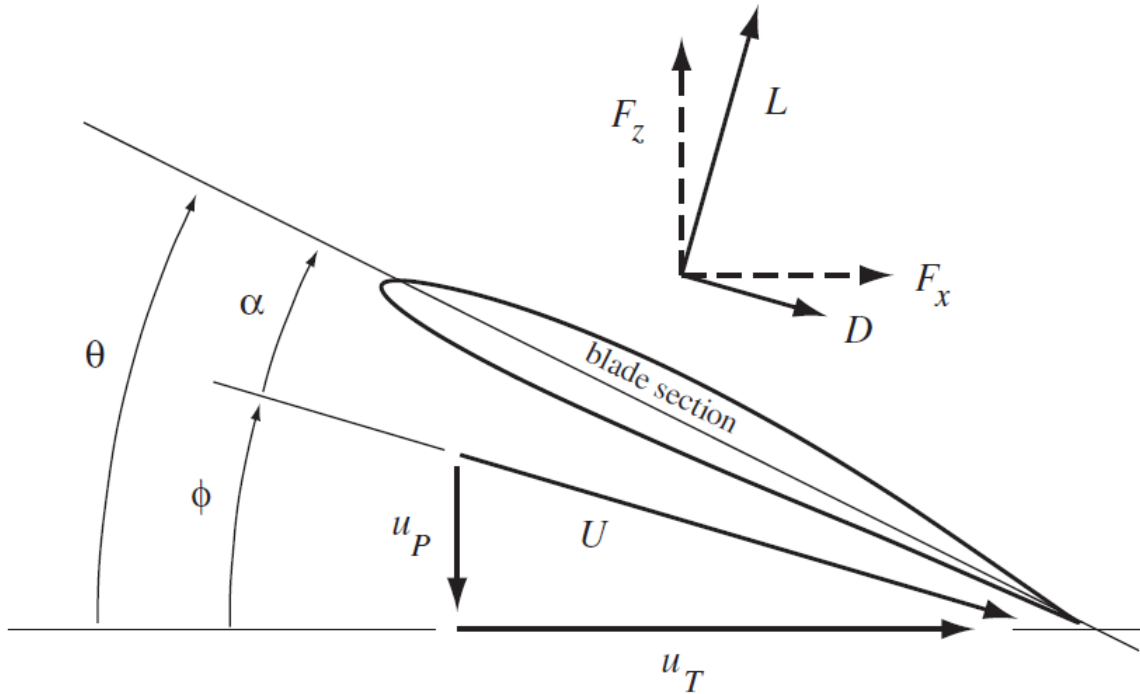


Figure 9.21: Blade element theory reference system

With respect to the reference system shown in the figure 9.21, figure 9.22 shows the results for collective angle θ , angle of attack α , and induced angle ϕ . Note the four-degree margin on the angle of attack imposed above.

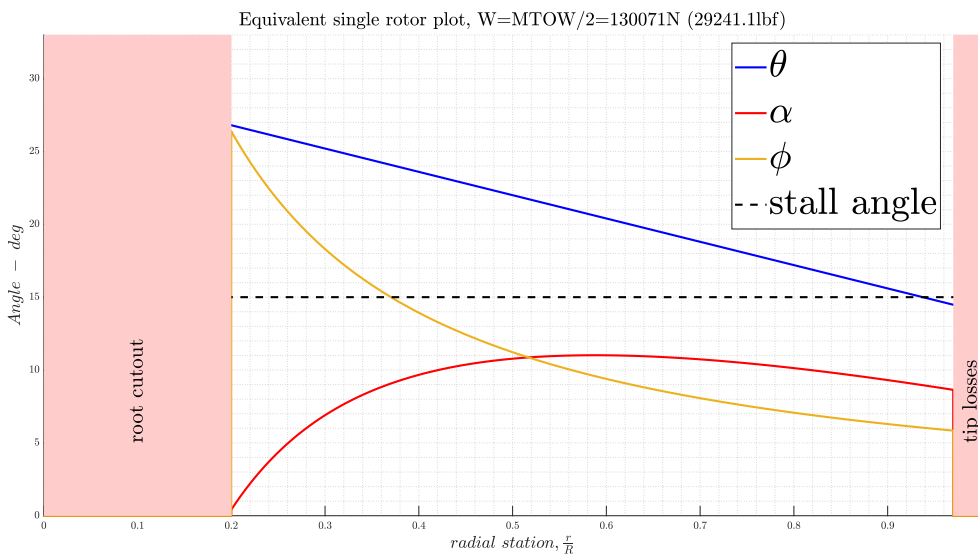


Figure 9.22: Notable angles results



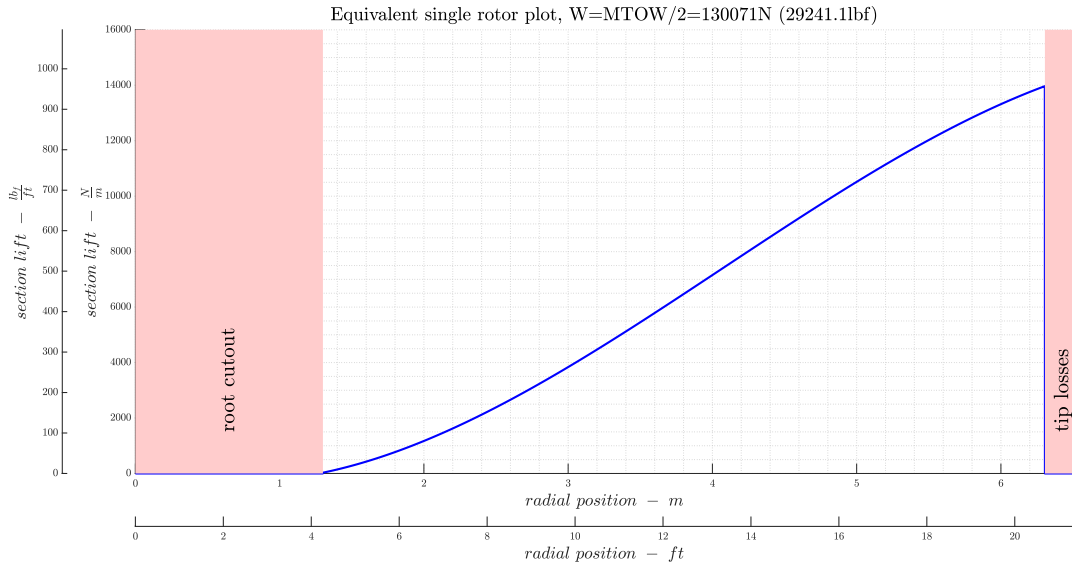


Figure 9.23: Blade lift distribution

Figure 9.23 reports the results of the lift distribution on the blade.

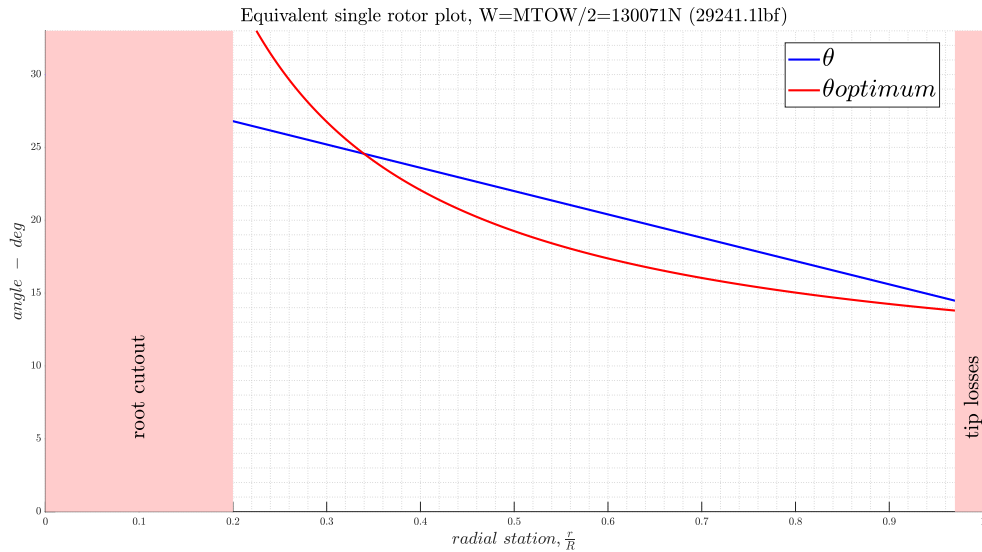


Figure 9.24: Blade twist

Finally, Figure 9.24 reports the difference between the optimum hyperbolic twist and the much simpler but still effective (and indeed quite similar) linear twist chosen.

9.3.4. Power loading

With the thrust part completed, it is possible to conclude the preliminary sizing by obtaining the relationship between disk loading and power loading given via blade element theory, equation 9.10, feeding the model with the parameters set in the previous section. Results for both MTOW and MMGW are reported, respectively Figures 9.25 and 9.27 (while the results on thrust (the previous section) for MMGW were not reported graphically as for MTOW but only in the final summary table for brevity, not being the worst case scenario).

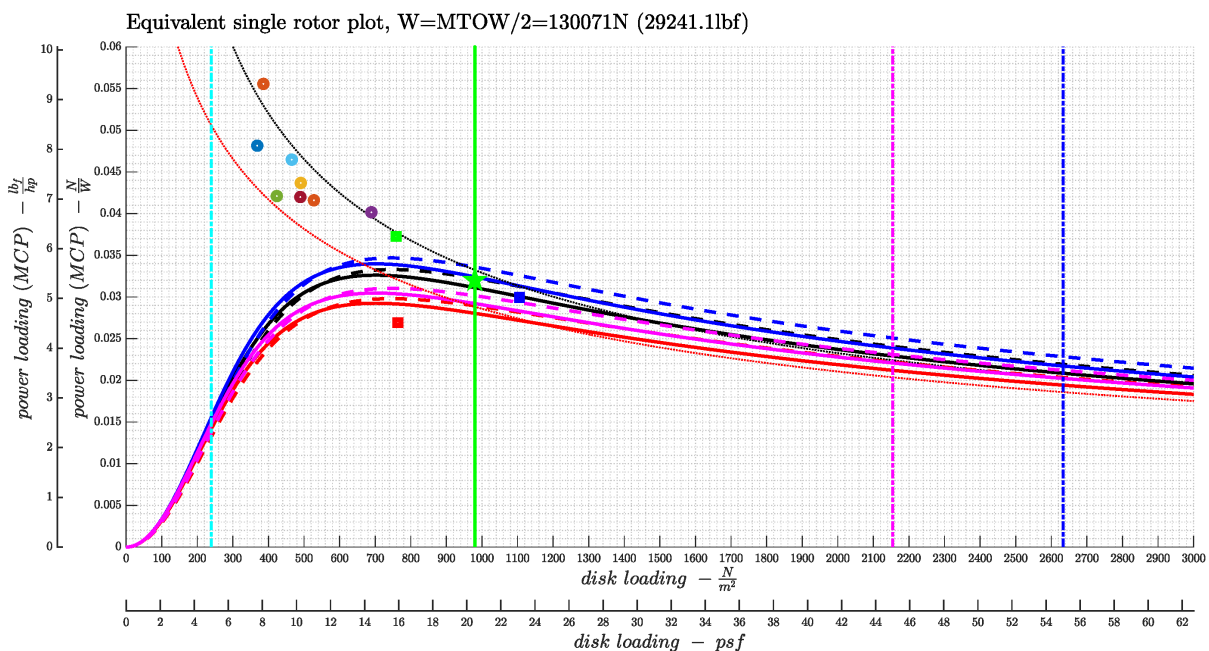


Figure 9.25: Sizing Matrix Plot (MTOW)



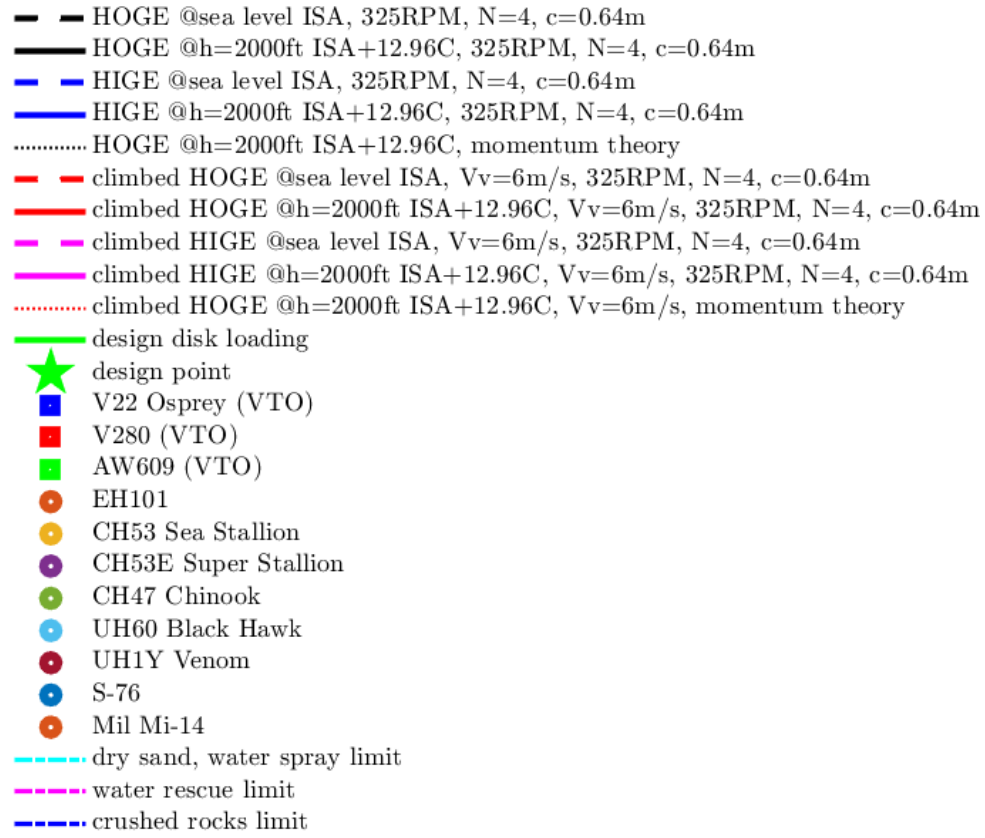


Figure 9.26: Legend of sizing Matrix Plot (MTOW)

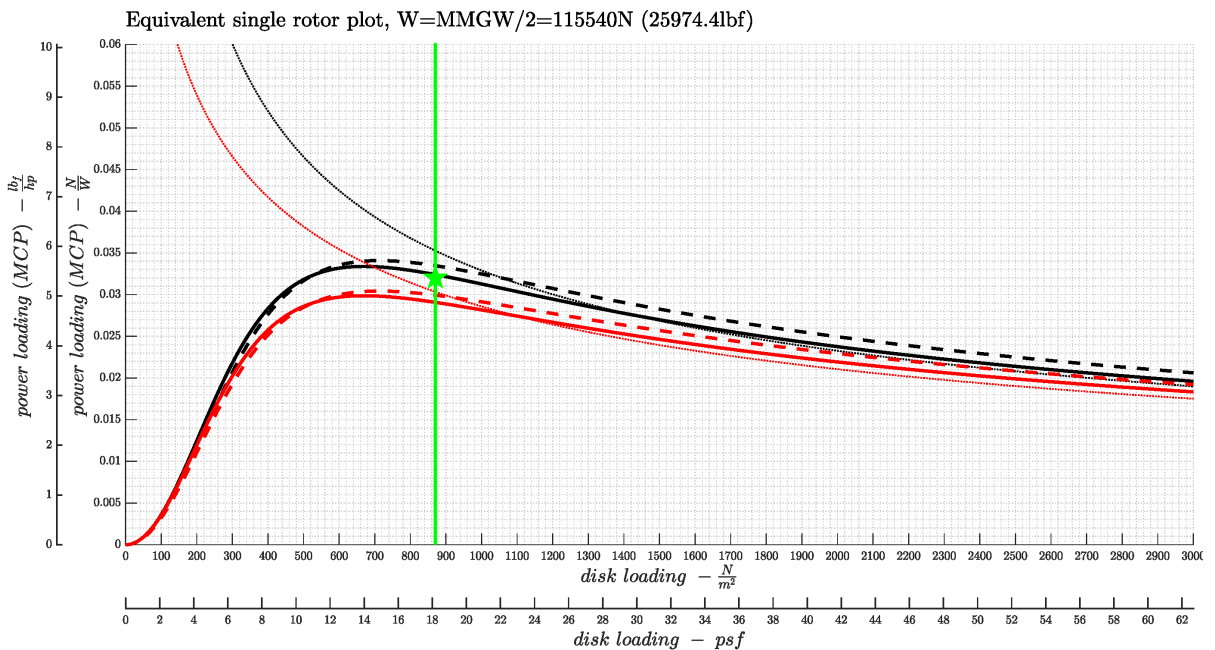


Figure 9.27: Sizing Matrix Plot (MMGW)

- HOGE @sea level ISA, 325RPM, N=4, c=0.64m
- HOGE @h=2000ft ISA+12.96C, 325RPM, N=4, c=0.64m
- HOGE @h=2000ft ISA+12.96C, momentum theory
- HOGE @sea level ISA, Vv=6m/s, 325RPM, N=4, c=0.64m
- HOGE @h=2000ft ISA+12.96C, Vv=6m/s, 325RPM, N=4, c=0.64m
- HOGE @h=2000ft ISA+12.96C, Vv=6m/s, momentum theory
- design disk loading
- ★ design point

Figure 9.28: Legend of sizing Matrix Plot (MMGW)

As required by the RFP [31], the HIGE case was considered only in MTOW. The ground effect was modeled as a 4% reduction on the required power [9].

Recall that the available design area is under the curves and that, for MTOW and MMGW conditions respectively of HIGE and HOGE are required, the design worst case scenario is at MTOW and then the design point is chosen accordingly.



9.3.5. Summary of preliminary sizing results

The following tables summarize the results of preliminary sizing:

Radius	N° blades	Ω	Twist	Taper	Chord	σ	Power loading
21.32ft (6.5m)	4	325RPM	-16° linear	1	2.09ft (0.64m)	0.1254	0.032

Table 9.4: Single rotor parameters

M	c_T	c_T/σ	\bar{C}_L	Disk loading	$\theta_{0_{\text{hovering}}}$
29,231lb (13,259kg)	0.0182	0.1451	0.8688	20.46psf (980 $\frac{N}{m^2}$)	30°

Table 9.5: MTOW results (equivalent single rotor)

M	c_T	c_T/σ	\bar{C}_L	Disk loading	$\theta_{0_{\text{hovering}}}$
25,966lb (11,778kg)	0.0161	0.1283	0.7710	18.17psf (870 $\frac{N}{m^2}$)	28.4°

Table 9.6: MMGW results (equivalent single rotor)

From the engine point of view, power loading being equal, the MTOW case is more stringent: a pair of turboshafts capable of delivering 5,450hp (4,064kW) each is needed.

9.3.6. Results analysis

It's now time to verify if all the requirements are fulfilled. The only requirement that in this procedure was not imposed a priori is the disk loading, which result is satisfactory, yet managing to achieve lower disk loading than the V22 Osprey.

Finally, a general look at the main competitors considered so far is due:

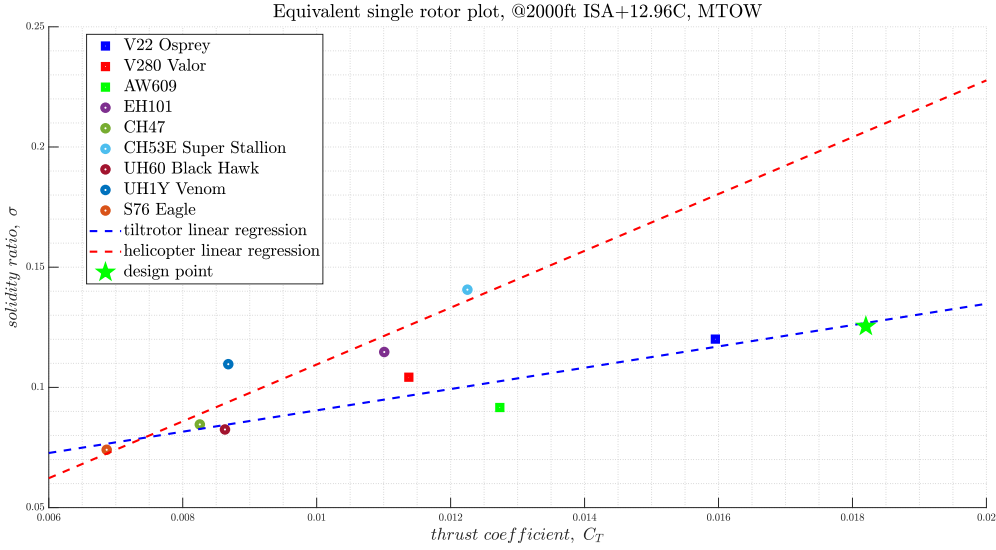
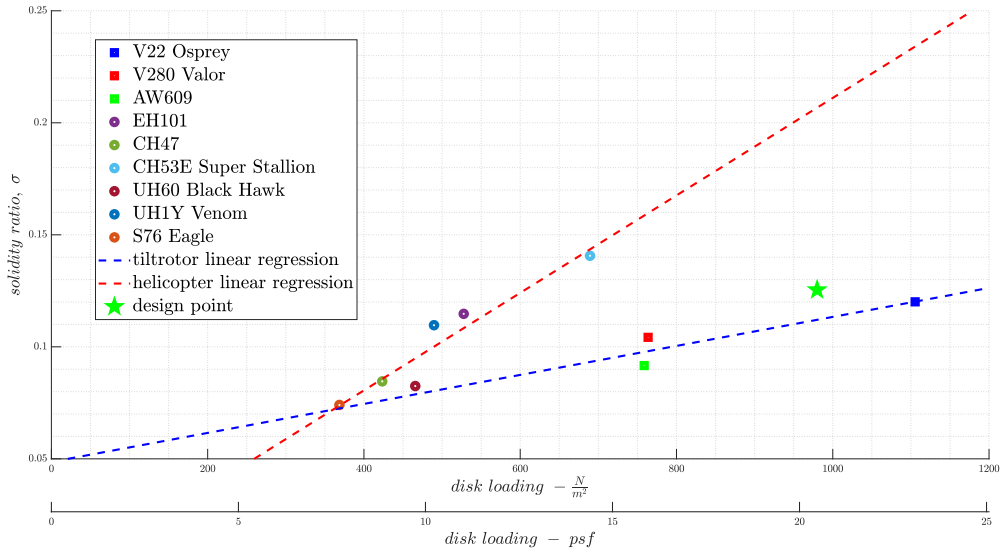
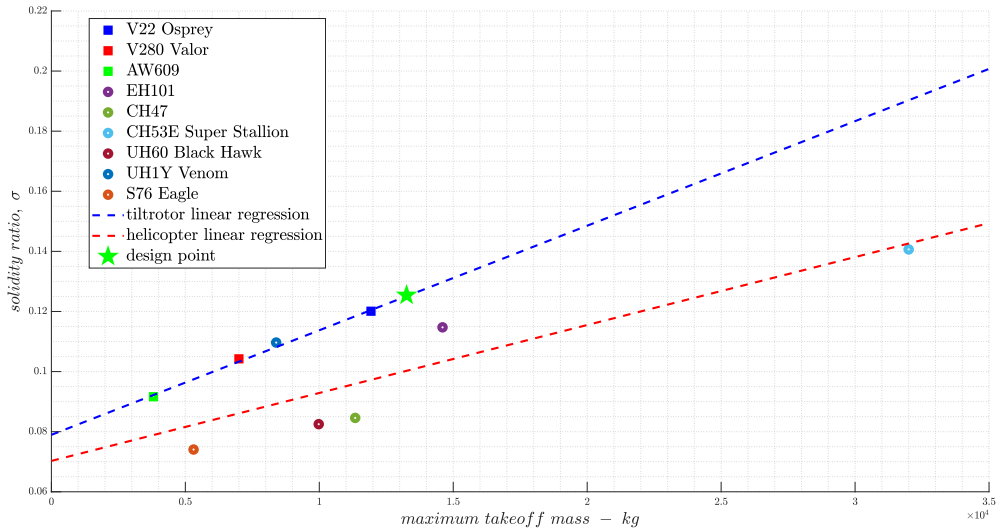
Figure 9.29: C_T - σ

Figure 9.29 shows the design point in the C_T - σ plane. The blade loading $\frac{C_T}{\sigma}$, that is a measure of the mean angle of attack of the blade, is similar to the tiltrotor class. Remembering the definition of thrust coefficient:

$$C_T = \frac{T}{\rho A_{rot}(\Omega R)^2} \quad (9.14)$$

Its high value is due to the fact that the blade loading of Raven 4 is in line with tiltrotors class, but the rotation speed, due to edgewise flight requirements is significantly lower, closer to helicopter class. This is indeed not a problem.



Figure 9.30: $DL-\sigma$ Figure 9.31: $MTOM-\sigma$

9.3.7. Code validation

Validation of the code was done using AgustaWestland's EH101 helicopter. In fact, also thanks to the material provided by *Centro Sperimentale Aeromarittimo* in Sarzana (IT), the output parameters of the design are known. So it is possible to impose the known parameters and check if the obtained design point corresponds with the real one.

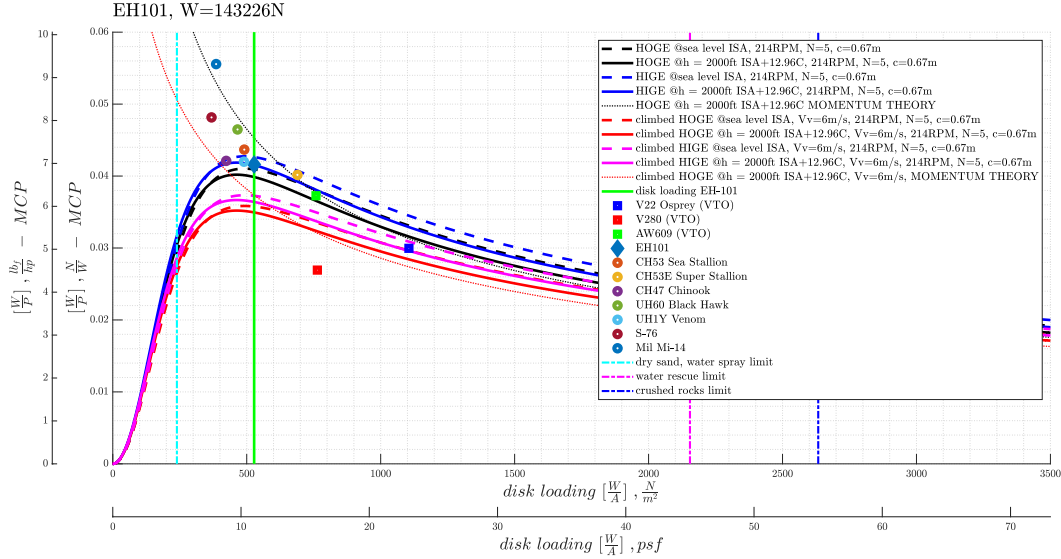


Figure 9.32: Validation by means of EH101

The result is shown in the figure 9.32 and is stunningly accurate, since the real EH101 design point is in the vicinity of the optimal zone predicted by the model, making it possible to assert the validity of the constructed model.



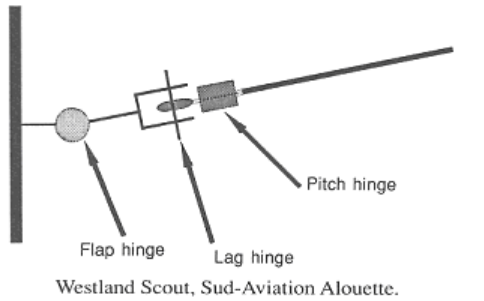
10 | Rotor design

Having finished the preliminary analysis from which the weight, jet thrust, rotorcraft power and main parameters, and surface area have been obtained, it's possible to move on to the detailed design of the aircraft components, i.e., rotors, wing, tail, fuselage, landing gear, propulsion system, control surfaces, and so on.

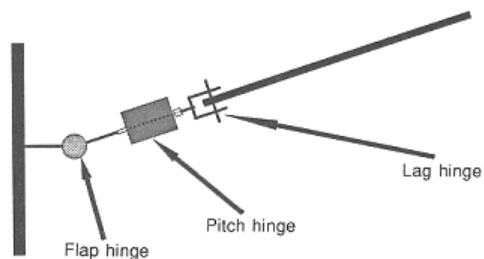
10.1. Rotor configuration

In this design, hover is an important feature, since fast advanced flight, i.e. over 110 kn, is done in fixed wing. The choice of a stiff-in-plane rotor might seem reasonable and straightforward. However, the need for folding imposes the presence of the flapping hinge. One hypothesis to consider is a rotor folding mechanism that blocks the flapping hinge. However, this would imply heavy time-repetitive stresses on the mechanism at high speeds, when the blade has a greater tendency to flapping, or in particularly abrupt maneuvers where loads on the disk can change rapidly. In other words, such a choice would significantly limit the rotorcraft-mode operational capability of the aircraft. This is a price you do not want to pay for this design. In addition, a fully articulated hub, although less responsive, is subjected to smaller loads because the hinges prevent the passage of moments on the shaft. This concept will be taken up later. Finally, such a choice greatly simplifies its study of blades aeroelastic phenomena and structural design of the rotor. The possibility of leaving the mechanism free to rotate however would not solve the problem, since the flapping of the blades would not be independent.

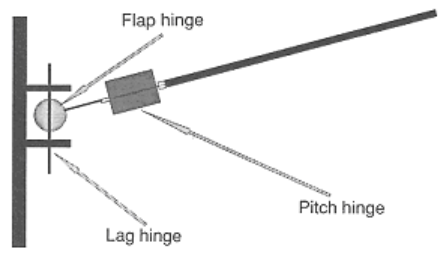
Hence, The *Ragno Technology* is, at least for the time being, set aside in favor of full articulated configuration with a different folding mechanism (Section 10.4). The hinges that need to be placed are: flapping hinge, lag hinge, feathering (or pitch) hinge. There are different solutions for ordering these hinges according to specific needs, as shown in the Figure 10.1.



Westland Scout, Sud-Aviation Alouette.



Boeing Vertol Chinook, Aerospatiale Gazelle.



Westland Wessex, Westland Sea King.

Figure 10.1: Different hinge order configurations

For the Raven 4 design the following order has been chosen (from the hub outward): flapping hinge, pitch hinge, lagging hinge. This identical configuration, in addition to adapting well to the needs of the folding mechanism, was adopted on the Boeing CH-47 Chinook and proved effective and reliable.

Unlike the flapping motion, which is naturally damped, a damper was inserted for the lag motion. In fact, in the latter the blade moves edgewise in the air, so it senses minimal drag. In contrast, the high drag experienced by the blade in the flapping motion generates a damping effect. Figure 10.2 shows the rotor hub without the folding mechanism for the sake of clarity. For the same reasons pitch link between pitch horn and swashplate are not reported to. Note that the pitch horn link lies on the flap hinge axis when pitch (or feathering) angle is zero. In Figure 10.2 the blade pitch angle is set as required for hovering at MTOW, i.e. 30°. For detailed measures refer to Chapter 23.



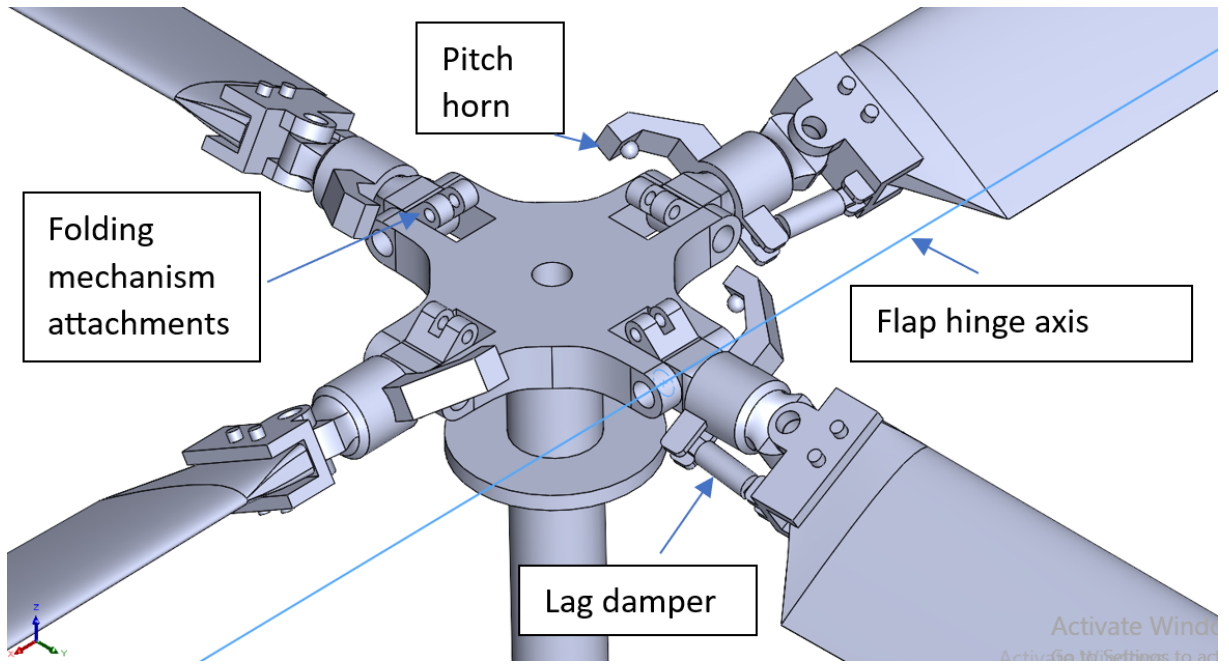


Figure 10.2: Right Hub detail, rotation counterclockwise from top view

Regarding the discussion of forces and moments on the shaft, observe Figure 10.3:

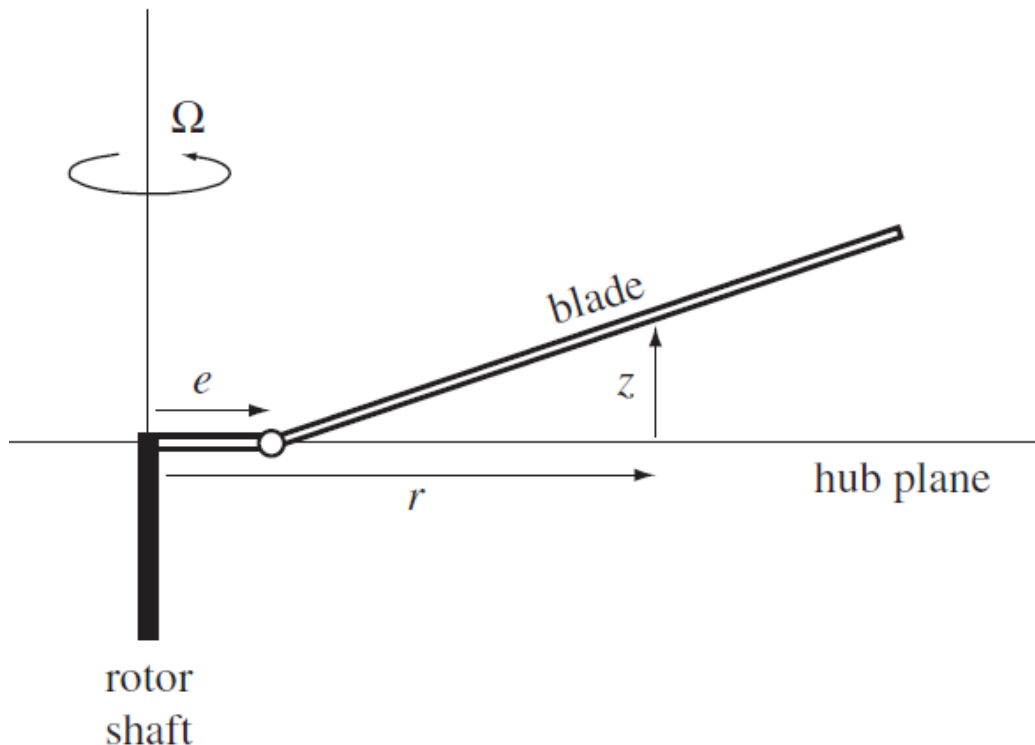


Figure 10.3: Flap motion with hinge offset

Due to the presence of the hinge the blade loads discharge there and no moment can pass through. If the hinge has no eccentricity, i.e. in the graph $e = 0$ in Figure 10.3, only forces act on the rotor mast. Otherwise, as with Raven 4, bending moments also act on the shaft, always smaller than in a hingeless case, but still present. This not only generates high structural loads on the hub (though giving the machine more responsiveness to control accordingly) but also has repercussions such as pretty high blade flapping frequency. Consider the normalized eccentricity over the blade radius:

$$\varepsilon = \frac{e}{R} \quad (10.1)$$

For Raven 4, $e = 0.5\text{ m}$; this was forced by the folding mechanism and the necessity to accommodate the 0.64 m chord blade on the nacelle. Hence for *Raven 4*, $\varepsilon = 0.075 = 7.5\%$. This is a higher value than the rotor average and should be kept in mind during the advanced study of the rotor.

10.2. Blade structure

The following paragraphs will deal only with a preliminary structural and aeroelastic analysis given the complexity of the topic. In fact, each helicopter rotor systems must start by acknowledging that the complexity of their construction and the interaction between their components causes the most difficulties for dynamic analysis. Moreover, rotor blades are fabricated from a variety of materials, each with its own set of physical properties. The blades twist and taper to varying degrees and the incorporation of different airfoil shapes over the length of the blade results in rotor blades that are non-uniform in their properties and highly complex in their dynamics.

A classic blade structure was chosen for the rotor with an outer shell, an inner "D" shape spar structure at the front of the profile to reinforce the leading edge, and an inner honeycomb core structure to be able to give better stiffness and compactness characteristics to the profile without compromising the weight of the blade.

In the outer shell we can find two main materials that go into sharing the outer profile of the blade. The front part is made of stainless steel to provide more stiffness, more strength for any impacts with external debris, and to shift the center of gravity toward the leading edge. Whereas the back part of the blade is made of a carbon fiber composite material.

As for the "D" shape spar, a composite material of fiberglass and graphite laminated together with epoxy binder was chosen to form fatigue-proof (infinite life) blades. The choice of using a composite material is perfect for aerodynamically efficient blades. They



can be designed to have any desired taper, twist, profile cross-section variation, and weight distribution from root to tip. In addition, selective incorporation of graphite is used to control blade stiffness and achieve the required structural and dynamic characteristics. The fill material chosen was a foam in the forward part and a nomex honeycomb core in the rear part.

There is then a glass fiber balance tube near the leading edge to move the center of gravity toward the leading edge to retard the appearance of flutter at high rotational speeds.

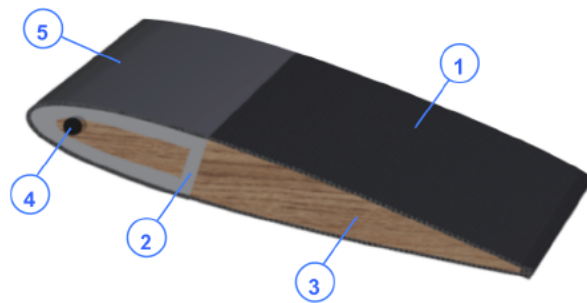


Figure 10.4: Section of the blade structure

ID	ELEMENT	MATERIAL	DENSITY [kg/m ³]
1	Skin	Composit carbon Fiber	1750
2	"D" Spar	Composit S2-Glass/Epoxy	1993
3	Filling	Honeycomb nomex Foam	200 150
4	Balance Tube	Steel	7800
5	Erosion Shield	Stainless steel	7800

Table 10.1: Material of the blade

10.3. Blade aeroelasticity

Having defined the main structure of the blade, along with the geometric characteristic, it is possible to evaluate its structural properties referring to mass distribution, bending stiffness distribution and torsional stiffness distribution.

Blade radius	21.3 ft (6.5 m)
Blade cutout	4.27 ft (1.3 m)
Blade chord	2.1 ft (0.64 m)
Twist	-16°
Lag hinge axis	3.12 ft (0.95 m)
Flap hinge axis	1.64 ft (0.5 m)
Pitch link	1.64 ft (0.5 m)
Pitch bearing	2.3 ft (0.7 m)

Table 10.2: Blade geometry and distance from hub center of rotor hinges

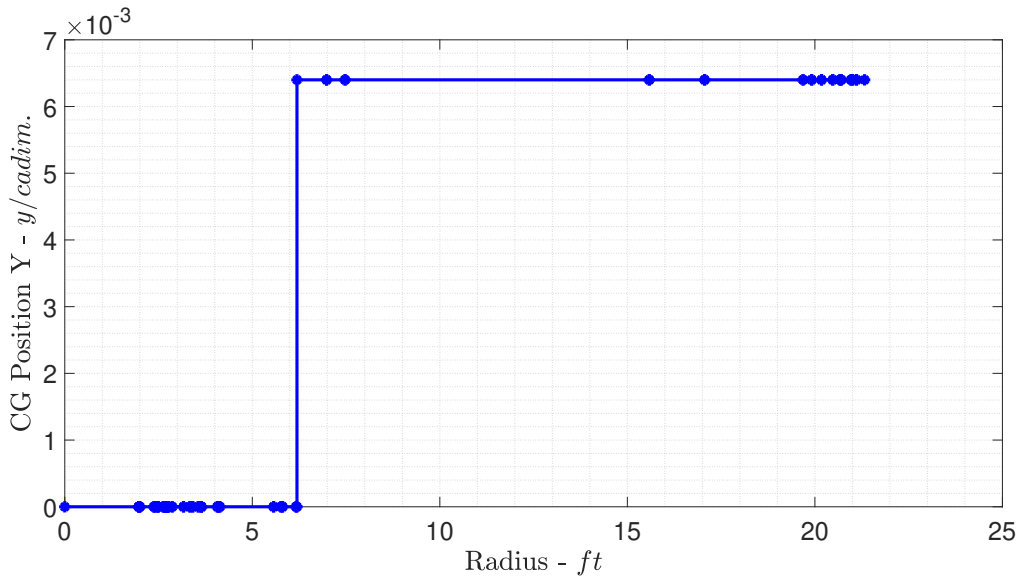


Figure 10.5: Position of CG

The model is built through a grid of 82 nodes along the blade divide in 5 nodes between the flap axis and the pitch bearing, and 75 nodes after the pitch bearing.

By reporting the linear twist chosen, the mass distribution, bending stiffness and torsional stiffness, it is possible to write the dynamic model to compute the rotating bending mode and the rotor torsional mode with their relative frequencies (Figures 10.7 and 10.8).



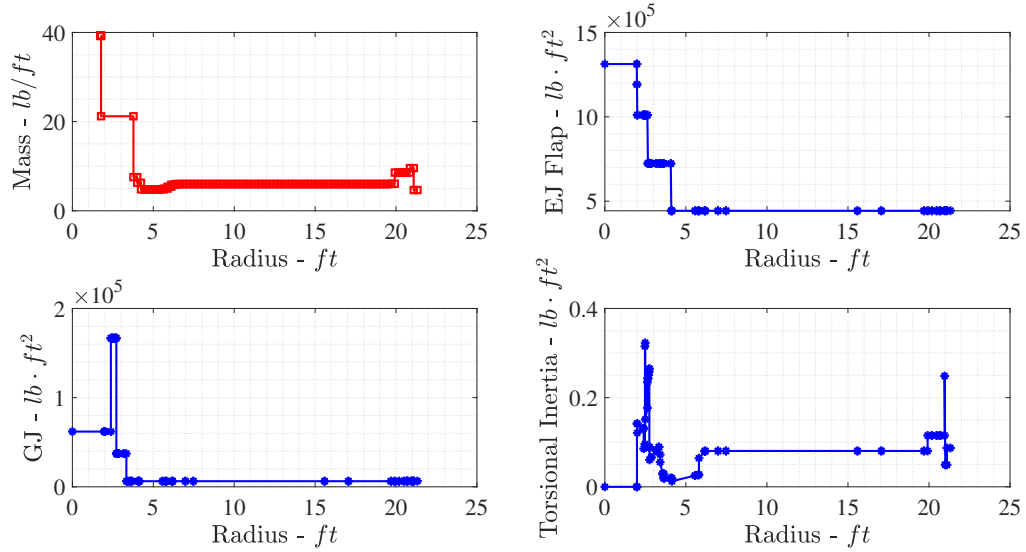


Figure 10.6: Property of the blade

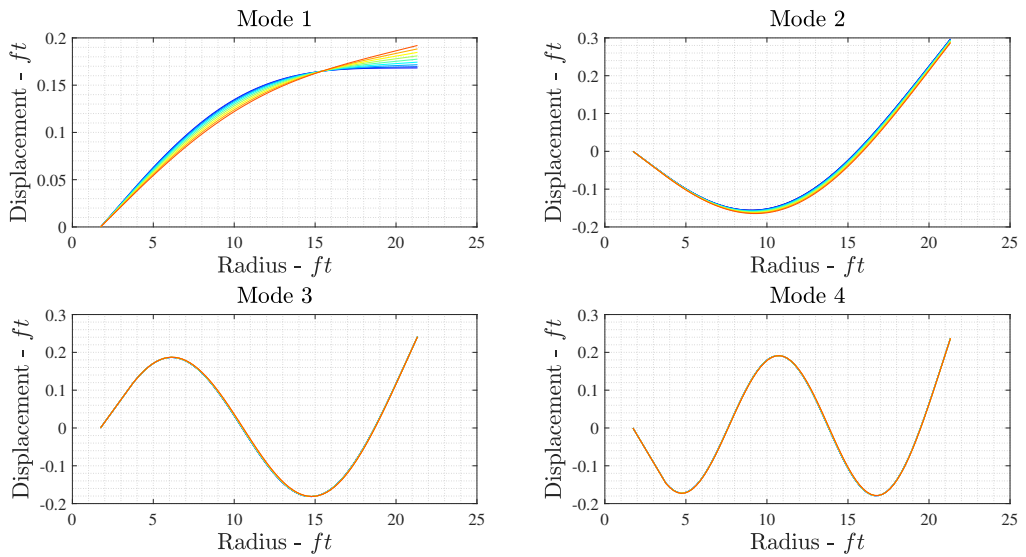


Figure 10.7: Bending modes of the blade

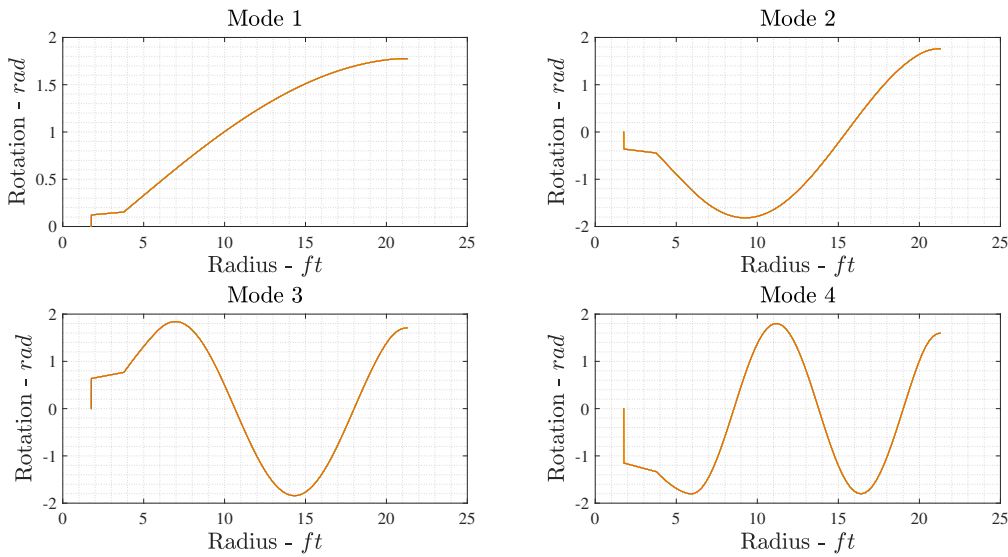


Figure 10.8: Torsion modes of the blade

The determination of normal mode shapes and frequencies of a rotating blade is important because:

- Normal modes can be used as generalized coordinates in blade dynamic response (a very few shapes are sufficient for a wide range of frequencies).
- In blade design, matching of periodic aerodynamics forces (at harmonic of the rotor angular velocity) and natural frequencies must be avoided, to avoid forcing blade dynamics in resonance.

In general, blade geometric, structural, and aerodynamic properties vary along the blade. The rotating mode shapes should be used but, on the basis of numerical analyses performed on blades with constant spanwise properties, it is known that while frequencies strongly depend on the angular speed, mode shapes are only lightly affected. In fact it can be seen from Figure 10.7 and 10.8 that just the first and second rotating mode show a slight difference from the non-rotating modes.

It can be seen that a typical mass distribution was chosen whereby there is a large mass after the flap hinge and a higher mass in tip to ensure better blade balance. The end of the blade also weighs more to ensure that the tip can be disassembled so that it can be replaced simply in case of its possible damage.

Structural modification of blade properties in general can simultaneously affect different modes. A more focused effect can be obtained by adding lumped masses at maximum displacement stations, or anti-nodal positions (possibly corresponding or close to nodal



positions for modes that do not need to be modified), in order to maximize the centrifugal stiffening effect.

Writing now the coupled bending-torsion system it is possible to visualize the dynamic model of the rotating blade, which will ultimately report the fan plot for a single rotor 10.9.

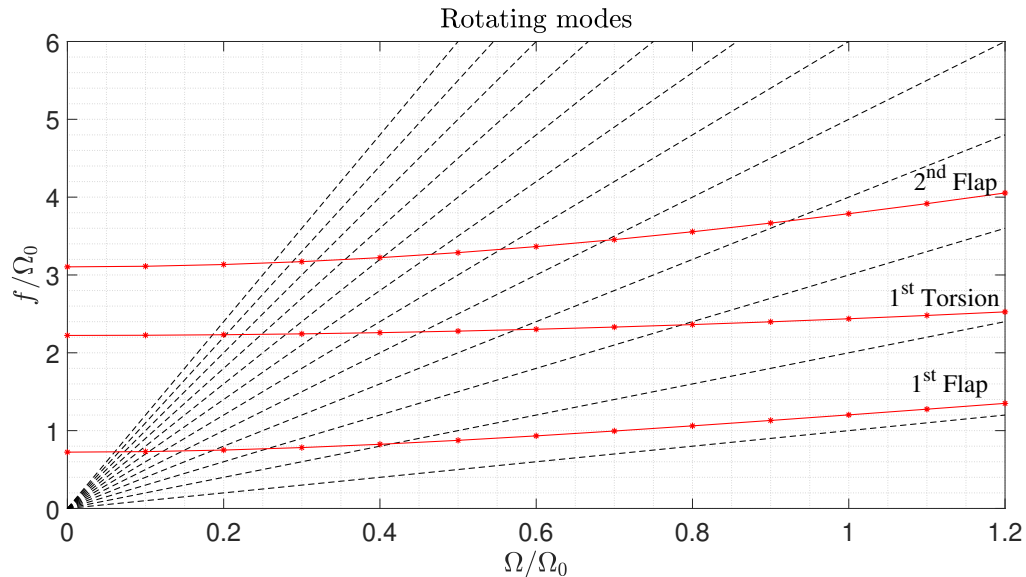


Figure 10.9: Fan Plot

In blade structural design, a stiffness and mass distribution has to be determined such that, in operational conditions, from 80% to 110% of the nominal rotor speed, the lowest natural frequencies are not excited by the aerodynamic forces acting on the rotor.

If some of the lowest harmonics (whose amplitude is larger) of the exciting forces are close to a natural frequency of the rotating blade, the response, and the associated stresses, could be excessive. In order to proceed with the in-flight folding of the blades, the blades will experience a strong pressure from the relative wind without rotating, and therefore without gaining additional rigidity from centrifugal force.

10.4. Folding mechanism: the *Multirail Technology*

The folding mechanism is based on the *Multirail Technology* designed specifically for this project. It consists of a hydraulic/electric telescopic actuator attached to the rotor head and to the flapping hinge with a proper arm.

What makes this system peculiar and unique is that, despite the fact that there is a locking

mechanism, during rotor operation each blade is able to flap freely and independently from the others.

The key idea of the system is a small rail on which the pins of each actuator can slide, Figure 10.10.

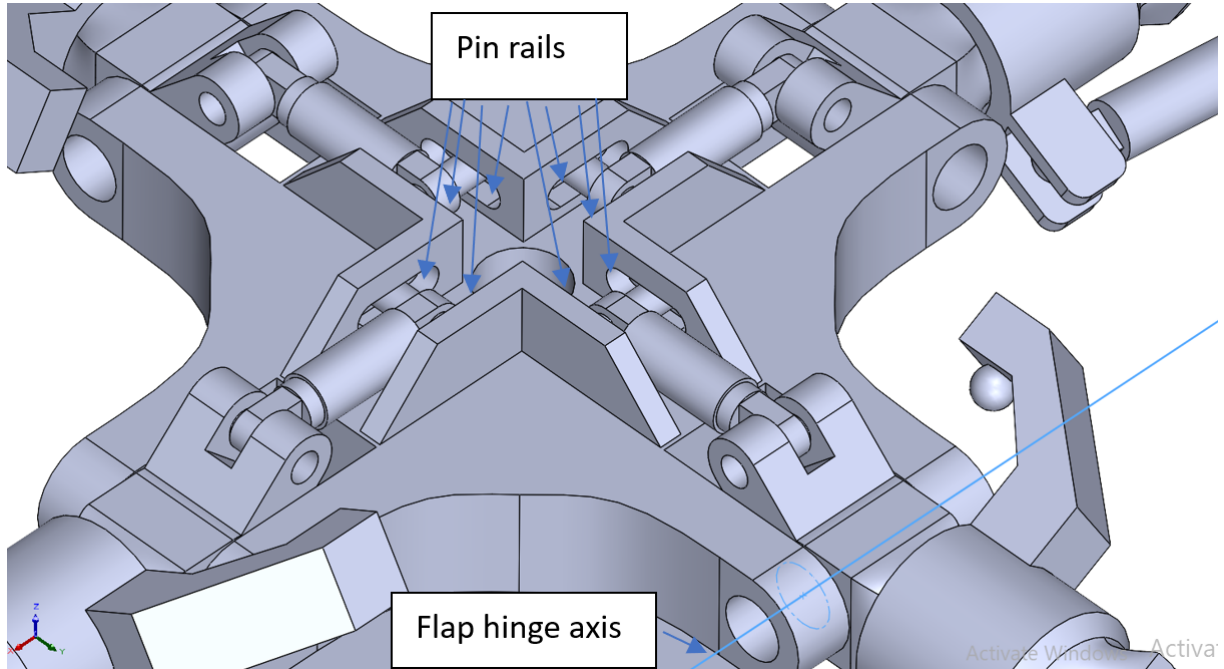


Figure 10.10: Pin rails (two for each actuator)

- Consider the rotor operational phase, Figures 10.11 and 10.11: the blades are kept open by centrifugal force, while the rail allow them to flap for a angle of approximately $\pm 20^\circ$ (kinematics detail will be discussed later; however, it is reasonable to think that this value is tuned during advanced development, and likely its neutral value is not the horizontal but the nominal upward tilt of the rotor in the operational phase). Obviously in this phase the actuator is fully collapsed.



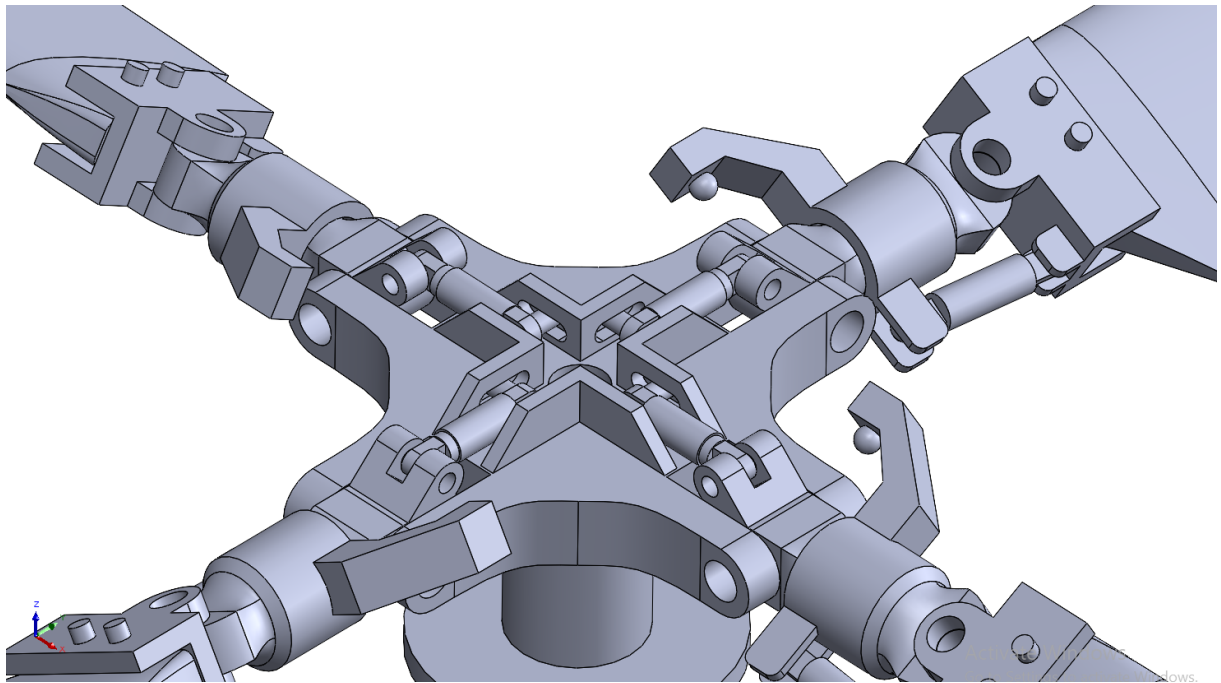


Figure 10.11: Rotor in operative phase

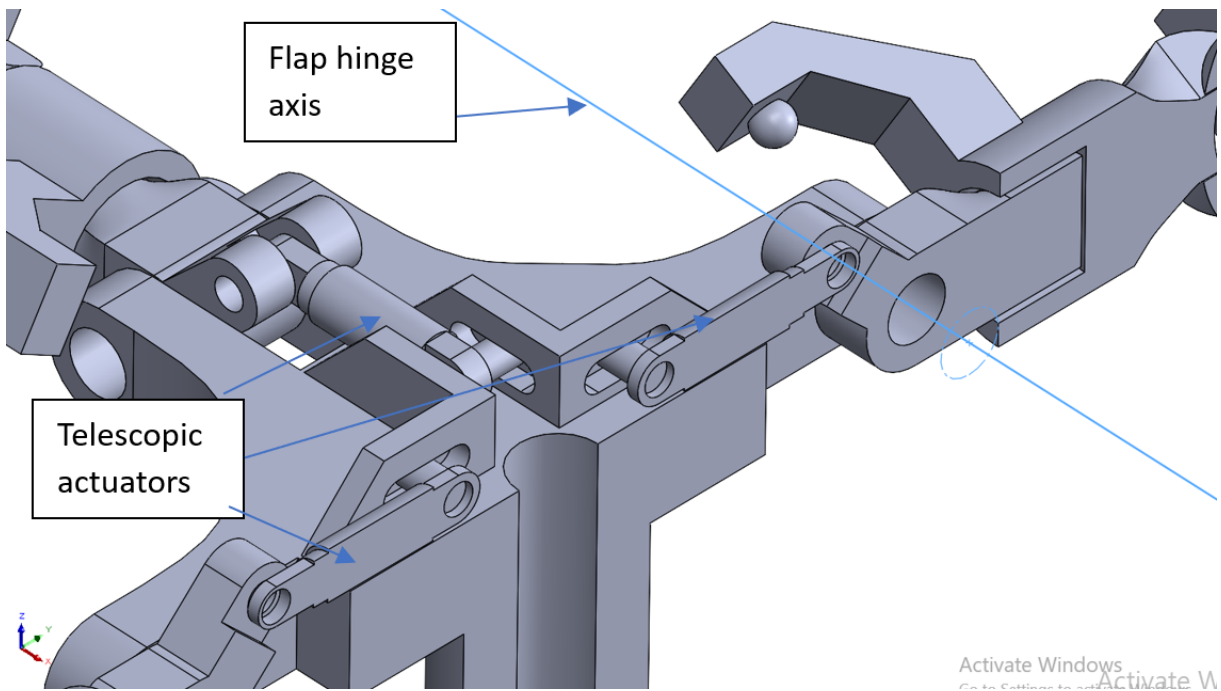


Figure 10.12: Figure 10.11 middle plane slice

- Consider the rotor in cruise phase, Figures 10.13 and 10.13: the blades are folded and held in place by activating appropriate electromagnets placed on the nacelle. In

this condition, the full extended actuator goes to the stop with the back of the rail, ensuring the success of the procedure.

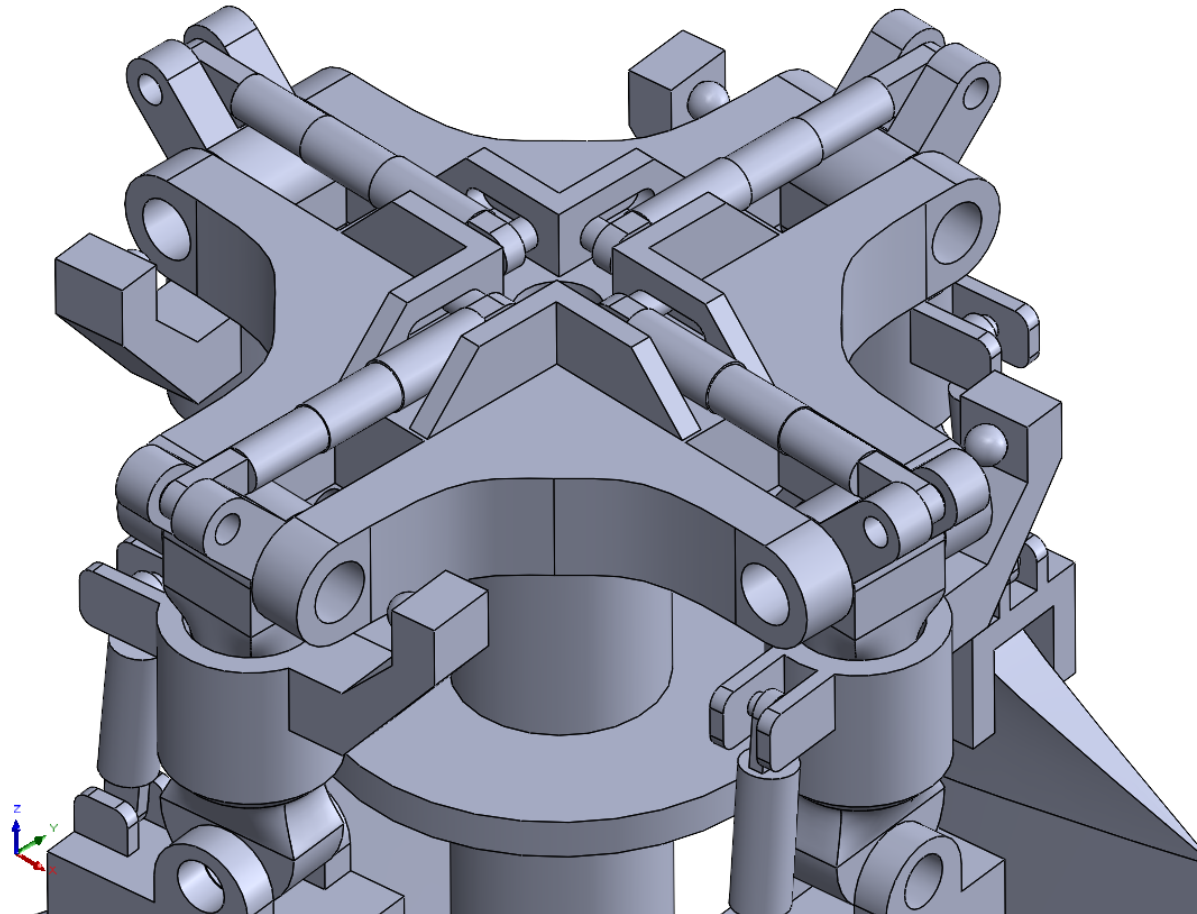


Figure 10.13: Rotor in cruise phase



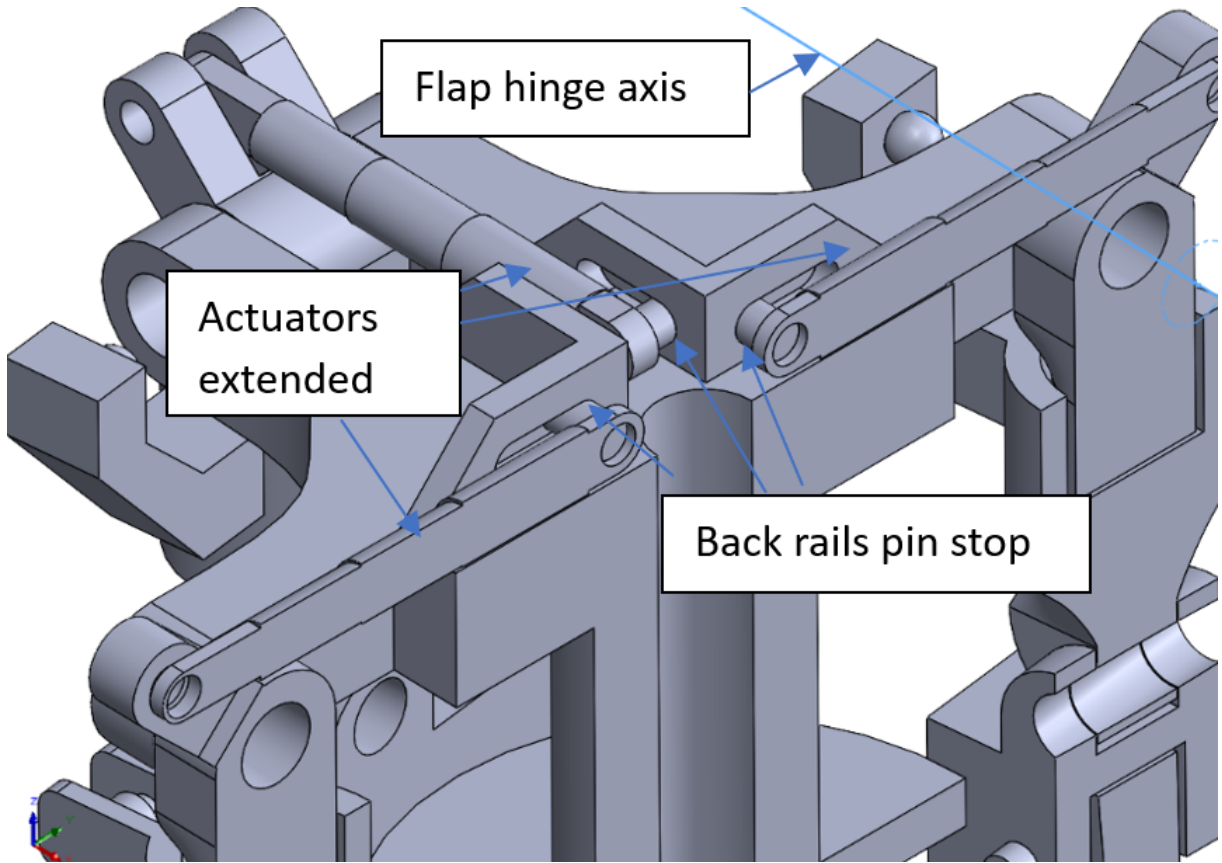


Figure 10.14: Figure 10.13 middle plane slice

10.5. Folding mechanism preliminary sizing

The purpose of this section is to set up the preliminary folding mechanism design in terms of forces, moments, powers, and closing time.

10.5.1. Kinematics

Consider the folding mechanism in open and closed position, as shown respectively in figure 10.16 and figure 10.15.

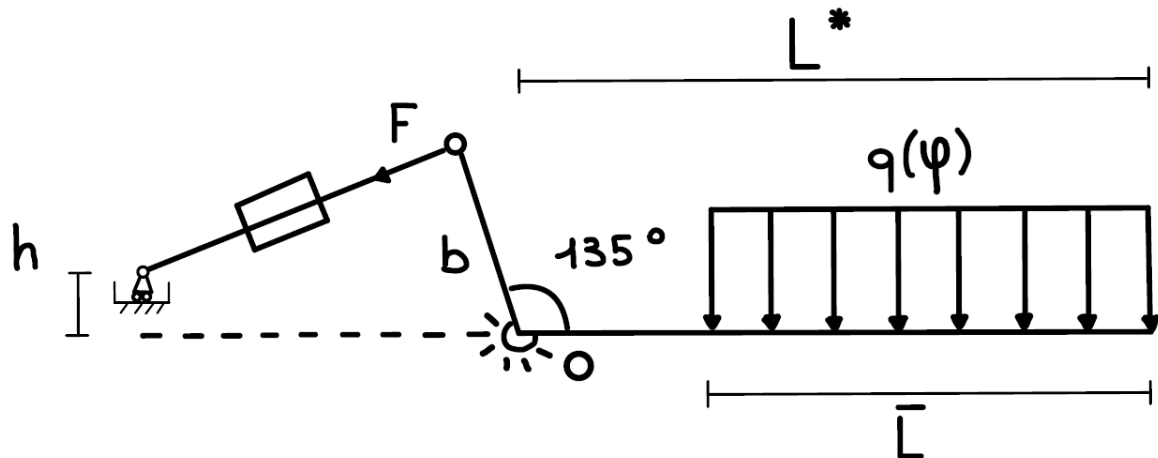


Figure 10.15: Open position

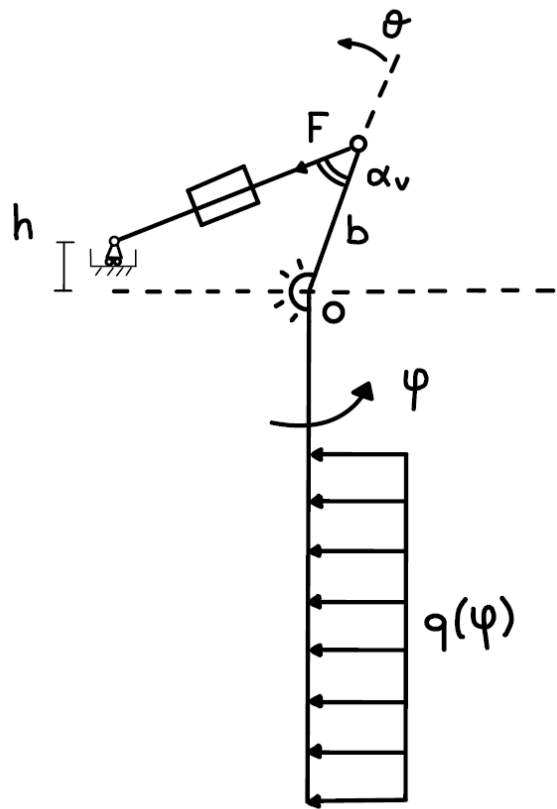


Figure 10.16: Closed position

Exploiting some trivial trigonometric consideration, the Force F and the bending moment



acting in O can be expressed as:

$$F = \frac{q\bar{L} \left((L^* - \bar{L}) + \frac{\bar{L}}{2} \right)}{b \sin(\alpha_v)} \quad (10.2)$$

$$M_O = q\bar{L} \left((L^* - \bar{L}) + \frac{\bar{L}}{2} \right) \quad (10.3)$$

knowing:

$$q = q_d c \sin(\phi) C_D \quad (10.4)$$

In this model the blade is suppose as a flat plate exposed to the free stream; q depend on ϕ since when the rotor is closed (i.e. $\phi = 0$) no aerodynamic forces act on the blade surface.

Note that in reality this situation never happens, since when the rotor axis is align with the free stream the folding procedure has started yet. Then this is a conservative approach. The choice to compute the bending moment in O follows the consideration that is the worst point from the point of view of bending moment.

Consider now figure 10.17:

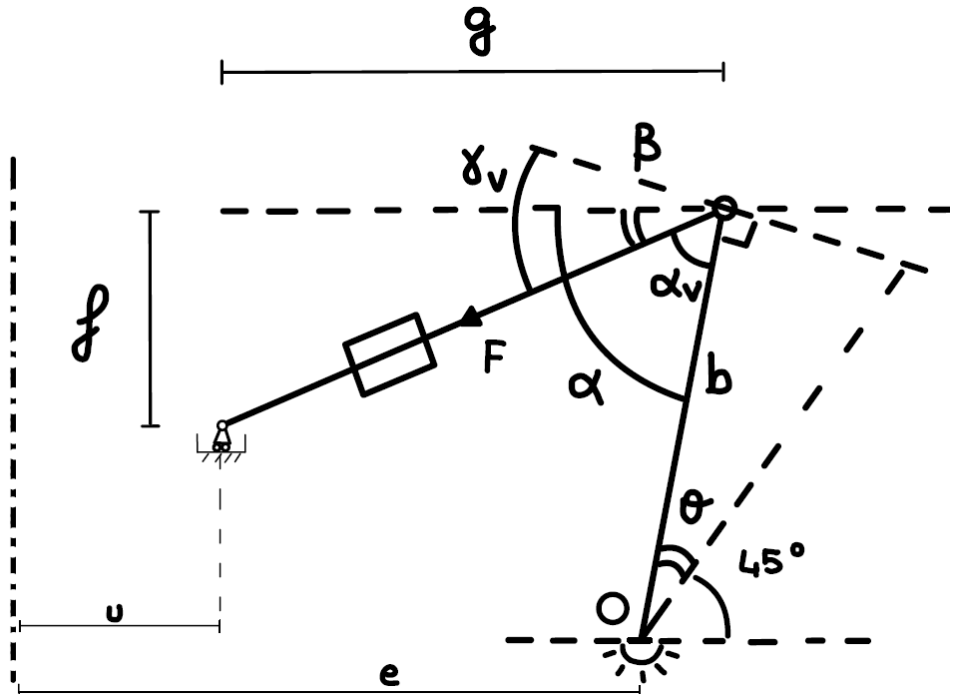


Figure 10.17: Transition screenshot

Follows:

$$\theta = \phi \quad (10.5)$$

$$\alpha = \theta + \frac{\pi}{4} \quad (10.6)$$

$$f = b \sin \alpha - b \sin \frac{\pi}{4} \quad (10.7)$$

$$g = e - u + b \cos \frac{\pi}{4} - \left(b \cos \frac{\pi}{4} - b \cos \left(\theta + \frac{\pi}{4} \right) \right) \quad (10.8)$$

$$\beta = \arctan \left(\frac{f}{g} \right) \quad (10.9)$$

$$\alpha_v = \alpha - \beta \quad (10.10)$$

$$\gamma_v = \frac{\pi}{2} - \alpha_v \quad (10.11)$$

$$(10.12)$$

Then the actuator velocity can be expressed as follow:

$$v_{act} = \dot{\theta} b \cos \gamma_v \quad (10.13)$$

As final consideration, the displacement of the actuator pin on the track was in this preliminary context ignored and its middle position taken.

10.5.2. Quasi-static force and moments

It is now possible to plot results for the actuator force F and the bending moment in O , M_O as a function of ϕ , respectively 10.18 and 10.19:



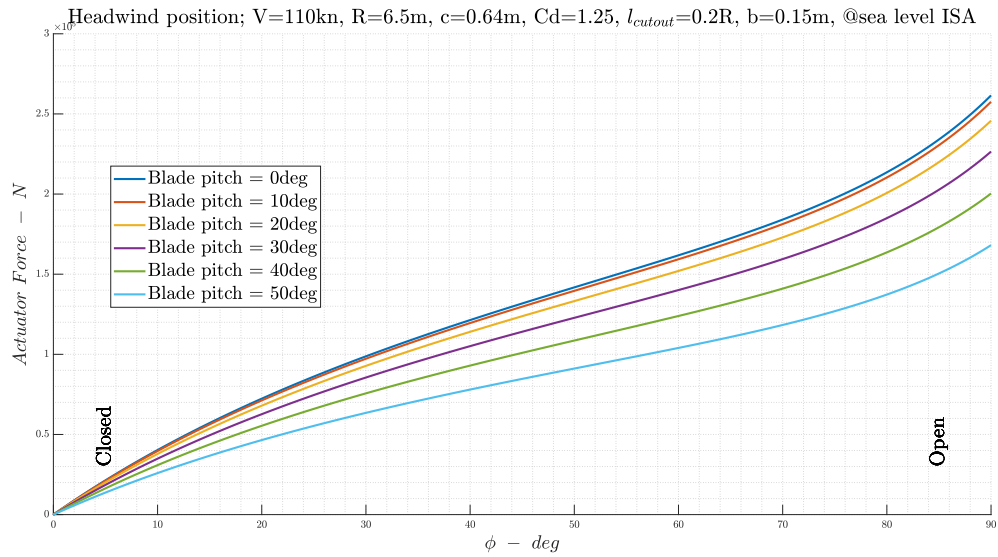


Figure 10.18: Actuator force

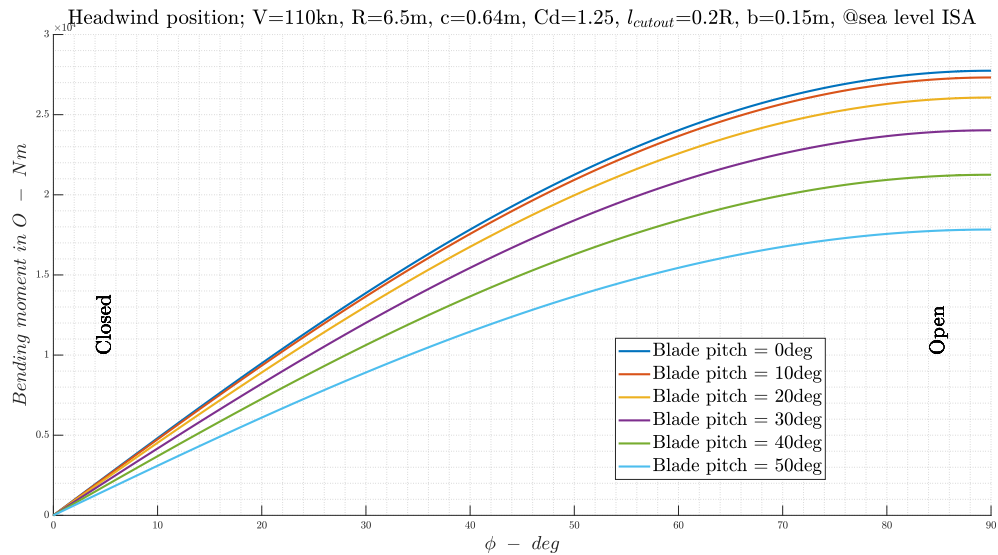


Figure 10.19: Bending moment in O

The plots are parameterized with respect to the blade pitch angle. In fact doing so it is possible to reduce the surface of the blade exposed to the free stream and thus the force.

10.5.3. Quasi-static power and time-to-fold

A reasonable time to fold the rotor could be $t_f = 45$ s.

Moreover, the power can be expressed as:

$$P = Fv_{act} = F\dot{\theta}b \cos \gamma_v \quad (10.14)$$

In doing so two possible procedure can be pursued:

10.5.3.1. Actuator speed constant

Imposing a fixed actuator speed to satisfy the time chosen (knowing the stroke), i.e. $v_{act} = 0.445\text{cm/s}$, it is possible to obtain the blade angular speed as:

$$\dot{\theta} = \frac{v_{act}}{b \cos \gamma_v} \quad (10.15)$$

Results are reported in 10.20 and 10.21:

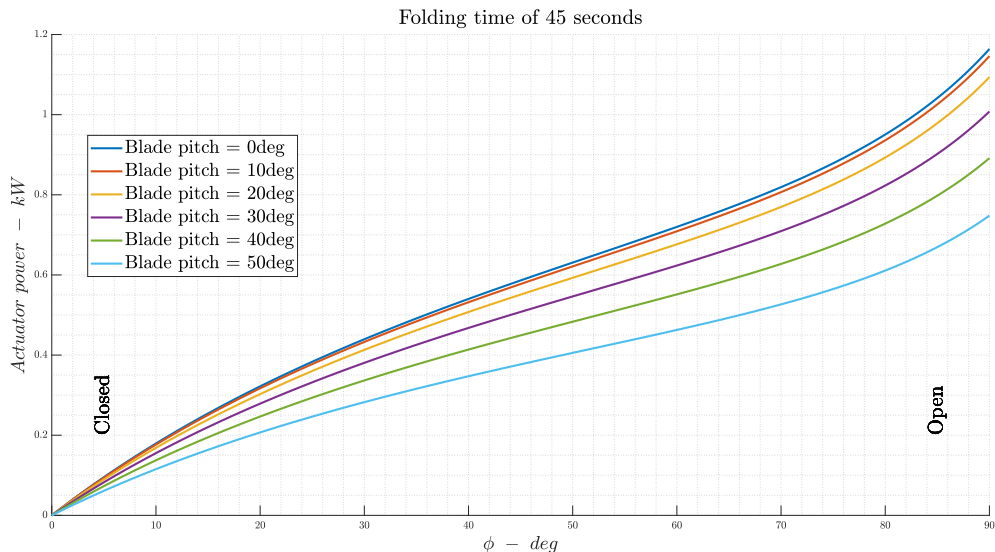
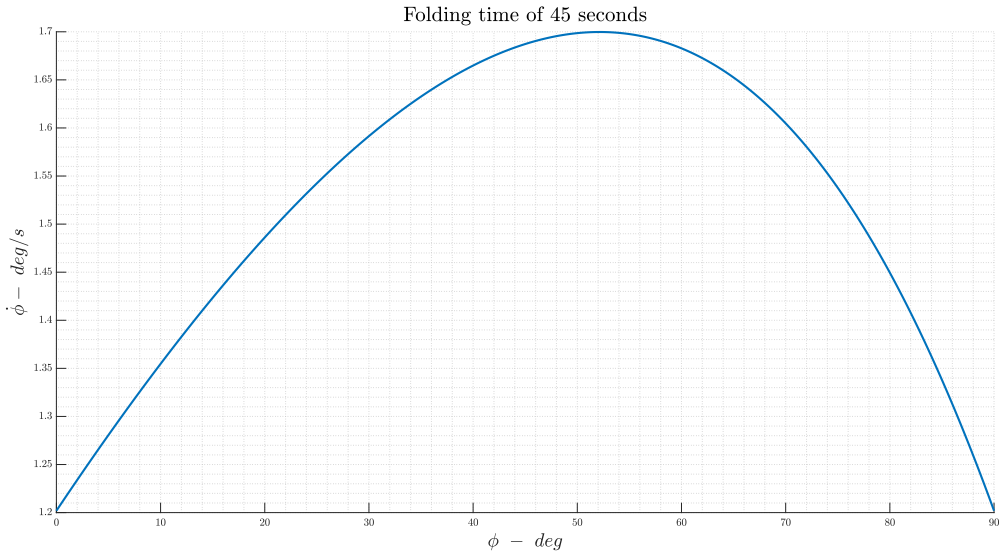


Figure 10.20: Actuator power for fixed actuator speed

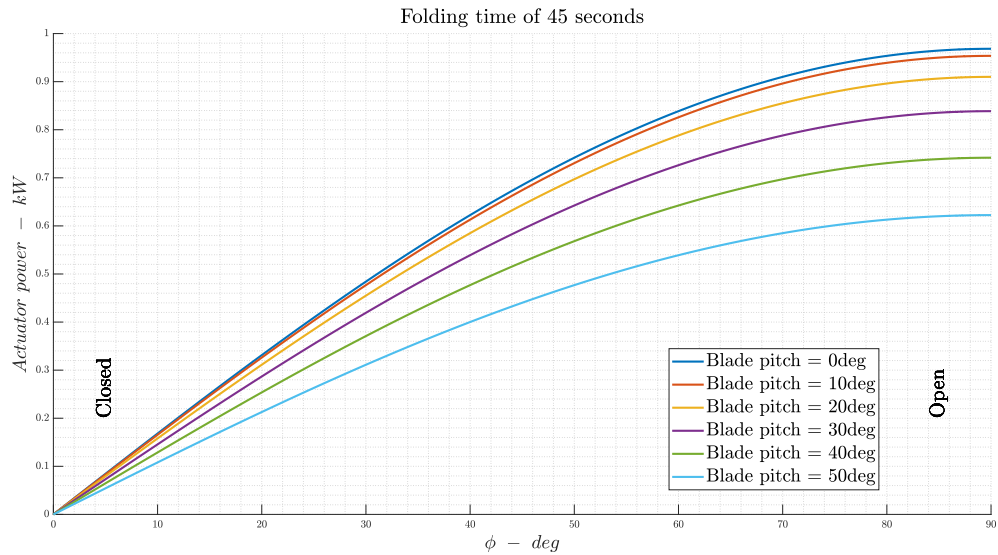


Figure 10.21: $\dot{\phi}$ for fixed actuator speed

10.5.3.2. Blade angular speed, $\dot{\phi}$, constant

Fixed the folding time, also $\dot{\phi}$ is fixed. In particular, for the time chosen $\dot{\phi} = 2^\circ/s$. The actuator speed can be obtained recalling equation 10.13.

Results are reported in 10.22 and 10.23:

Figure 10.22: Actuator power for fixed $\dot{\phi}$

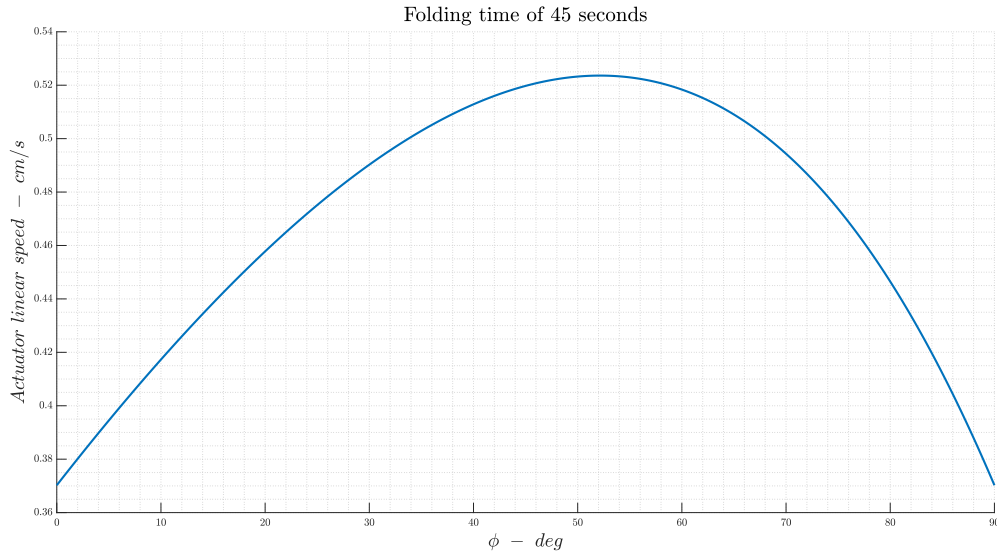


Figure 10.23: Actuator linear speed for fixed $\dot{\phi}$

10.5.4. Folding mechanism preliminary sizing results

Note that the peak of power required is slightly higher for the fixed actuator speed case. However, this is the typical way of operation of linear actuators

The following table 10.3 sum up the main characteristic required by the actuator:

Collapsed length	0.254 m
Extended length	0.505 m
Stroke	0.251 m
Actuator speed	0.45 cm/s
Maximum force	16 tons
Maximum power	1.2kW

Table 10.3: Actuator preliminary required characteristics

10.6. Blade Airfoil Section

The airfoils of rotor blades are chosen to give the rotor good aerodynamic efficiency while allowing the structural requirements of the blade to be satisfied.

The rotor blade section operates over a wide range of conditions and therefore different desirable characteristics are associated with each of them:



- hover, characterised by moderately high angle-of-attack and Mach number, the rotor is recommended to have a low drag and high lift-to-drag ratio.
- forward flight, where a particular phenomenon arises on the blades (see Figure 10.24), namely that the advancing blade perceives a very high speed, making it more sensitive to drag-divergence mach number (M_{dd}), while the retreating blade is subjected to a lower speed and therefore must have good stall characteristics (including a high maximum lift coefficient).

In addition, the airfoil should have a small pitching moment in order to minimize control system loads, especially in forward flight.

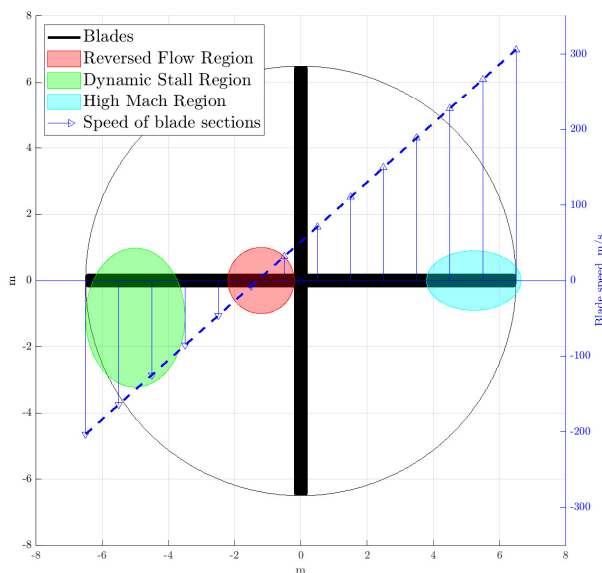


Figure 10.24: Critical areas of the rotor in forward flight at 100 kn

The two objectives of low M_{dd} and high $C_{l_{max}}$ result in design conflicts for new airfoils, as improvements in divergence Mach number require thin airfoils with limited camber while improvements in $C_{l_{max}}$ requires thicker airfoils with greater camber. So, the best way to solve this conflict is to use different airfoil along blade: an airfoil that provides a high $C_{l_{max}}$ can be used in the inboard blade, while an airfoil that delays the drag-divergence Mach number can be used at the tip. Anyway, as also proposed by Reference [9], in early stages of the project for simplicity of construction, a moderately thick airfoil with the same section over the entire span may be considered.

In the case of this project, the purpose of the rotor is to ensure vertical take-off and landing, and achieve the conversion speed. So, the rotor characteristics in forward flight

can be considered of secondary importance. Therefore, the most important requirements in rotor design are to reduce the airfoil drag in hover and maximize the lift-to-drag ratio. While, less important are the requirements of maximum lift coefficient, high critical mach, and low pitching moment.

Some airfoils were then analyzed on XFLR5 based on the advice of reference [9]. The procedure for choosing the best airfoil is the following one:

1. analyze all airfoils using XFLR5.
2. define a cost function (c) for each airfoil feature so that there are always values between 0 (worst case) and 1 (best case). In this case the cost functions are:

- for drag coefficient: $c_1 = 1 - \frac{C_{d(L/D)max} - (C_{d(L/D)max})_{min}}{(C_{d(L/D)max})_{min} - (C_{d(L/D)max})_{max}}$
- for lift-to-drag ratio: $c_2 = \frac{(C_l/C_d)_{max} - ((C_l/C_d)_{max})_{min}}{((C_l/C_d)_{max})_{max} - ((C_l/C_d)_{max})_{min}}$
- for pitching moment coefficient: $c_3 = 1 - \frac{|C_{m0}|}{|C_{m0}|_{max}}$
- for maximum lift coefficient: $c_4 = \frac{C_{lmax} - (C_{lmax})_{min}}{(C_{lmax})_{max} - (C_{lmax})_{min}}$
- for pressure coefficient at maximum thickness: $c_5 = \frac{C_{pmin} - (C_{pmin})_{min}}{(C_{pmin})_{max} - (C_{pmin})_{min}}$

3. normalize the results of the cost functions with respect to their sum, and weigh each profile normalized feature by a value chosen by the project team.

All the results discussed above are plotted and tabulated in Figures 10.25 and 10.26, and in Tables 10.4, 10.5 and 10.6.



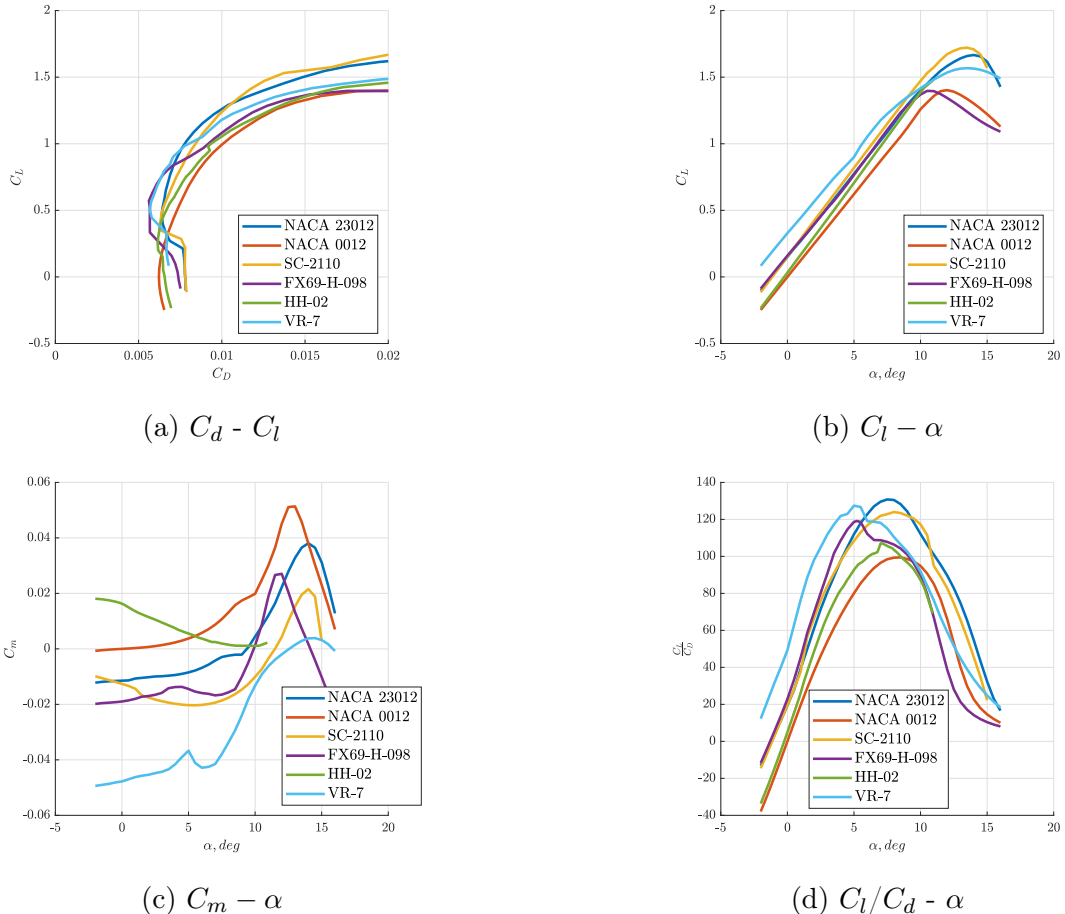
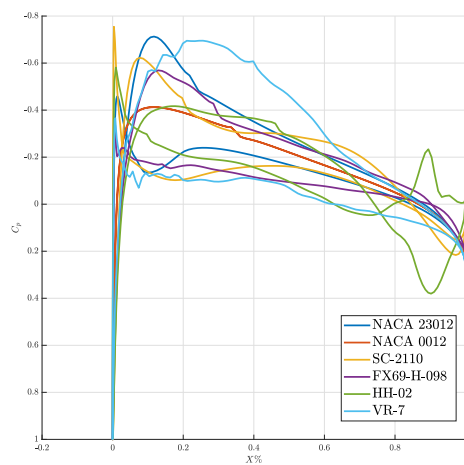
Figure 10.25: Aerodynamic curves estimated with XFLR5 ($Re = 4*10^6$, $M = 0.4$)

Figure 10.26: Pressure distribution for outboard blade airfoil sections

	23012	0012	SC-2110	FX69-H-098	HH-02	VR-7
$C_{d_{(L/D)max}}$	0.008309	0.010592	0.009813	0.006699	0.009346	0.007062
$(C_l/C_d)_{max}$	130.80	99.48	123.98	119.13	107.0	127.42
C_{m_0}	-0.01147	0	-0.01263	-0.01897	0.01628	-0.04777
$C_{l_{max}}$	1.67	1.40	1.72	1.40	1.48	1.57
$C_{p_{min}}$	-0.71284	-0.41263	-0.62229	-0.56913	-0.58101	-0.69520

Table 10.4: Features of rotor blade airfoil obtained from XFLR5 ($Re=4 \cdot 10^6$, $M=0.4$)

	23012	0012	SC-2110	FX69-H-098	HH-02	VR-7
c_1	0.586403	0	0.199894	1	0.320029	0.906689
c_2	1	0	0.782107	0.627251	0.240004	0.892030
c_3	0.759987	1	0.735647	0.602837	0.659174	0
c_4	0.829445	0.017064	1	0	0.239950	0.525596
c_5	0	1	0.301622	0.478698	0.439126	0.058759

Table 10.5: Cost function for features of rotor blade airfoil

	23012	0012	SC-2110	FX69-H-098	HH-02	VR-7	Weight
\bar{c}_1	0.194623	0	0.066344	0.331893	0.106216	0.300924	35%
\bar{c}_2	0.282383	0	0.220853	0.177097	0.067773	0.251894	35%
\bar{c}_3	0.202251	0.266124	0.195772	0.160429	0.175422	0	10%
\bar{c}_4	0.317545	0.006533	0.382840	0	0.091862	0.201219	10%
\bar{c}_5	0	0.438942	0.132395	0.210121	0.192751	0.025792	10%
Weighted sum	21.9	7.1	17.2	21.5	10.7	21.6	100%

Table 10.6: Cost function of rotor blade airfoil normalized with respect the sum

In conclusion, NACA 23012 is shown to be the best solution as blade airfoil. One problem with the chosen airfoil is the low $C_{p_{min}}$ (and thus the low critical mach). A good alternative would be to choose the FX69-H-098 airfoil, which has good aerodynamic characteristics with a higher $C_{p_{min}}$; or even better, in advanced stages of the project, one could consider to design a blade with multiple airfoils.



11 | Wing Design

The primary function of the wing is to produce sufficient lift while generating minimum drag, and minimum pitching moment.

11.1. Introduction

As suggested in Reference [29], during the wing design process, 18 parameters must be determined. They are as follows:

1. Wing reference area (S_{ref});
2. Number of wings;
3. Vertical position relative to the fuselage (high, mid, or low wing);
4. Horizontal position relative to the fuselage;
5. Airfoil section;
6. Aspect ratio (AR);
7. Taper ratio (λ);
8. Tip chord (C_t);
9. Root chord (C_r);
10. Mean aerodynamic chord (MAC or \bar{C});
11. Span (b);
12. Twist angle (or washout) (α_t);
13. Sweep angle (Λ);
14. Dihedral angle (Γ);
15. Incidence (i_w);
16. High-Lifting Devices;

17. Aileron;
18. Other wing accessories.

The known parameters are: wing reference from SMP (Chapter 9), number of wings and vertical position from the configuration (Chapter 7). Other parameters like horizontal position of the wing and aileron will be discussed after the fuselage and tail design.

The remaining parameters can be divided into three macrocategories:

- I. Airfoil section.
- II. Finite wing parameters.
- III. High Lift Device and other accessories.

11.2. Airfoil section

Using the method proposed by the Reference [29], a series of possible airfoils were selected, which were then analyzed individually to find the best configuration.

Specifically, the list of possible airfoils was chosen through the calculation of the lift coefficient needed in cruise and in the conversion phase.

$$C_{l_{cruise}} = \frac{W_{avg} g}{0.5 \rho_{cruise} V_{cruise}^2 S} \frac{1}{0.95 * 0.9} \quad (11.1)$$

$$C_{l_{conversion}} = \frac{W_{to} g}{0.5 \rho_{conversion} \tilde{V}_{conversion}^2 S} \frac{1}{0.95 * 0.9} - \Delta C_{L_{flap}}$$

With $W_{avg} = \frac{1}{2}(W_i^{cruise} + W_f^{cruise}) = 54,593 \text{ lb}$, $V_{cruise} = 450 \text{ kn}$, $\Delta C_{L_{flap}} = 1.3$ for slotted flaps, and $\tilde{V}_{conversion} = V_{conversion} - 10 \text{ kn} = 100 \text{ kn}$.

In addition, considering a cruise airspeed of 450 kn, the airfoil thickness must be lower than 12% of the chord.

Figure 11.1 shows the design point, thanks to which many profiles could be excluded a-priori. The profiles that will be analyzed are as follows:

- NACA 63 – 209
- NACA 64 – 210
- NACA 63A – 210
- NACA 66₁ – 212
- NACA 65₁ – 212



- NACA 64A – 210
- NACA 2408
- NACA 1410
- NACA 64 – 209
- NACA 64₁ – 112
- Whitcomb

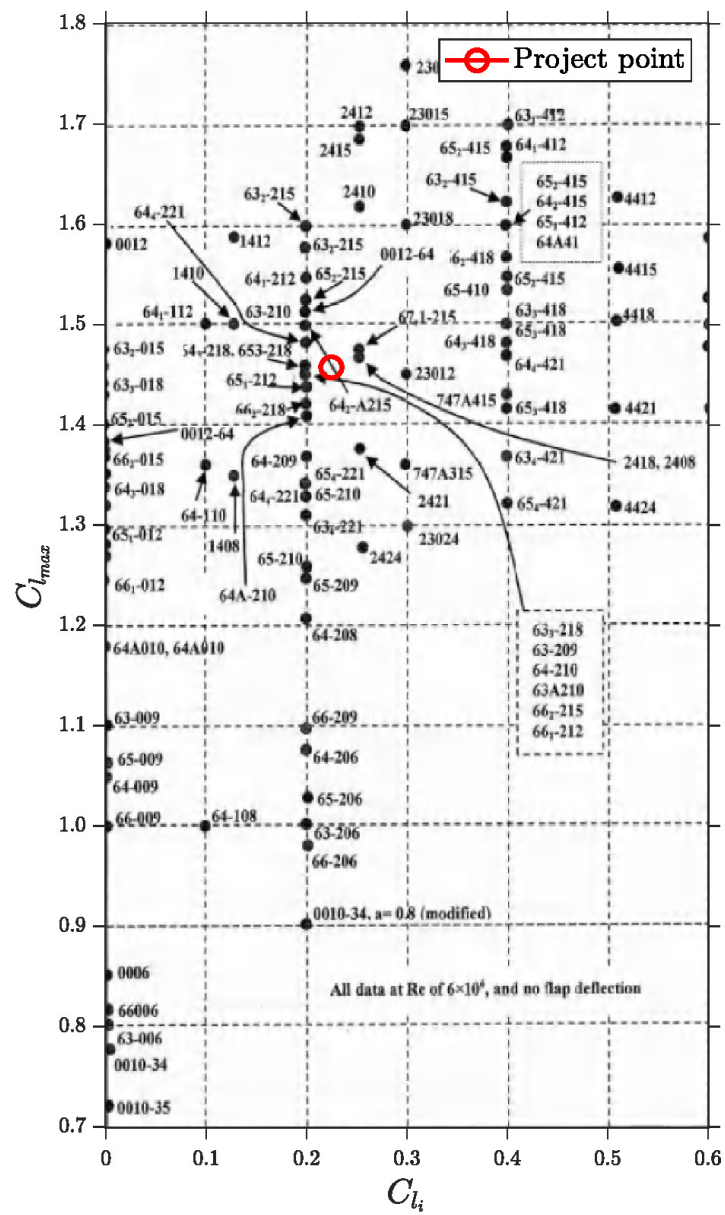


Figure 11.1: Project point for wing airfoil (from Reference [29])

So, airfoils that matched values in Equation 11.1 were then analyzed in more detail on XFLR5 under the two most important conditions:

1. Mach 0, $h = 2000$ ft and $\text{Re} = 1.1 \cdot 10^7$, for the conversion phase
2. Mach 0.71, $h = 20000$ ft and $\text{Re} = 2.8 \cdot 10^7$, for the cruise phase

Then, the procedure for choosing the best airfoil is the same used for the rotor airfoil (Section 10.6) and it is the following one:

- a) Analyze all airfoil using XFLR5 in the two flight conditions considered. Figures 11.2, 11.3, 11.4, 11.5, 11.6, and 11.7 show the results of these analysis on XFLR5.

As already anticipated, the purpose of the wing in this design is to provide both high-speed cruise in best range attitude and conversion from the jet phase to the rotorcraft phase at low speed (and without ground effect); therefore, the parameters considered for the choice of the wing airfoil are $C_{d_{min}}$, $(\sqrt{C_l}/C_d)_{max}$ and C_{m_0} for cruise, while $C_{l_{max}}$ and C_{m_0} for the conversion phase. Table 11.1 lists the values of these parameters for the selected airfoils.

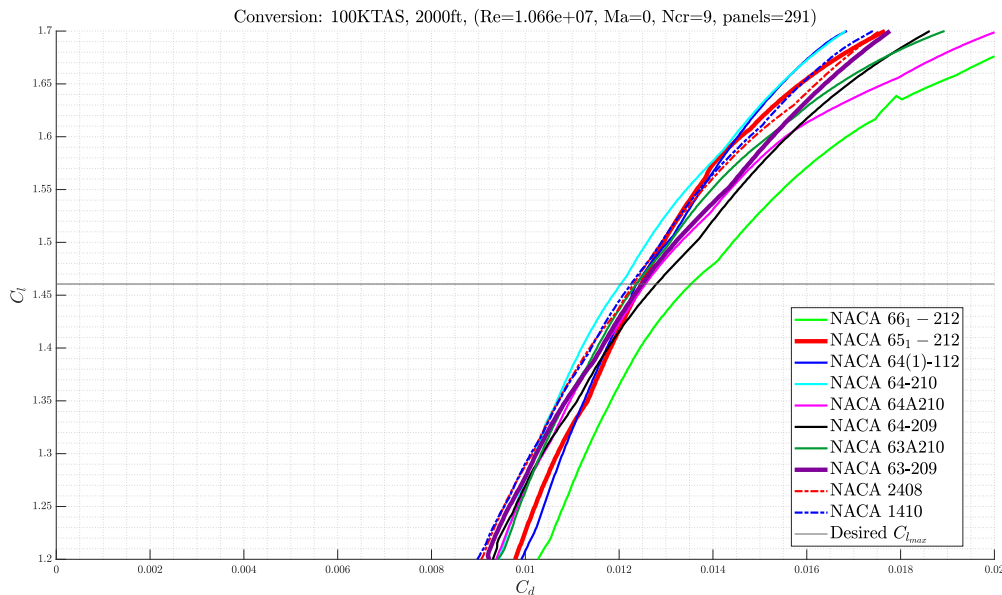
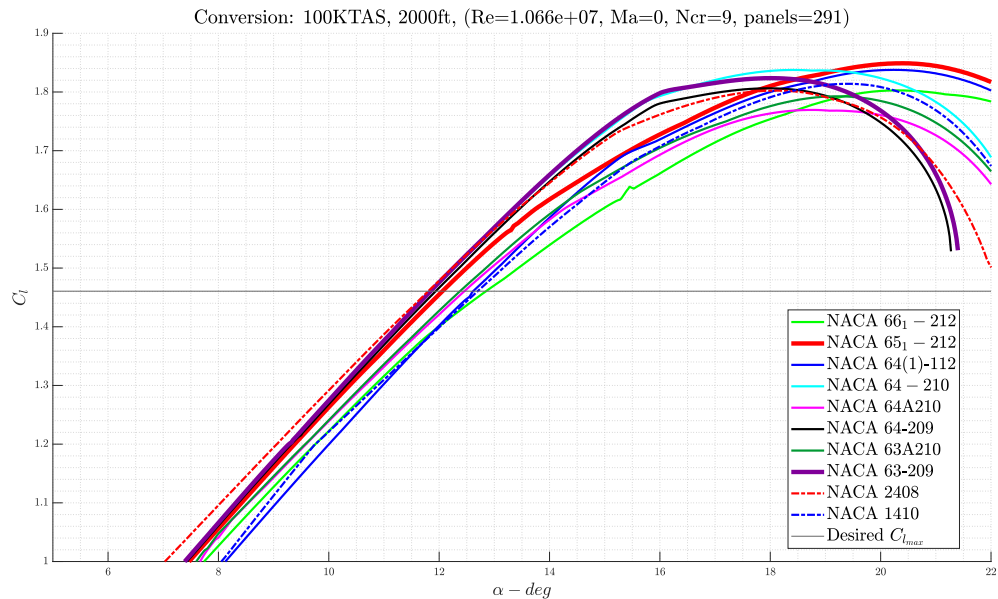
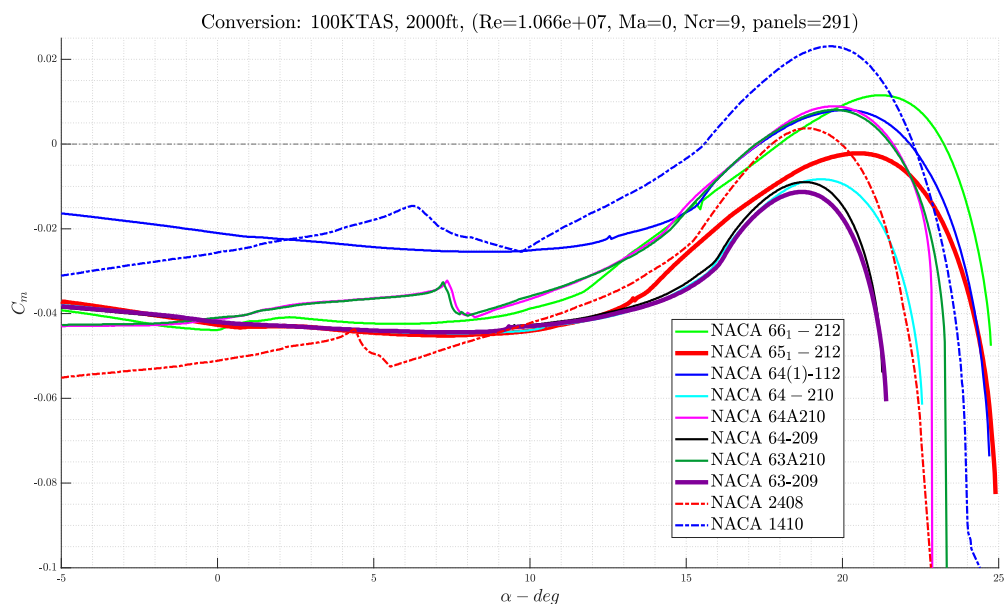
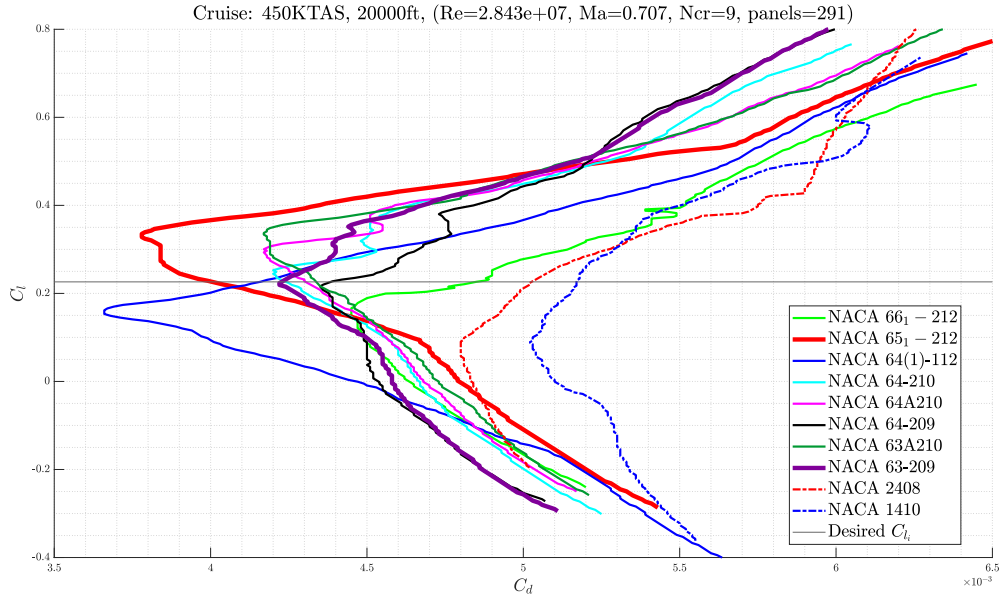
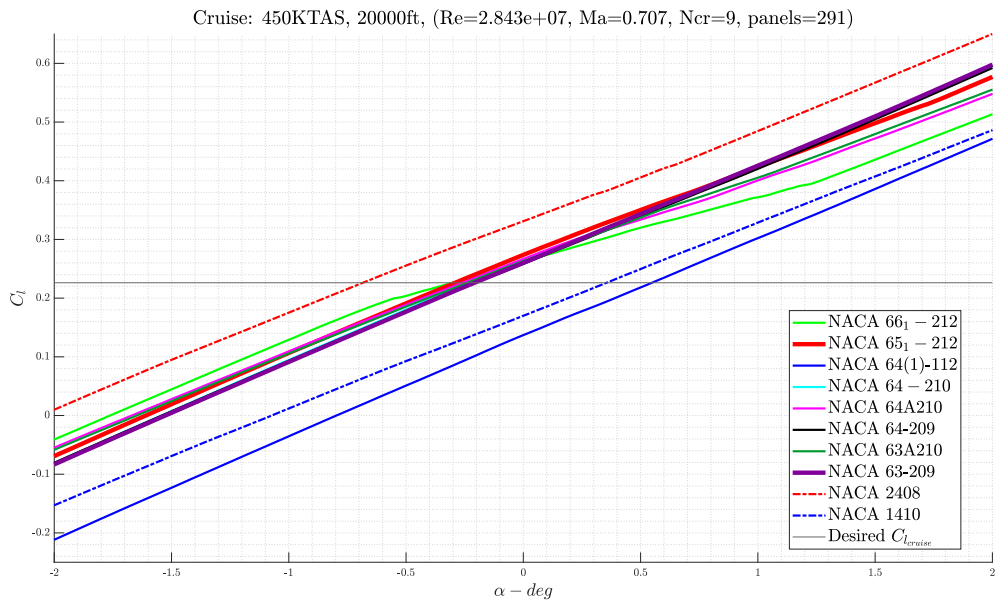
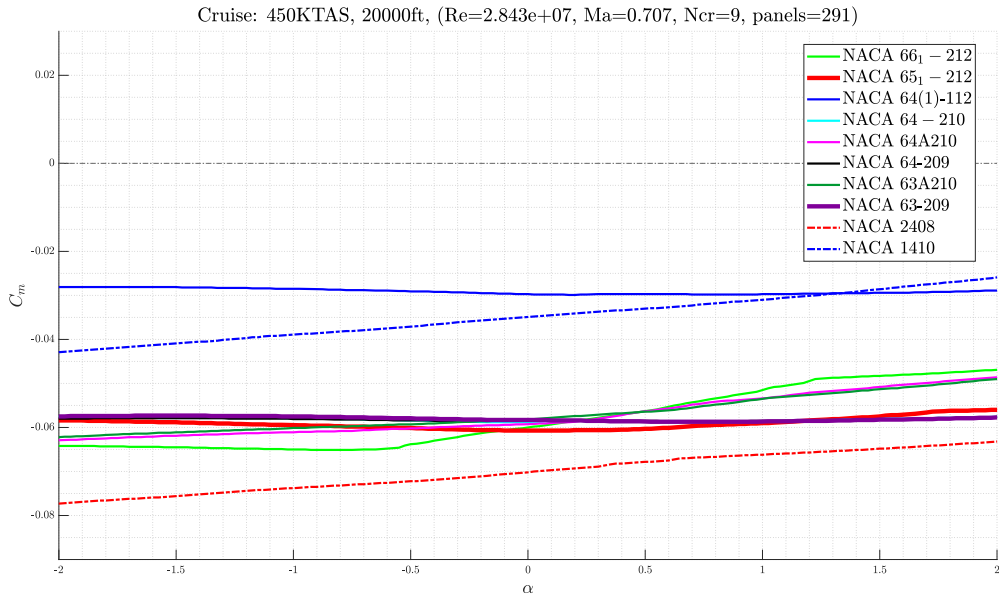


Figure 11.2: $C_d - C_l$ in conversion phase



Figure 11.3: C_l - α in conversion phaseFigure 11.4: C_m - α in conversion phase

Figure 11.5: C_d - C_l in cruise phaseFigure 11.6: C_l - α in cruise phase

Figure 11.7: C_m - α in cruise phase

Airfoil	$C_{d_{min}}^{cruise}$	$(\sqrt{C_l}/C_d)_{max}^{cruise}$	$C_{m_0}^{cruise}$	$C_{m_0}^{conversion}$	$C_{l_{max}}^{conversion}$
63 – 209	0.00422	149.7	-0.0583	-0.0420	1.824
64 – 210	0.00425	144.7	-0.0588	-0.0421	1.838
63A210	0.00434	141.4	-0.0582	-0.0410	1.793
66 ₁ – 212	0.00483	127.9	-0.0600	-0.0439	1.803
65 ₁ – 212	0.00399	154.1	-0.0607	-0.0426	1.849
64A210	0.00431	140.8	-0.0592	-0.0413	1.769
2408	0.00502	147.1	-0.0702	-0.0511	1.802
1410	0.00517	136.8	-0.0349	-0.0256	1.814
64 – 209	0.00439	149.3	-0.0584	-0.0422	1.806
64 ₁ – 112	0.00416	134.5	-0.0297	-0.0210	1.838
Whitcomb	0.00706	130.6	-0.1669	-0.1387	2.327

Table 11.1: Parameters of wing airfoil

- b) Define cost functions (c) for each airfoil feature so that there are always values between 0 (worst case) and 1 (best case). The cost function are:

- for drag coefficient: $c_1 = \frac{C_{d_{min}}^{cruise} - (C_{d_{min}}^{cruise})_{max}}{(C_{d_{min}}^{cruise})_{min} - (C_{d_{min}}^{cruise})_{max}}$
- for lift-to-drag ratio: $c_2 = \frac{(\sqrt{C_l}/C_d)_{max} - ((\sqrt{C_l}/C_d)_{max})_{min}}{((\sqrt{C_l}/C_d)_{max})_{max} - ((\sqrt{C_l}/C_d)_{max})_{min}}$

- for pitching moment coefficient in conversion: $c_3 = 1 + \frac{|C_{m0}^{conv}| - |C_{m0}^{conv}|_{min}}{|C_{m0}^{conv}|_{min} - |C_{m0}^{conv}|_{max}}$
- for pitching moment coefficient in cruise: $c_4 = 1 + \frac{|C_{m0}^{cruise}| - |C_{m0}^{cruise}|_{min}}{|C_{m0}^{cruise}|_{min} - |C_{m0}^{cruise}|_{max}}$
- for maximum lift coefficient: $c_5 = \frac{C_{l_{max}}^{conv} - (C_{l_{max}}^{conv})_{min}}{(C_{l_{max}}^{conv})_{max} - (C_{l_{max}}^{conv})_{min}}$

In Table 11.2 are presented the values of these cost functions.

Airfoil	c_1	c_2	c_3	c_4	c_5
63 – 209	0.925081	0.833249	0.821580	0.791545	0.097220
64 – 210	0.915309	0.642554	0.820731	0.788265	0.122332
63A210	0.885993	0.517484	0.830076	0.792638	0.041614
66 ₁ – 212	0.726384	0	0.805438	0.779155	0.059731
65 ₁ – 212	1	1	0.816483	0.774052	0.142601
64A210	0.895765	0.493078	0.827528	0.784985	0
2408	0.664495	0.733608	0.744265	0.704810	0.059193
1410	0.615635	0.341145	0.960918	0.790816	0.066009
64 – 209	0.869707	0.816968	0.820306	0.790816	0.066009
64 ₁ – 112	0.944625	0.251165	1	1	0.122511
Whitcomb	0	0.104176	0	0	1
Summation	8.442997	5.733428	8.447324	8.168367	1.791031

Table 11.2: Cost functions of wing airfoil

- c) Normalize the results of the cost functions (\bar{c}) with respect to their sum, and weight each profile normalized feature by a value chosen by the project team; the airfoil with the highest weighted sum is the best one. Specifically, the following weights were chosen:
- 45% for minimum drag (in cruise)
 - 25% for $(\sqrt{C_l}/C_d)_{max}$ (in cruise)
 - 5% for pitching moment in cruise
 - 10% for pitching moment in conversion phase
 - 15% for maximum lift coefficient (in conversion phase).

These normalized and weighted values are in Table 11.3.



Airfoil	\bar{c}_1	\bar{c}_2	\bar{c}_3	\bar{c}_4	\bar{c}_5	Weighted sum
63 – 209	0.109568	0.145332	0.097259	0.096904	0.054281	10.835
64 – 210	0.108410	0.112072	0.097159	0.096502	0.068302	10.159
63A210	0.104938	0.090257	0.098265	0.097038	0.023235	8.795
66 ₁ – 212	0.086034	0	0.095348	0.095387	0.033350	5.802
65 ₁ – 212	0.118441	0.174416	0.096656	0.094762	0.079619	12.325
64A210	0.106096	0.086001	0.097963	0.096101	0	8.384
2408	0.078704	0.127953	0.088107	0.086285	0.033050	8.549
1410	0.072917	0.059501	0.113754	0.117784	0.044567	7.164
64 – 209	0.103009	0.142492	0.097108	0.096814	0.036855	10.206
64 ₁ – 112	0.111883	0.043807	0.118381	0.122423	0.068403	8.952
Whitcomb	0	0.018170	0	0	0.558338	8.829
Weight	45%	25%	10%	5%	15%	100%

Table 11.3: Normalized cost functions of wing airfoil

From these analyses, the best result would be the NACA 65₁ – 212; however, to improve the lift distribution on the wing (see Section 11.3.5), the Team decided to choose a mixed configuration:

- NACA 65₁ – 212 on all of the inboard wing.
- NACA 63 – 209 on wingtip, which is the second best result from Table 11.3, and allows to reduce thickness and lift generated without big aerodynamic disadvantages.

Note that with "inboard wing" (or "inner wing") it meant the part of the wing between the fuselage and the rotor nacelle, while with "outboard wing" (or "outer wing") it meant the part of wing between the rotor nacelle and the wingtip.

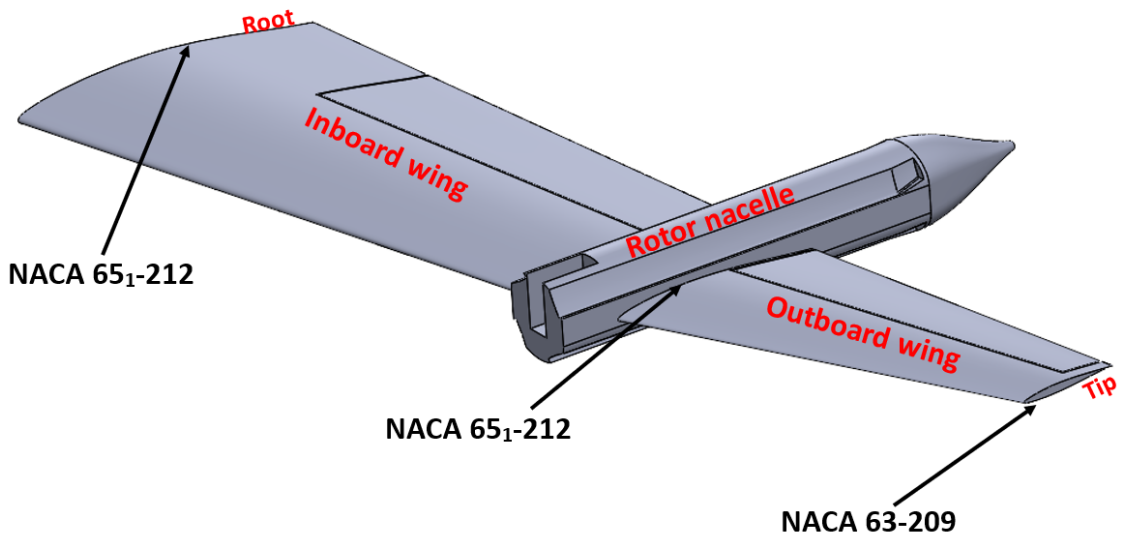


Figure 11.8: Airfoil sections along the wingspan

11.3. Finite wing parameters

During this section, historical data, analytical formulas, and software based on Vortex Lattice Method (such as XFLR5) will be exploited to derive the various parameters.

Raven 4 will be capable to fly at high subsonic speed, but the software XFLR5 is valid only for subsonic flow; it is possible to extend its validity range to high subsonic flow through the Prandtl-Glauert correction:

$$C_p = \frac{C_p^{(uncomp)}}{\sqrt{1 - M^2}} \quad \& \quad C_l = \frac{C_l^{(uncomp)}}{\sqrt{1 - M^2}} \quad (11.2)$$

11.3.1. Wing incidence

The wing incidence (i_w) is the angle between the fuselage center line and the wing chord line at its root.

This angle must satisfy the following design requirements:

- The wing setting angle must be such that the fuselage generates minimum drag during cruising flight (i.e., the fuselage angle of attack must be zero in cruise).
- The wing must be able to generate the desired lift coefficient during cruising flight.
- The wing must produce minimum drag during cruising flight.



- The wing setting angle must be such that the wing angle of attack could be varied safely (in fact increased) during take-off operation.

An iterative approach was followed; in fact, initially, having no other data available, the wing incidence was provisionally fixed by exploiting only the $Cl - \alpha$ plot of the airfoil. Subsequently, knowing the whole-wing data, through analytical methods and VLM simulations on XFLR5, a wing incidence of 1.6° was chosen.

This angle may be modified after the design of other components. For instance, “a fuselage with large upsweep over the rear portion to accept aft cargo doors may have its minimum drag at a small positive angle of attack. In such cases, the wing incidence will be reduced accordingly” [29].

11.3.2. Aspect ratio

To compensate the effects of the other parameters, especially sweep angle, the aspect ratio is increased slightly, without deviating too much from the preliminary choice. Thus, an aspect ratio of 9 is selected, so that some advantage is gained on aerodynamics features, without increasing the wingspan excessively.

11.3.3. Taper ratio

The primary reasons of having a tapered wing are:

- Weight
- Elliptical lift distribution
- Lower stall speed on tip (for lateral control and stability)

All these reasons are indispensable for this project, since the wing is quite large, and the aircraft must be optimized for both high speeds during cruise and low speeds during the conversion phase from rotorcraft to jet mode. Despite this, the presence of the turboshaft engines and rotors in the middle of the wing prevent the taper ratio from being optimized to the fullest at this stage of the project, because stresses and weights are not fully defined in the preliminary design, so the project team decided to maintain a fairly large wing chord at the rotor nacelle, following a more conservative approach. Specifically, in the first part of the wing the taper ratio is equal to 0.7; this choice will obviously only bring disadvantages, making the wing less aerodynamic and heavier, but it guarantees a wing chord of 9.43 ft (2.88 m) at the rotor nacelles.

For the outboard part of the wing it's possible to make a more detailed analysis. As can also be seen from Reference [11], the optimal global taper ratio value is 0.3, so that the taper ratio of the outer wing should be 0.43; this value allows to have all the advantages seen on the previous list, and also ensuring minimum drag. However, since the outer wing is responsible for a small portion of the overall aerodynamics, it will be possible to make slight changes to the taper ratio to improve other characteristics, such as stability and controls.

$\lambda_{inboard\ wing}$	$\lambda_{outboard\ wing}$	C_{root}	C_{middle}	C_{tip}	b_{wing}
0.7	0.43	13.5 ft (4.1 m)	9.4 ft (2.9 m)	4.0 ft (1.2 m)	81.14 ft (24.73 m)

Table 11.4: Taper ratio and wing chords

11.3.4. Sweep angle

Sweep angle delays effects of compressibility, and affects both lateral-directional static stability and longitudinal position of the center of gravity, which is a critical aspect for a rotorcraft configuration.

After analysis on XFOIL of pressure distribution of the selected airfoil *NACA 651 – 212* (Figure 11.9), it was observed that without sweep angle, in cruise the critical Mach would be equal to 0.718, which is less than cruise speed requested in the RFP (“ $V_{cruise} = 450$ kn at 20000 ft”), so it is necessary to have a swept wing.



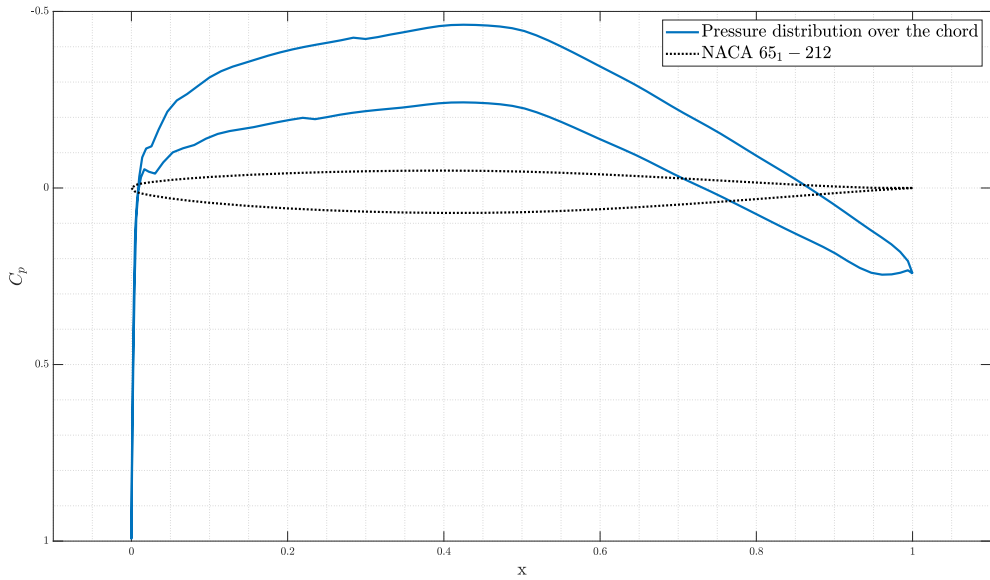


Figure 11.9: Pressure distribution over wing airfoil (NACA 65(1)-212)

Therefore, to ensure, with an acceptable safety marginal, that critical Mach will not reach during cruise, it was chosen a sweep angle of 14° considering the 50% chord (location of maximum thickness of the airfoil), or 18° for the leading edge sweep angle. Instead, the outer wing must have a leading edge sweep angle of 30° to ensure a taper ratio of 0.43 and to avoid compressibility effects on aileron in cruise.

It can be seen that this sweep angle value is slightly lower than in other aircraft (Reference [29] and [24]), because sweeping the wings back also moves back the rotors for vertical take-off; this implies three major problems: stricter limits on the static margin, rotor flow too close to the tail and more difficulty being trimmed in the rotorcraft mode.

Figure 12.11 shows a first, preliminary, representation of the wing; from this preliminary shape of the wing, a mean aerodynamic chord of 10.322 ft (3.146 m) is derived.

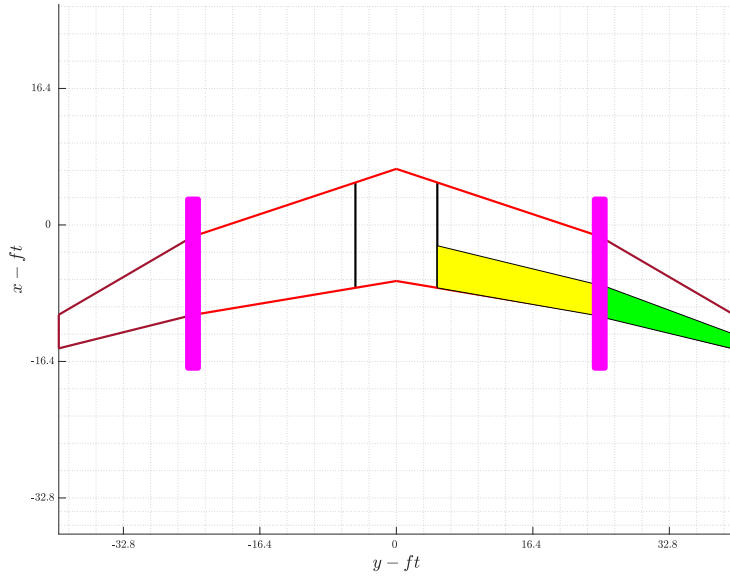


Figure 11.10: Top view of the wing

Major side effects of the sweep angle are:

- Change in Lift distribution, as can be seen from Figure 11.11, which shows an example of realistic lift distribution for a swept and for a straight wing.

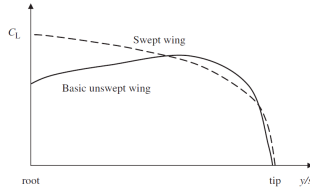


Figure 11.11: Typical variation of lift distribution over the wing due to sweep angle

- Reduction of the wingspan, and so reduction of the aspect ratio:

$$AR_{eff} = b_{eff}^2 / S = AR * \cos^2(\Lambda) = 8.47 \quad (11.3)$$

- Increase stall speed, governed by the following semi-empirical relationship [29]:

$$C_{L_{max}} = C_{l_{max}} (0.86 - 0.002(\Lambda[deg])) = 1.53 \quad (11.4)$$

- Reduction of the wing lift curve slope governed by a modified equation based on Prandtl-Glauert correction:

$$C_{L_\alpha} = \frac{2\pi AR}{2 + \sqrt{AR^2(1 + \tan^2(\Lambda) - M^2) + 4}} = 5.95 \quad (11.5)$$



- Dihedral effect on lateral stability:

$$C_{L\beta} \propto -\sin(2\Lambda_{LE}) = -0.47 \quad (11.6)$$

- Reduction in effectiveness of control surfaces and high lift devices, which will have to be larger.

Table 11.5 summarizes the parameters influenced by the sweep angle

$\Lambda_{LE}^{inboard\ wing}$	$\Lambda_{LE}^{outboard\ wing}$	AR_{eff}	$C_{L_{max}}$	$C_{L\alpha}$	$C_{L\beta}$	MAC
18°	30°	8.47	1.53	5.95	-0.47	10.32 ft (3.15 m)

Table 11.5: Sweep angle and wing chords

11.3.5. Twist angle

The two main functions of the twist angle are delay the stall of the wingtip (so that the stall occurs firstly on the root) and to have an elliptical lift distribution. There are two types of twist angle:

1. Aerodynamic twist when the tip airfoil section and root airfoil section are not the same.
2. Geometric twist when the tip incidence and root incidence are not the same.

In this project, a mixed configuration was chosen. Thus, it was decided both to use an different airfoil at the tip which is similar to the one selected for the inboard wing, but thinner (i.e., NACA 63-209), and to apply a small geometric twist.

In particular, in order to have a lift distribution as elliptical as possible, it's sufficient to impose a twist angle of -2.8° at the tip and 1.6° at the root of the wing. In addition, it was decided to keep the part of the wing where the rotor nacelle will be located at an angle equal to zero; in this way, both the fuselage and the rotor nacelle will have zero AoA in cruise. This means that there are two different linear twist along the wing, as seen in Figure 11.12.

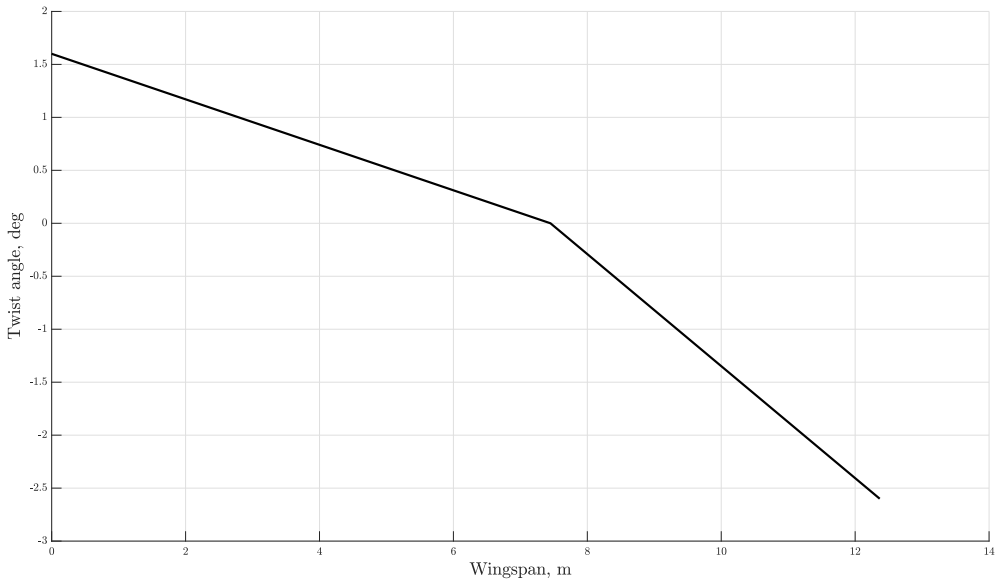


Figure 11.12: Twist angle along the wingspan

11.3.6. Dihedral angle

As a reminder, a laterally statically stable aircraft must produce a negative rolling moment to return to the original wing-level situation. This is technically translated into a negative dihedral effect ($C_{L\beta} < 0$). A more negative $C_{L\beta}$ means more spiral stability, but at the same time less dutch-roll stability.

A dihedral angle (Γ) can be positive or negative (also called anhedral); the role of a positive dihedral angle is to induce a positive increase in angle of attack ($\Delta\alpha \approx \beta\Gamma$), and this will increase the lateral stability, vice versa for a negative dihedral angle.

Due to the swept-back and high wing, our aircraft is already more laterally stable than necessary, and so less controllable. Thus, the team opted for a negative dihedral angle. Since there are no major limits on the clearance between engines and ground, the best way to size the anhedral angle would be through a balance between lateral stability and roll control. Unfortunately, such a detailed analysis would be complicated to sustain at this point of the project, so it was decided to choose the angle value by exploiting historical data of existing aircraft from Reference [24].

Therefore, as a starting point a dihedral angle of -3.5° is selected, but the exact value might change at later stages of the project, e.g., to improve stability/controllability of the whole aircraft.



11.3.7. Lift and load distribution

Both lift and load distribution are important in wing design and are preferred to be elliptical. Specifically, the distribution of lift coefficient CL per unit span along the wing is referred to as lift distribution, while the variation of “lift coefficient times sectional chord (C.CL)” along the span is referred to as the load distribution.

An elliptical lift distribution guarantees flight safety in the event of stall, because the aileron (on tip) could be still effective, and also yields the minimum induced drag. Furthermore, the bending moment at wing root is a function of load distribution, so if the load distribution is concentrated near the root the bending moment is considerably less than when it's concentrated near the tip.

Hence, considering the parameters chosen in the previous paragraphs, i.e., twist angle, taper ratio, and sweep angle, the lift and load distributions obtained are shown in Figures 11.13 and 11.14. These distributions are obtained from a simplified VLM simulation on XFLR5, in order to consider also the contributions of the fuselage and nacelles.

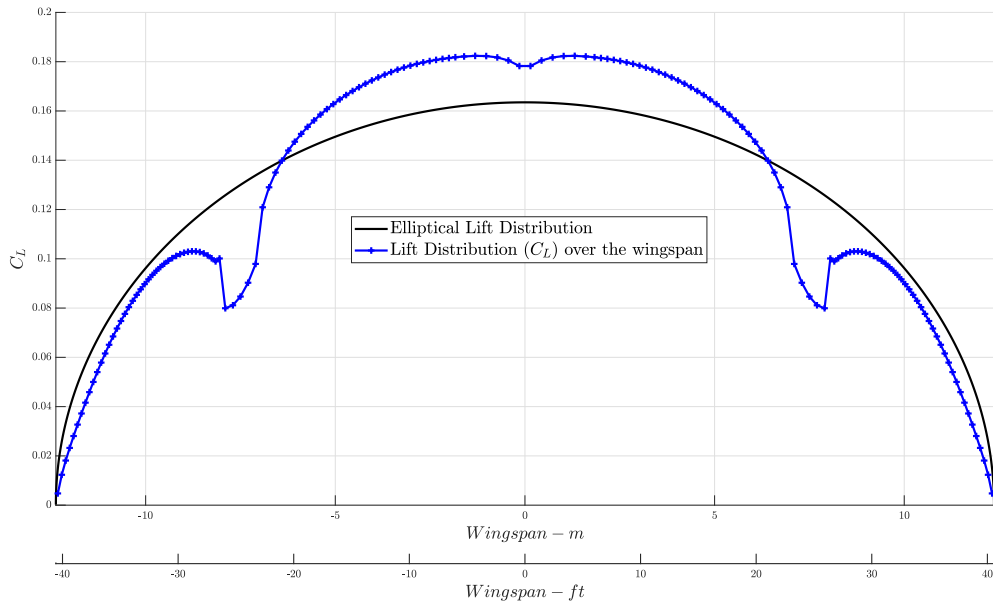


Figure 11.13: Lift Distribution

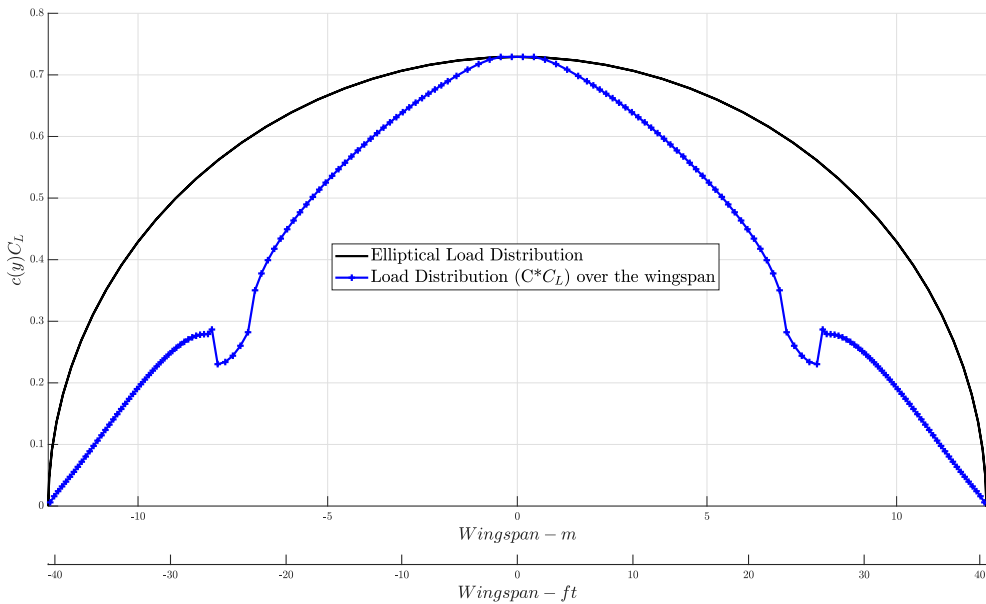


Figure 11.14: Load Distribution

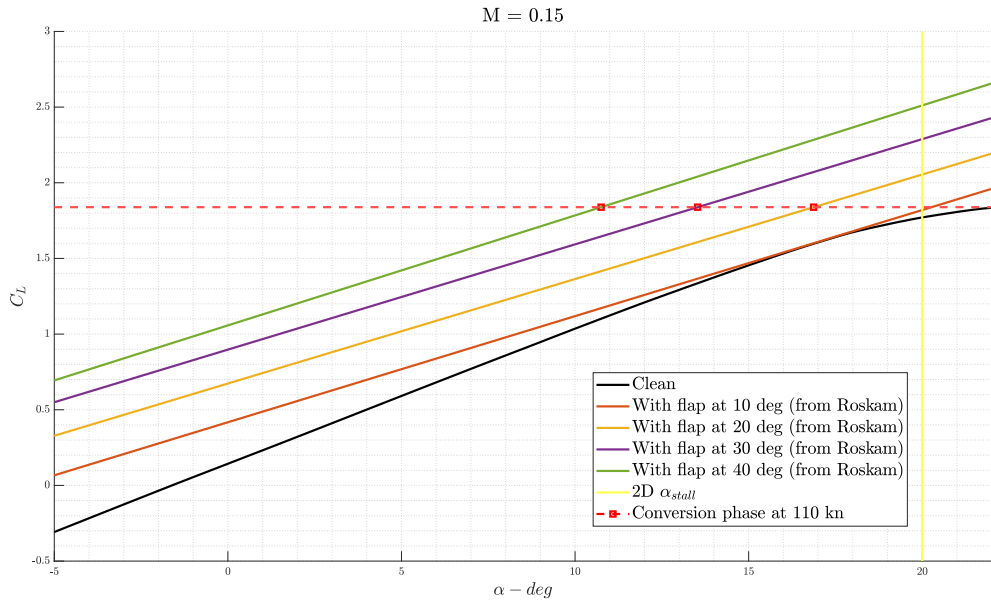
11.4. High Lift Device

In order to reduce the download in hover, the Team selected an extended slotted flap configuration all over the wingspan with a chord of 40% of the wing chord. Precisely, a traditional flap was designed in the inboard wing and a flaperon in the outboard wing to provide also control in roll. The main disadvantage of flaperons is the loss of roll control effectiveness when the flaps are down, so care was taken to ensure that all flight phases in airplane mode could be performed using only the inboard wing flaps.

In this way, the flaps on the outer wing will only be used when the rotors are unfold (especially in hover, with slotted flap deflected by 80-90°).

The design of the wing flaps was handled by both VLM software and Roskam's analytical methods (Reference [26]). Thus, the effect of the inner flaps alone on the lift coefficient can be seen in the Figure 11.15. From a preliminary analysis it is observed that the conversion phase from rotorcraft mode to jet mode (and vice versa) at 110 kn (56.6 m/s) will be feasible while keeping flaps deflected by an angle between 20° and 40°.



Figure 11.15: $C_L - \alpha$ curve with slotted flap (at Mach = 0.15)

11.5. Analysis on XFLR5

Finally, main parameters of the wing obtained from VLM viscous analysis on XFLR5 are in Table 11.6.

$C_{L_{max}}^{clean}$	1.77	$C_{d_0}^{clean}$	0.0050
$C_{L_{max}}^{flap}$	2.50	α_0	-2.00°
C_{L_α}	4.659 rad ⁻¹	C_{L_0}	0.16

Table 11.6: Aerodynamic results for the wing isolated @ $Ma = 0$

12 | Tail design

In general, the tail is initially designed based on trim requirements, and later revised based on stability and control requirements. So, tail design consists of an iterative process because knowledge of the whole aircraft is necessary. The proposed procedure is the one presented in M.H. Sadraey's Aircraft design book [29]. The design of the vertical and horizontal tails might be performed almost in parallel. However, there is one step in the advanced vertical tail design (i.e. spin recovery) where, the effect of the horizontal tail into the vertical tail must be investigated.

12.1. Tail configuration

12.1.1. Tail location

The vertical tail, if present, is forced to be in the aft fuselage portion due to stability reasons. In fact as will be discussed in Chapter 19, the condition for the directional control-fixed static stability is: $N_{CG|\beta} > 0$, or in the Borri's formulation, $x_{CG} - x_B > 0$, i.e. the CG must lie ahead of the directional aerodynamic center.

In general, the vertical tail, unless there is some special reason, is placed at the top of the fuselage again for stability reasons. In fact as will be discussed in Chapter 19, the condition for the lateral control-fixed static stability is: $L_{CG|\beta} < 0$, or in the Borri's formulation, $z_{CG} - x_B > 0$, i.e. the CG must lie below the directional aerodynamic center. Sometimes an extension of the vertical tail in the ventral area could be introduced in order to reduce an excessive lateral static stability or to limit the undesirable effect of adverse roll/yaw coupling as well as improve spin recovery characteristic. However, in the Raven 4 design, these needs do not seem to arise at the beginning, recalling also that the rear cargo bay requires free space to be operated smoothly.

Generally speaking, concerning excessive stability condition, recall that stability is the opposite of controllability, where controllability is intended as the capability to break the equilibrium.

Based on its longitudinal location, the horizontal tail could be:

- aft horizontal tail
- fwd horizontal tail, also called canard
- aft and fwd tail, called triplane

In the case of special requirements, such as extreme stealth features , the horizontal tail may be absent. This, however, leads to significant complications in aircraft design since longitudinal stability requirements are met through special wing airfoils.

The advantages and disadvantages of these configurations are numerous and depend on the specific case as detailed in Reference [29]. In general, the canard configuration is aerodynamically more efficient, contributing positively to the generation of lift in a condition at the equilibrium of static stability; however, the analysis of the flight mechanics becomes more complex, think for example of the effect of the tail wake on the wing. Moreover, some theoretical aerodynamic advantage of a three-wing configuration clashes with a complicated structural design.

To quote the Sadraey's book: "The basic rule for the selection of the tail configuration is as follows. In general, the conventional aft tail configuration is often able to satisfy all the design requirements, unless one or more requirements imply another configuration. Thus, it is recommended to begin with a conventional aft tail configuration and then to evaluate its features against the design requirements. If one or more requirements are not satisfied, change to a new configuration nearest the current configuration until all the requirements can be satisfied".

As there was no hostile reason for the aft tail configuration, this was chosen in the design of the *Raven 4*.

12.1.2. Aft tail configuration

An aft tail has several configurations that are all able to satisfy the design configurations in this specific case:

- Conventional inverted T tail
- T-tail
- V-tail
- H-tail



- Cruciform
- Twin vertical tail

While choosing the configuration, the presence of the jet engine in the tail zone must be accounted for. In fact, the placement of the engine inside the tail cone was avoided, since it would have implied structural complexity and obstruction in the aft fuselage, reduced maintainability and worse thermal stealthiness.

Among the many advantages and disadvantages of each configuration, accurately described in [29], a V-tail configuration was chosen since it seems to satisfy well with the constraints of the design:

- it can be used as a shield to reduce the heat signature of the aircraft, which would make it a more difficult target for shoulder-fired missiles, a threat that for an aircraft that has to do penetration and extraction in hostile territory seems relevant
- a reduced radar cross section, once again a key feature for the success of this aircraft
- easier positioning of the jet engine, which does not have to be integrated into the vertical tail.
- reduction in tail area and consequently in aerodynamic drag.

However, it is important to be aware that this choice also has its difficulties:

- deficiencies in maintaining the aircraft longitudinal and directional stability
- increased susceptibility to dutch-roll tendencies
- enhanced phenomenon of adverse roll/yaw coupling induced by ruddervator control
- complex and coupled ruddervator control system

From Reference [24] a method to design a V-tail is presented, which consists in consider a conventional tail configuration to find the horizontal and vertical tail surface, and then project them in the V-tail oriented plane in order to compute a dihedral angle with respect to the horizontal plane. This angle is also called "butterfly angle" in literature and it's defined as:

$$\Gamma_H = \text{atan}(S_V/S_H) \quad (12.1)$$

Finally, since the aircraft does not have maneuvering speed (all-moving tail required) or flight cost (adjustable tail required) as primary characteristics, a fixed tail was chosen at

this stage of the design, which is lighter, cheaper, and safer given the reduced number of moving components.

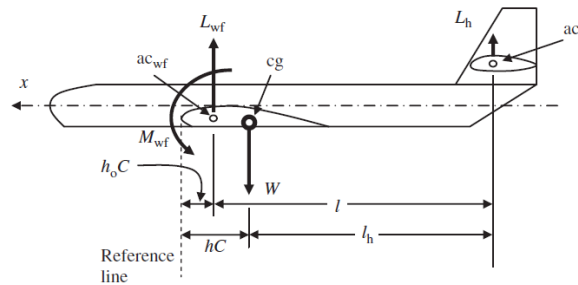
12.2. Tail volume coefficient

Sizing the empennage by directly analyzing the longitudinal and directional stability of the aircraft would be too difficult and in fact useless at this stage of the conceptual design. Therefore, the simplified "tail volume" approach is used. It consists in analyse the tail starting from the horizontal and vertical tail volume defined respectively as:

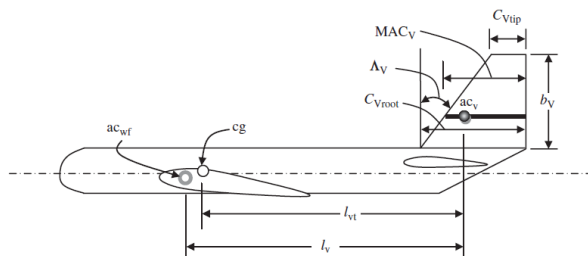
$$\bar{V}_H = \frac{lS_h}{\bar{C}S} \quad (12.2)$$

$$\bar{V}_V = \frac{l_v S_v}{bS} \quad (12.3)$$

refer to Figure 12.1 for details. These non-dimensional parameters have a limited range of values for existing aircraft and also are not a function of the aircraft size or weight but rather on its operational characteristics. The tail volume coefficient is an indication of the handling quality in stability and control. As \bar{V} increases, the aircraft tends to be more stable and less controllable.



(a) Horizontal tail framework



(b) Vertical tail framework

Figure 12.1: Tail design framework



Aircraft Type	Raymer	Roskam	Torenbeek	Howe	Schaufele	Jenkinson	Nicolai
Sailplane	0.500		0.500				
Civil props							
Homebuilts	0.500	0.467					
Personal					0.48-0.92		
GA ^a - Single engine	0.700	0.667		0.650			
GA ^a - Twin engine	0.800	0.786		0.850			
Commuter					0.46-1.07		
Regional Turboprop	0.900	1.075	1.006	1.000	0.83-1.47		
Jet							
Business Jets		0.721	0.691	0.700	0.51-0.99		
Jet transport	1.000	1.010	0.904	1.200	0.54-1.48	0.875	
Supersonic			0.535				
Cruise Airplanes							
Military							
Jet Trainer	0.700	0.639		0.650			
Jet Fighter	0.400	0.362			0.20-0.75		0.307
Military Transport	1.000	0.891	0.850	0.650			
Special Purpose							
Agricultural	0.500	0.526					
Flying Boat	0.700	0.641					

^a GA stands for General Aviation

Figure 12.2: Horizontal tail volume statistics collection from different literature

Aircraft Type	Raymer	Roskam	Howe	Toren. ^a	Schaufele	Jenk. ^b	Nicolai
Sailplane	0.020		0.018				
Civil props							
Homebuilts	0.040	0.036					
Personal					0.024 ... 0.086		
GA- single engine	0.040	0.043	0.050				
GA- twin engine	0.070	0.062	0.065				
Commuter					0.041 ... 0.097		
Regional Turboprop	0.080	0.083	0.080	0.077	0.065 ... 0.121		
Jet							
Business Jets		0.073	0.065	0.069	0.061 ... 0.093		
Jet transport	0.090	0.079	0.090	0.074	0.038 ... 0.120	0.076	
Supersonic			0.062	0.065			
Cruise Airplanes							
Military							
Military Trainer	0.060	0.061	0.065				
Military Fighter	0.070	0.077			0.041 ... 0.130		0.064
Military Transport	0.080	0.073	0.065				
Special Purpose							
Agricultural	0.040	0.032					
Flying Boat	0.060	0.050					

^a Toren. stands for the author Torenbeek

^b Jenk. stands for the author Jenkinson

Figure 12.3: Vertical tail volume statistics collection from different literature

Figures 12.2, 12.3 summarize extensive research work in the literature on different tail volumes for different categories of aircraft. Analyzing these statistical results a first guess of $\bar{V}_H = 0.9$ and $\bar{V}_V = 0.06$ is selected. In choosing the values practical considerations, e.g., not being able to manifest the asymmetric thrust situation (there being only one central motor) were made.

12.3. Optimum tail arm

One of the tail parameters that must be determined during the tail design process is the tail arm (l_t), which is the distance between the tail aerodynamic center and the aircraft center of gravity. The tail arm serves as the arm for the tail pitching moment (i.e., tail lift multiplied by tail arm) about the aircraft cg to maintain the longitudinal trim. To determine the tail arm one must establish the criteria based on the design requirements. Two basic tail parameters which interact most are the tail arm and tail area; the latter is responsible for generation of the tail lift. As the tail arm is increased, the tail area must be decreased, while as the tail arm is reduced, the tail area must be increased. Both short arms (as in fighters) and long arms (as in most transport aircraft) are capable of satisfying longitudinal trim requirements, given the appropriate necessary tail area. But the question is, what tail arm is optimum? To answer this question, one must look at the other design requirements. Two very significant aircraft general design requirements are low aircraft weight and low drag. Both of these may be combined and translated into the requirement for a low aircraft wetted area. As the horizontal tail arm is increased, the fuselage wetted area is increased, but the horizontal tail wetted area is decreased. Also, as the horizontal tail arm is decreased, the fuselage wetted area is decreased, but the horizontal tail wetted area is increased. Hence, we are looking to determine the optimum tail arm to minimize drag, which in turn means to minimize the total wetted area of the aft portion of the aircraft.

A possible model to solve the optimization problem is proposed by [29] as:

$$l_{opt} = K_C \sqrt{\frac{4 \text{ } MAC \text{ } S_{wing} \text{ } V_H}{\pi \text{ } D_{fus}}} = 35.00 \text{ ft} = 11.67 \text{ m} \quad (12.4)$$

where D_{fus} is the maximum diameter of the fuselage and K_C is a correction factor equal to 1.25. Figure 12.4 shows the function behaviour.



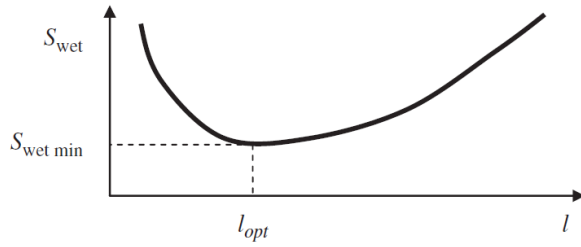


Figure 12.4: The variation of wetted area with respect to tail arm

12.4. Horizontal and vertical tail surface

Finally, it's possible to compute the horizontal and tail surface from [29], and the butterfly angle of V-tail from [24]:

$$S_H = \frac{MAC \ S_{\text{wing}} \ V_H}{l_{\text{opt}}} = 206.13 \text{ ft}^2 = 19.15 \text{ m}^2 \quad (12.5)$$

$$S_V = \frac{b_{\text{wing}} \ S_{\text{wing}} \ V_V}{l_{\text{opt}}} = 108.07 \text{ ft}^2 = 10.04 \text{ m}^2 \quad (12.6)$$

Thus, the first guess of butterfly angle, figure 12.5, is:

$$\Gamma_H = \text{atan}(S_V/S_H) = 27.7^\circ \quad (12.7)$$

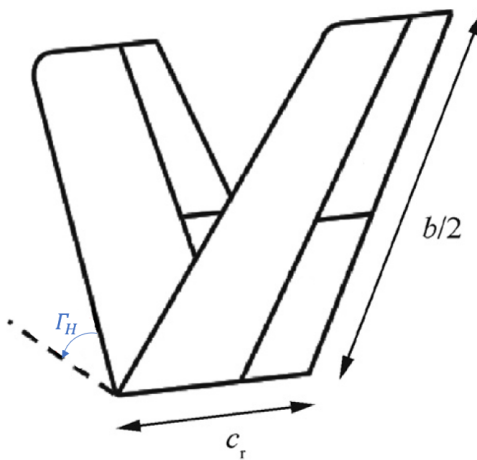


Figure 12.5: Definition of butterfly angle

12.5. V-tail parameters

At this point, the planform geometry of the V-tail can be analyzed assuming it as the horizontal tail. Parameters to be defined are:

- tail desired lift coefficient in cruise trim condition.
- airfoil section.
- sweep angle.
- aspect ratio and taper ratio.
- incidence.

12.5.1. Tail desired lift coefficient in cruise trim condition

Referring to figure 12.1a, the tail lift coefficient to satisfy the equilibrium in cruise condition can be obtained as:

$$C_{L_h} = \frac{1}{\eta_H V_H} [C_{m_0}^{wf} + C_L^{cruise} (h - h_0)] \quad (12.8)$$

where:

- $C_{m_{af}} = -0.068$ is the wing airfoil section pitching moment in cruise conditions
- $C_{m_0}^{wf} = C_{m_{af}} \frac{AR \cos^2 \Lambda}{AR + 2 \cos \Lambda} + 0.01 \alpha_t = -0.0455$ is wing/fuselage pitching moment coefficient.
- $C_L^{cruise} = 0.22$ is aircraft cruise lift coefficient.
- $(h_0 - h) = 0.1$ is the static margin chosen for the first iteration.
- $\eta_H = 0.85$ is the tail efficiency, i.e., the ratio between dynamic pressure at tail and the aircraft dynamic pressure. Tail position in the present case should be sufficiently out of the wing wake, however, a conservative value was chosen for the first iteration.

Therefore, from this calculation, the horizontal tail lift coefficient is: $C_{L_h} = -0.0875$.

Note that since the equilibrium at moments is computed with respect to the center of gravity, knowledge of the position of the center of gravity enters the equation through the static margin.



12.5.2. Airfoil section

From Reference [29] a symmetric tail airfoil is a reasonable first choice. Moreover, the horizontal tail must be clean of compressibility effect, this leads an airfoil thinner than wing airfoil. In addition, the Team also decided to introduce another evaluation parameter, which is minimizing the drag coefficient. Hence, the choice for the tail airfoil fell on the *NACA 63A010*, which is a symmetrical, 2% thinner w.r.t wing airfoil, laminar airfoil. Figure 12.6 and Table 12.1 provides the characteristic features for the NACA 63A010 airfoil section.

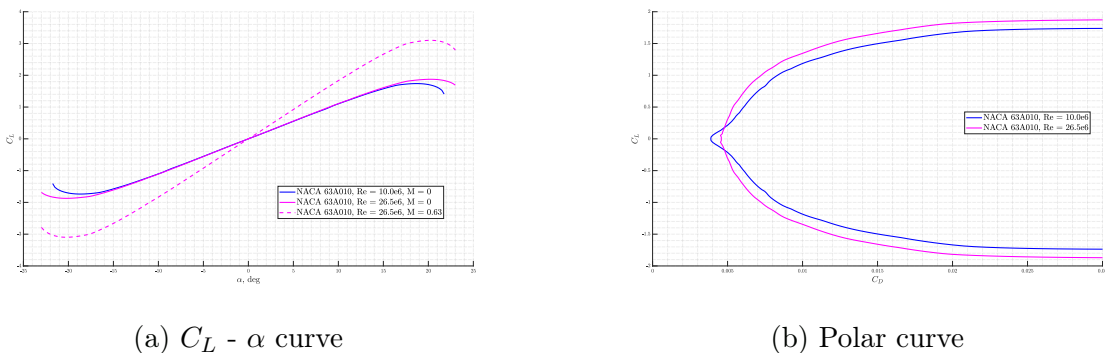


Figure 12.6: NACA 63A010 results

C_{l_i}	$C_{d_{min}}$	C_m	$(C_l/C_d)_{max}$	α_0	α_s	$C_{l_{max}}$	C_{l_α}	$(t/c)_{max}$
0	0.0045	0	141.3	0°	18.5°	1.74	8.9 (1/rad)	10%

Table 12.1: NACA 63A010 characteristics

12.5.3. Sweep angle

The purpose of the sweep angle is to avoid the critical mach on the tail.

From historical data, available in Reference [29] and [24] a sweep angle $\Lambda_{tail} = 30^\circ$ is chosen for the tail. This value is probably overestimated, but it allows for a large margin over the critical mach, and it slightly moves back the aerodynamic center of the tail, increasing the stability of the aircraft.

12.5.4. Aspect ratio and taper ratio

Reference [29] propose an empirical formula to compute the first guess the tail aspect ratio, starting from the wing:

$$AR_{tail_{eff}} = \frac{2}{3} AR_{wing} \cos(\Lambda_{tail}) = 6 \cos(30^\circ) = 4.5 \quad (12.9)$$

The taper ratio of the tail is not so important as it is for the wing, because the elliptical lift distribution is not a requirements for the tail; thus, the main motivation behind the value for the tail taper ratio is to lower the tail weight. Typically, the tail taper ratio is smaller than wing taper ratio. However, it's been observed that existing V-tailed aircraft have higher average taper ratio values than conventional aircraft, so a taper ratio of $\lambda = 0.5$ is selected.

12.5.5. Incidence

The tail angle of incidence (i_{ht}) primary requirement is to nullify the pitching moment about CG at cruising flight with zero elevator deflection. To do, first compute the tail required angle of attack:

$$\alpha^{ht} = \frac{C_L^{ht}}{C_{L|\alpha}^{ht}} = -1.16^\circ \quad (12.10)$$

where $C_{L|\alpha}^{ht} = 3.33 rad^{-1}$ is known for the designed tail and C_L^{ht} has been computed in subsection 12.5.1.

Now the tail incidence can be computed as follow:

$$i_{ht} = \alpha^{ht} - \alpha^f + \varepsilon \quad (12.11)$$

where $\alpha^f = 0$ is the fuselage angle of attach and it is zero in cruise since the wing incidence has been properly set to obtain this result; ε is the downwash that the tail suffers being positioned behind the primary lifting surface and can be computed by means of a simplified linear model as follow:

$$\varepsilon = \frac{\partial \varepsilon}{\partial \alpha} \alpha_w + \varepsilon_0 \quad (12.12)$$

where:

$$\frac{\partial \varepsilon}{\partial \alpha} = \frac{2C_{L|\alpha}^w}{\pi AR} \quad \varepsilon_0 = \frac{2C_L^w}{\pi AR} \quad (12.13)$$



Results from this linear model have been slightly reduced considering that for this specific case the tail is not completely soaked in the wing wake.

From equation 12.11, $i_{ht} = -0.963^\circ \sim -1^\circ$.

Note that the negative incidence of the aft tail, also known as longitudinal dihedral, is synonymous with longitudinal static stability. The term longitudinal dihedral was invented by tail designers to transfer the technical meaning of the wing dihedral angle from the yz plane to a similar angle in the aircraft xz plane. As the aircraft lateral stability benefits from the wing and tail dihedral angles, the aircraft longitudinal stability will be improved by a geometry referred to as the aircraft longitudinal dihedral angle.

12.5.6. Summary of tail parameters

Table 12.2 summarizes the obtained parameters for the V-tail:

Λ_{LE}	AR	AR_{eff}	b_{tail}	λ	C_{root}	C_{tip}	i_{tail}	$C_{L_\alpha} @ M = 0$
30°	6	4.5	32.34 ft (9.86 m)	0.5	9.58 ft (2.92 m)	4.79 ft (1.46 m)	-1°	3.321 rad^{-1}

Table 12.2: V-tail parameters

12.6. Final Results for wing and tail together

Final aerodynamic parameters for wing and tail together, obtained by XFLR5 and empirical formulas, are presented in table 12.3 and Figures 12.7, 12.8.

$max(C_L/C_D)$	35.95	$\alpha((C_L/C_D)_{max})$	1.60 deg
$max(\sqrt{C_L}/C_D)$	69.18	$\alpha((\sqrt{C_L}/C_D)_{max})$	0.40 deg
$max(C_L^{1.5}/C_D)$	23.91	$\alpha((C_L^{1.5}/C_D)_{max})$	4.90 deg
$C_{L_{max}}^{clean}$	1.91	$C_{d_0}^{clean}$	0.0075
$C_{L_{max}}^{flap}$	2.65	α_0	-1.12 deg
C_{L_α}	4.979 rad^{-1}	C_{L_0}	0.14

Table 12.3: Aerodynamic results @ $Ma = 0$

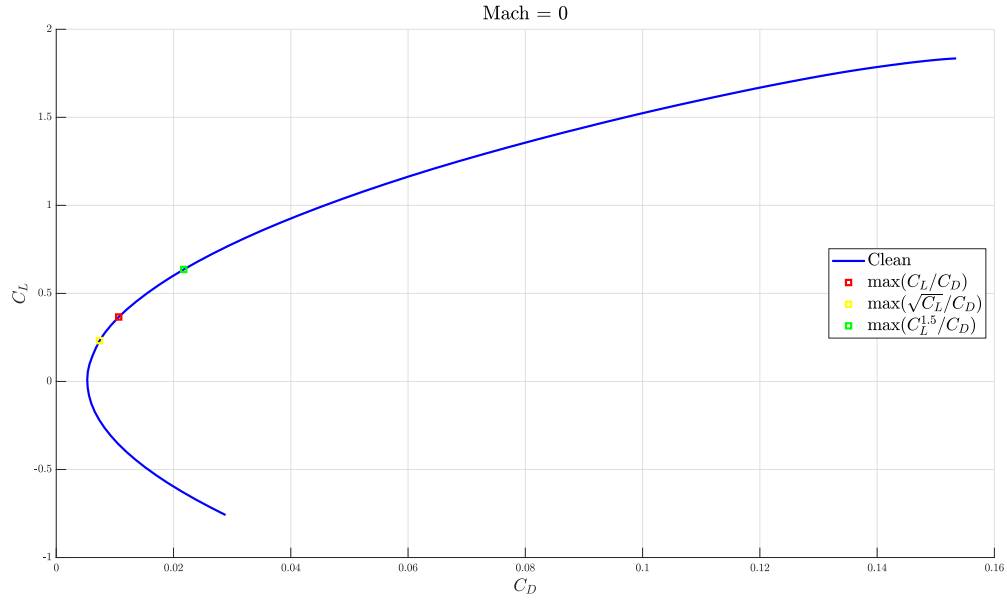


Figure 12.7: Polar curve (from viscous simulation on XFLR5)

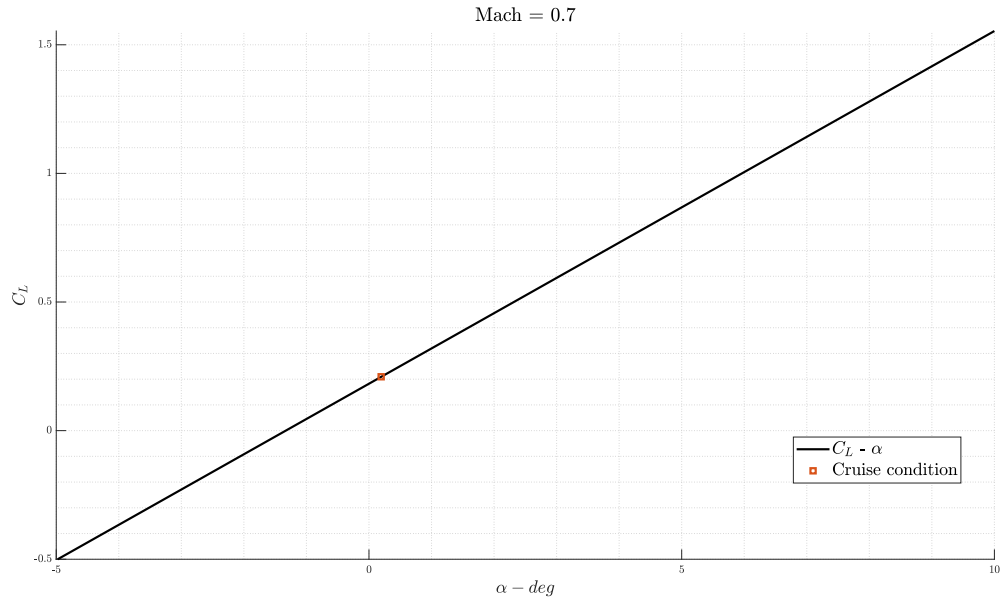


Figure 12.8: C_L - α (XFLR5)



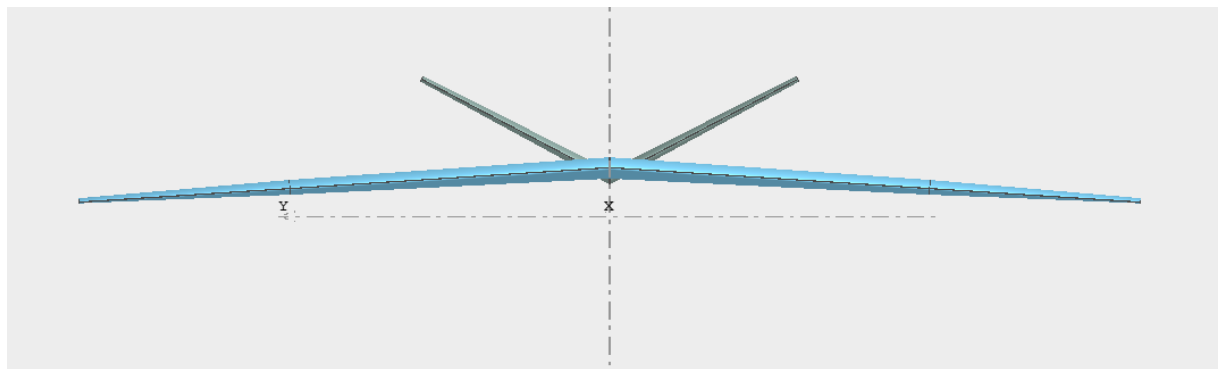


Figure 12.9: Front view of wing and tail (XFLR5)

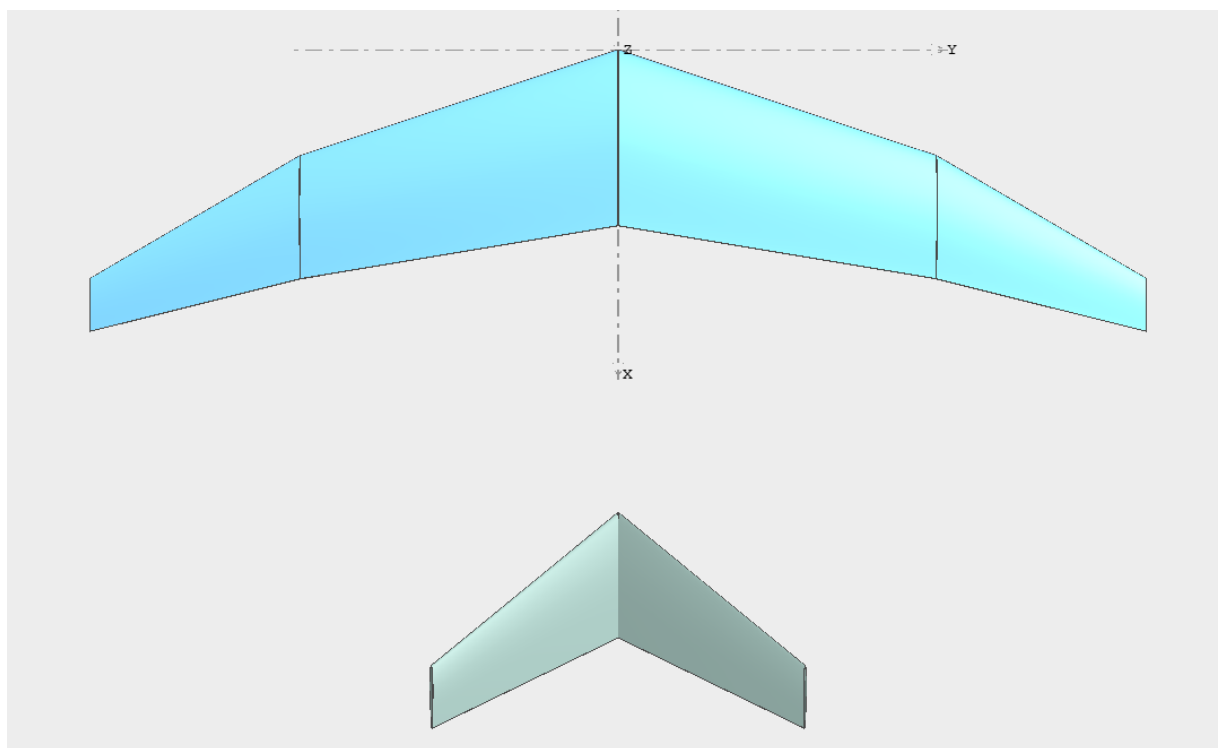


Figure 12.10: Top view of wing and tail (XFLR5)

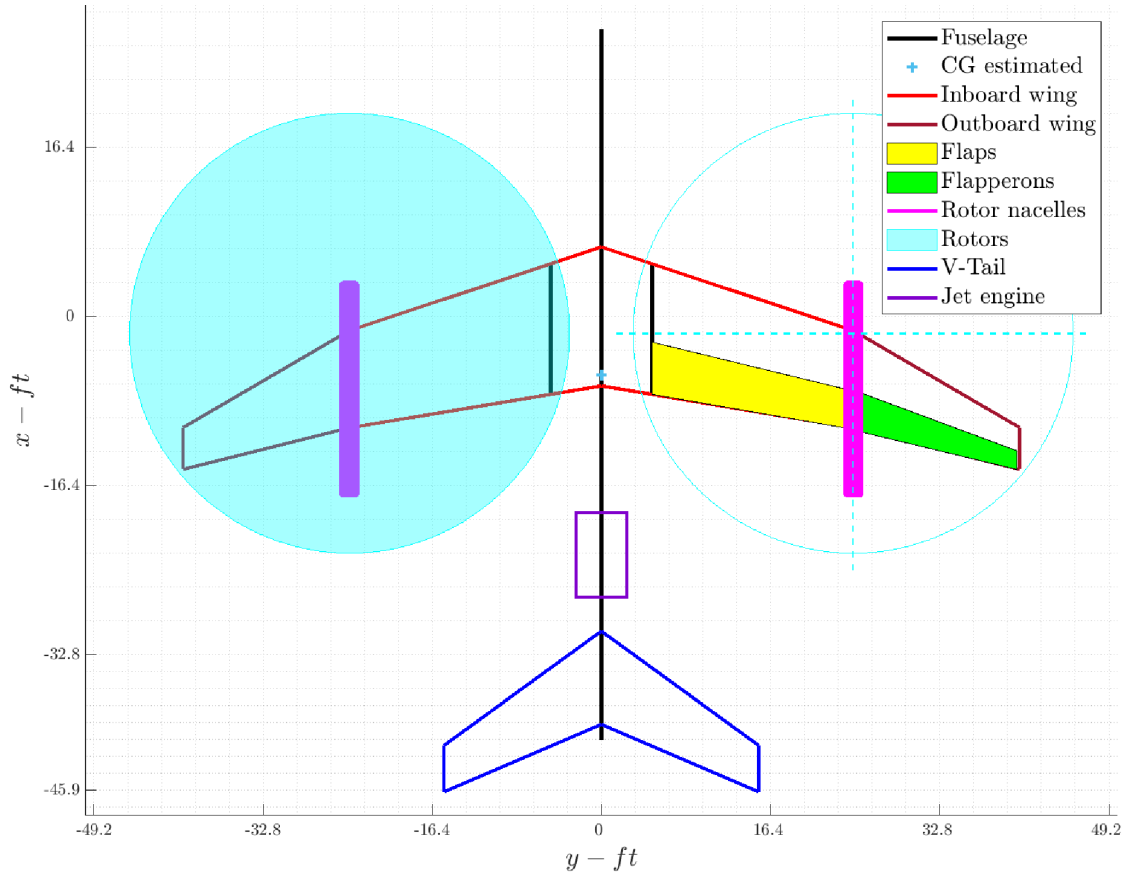


Figure 12.11: Top view of the preliminary aircraft



13 | Fuselage design

The main function of the fuselage is to contain the payload, that is the useful load that the aircraft can carry, so it doesn't include pilot, crew or fuel. Furthermore, some secondary functions can be identified, such as accommodation of pilots, crew members, landing gear, fuel tanks and all the systems.

In the design process of the fuselage some important aspects should be taken into account. From an aerodynamic point of view, the external shape of the fuselage should be designed with the ideal objective of generate the lowest drag and contribute positively to the lift generation. The fuselage should also have a low weight and, at the same time, carry high structural flight loads and provide protection against environmental hazards such as lightning.

The process followed for the design of the fuselage is described below:

1. Identification of payload and other design requirements
2. Choice of fuselage configuration and internal dimensions
3. Definition of some control sections
4. Conic lofting
5. Description of internal arrangement

These phases have been identified from the guidelines illustrated in several books as Sadraey [29], Roskam Part I and II [23] [24], Torenbeek [34].

13.1. Design requirements

The first step in the fuselage design process is the identification of the payload and operational requirements, that represent the constraints that have to be respected by the external shape of the fuselage. This stage includes the determination of the dimensions and the volume occupied by the payload and the other elements, that can be divided in subsections, such as cargo bay, cockpit, landing gear and on-board systems, that will be analyzed separately.

13.1.1. Cargo section

The dimensions of the cargo bay are indicated in the RFP: "an internal cargo bay with dimensions of 6.5 ft (1.98 m) high, 8 ft (2.43 m) wide, 30 ft (9.14 m)". It is located in the central part of the fuselage, in order to accommodate the payload near the center of gravity of the aircraft.

The floor of cargo bay should be at approximately 5 ft (1.5 m) off the ground to allow direct loading and unloading of the payload [19]. This requirement will have consequences on the design of the landing gear and the rear door.

13.1.2. Flight deck

For the design of the flight deck statistical data and specific requirements for this case are analyzed.

For the overall length of the flight deck, the typical value for a two crew members flight deck has been chosen: $L = 105$ in (2.67 m) [34]. The width has been chosen considering that has been selected a side-by-side configuration for pilot and copilot seats and taking into account the space occupied by each crew member have been selected the typical dimensions of the seats and the "recommended clearances around vehicle operator's station to accommodate a soldier dressed in arctic clothing" [15].

Furthermore, visibility requirements are considered: military standards require a 17 degrees over-nose angle for transport aircraft [29]. In this case the windshield is designed in order to get a longitudinal visibility angle $\alpha = 19^\circ$ and a lateral visibility angle $\beta = 33^\circ$.

In Table 13.1 are summarized dimensions of flight deck.

Length	105 in (2.67 m)
Maximum height	83 in (2.10 m)
Maximum width	117 in (2.97 m)

Table 13.1: Dimensions of the flight deck



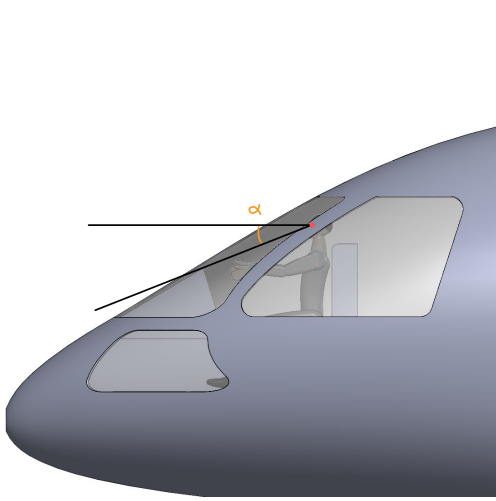


Figure 13.1: Flight deck lateral view



Figure 13.2: Flight deck front view

13.1.3. Fuel tanks

Volume occupied by fuel tanks in the fuselage depends on how much fuel can be stored in the wing. An initial estimation can be done starting from the values of fuel weight identified in the preliminary sizing and the geometry of the wing described in Section 11.

Assuming that the fuel is JP-8, a jet fuel used widely by the US military, that is characterized by a density within the range of 6.47-7.01 lb/U.S. gallon (0.775 – 0.840 kg/liter) and knowing that the weight of the fuel is 13016 lb (5904 kg), it is easy to obtain that the volume necessary to store the fuel is 258.21 ft³ (7.31 m³).

The volume available in the wing is calculated taking into account the space occupied by structural elements and control surfaces.

	Volume	Percentage
Total	258.21 ft ³ (7.31 m ³)	100 %
Right wing tanks	43.54 ft ³ (2.21 m ³)	30.23 %
Left wing tanks	43.54 ft ³ (2.21 m ³)	30.23 %
Fuselage tanks	89.55 ft ³ (2.89 m ³)	39.54%

Table 13.2: Preliminary volume of fuel tanks

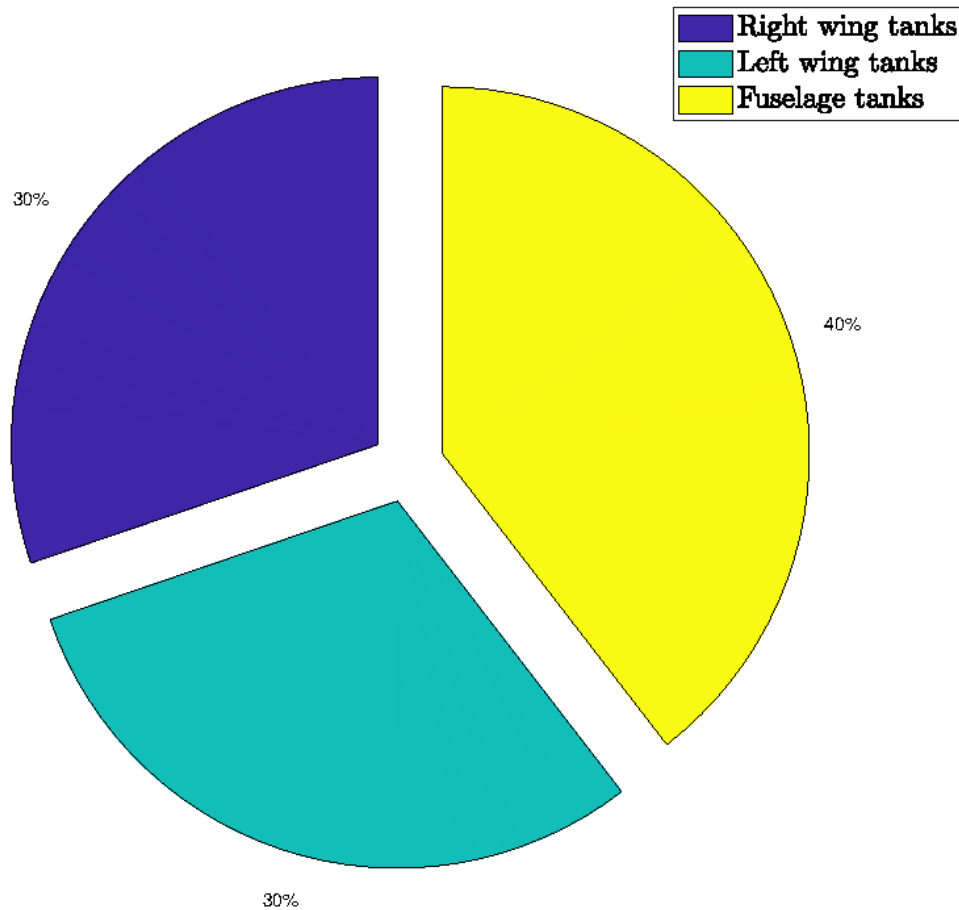


Figure 13.3: Preliminary volume of fuel tanks

It can be stored in tanks located above the cargo bay so as to be near to the jet engine and the rotor engines on the wing to reduce the dimensions of the fuel system. In this configuration the fuel, that represents about the 20% of the weight of the aircraft, is placed near the CG, avoiding problems of balance.

13.1.4. Landing gear

An initial sizing of the landing gear is performed in order to compute the volume occupied in the fuselage by it. The aspects that have to be analysed for its design are configuration, attachment to the aircraft, wheels, tires, shock absorbers and gear retraction geometry.

For the design of the landing gear two options are considered: the first one is a typical aircraft landing gear which can sustain a standard take-off and landing, while the second option is to admit only the possibility of a vertical take-off and landing.

The second alternative includes two possible configurations: wheel landing gear and skid



type landing gear. However, the second one is used for small-sized helicopter and it goes to complicate ground movement. Therefore, a wheel landing gear type solution was followed.

It is now necessary to verify if the wheel landing gear can allow a standard landing and takeoff or if the reduced loads on the tyres and strut can permit a smaller landing gear, which can be convenient in terms of space.

Going deeper into the case of a typical aircraft landing gear, the configuration chosen is the most commonly used, the tricycle gear, with two main wheels aft of the CG and an auxiliary wheel forward of the CG. In this arrangement landing visibility is improved, the aircraft is stable on ground and can be landed at a fairly large “crab” angle.

13.1.4.1. Sizing

Wheels and tires sizing, that includes the selection of number of tires, diameter and width, is carried out starting from the loads supported by the main and the nose gear. At this preliminary stage, it's assumed that the main gear carries 90% of aircraft weight and the nose gear remaining 10%. These values should be increased about 25% to allow for later growth of the aircraft weight.

In order to reduce the dimensions of each tire has been selected a configuration with two wheels per strut. A distribution of loads over multiple wheels allows operations on relatively soft fields and it's a better choice from the safety point of view in the event of a flat tyre. Similarly for nose landing gear, a configuration with two wheel is better for load distribution, safety and from a point of view of maneuverability.

Mass on each wheel of the main gear: $M_W = 14292.76 \text{ lb} (6483.09 \text{ kg})$

Mass on each wheel of the nose gear: $M_W = 3176.17 \text{ lb} (1440.69 \text{ kg})$

Once the static load per wheel is computed, the diameter and width of each tire can be chosen through a statistical approach developed from data in Taylor, J., Jane's All the World Aircraft, Jane's, London [7] as shown in [19]:

$$\text{diameter} = AM_W^B \quad (13.1)$$

$$\text{width} = AM_W^B \quad (13.2)$$

For a transport/bomber aircraft the values of A and B are shown in 13.3:

	Diameter	Width
A	1.63	0.1043
B	0.315	0.480

Table 13.3: Values for statistical tire sizing in inches

In order to compute an initial sizing, margins related to the centrifugal force of rotation of the wheels and a margin related to the wear were considered, to take into account wheel's deformation for the total dimension of the landing gear.

The dimensions obtained are shown in Table 13.4.

	Diameter	Width
Main landing gear	38 in (0.96 m)	12.6 in (0.32 m)
Nose landing gear	22.8 in (0.58 m)	5.9 in (0.15 m)

Table 13.4: Tires preliminary sizing

With the data obtained in Chapter 15, i.e. the center of gravity position and the calculated loads in relation to the relative position between the landing gear and the aircraft's center of gravity, a final decision was made regarding the selection of tires available in the market. To accomplish this, the catalog "Global Aviation Tires" from the Goodyear Tire & Rubber Company [2] was utilized.

The updated results are shown in Table 13.5, Table 13.6 and Table 13.7.

	Values
Maximum static main gear load (per strut)	21,857 lb (9,914 kg)
Maximum static nose gear load	19,219 lb (8,7178 kg)
Minimun static nose gear load	14,748 lb (6,689 kg)
Dynamic nose gear load	6,695 lb (3,304 kg)

Table 13.5: Loads sizing



	Values
Main gear tire static load	13,661 lb (6,196 kg)
Nose gear tire static load	12,012 lb (5,449 kg)
Nose gear tire dynamic load	4,533 lb (2,065 kg)
Maximum ground speed	110 kn (57 m/s)
Pressure desired	33-55 Psi

Table 13.6: Tires sizing (considering 25% of margin for loads)

Size	Construction		Service rating			
	TT or TL	Rated Speed	Rated Load	Rated Inflation	Max Braking Load	
15.00-16	TL	160	19,700	80	28,560	
Part N°	Inflated dimension				Flat tire radius	
	Outside diameter		Section Width			
	Max	Min	Max	Min		
156T66G1	42.4	41.4	15.3	14.4	11	

Table 13.7: Tire sizing (considering 25% margin for loads)

The loads that the tires could withstand, the maximum rotational speed of the tires, and the pressure of the tires were followed as criteria for selection so that they could allow the widest margin of operation on rough terrain without increasing the size of the wheels too much due to low pressure.

13.1.4.2. Geometry of the landing gear

In the choice of geometry and the retraction kinematics of both the rear and front landing gear, the goal was to save the maximum volume. Thereby achieving a more compact solution that would not compromise the fuselage configuration too much. Since this is a high-wing aircraft, the only solution available is to place the landing gear in the fuselage under the internal cargo floor.

Hence, opting to place the front and rear undercarriage in the fuselage, the idea of using a radius link to rotate wheel 90 deg was considered, optimizing the necessary vertical space.

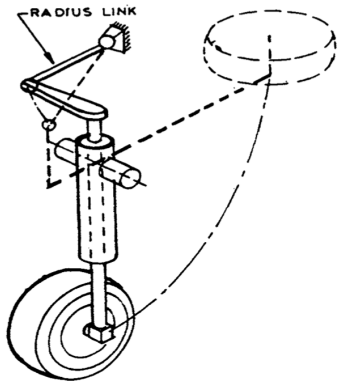


Figure 13.4: Radius link to rotate wheel 90 deg.

In the most convenient choice for the geometry of the main landing gear and nose landing gear, reference book [4] provided the guidelines.

The existing geometry on British Aerospace's BAe-146 was chosen for the main landing gear.

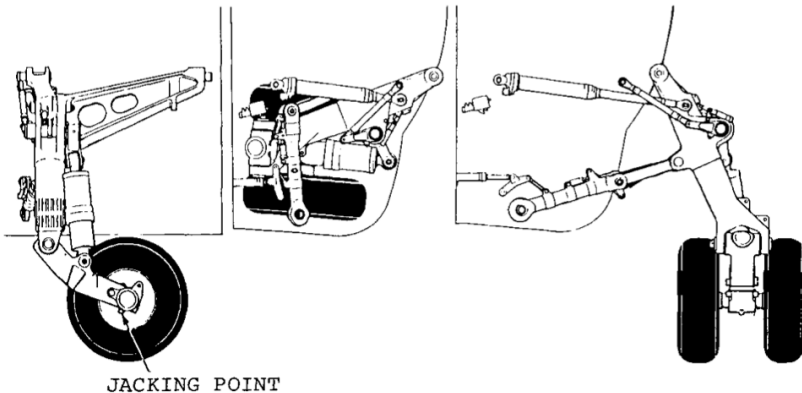


Figure 13.5: Retraction system of BAe-146 main gear.

Regarding the nose landing gear, it was chosen to adopt a solution with a radius link to rotate wheel 90 deg under the cockpit, similarly to what was chosen for the main gear. Due to a space problem for the feedback it was chosen to have it retracting back under the cockpit. This solution does not turn out to be the best one from a safety point of view because it does not allow full deployment of the landing gear for wind force by taking advantage of the forward motion. In order not to incur such a lack of safety, a manual emergency pneumatic mechanism may be added in case of failure.

It has been chosen a retractable landing gear because the aircraft will reach very high speed, about 450 ktas, which would cause an increase in drag which cannot be acceptable.



Consistent with this decision, from a point of view of the fuselage, pods were introduced to protect the housing of the main landing gear, as this did not turn out to be small enough to require its use.

13.2. External design

In order to design the external shape of the fuselage, starting from the constraints imposed by the required internal volume, several cross-sections have been defined. The entire aircraft has been divided in four parts:

- Nose: characterised by 3 cross-sections
- Flight deck: described by 3 cross-sections
- Central fuselage: described by 3 cross-sections
- Rear fuselage: described by 4 cross-sections

Once the cross-sections have been designed, with the help of a CAD system, they are connected through longitudinal lines, providing a smooth aerodynamic contour.

During this phase has been taken into account that the angle of the rear fuselage must not exceed 20° in order to avoid vortex generation.

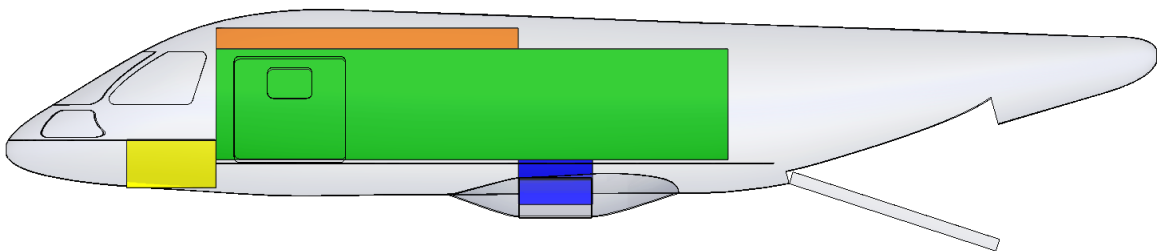


Figure 13.6: Design requirements and external shape of the fuselage

In Figure 13.6 are shown the components that the fuselage must contain:

- Cargo bay: green
- Main landing gear: blue
- Nose landing gear: yellow
- Fuel tanks: orange

13.2.1. Length-to-Diameter ratio

Two fundamental parameters that characterize the shape of the fuselage are length and diameter, therefore the adimensional quantity length-to-diameter ratio L/D represents a useful parameter to compute and study. It's possible to determine its optimal value for specific design objectives.

In order to obtain the lowest zero-lift drag, its expression has to be written as a function of the length-to-diameter ratio:

$$C_{D_0} = K \left(1 + \frac{60}{(L/D)^3} + 0.0025 \left(\frac{L}{D} \right) \right) \left(\frac{L}{D} \right) \quad (13.3)$$

The differentiation of this equation leads to the optimal value:

$$\left(\frac{L}{D} \right)_{opt} = 5.1 \quad (13.4)$$

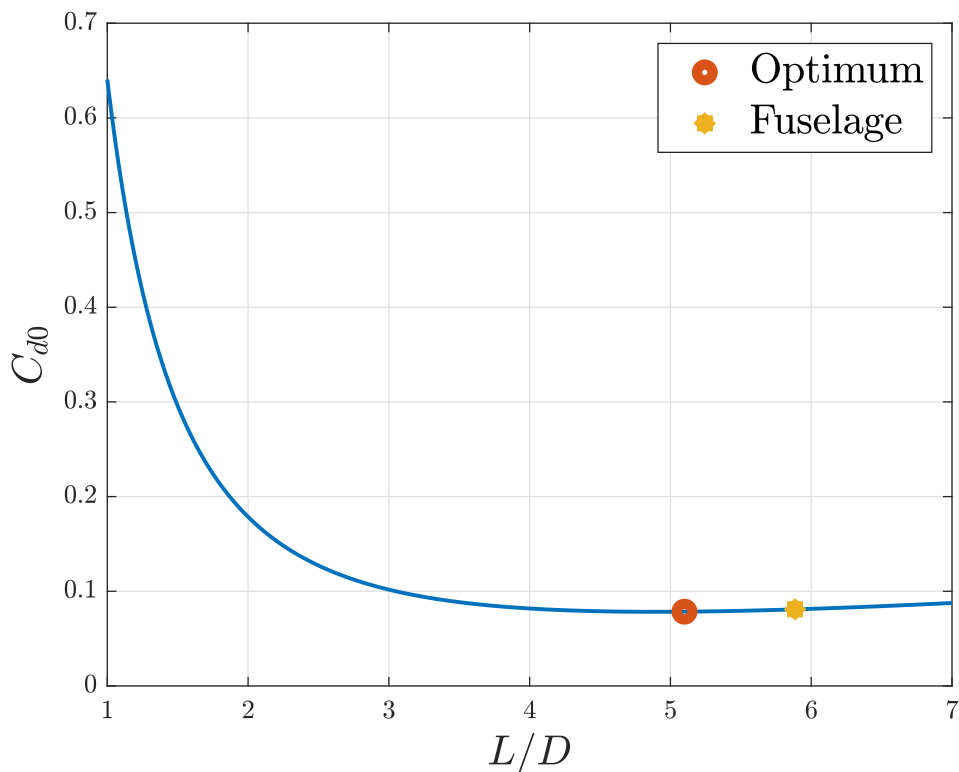


Figure 13.7: Relation between C_{d0} and L/D



As can be seen in Figure 13.7, the values of length and diameter (Table 13.8) that have been obtained for the fuselage are very close to the optimal value.

L	67.65 ft (20.62 m)
D	11.32 ft (3.45 m)
L/D	5.98

Table 13.8: Length and maximum diameter

13.3. Internal arrangement

As discussed in Chapter 5, the aircraft internal arrangements may be configured for combat search and rescue operation, VIP transportation, troop transportation and delivery of supplies.

Therefore, three different configurations were envisioned:

1. Troops: 12 soldiers on each side (24 in total), Figure 13.8
2. Troops and cargo: 6 soldiers on each side (12 in total) and a pallet 463L, Figure 13.9
3. Cargo: supplies and other materials, Figure 13.10

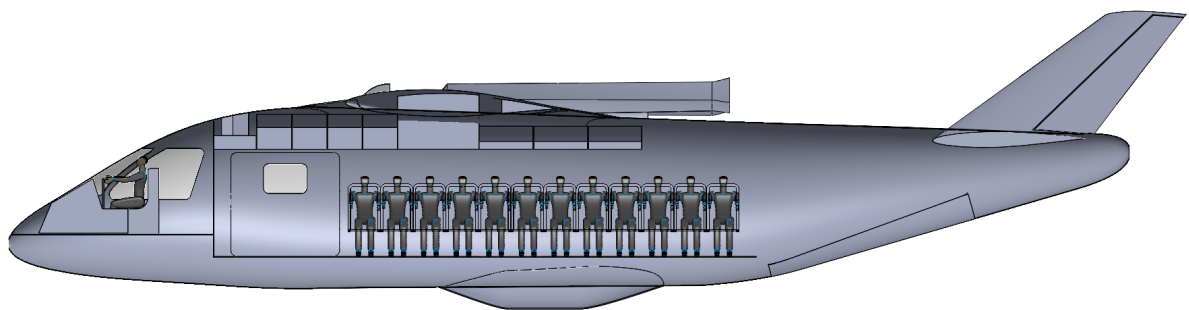


Figure 13.8: Troops configuration

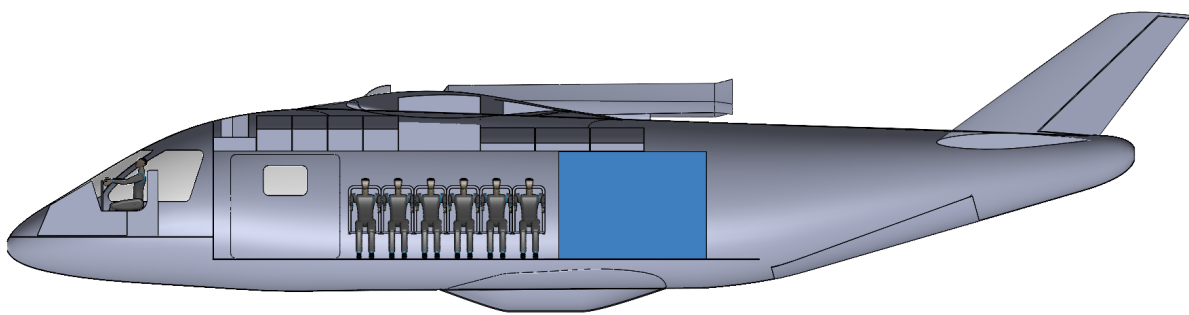


Figure 13.9: Troops and cargo configuration

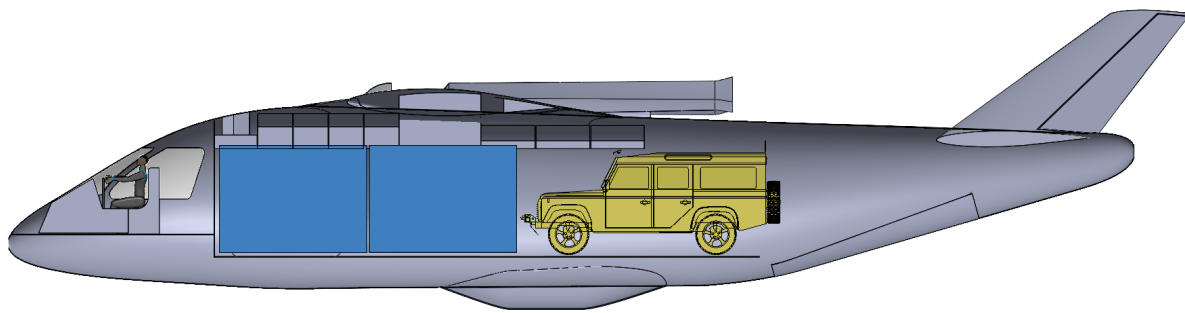


Figure 13.10: Cargo configuration



14 | Propulsion and onboard systems

The flight envelope (speed-altitude envelope) of an airplane has an important bearing on the choice of the type of propulsion system.

As we have already seen in the market analysis and in the preliminary sizing, the necessary engine to reach the required performance in cruise phase, it is a jet engine. Therefore the selection of the propulsion system type has been already done. On the other hand, regarding the type of propulsion for vertical sustenance, the choice is more delicate.

A conventional wisdom says that is undesirable to "mix" different types of power plant in one airplane. Different types of propulsion system call for different operating procedures. This certainly increases the crew workload which is not desirable. Moreover, maintenance will become more costly when different types of propulsion system are used in the same airplane. However, given the mission and performance objectives, such a choice will be necessary. For this reason, a high level of digitalization in the command chain with high reliability will be mandatory to alleviate the workload of the pilots.

14.1. Jet engine

14.1.1. Choice of the engine

The thrust rating needed to meet the requirements set it has been obtained from the final results of the preliminary sizing. A minimum thrust of 18,120 lbf (80.5 kN) will be required in order to meet the demand climb performance, climb time, maneuvering and cruising flight performance.

In the determination of the engine and the number of them, there are two possibilities to follow:

- A new engine will be developed for the proposed design
- An existing engine must be used

In the first case, the engine(s) can be tailored to the project design. However the development and the certification of a new power plant is expensive and it takes a long lead time which it is not necessary in this case due to the fact that there are already many jet engines that would be suitable with the required specifications.

The number of engine to be used is not a constraint, for this reason, it has been considered the possibility of either installing a single engine or mounting two smaller engines. A list of candidate engines which are available on the market has been done, looking at the information available in Reference [7] and [35] or directly on company brochures. It was decided to select from all available engines, starting with the least bulky and most high-performing military ones at the same weight. Fuel efficiency and ease of maintenance were sacrificed in order to gain in performance and weight, as the aircraft was designed to operate in military zones.

Ultimately, a single jet engine configuration was chosen so that savings could be made in weight, drag, and cost. This was a decision made because of the presence of the two turboshaft motors that provide redundancy on the propulsive system.

The final candidates as jet engine are listed below:

	JT3D-7	F118-GE-100	Iroquis PS-13	BR715-55	CFM56-9
Thrust, lbf	19,000	19,000	19,350	19,883	20,000
Weight, lb	4,341	3,199	4,650	4,546	4,253
SFC, (lb/hr)/lbf	0.52	0.37	0.85	0.37	0.38
Diameter, in	53	46.5	42	60.2	56

Table 14.1: Jet Engines Comparison

To ensure both the necessary thrust and dry weight and fuel consumption, the jet engine chosen by the team is the **F118-GE-100**. Other advantages of this choice are:

- The small diameter size, which allows for a smaller footprint.
- F118 engines are military turbofan still used today in two similar variants on B-2 Spirit and Lockheed U-2S Dragon Lady. This should favor engine production and maintenance chain.



Listed below in 14.2 are the main features of the turbofan F118-GE-100.

Performance	
Maximum thrust	19,000 lbf (84.5 kN)
Continuous thrust	17,000 lbf (75.6 kN)
Overall pressure ratio	35:1
Bypass ratio	1.3:1
Air mass flow	287 lb/s (130.2 kg/s)
Specific fuel consumption @ Sea level	0.37 (lb/hr)/lbf, or 1.05e-5 (kg/s)/N
Specific fuel consumption @ Cruise altitude	0.5 (lb/hr)/lbf, or 1.42e-5 (kg/s)/N
Thrust-to-weight ratio	5.9:1
Dry weight	3,199 lb (1,451 kg)
Dimensions	
Diameter:	46.5 in (118 cm)
Length:	101 in (255 cm)
Components	
Type:	Two spool turbofan
Compressor:	Axial compressor with 1 stage fan, 2 stages low-pressure compressor and 9 stages high-pressure compressors
Combustors:	Annular
Turbine:	1 stage high-pressure turbine and 2 stages low-pressure turbine

Table 14.2: Specifications F118-GE-100



Figure 14.1: F118-GE-100

Another configuration considered in the preliminary phase is to use jet engines also for vertical flight. The most suitable engine for this configuration would be the Pratt & Whitney F135-PW-600, which is an afterburning turbofan developed for the Lockheed Martin F-35 Lightning II. It has a two-cycle Short Take-Off Vertical Landing (STOVL) variant used in the F-35B.



Figure 14.2: Pratt & Whitney F135-PW-600

It was taken into account to consider also the possibility to power the two rotors through the use of a shaft that extracted power from the drive shaft to deliver through the use of gear boxes and transmissions. With this configuration the nozzle will not be direct downward as in the F-35 to avoid strong downwash wind at high temperature, which could be a problem for ground operation. Unfortunately, this mechanism was not applicable due to two main factor:

- The engine jet would never be able to not provide longitudinal thrust, risking control difficulties in idle, high, hover and vertical flight phase. In addition, it would be very inefficient, because of the longitudinal thrust which would have to be counteracted by the rotor blades.
- Moreover, even if we could redirect the nozzle in a safety way, the power provided would not be enough to sustain the vertical flight or the hover phase.

Taking advantage of this propulsion system, in a initial preliminary configuration phase of the project has been take into account also the possibility to sustain the flight with 2 engine Pratt & Whitney F135-PW-600 mimicking the propulsion system of the F-35B. However, even in this case the same problems listed above would be encountered.



14.1.2. Position of the engine

Regarding the possible arrangements, the main guideline concern drag and balance installation, inlet requirements and resulting effect on 'installed' power and efficiency, accessibility and maintainability, ground operation and sensitivity to foreign object damage.

Regarding the longitudinal position, a tail mounted engine configuration was chosen due to the particular configuration of Raven 4. Considering the two rotors on the wing, the side doors and the rear ramp for access to the cargo compartment, the only valid position was a tail mounted engine. Thus, the two possible locations for a single engine tail-mounted are:

1. Overhead the aft fuselage
2. Buried in the fuselage

Despite issues regarding aerodynamic drag and weathering resistance, a configuration with engine located overhead the aft-fuselage was chosen because of these reasons:

- Reduction of the thermal trace due to the exhaust gases covered by the V-tail, disfavoring detectability from heat-seeking missile.
- Ease of maintenance and assembly
- Possibility of arranging a rear cargo ramp located in the aft fuselage.
- Avoid possible structural complications given by the presence of both the buried engine and the rear ramp

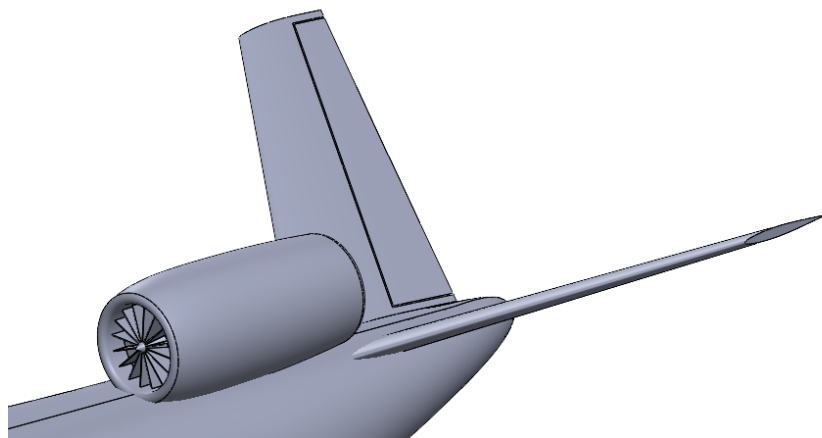


Figure 14.3: Jet-engine position

14.1.3. Safety consideration

In the placement of the engine overhead the aft fuselage, attention was paid to the temperature of the exhaust gases so that they would not make access to the rear ramp impractical in fast cargo compartment loading and unloading procedures. In fact, for the high temperatures it will be necessary to thermally insulate the fuselage structure at the tail proximity from the exhaust gases to avoid excessive deterioration due to the high temperatures. Furthermore, this care was also taken in choosing the final position of the engine so that no primary structure is placed too close to exhaust gases.

Along with such safeguarding of the structure, all those emergency systems that are useful for a well-designed propulsion system such as fire-fighting and de-icing systems within the engine must be considered.

As reported in the concluding Chapter 25 special attention and investigation should be devoted in future developments regarding the possible ingestion of debris by the jet engine in the rotorcraft-mode flight phases as in hover.

In this regard, it will be necessary to develop protective systems for the engine air intake that can be removable in a controlled manner so that the performance of the air intake and the inlet flow to the engine during cruise phases will not be disturbed.

14.2. Turboshaft engines for rotors

The Primary Mission profile described in the RFP requires a 2-min Hover In Ground Effect (HIGE) takeoff and a 2-min mid-mission Landing Zone (LZ) Hover Out of Ground Effect (HOGE) at Mid-Mission Gross Weight (MMGW). Where in this second scenario the aircraft shall be capable of using no more than 90% of the engine Maximum Rated Power (MRP) or 100% of the gearbox and/or motor torque at an ambient condition of 2000 ft (609.6 m) MSL and 85°F (24°C). These will be the two sizing conditions of the power needed for our rotors.

Therefore, in order to choose the engine, the necessary power to perform these phases has been analyzed.

In the Chapter 9 we obtained the design point for the required power available on board for the rotorcraft mode given in the Table 9.4. Therefore, starting with the request of maximum continuous power equal to 5400 hp (4064 kW) it's been selected a turboshaft engine of the General Electric Company. Since there are not many engines available to deliver that much power, priority was given to the same company that could also



provide an adequate jet engine for our requirements. So as to give priority to be able to sign the same engine supply contract for the same aircraft, without going into multiple collaborations with multiple different companies probably creating interference and design slowdowns at the project management level. For these reasons, the T408-GE-400 engine was selected (Figure 14.4).



Figure 14.4: Turboshaft engine T408-GE-400

The engine selected, as reported in General Electric's program briefing [3], was developed starting in 2007 by General Electric's in collaboration with Sikorsky, a Lockheed Martin Company. The T408 turboshaft was chosen to power the CH-53K beating out the Pratt & Whitney Canada PW150 and the Rolls Royce AE1107 Liberty. Its development starts from the U.S. Army's proven GE27 engine technology and the T407 turboprop technology developed for the U.S. Navy.

Features of the engine include resistance to sand erosion and saltwater corrosion. In addition, the thruster is designed to be stall-free under all conditions and the maintenance and service costs will be reduced due to fewer parts to be replaced.

Performance	
Maximum rating power	7,500 hp (5,593 kW)
Maximum continues power	6,375 hp (4,750 kW)
Overall pressure ratio	18.6 : 1
Specific fuel consumption @ Sea level	0.4 lb/(hp · h) (0.24 kg/kWh)
Power-to-weight ratio	6.8 shp/lb (11.2 kW/kg)
Dry weight	1104.7 lb (501.1 kg)
Dimensions	
Diameter:	27 in (68.6 cm)
Length:	57.5 in (146.1 cm)
Components	
Type:	Turboshaft
Compressor:	Five-stage axial compressor coupled to a single centrifugal stage
Combustors:	Single low-emission annular combustor
HP Turbine:	Two-stage axial high-pressure (HP) turbine drives the compressor section
LP Turbine:	Three-stage axial low-pressure (LP) turbine (a.k.a. power turbine), drives the output shaft
Other features:	Dual-channel full-authority digital electronic control (FADEC) system with advanced health monitoring functions
Marketing data	
Cost production:	\$2.8 million (€2.52 million)
Price:	\$4 million (€3.6 million)

Table 14.3: Specifications T408-GE-400



14.3. Drive system

In the event of engine failure it is necessary to have power available to drive both rotors, to avoid asymmetric thrust and the consequent generation of a rolling moment. In order to overcome this problem, turboshaft engines are interconnected by a mechanical drive system that is able to redistribute power to both rotors. It is composed by a central gearbox placed in the central part of the wing, above the cargo bay, and a drive shaft.

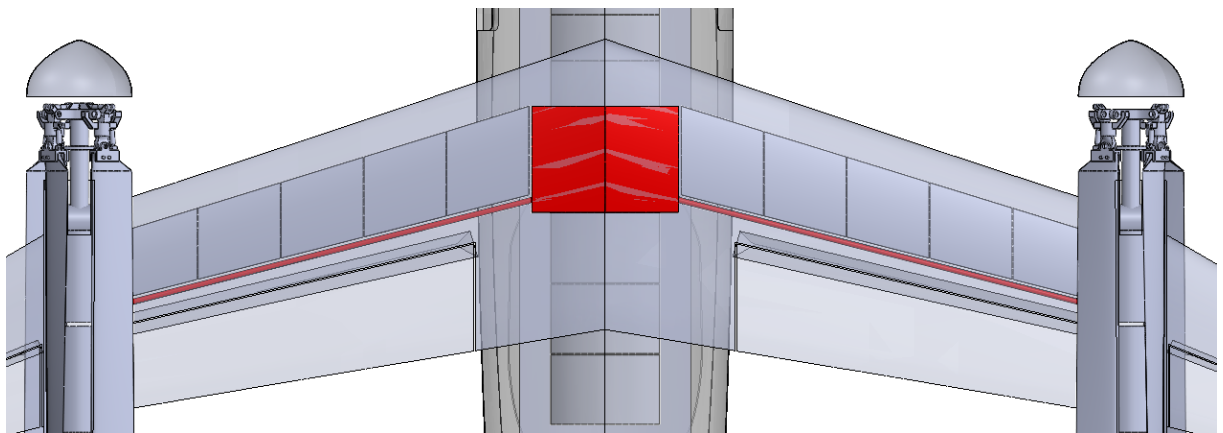


Figure 14.5: Drive system

14.4. Fuel system

The aim of the fuel system is to contain, distribute and maintain in the adequate conditions of pressure and temperature the fuel. Its main components are the fuel tanks, fuel lines, fuel pumps and fuel-management controls.

As already described in Section 13, the fuel tanks are located in the wings and in the upper part of the fuselage. In more detail, the fuel tanks are divided into 4 main groups: two in the wings, one in the front part of the fuselage, and one in the rear. Each tank is further divided into multiple sections, both for safety reasons and to use fuel distribution for aircraft balance. The division of the tanks and their positions inside the fuselage are shown in Figure 14.6.

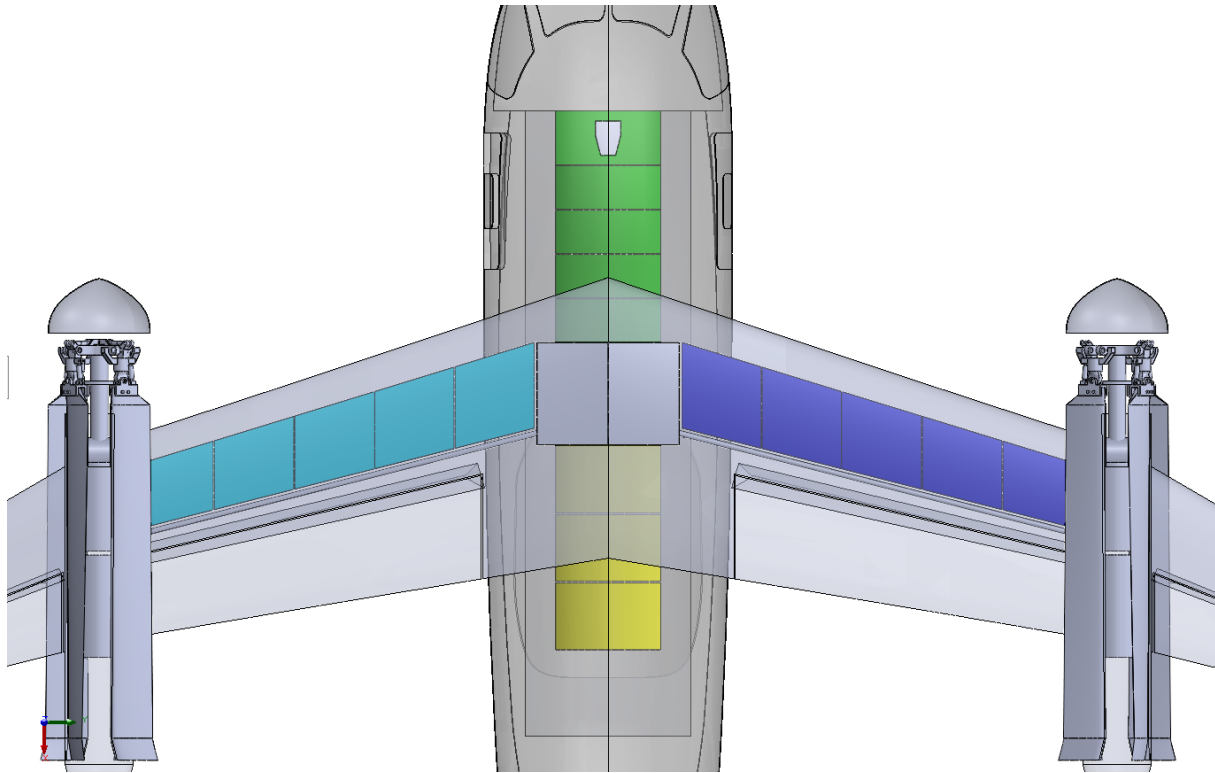


Figure 14.6: Fuel tanks

The total volume of the tanks is larger than the one determined in Chapter 13, in order to have the possibility of transfer the fuel from one tank to another and move the center of gravity of the aircraft if necessary. The updated volume distribution is shown in Figure 14.7 and Table 14.4.

	Volume	Percentage
Total	258.21 ft ³ (8.55 m ³)	100 %
Right wing tanks	43.54 ft ³ (2.21 m ³)	25.85 %
Left wing tanks	43.54 ft ³ (2.21 m ³)	25.85 %
Front fuselage tanks	89.55 ft ³ (2.56 m ³)	29.95%
Rear fuselage tanks	89.55 ft ³ (1.56 m ³)	18.25%

Table 14.4: Volume of fuel tanks



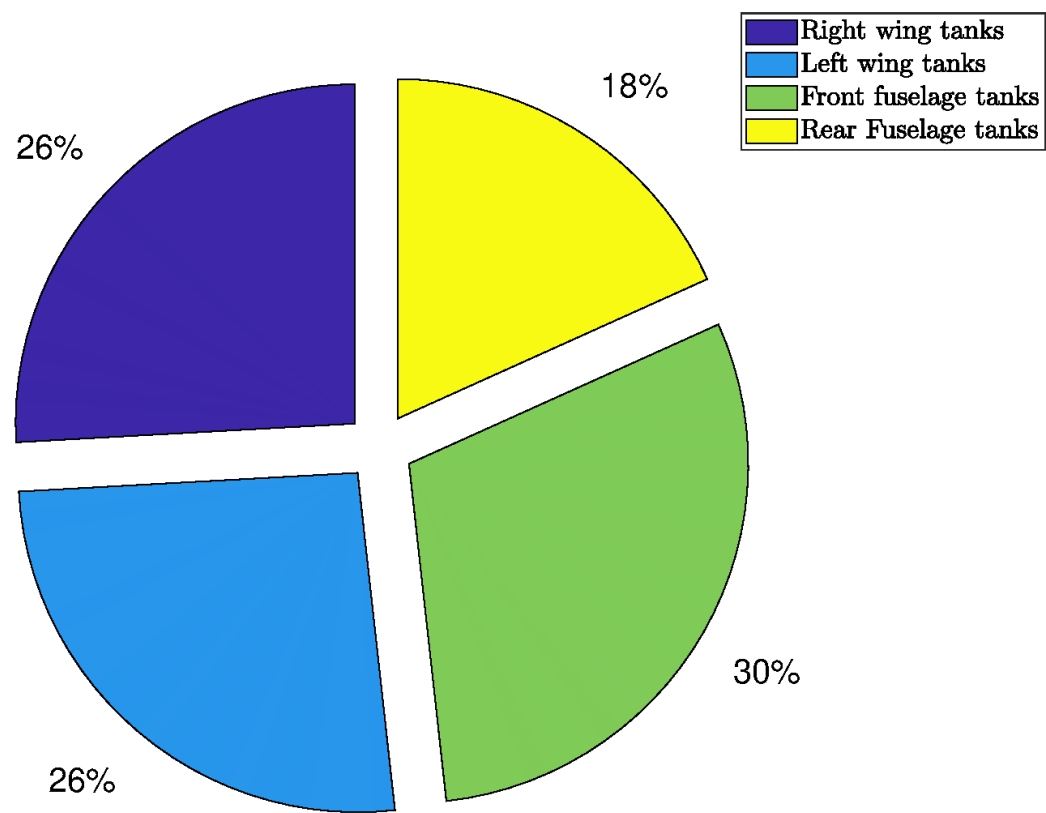


Figure 14.7: Volume of fuel tanks

Larger tanks allow for the storage of greater quantities of fuel, which would enable longer journeys. This potential will be examined in Chapter 18.

In order to maintain a correct distribution of the fuel within the fuel tanks, the aircraft is equipped with 2 fuel transfer pumps controlled by a fuel-management system and placed in the central box used to move the fuel from the wing to the fuselage and between front and rear fuselage tanks. Furthermore, there are 3 fuel booster pumps, used to feed the engine with the correct amount of fuel to prevent aeration and cavitation at high altitudes.

14.4.1. In-flight refueling

In order to extend its operational range capability and flexibility, the aircraft is able to perform in-flight refueling through flying boom. This system allows the aircraft to receive fuel from tanker aircraft while in mid-flight, significantly extending its endurance and reach. The IFR system on a military cargo aircraft comprises several key components, including a refueling receptacle, hoses, pumps and a control panel.

According to military specifications, in-flight refueling falls under Phase A category mis-

sions, which are the most critical ones, so the actual feasibility of the in-flight refueling will be better analyzed in Chapter 16.

14.5. Electrical system

On most aircraft it is necessary to have both DC current and AC current, but typically electrical power is generated in one way and then converted through inverters or rectifier.

A typical modern electrical system in military aircraft employs engine-driven generators 115V/200V, 400 Hz, 3-phase AC, oil cooled, constant frequency generators. The main advantage of AC power is that it operates at a higher voltage: 115 VAC rather than 28 VDC for the DC system. The lower the current the lower are losses such as voltage drops (proportional to current) and power losses (proportional to current squared).

Therefore, as power generating system have been chosen 4 engine-driven generators 115 VAC, constant frequency 400 Hz, each rated at 60 kVA. Two of them are connected to the central gearbox of the drive system, while the other two are powered by the jet engine. Two generators are sufficient to feed aircraft electrical needs, therefore each couple of generators can be used alternatively depending on the flight phase: during hovering electrical energy can be converted from the jet engine and in cruise phase from the drive system. Furthermore, in case of failure of one of the propulsion systems, the other can act as emergency power system.

14.6. Instrumentation and avionics

The instrumentation to be carried on board would be that related to instrumentation flight. In fact, the Instrument Flight Rules (IFR) refer to a set of regulations and procedures that allow pilots to operate an aircraft solely by reference to instruments in the cockpit, without visual reference to the outside environment. This capability is crucial for military cargo aircraft, enabling them to perform missions in adverse weather conditions, low visibility, or airspace congestion. The instrumentation for IFR on a military cargo aircraft encompasses a suite of advanced avionics, navigation aids and communication systems.

- *Flight Management System (FMS)*: to assist in flight planning, navigation, and management of the aircraft's systems. It integrates GPS, inertial navigation, and other sensors to provide accurate position information, route planning, and guidance.
- *Attitude and Heading Reference System (AHRS)*: the AHRS provides critical data



regarding the aircraft's attitude (pitch, roll, and yaw) as well as its heading. This information is essential for maintaining stable flight, especially in low-visibility conditions.

- *Primary Flight Display (PFD) and Multi-Function Display (MFD)*: presents essential flight information to the pilot such as airspeed, altitude, attitude, vertical speed, and heading. The MFD provides additional situational awareness, including navigation charts, weather data, and system status.
- *Autopilot System*: aids in maintaining a stable and precise flight path, relieving the pilot of some of the manual control tasks. It interfaces with the FMS and other navigation systems to follow programmed routes.
- *Radar and Weather Systems*: radar systems allow the aircraft to detect other aircraft, terrain, and weather conditions even when visibility is poor. Weather radar provides critical information about precipitation, turbulence, and storms.
- *Communication and Navigation Equipment*: this includes VHF/UHF radios for communication with air traffic control, as well as navigation aids such as VOR (VHF) and NDB (Non-Directional Beacon) receivers for accurate navigation along airways and approaches.
- *Inertial Navigation System (INS) and Global Positioning System (GPS)*: they can provide accurate position, velocity, and time information, enabling the aircraft to navigate precisely, especially when GPS signals are available.
- *Traffic Collision Avoidance System (TCAS)*: TCAS is a safety feature that assists in avoiding mid-air collisions by providing information about nearby aircraft and issuing alerts if necessary.
- *Flight Data Recorder and Cockpit Voice Recorder*: safety devices that record flight data and cockpit conversations, respectively, for analysis in the event of an accident or incident.



Figure 14.8: Cockpit view



15 | Structural sizing and weight analysis

Now that the principal components of the aircraft have been designed, the structure and the mass of the aircraft can be analyzed in detail.

The procedure followed in this chapter is described below:

1. Preliminary mass breakdown: description of the known component masses
2. Material selection
3. Structural sizing
4. Final mass breakdown
5. Center of gravity analysis

15.1. Preliminary mass breakdown

The estimate of the aircraft mass obtained in the preliminary sizing can be updated with calculations based on components geometry, dimensions and materials.

The aircraft maximum take-off mass can be divided in four main groups: payload, crew, fuel and empty weight. While payload, crew and fuel are known from design and mission requirements, empty weight must be computed. It can be further subdivided into structure, propulsion and equipment: propulsion components and equipment masses are obtained with a statistical approach, as shown in [19], while structural masses will be refined during structural sizing.

15.2. Material selection and properties

A preliminary detailed analysis of the typical aerospace material used is need to conduct a more accurate estimation of the aircraft's empty weight. A comparison in term of weight, maintainability, cost, property is done to make a better choice for the project. Materials

taken into account are: aluminum alloys, steel, titanium and composite.

Aircraft are most often composed of aluminum alloy, as this is a material that is resistant to impact, weight and torsion, and is both flexible and lightweight. The main alloys that are used in the aviation industry are the 7000-group alloys of aluminum, zinc and magnesium or the 2000-group alloys of aluminum and ram.

Property	Al-2024-T3	Al-7075-T6
Density	0.1 lb/in ³ (2780 kg/m ³)	0.102 lb/in ³ (2810 kg/m ³)
Tensile modulus	10600 ksi (73.1 GPa)	10400 ksi (71.1 GPa)
Shear strength	41000 psi (283 MPa)	48000 psi (331 MPa)
Ultimate tensile stress	70000 psi (483 MPa)	83000 psi (572 MPa)
Yield tensile stress	50000 psi (345 MPa)	73000 psi (503 MPa)

Table 15.1: Aluminium alloys properties

Generally, the strongest materials are also relatively dense, i.e. they have lower goodness index; moreover, the increase in strength and stiffness of a material also leads to a decrease in its ability to resist impacts. Faced with this difficulty in finding the right compromise, composite materials offer a possible solution increasingly used by aircraft manufacturers. Interest in such materials continues to grow given their special features of having low-electricity, corrosion resistance, aircraft strength, aircraft tailoring if needed, and having a flexible design that can be adapted to design requirements.

Thus, composite materials have very high structural properties with goodness indices much higher than those of conventional materials. These characteristics allow the manufacture of components with weight savings of up to 30%.

For this reason, a cost difference was estimated between an aircraft primarily composed of aluminum and a lighter-weight aircraft with higher technological materials 22.2.5. Based on cost-related trade studies, the two alternatives were found to be equivalent in terms of costs due to the increased structural complexity that would arise with a significant carbon component. No clear advantages were found in using composite materials, leading to the choice of a more standard configuration, maintaining the aluminum structure. However, the choice to use composite material was limited to the aerodynamic control surfaces of the main wing and the radar dome. It was preferred to keep the tail control surfaces in aluminum since they are located close to the jet engine exhaust gases and may experience long-term stresses due to harmful temperatures.



Property	Graphite/Epoxy	S2-Glass/Epoxy
Density [kg/m^3]	1522	1993
Tensile modulus [GPa]	241,3 (35 Msi)	48 (7 Msi)
Shear stress [MPa]	90 (13 ksi)	82 (12 ksi)
Ultimate tensile stress [MPa]	1448 (210 ksi)	1523 (221 ksi)
Compressive strength [MPa]	1180 (172 ksi)	850 (124 ksi)
Cost	30 \$/lb	13 \$/lb

Table 15.2: Composite material properties

Other materials will be presented such as acrylic for pilots' windshields and cargo windows, or such as titanium for aerodynamic control surface joints and rotor hub.

Materials that have been chosen for each component of the structure are illustrated in Table 15.3:

Material	Component
Al-2024-T3	Skin, V-tail and Ruddervators
Al-7075-T6	Wing frame, Fuselage frame, Landing gear
Graphite/Epoxy	Flaperons, Ailerons
S2-Glass/Epoxy	Radar dome
Acrylic	Windows, Cockpit windshield
Titanium	Rotor hub, Junction

Table 15.3: Components material

15.3. Structural sizing

For the structural analysis of the aircraft has been used *NeoCASS*, a software developed at Politecnico di Milano, completely written in Matlab. It provides 2 modulus:

1. GUESS (Generic Unknown Estimator in Structural Sizing): used to improve the prediction of structural weight.
Starting from the description of the aircraft, some mass configurations and sizing maneuvers, it performs an initial structural sizing and generates a stick model. The description of the aircraft is contained in a .xml file, where geometrical and technological characteristics are defined through AcBuilder modulus.
2. SMARTCAD (Simplified Models for Aeroelasticity in Conceptual Aircraft Design): modulus for the numeric aero-structural analysis.

It takes as input the stick model of the aircraft and computes static and dynamics aeroelastic characteristics.

The complete scheme is shown in Figure 15.1:

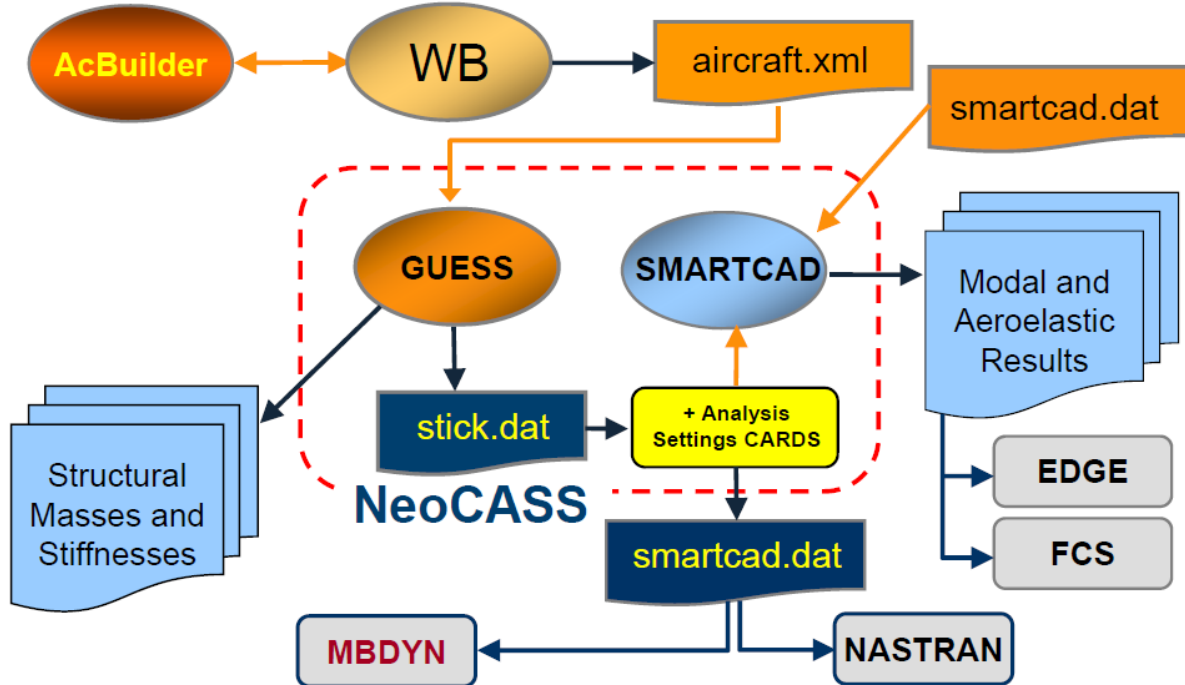


Figure 15.1: Neocass architecture [28]

15.3.1. V-n diagram

The V-n diagram shows the boundaries, in terms of airspeed and load factor, within the aircraft must operate to avoid structural damage. It is drawn at Maximum Take-Off Weight at sea level following the procedure described in [25] for military airplanes.

V-n diagram is the combination of maneuvering and gust envelopes, but gust induced load factors are normally not critical for military airplanes with limit load factor above 3 [25]. In order to construct it some quantities must be computed:

- maximum load factor: $n_+ = 3.5$
- minimum load factor: $n_- = -1.4$
- level-flight maximum speed: $V_H = 328 \text{ kn} (169 \text{ m/s})$
- limit speed: $V_L = 1.45V_H = 476 \text{ kn} (245 \text{ m/s})$
- stall speed: $V_S = 131 \text{ kn} (67.24 \text{ m/s})$



- stall speed with flap extended: $V_{S0} = 100 \text{ kn}$ (51.44 m/s)

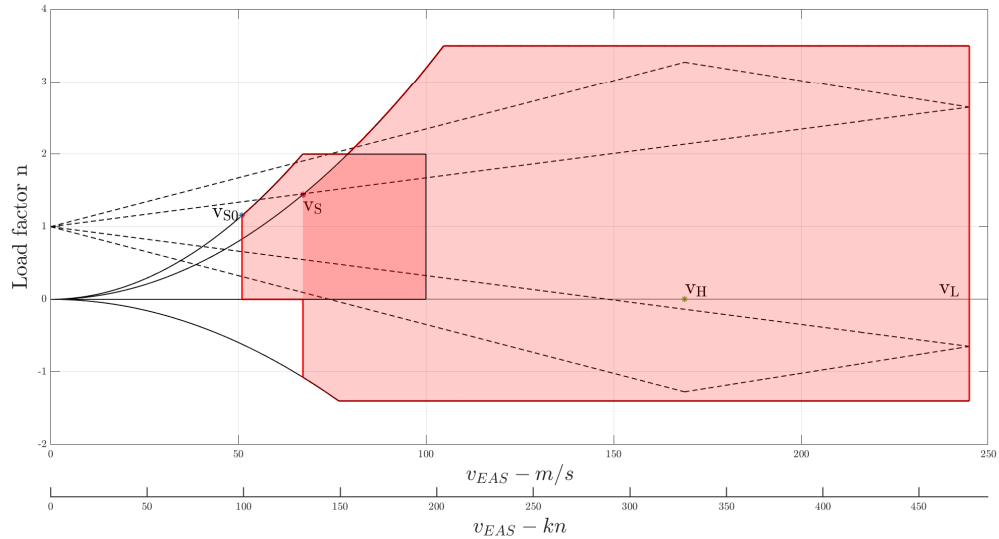


Figure 15.2: V-n diagram

15.3.2. Sizing maneuvers

In order to size the aircraft, it was analyzed as if it were a conventional aircraft, assuming that the highest internal forces would occur only during traditional flight. The critical maneuvers were defined as shown in Table 15.4, based on those presented in the CS-25 certification, adapted and expanded for the required load factor and flight envelope. Each of them performs at different altitudes and different deflections of the control surfaces.

Maneuver ID	Description	Velocity
1-4	Maximum Load Factor	V_H, V_L
5-16	Sudden aft movement of pitch control	V_B, V_C, V_L
17-24	Aileron deflection	$V_B,$
25-30	Gust	V_H, V_L
31-32	Tail down landing	V_F at V_{SINK}

Table 15.4: Sizing maneuvers

	Value	Meaning
V_H	328 kn (169 m/s)	Design Cruise Speed
V_L	476 kn (245 m/s)	Design Limit Speed
V_B	202 kn (104 m/s)	Maneuvering Speed
V_F	100 kn (51 m/s)	Stall speed with flap
V_{SINK}	12 fps (3.6 m/s)	Sink speed in landing

Table 15.5: Reference equivalent airspeed for sizing maneuvers

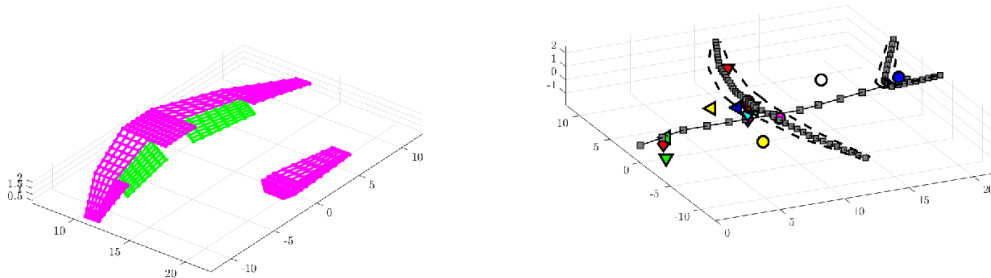


Figure 15.3: Aerodynamic model of Neo- CASS Figure 15.4: Structural model of Neo- CASS

15.3.3. Mass configurations

In order to perform the structural sizing of the aircraft it is also necessary the definition of some mass configurations in which perform the sizing evaluation. Each configuration chosen is defined through percentage of payload (passengers and baggage), fuel and position of them with respect to the CG.

	Crew	Payload	Fuel
Configuration 1	100%	100%	100%
Configuration 2	100%	0%	100%
Configuration 3	100%	100%	50%

Table 15.6: Mass configurations



15.3.4. Component design loads

Once Guess has been executed, the tool evaluates the maximum internal forces for each section of the fuselage, wing and v-tail for each mass configuration and maneuver. In this way, Guess sizes the structure based on the maximum internal forces that the structure may experience depending on the mass configuration and maneuver the aircraft will undergo.

As an example, the following figures represent the bending, torque and shear at 5% of the tail semi-span from the fuselage center line for the v-tail of configuration number 1. Specifically, NeoCASS generates the green envelope, with its points representing different structural conditions in which the airplane can safely operate. The sizing is then carried out by considering the intersection of the maximum values between the two internal forces compared.

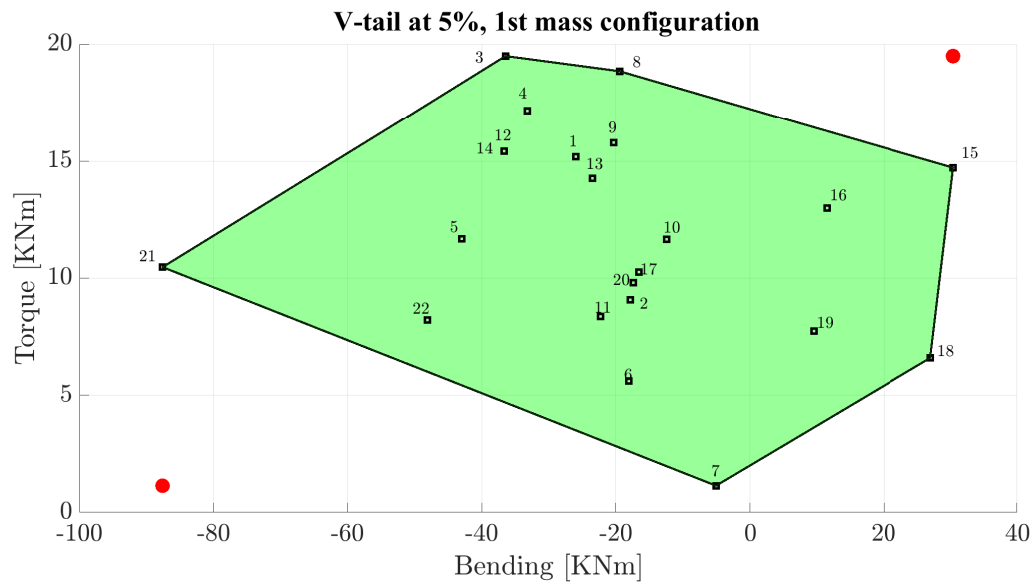


Figure 15.5: V-tail torque bending

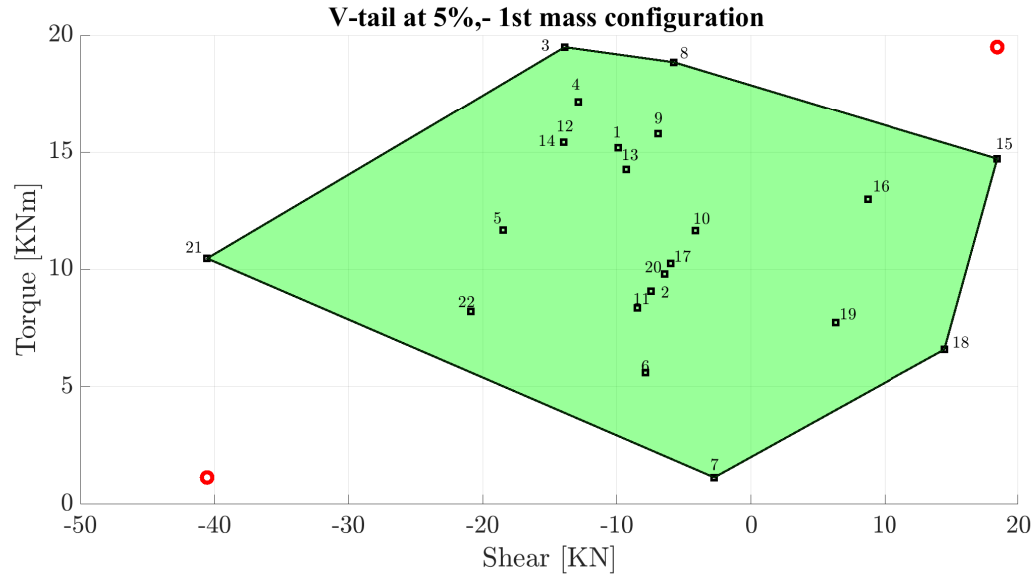


Figure 15.6: V-tail torque shear

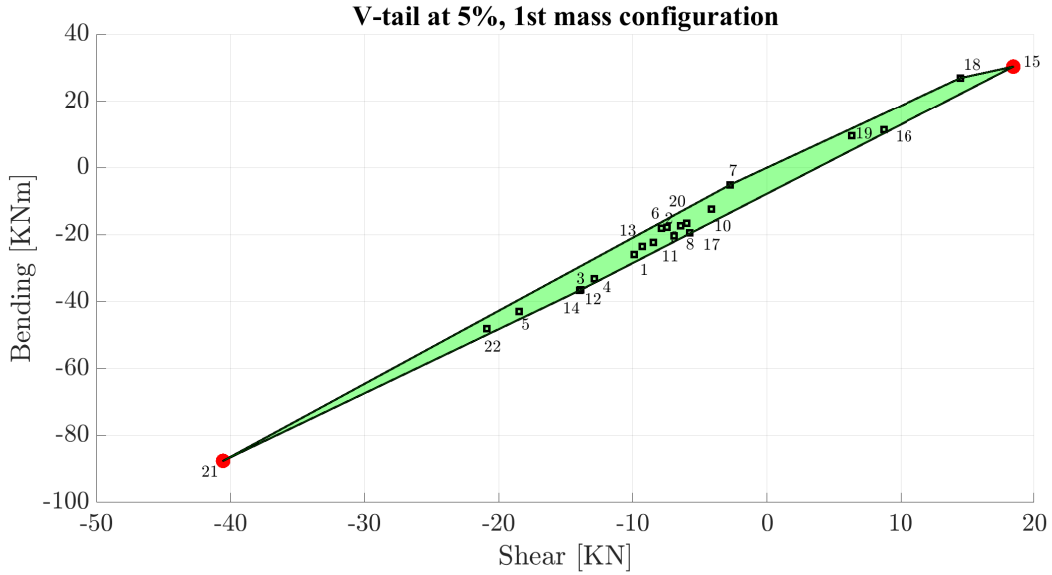


Figure 15.7: V-tail bending shear

Furthermore, it is possible to identify which mass configurations size the various sections of the v-tail. In this case, we can observe that for all v-tail sections, mass configuration 2 of the aircraft is the worst, as it sizes all the sections of the v-tail.



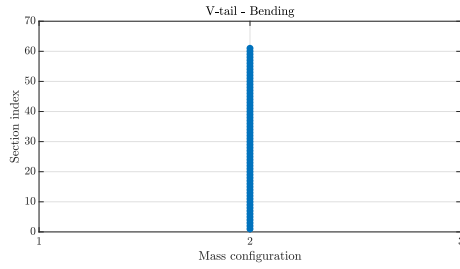


Figure 15.8: V-tail bending

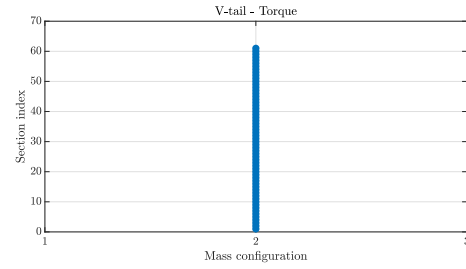


Figure 15.9: V-tail torque

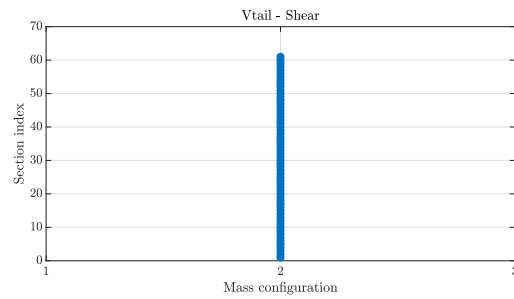


Figure 15.10: V-tail shear

Finally, it is also possible to observe, for each individual section of the tail, not only the sizing mass configuration but also the maneuver that will govern the sizing for each section of the tail.

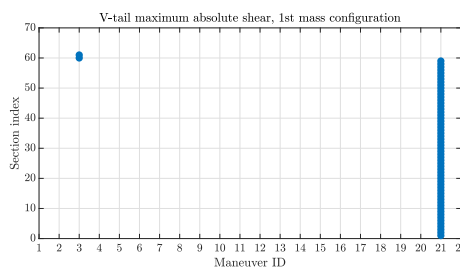


Figure 15.11: V-tail max shear

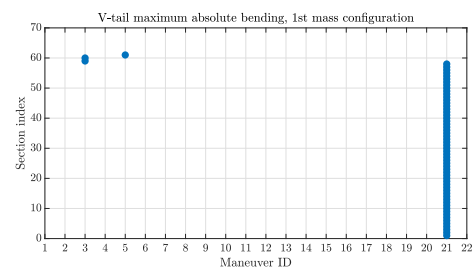


Figure 15.12: V-tail max bending

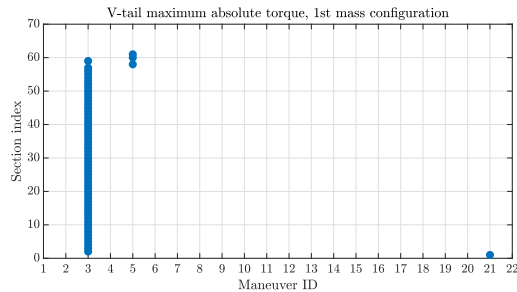


Figure 15.13: V-tail max torque

The above-mentioned graphs can indeed be reproduced for the fuselage, wing, and tail. Additionally, for the first three figures, they can also be reproduced for different percentages of span-wise positions on wing, tail and fuselage.

To conclude, the NeoCASS suite provides diagrams reporting the trend of mass distribution both for the fuselage and lifting surfaces, the trend of out-of-plane and section-wise moment of inertia, and the trend of section-wise sizing bending, shear force, and torque again both for the fuselage and for the lifting surfaces. For example, the trend of mass along the fuselage center line is depicted respectively in Figure 15.14.

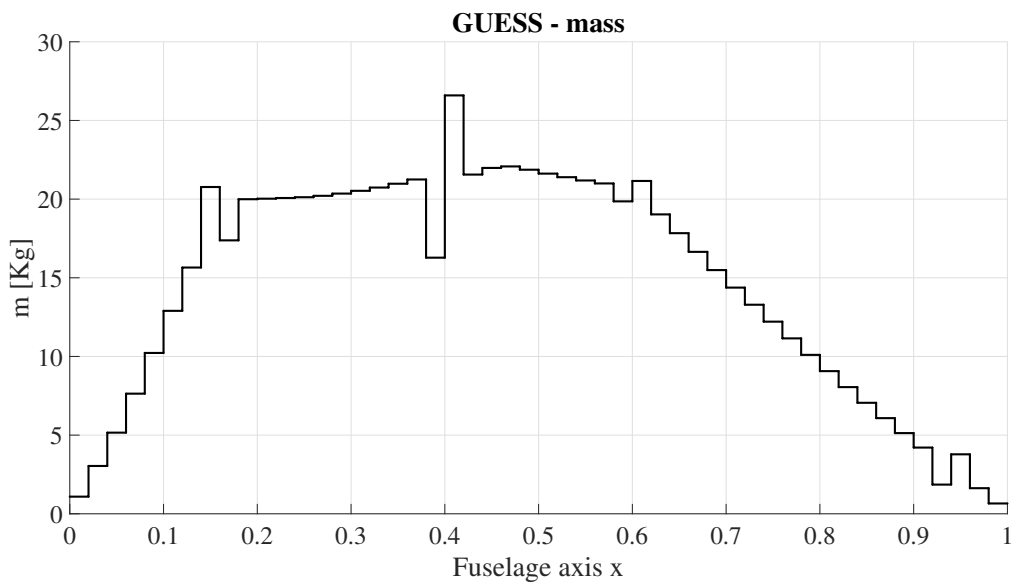


Figure 15.14: Mass distribution along the fuselage



15.3.5. Trim and modal analysis

To verify the structural model and explore the deformed model, a static aerelastic analysis in cruise trim (Figure 15.15) and a modal analysis (Table 15.7) were performed.

In the static aerelastic analysis in cruise trim, a deformation mainly of symmetrical bending of the wing and tail upward can be observed. In figure 15.15 the deformed model is shown with a scaling factor on the displacements equal to 10 to emphasize the deformations. In fact, the deformation turn out to be very small due to the structural stiffness required for the presence of the rotors at the wingtips.

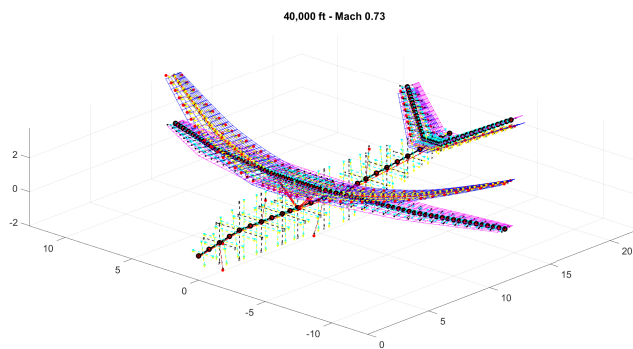


Figure 15.15: Deformed model for trim analysis in cruise at 40,000 ft. A scale factor equal to 10 is been chosen to better observe structural deflection.

In the modal analysis performed which is useful for the validation of the structural sizing and for the calculation of the flutter velocity, we can observe the first 20 structural modes where the first 6 correspond to the rigid modes of the aircraft (Table 15.7). As an example, we show the depiction of the first symmetric and antisymmetric structural mode resulting from the modal analysis (Figures 15.16 and 15.17).

ID	Frequency [hz]	ID	Frequency [hz]
1	3.89e-06	11	7.56627
2	7.59e-06	12	11.1605
3	1.03e-06	13	12.3562
4	1.38e-05	14	12.8762
5	2.07e-05	15	13.0584
6	2.12e-05	16	13.8064
7	3.01808	17	15.6330
8	5.36374	18	16.3224
9	6.47191	19	17.7300
10	6.74435	20	18.1530

Table 15.7: First 20 structural modes

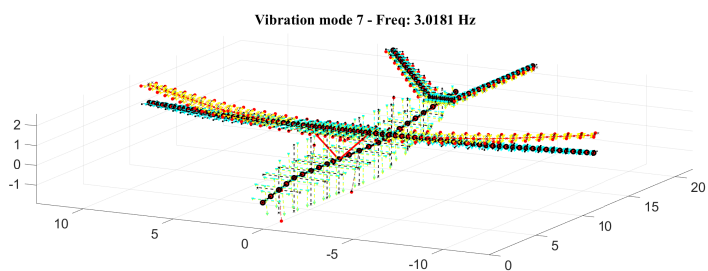


Figure 15.16: Mode 7

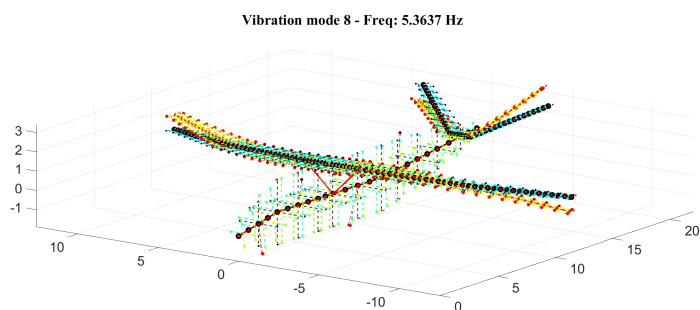


Figure 15.17: Mode 8



15.3.6. Flutter analysis

Flutter is a critical phenomenon in aircraft design that poses a significant challenge. It refers to the self-excited, oscillatory motion experienced by aircraft structures when subjected to aerodynamic forces which leads to unstable vibrations, potentially leading to catastrophic consequences if not properly addressed.

Understanding flutter is crucial in aircraft design to ensure the safety and performance of the vehicle. Flutter can occur in various flight conditions, such as during high-speed flights, maneuvers, or encounters with turbulent air. The complex interaction between the aircraft's structure, aerodynamics, and control systems makes flutter analysis a multidisciplinary endeavor, requiring expertise in structural mechanics, aerodynamics, and control engineering. Since the study and mitigation of flutter play a vital role in ensuring the structural integrity and stability of aircraft, a flutter analysis has been conducted to determine if the phenomenon of flutter occurs and, if necessary, revise the aircraft design or reduce the defined flight envelope.

To perform such analysis, a function of the NeoCASS environment was utilized, which is used for structural design. Specifically, a modal analysis was conducted as described in paragraph 15.3.5 for each of the three analyzed configurations. By defining a range of velocity, air density, and Mach number, it becomes possible to study the frequency-velocity and damping-velocity plots to determine if any instability phenomena occur for each mass configuration.

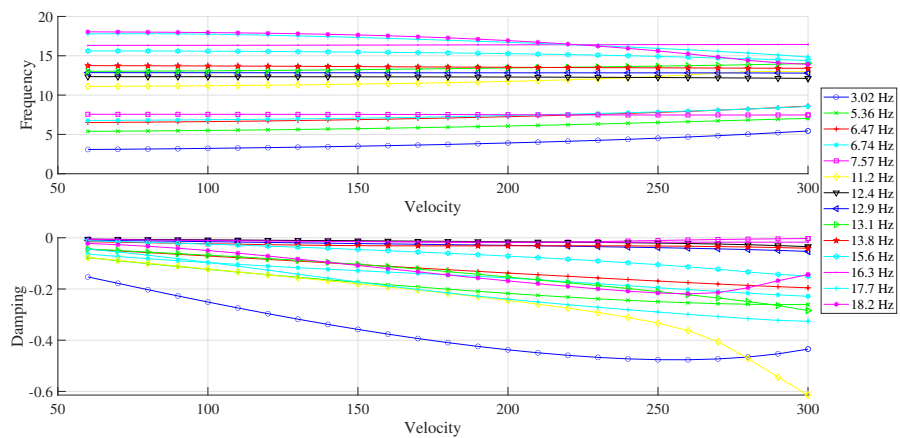
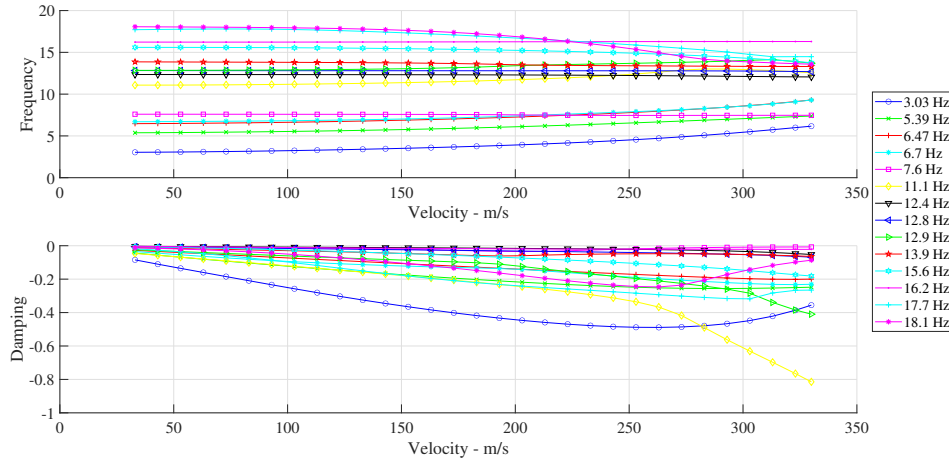
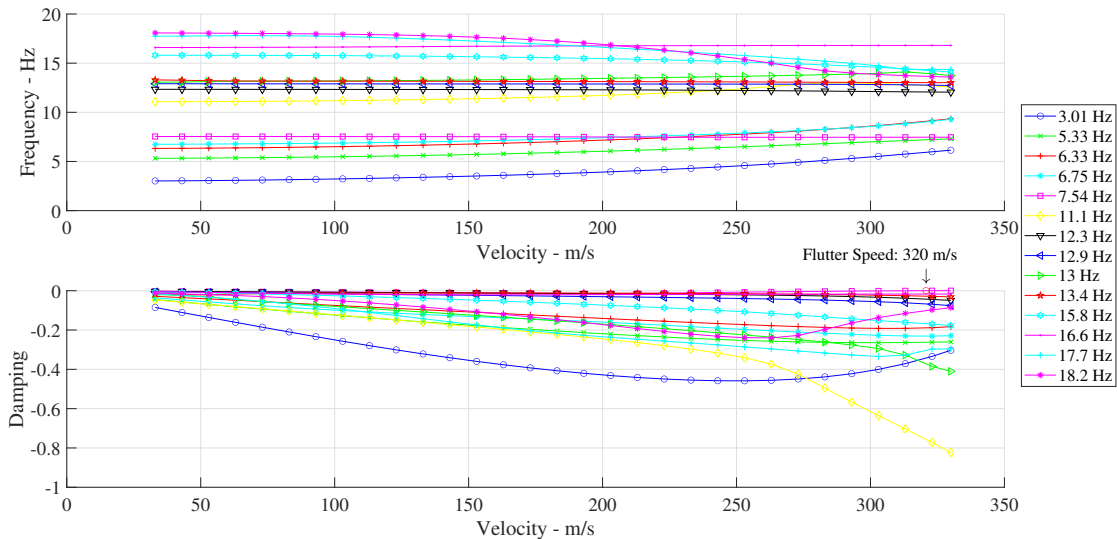


Figure 15.18: Flutter 1st mass configuration

Figure 15.19: Flutter 2nd mass configurationFigure 15.20: Flutter 3rd mass configuration

As it can be noticed in Fig.15.18 and Fig.15.19 there is no coalescence of frequencies and the damping indicator related to the velocity never became positive. these two information can assert that no flutter is supposed to arise below 330 m/s. Since the maximum velocity available in flight envelope is defined as the V_{limit} equal to 211 m/s, no flutter is present inside the flight envelope for the first two mass configurations analyzed.

As for configuration number three, the onset of flutter instability can be observed at a velocity of 320 m/s in Fig.15.20. This configuration has proven to be more critical in



terms of structural-aerodynamic coupling. However, this instability remains acceptable as it occurs well above the margin of 15% on the set maximum velocity (VNE) as it is required from MIL-A-8870C [14].

Just like for the flutter analysis, the compatibility of the flight envelope with the occurrence of the instability phenomenon related to dynamic divergence pressure was verified using the NeoCASS software.

Mass Configuration	Dynamic pressure [Pa]
1	193,269
2	191,956
3	194,228
Divergence speed	1080 <i>kn</i> (560 <i>m/s</i>)

Table 15.8: Dynamic pressure for divergence instability

By knowing the dynamic divergence pressure it is possible to determine the velocity at which divergence occurs taking account the worst configuration. Since this velocity value is very high due to the great weight present on the wing tip, we can conclude that divergence cannot happen inside the flight envelope for all three mass configurations.

15.4. Final mass breakdown

In the structural sizing the masses and weights of the structural components were estimated, therefore the final mass breakdown and the position of each component are reported in Table 15.9.

In order to describe the position of the components, a reference system has been defined as follow:

- x-axis along the fuselage center line, positive toward the tail: longitudinal position measured starting from the nose of the aircraft
- y-axis along the right wing: lateral position measured starting from the fuselage center line
- z-axis positive upward: vertical position measured starting from the fuselage center line

As required in the RFP [31], a weight contingency of 5% has been applied to the sum of the component weights.

	Mass	CG X position	CG Z position
STRUCTURE			
Wing	6243 lb (2832 kg)	30.15 ft (9.19 m)	4.33 ft (1.32 m)
Rotor groups	1852 lb (840 kg)	28.87 ft (8.80 m)	7.97 ft (2.43 m)
V-tail	1975 lb (896 kg)	66.89 ft (20.39 m)	3.97 ft (1.21 m)
Fuselage	2822 lb (1280 kg)	30.45 ft (9.28 m)	-1.09 ft (-0.33 m)
Jet nacelle	661 lb (300 kg)	45.93 ft (14.00 m)	6.59 ft (2.01 m)
Turboshaft nacelles	921 lb (418 kg)	32.00 ft (9.75 m)	2.89 ft (0.88 m)
Main landing gear	2623 lb (1190 kg)	31.17 ft (9.50 m)	-6.20 ft (-1.89 m)
Nose landing gear	567 lb (257 kg)	6.56 ft (2.00 m)	-6.20 ft (-1.89 m)
PROPELLION			
Jet engine	3199 lb (1451 kg)	45.93 ft (14.00 m)	6.59 ft (2.01 m)
Turboshaft engines	2209 lb (1002 kg)	36.09 ft (11.00 m)	2.89 ft (0.88 m)
Turboshaft gearboxes	1764 lb (800 kg)	31.13 ft (9.49 m)	2.89 ft (0.88 m)
Fuel system	1111 lb (504 kg)	24.61 ft (7.50 m)	4.33 ft (1.32 m)
Drive system	816 lb (370 kg)	27.23 ft (8.30 m)	3.28 ft (1.00 m)
EQUIPMENT			
Flight controls	1343 lb (609 kg)	9.84 ft (3.00 m)	-1.00 ft (-0.33 m)
Instruments	298 lb (135 kg)	4.92 ft (1.50 m)	-1.00 ft (-0.33 m)
Hydraulics	330 lb (150 kg)	24.61 ft (7.50 m)	4.33 ft (1.32 m)
Pneumatic	330 lb (150 kg)	24.61 ft (7.50 m)	4.33 ft (1.32 m)
Electrical	1102 lb (500 kg)	24.61 ft (7.50 m)	4.33 ft (1.32 m)
Avionics	2205 lb (1000 kg)	4.92 ft (1.50 m)	-1.00 ft (-0.33 m)
Air conditioning	661 lb (300 kg)	24.61 ft (7.50 m)	4.33 ft (1.32 m)
Anti-icing	132 lb (60 kg)	24.61 ft (7.50 m)	4.33 ft (1.32 m)
Load and handling	594 lb (269 kg)	24.61 ft (7.50 m)	4.33 ft (1.32 m)
MEP	1000 lb (454 kg)	27.36 ft (8.34 m)	0 ft (0 m)
EMPTY MASS	34758 lb (15767 kg)	30.68 ft (9.35 m)	2.2 ft (0.87 m)
USEFUL LOAD			
Crew (Pilot and co-pilot)	500 lb (227 kg)	6.00 ft (1.83 m)	-2.55 ft (-0.78 m)
Crew (Loadmaster)	250 lb (113 kg)	27.36 ft (8.34 m)	0 ft (0 m)
Fuel	13012 lb (5902 kg)	25.91 ft (7.90 m)	3.58 ft (1.09 m)
Payload	7218 lb (3274 kg)	27.36 ft (8.34 m)	0 ft (0 m)
MTOM	55746 lb (25283 kg)	28.87 ft (8.80 m)	2.33 ft (0.77 m)
MTOM + 5%	58525 lb (26546 kg)	28.87 ft (8.80 m)	2.33 ft (0.77 m)

Table 15.9: Mass breakdown at MTOM



It's important to note that the data presented in the table pertains to the conditions specified by the Primary Mission Profile, i.e. vertical take-off at maximum weight. In the case of conventional take-off, the aircraft center of gravity changes since the rotors are folded, causing their center of gravity to move rearward and closer to the wings. Table 15.10 includes values that differ between the two cases.

	Rotorcraft mode	Jet mode
Rotor group CG X position	8.80 m	9.71 m
Aircraft CG X position	8.80 m	8.90 m
Rotor group CG Z position	2.43 m	0.88 m
Aircraft CG Z position	0.77 m	0.71 m

Table 15.10: CG positions

In figure 15.21 is shown the percentage distribution of masses, which can be compared with the one obtained in the weight estimation in chapter 9, figure 9.4.

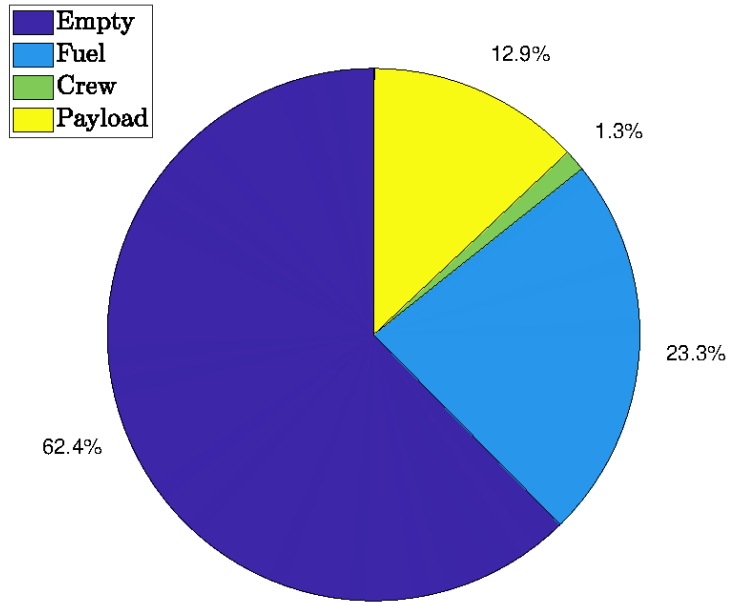


Figure 15.21: Mass breakdown pie chart

15.5. Center of gravity range analysis

In order to study the stability and the controllability of the aircraft, the knowledge of the center of gravity range is of primary importance. During the flight the fuel is consumed

and the CG varies longitudinally, laterally and vertically. Furthermore, the aircraft can be loaded with several mass configurations, each one of which is characterized by a different CG position.

In order to compute the limit positions of the center of gravity the procedure described in [29] has been followed:

- The most aft gravity center of the aircraft can be computed starting from the maximum take-off mass of the aircraft and the corresponding CG position and then removing all removable loads whose gravity center is in front of the one at MTOM. This procedure must be iterated until no removable loads are present in front of it.
- The most forward gravity center of the aircraft can be computed starting from the maximum take-off mass and the corresponding CG. All removable loads with a CG after the MTOM CG must be removed.

In this analysis, it has been taken into account the fact that the aircraft is capable of flying in two different configurations: with open and folded rotors.

15.5.1. Rotorcraft mode

For rotorcraft mode flight, there is a crucial aspect that must be taken into consideration, i.e. the longitudinal position of the rotor axis of rotation must be as close as possible to the center of gravity, in order to have a moment generated by the rotor thrust equal to zero. It is possible to achieve this condition for all flight conditions thanks to the presence of fuel tanks both in the front and rear of the fuselage, along with pumps that move fuel as needed, as illustrated in the Chapter 14.

However, the two extreme positions of the center of gravity have been calculated to analyze the aircraft's stability in the event of pump failure or in conditions where there is not enough fuel on board.

The results obtained are the following:

	CG_{for}	CG_{aft}
Longitudinal position	28.67 ft (8.74 m)	30.74 ft (9.37 m)
Vertical position	2.95 ft (0.90 m)	2.30 ft (0.70 m)

Table 15.11: CG range rotorcraft mode

The center of gravity lateral excursion can be considered null because the payload is



assumed to be distributed uniformly in the cargo bay, that is symmetric with respect to the FCL.

It is convenient to express the aircraft longitudinal CG in terms of percentage MAC:

$$h = \frac{X_{CG} - X_{LE}}{MAC} \quad (15.1)$$

	Absolute position	% MAC
Maximum take-off mass	28.87 ft (8.80 m)	50 %
Most forward	28.67 ft (8.74 m)	48 %
Most aft	30.74 ft (9.37 m)	67 %
Range	1.94 ft (0.59 m)	19 %

Table 15.12: Longitudinal position of CG in rotorcraft mode

15.5.2. Jet mode

Knowledge of the center of gravity range is even more crucial for the jet configuration, as it directly impacts the aircraft's stability. In this case as well, the center of gravity position is adjustable thanks to the fuel system pumps, so barring any failures, the center of gravity will not reach the extreme positions. Thus, by adjusting the center of gravity within the calculated range, it is possible to adapt the stability and controllability to the specific flight phases.

The results obtained are the following:

	CG _{for}	CG _{aft}
Longitudinal position	28.71 ft (8.75 m)	30.87 ft (9.41 m)
Vertical position	2.76 ft (0.84 m)	1.77 ft (0.54 m)

Table 15.13: CG range jet mode

	Absolute position	% MAC
Maximum take-off mass	27.72 ft (8.90 m)	53 %
Most forward	27.62 ft (8.75 m)	48 %
Most aft	30.45 ft (9.41 m)	68 %
Range	2.82 ft (0.64 m)	20 %

Table 15.14: Longitudinal position of CG in jet mode

The relationship between these results and the aircraft's stability and controllability will be analyzed in more detail in Chapter 19.

15.5.3. CG variation during Primary Mission

A more detailed analysis of the longitudinal position of the CG for each phase of flight has been done for the Primary Mission, and it is illustrated in Figure 15.22.

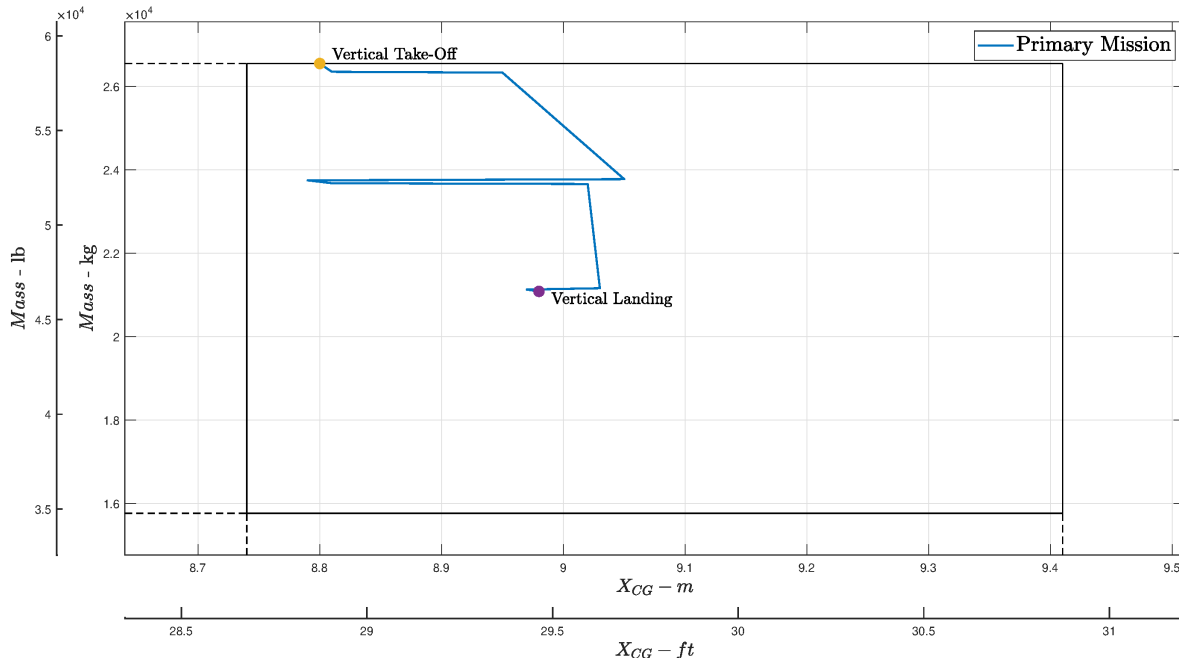


Figure 15.22: CG envelope

Figure 15.22 illustrates how, during the Primary Mission, thanks to the fuel system pumps, the aircraft's center of gravity remains in the front part of the envelope.



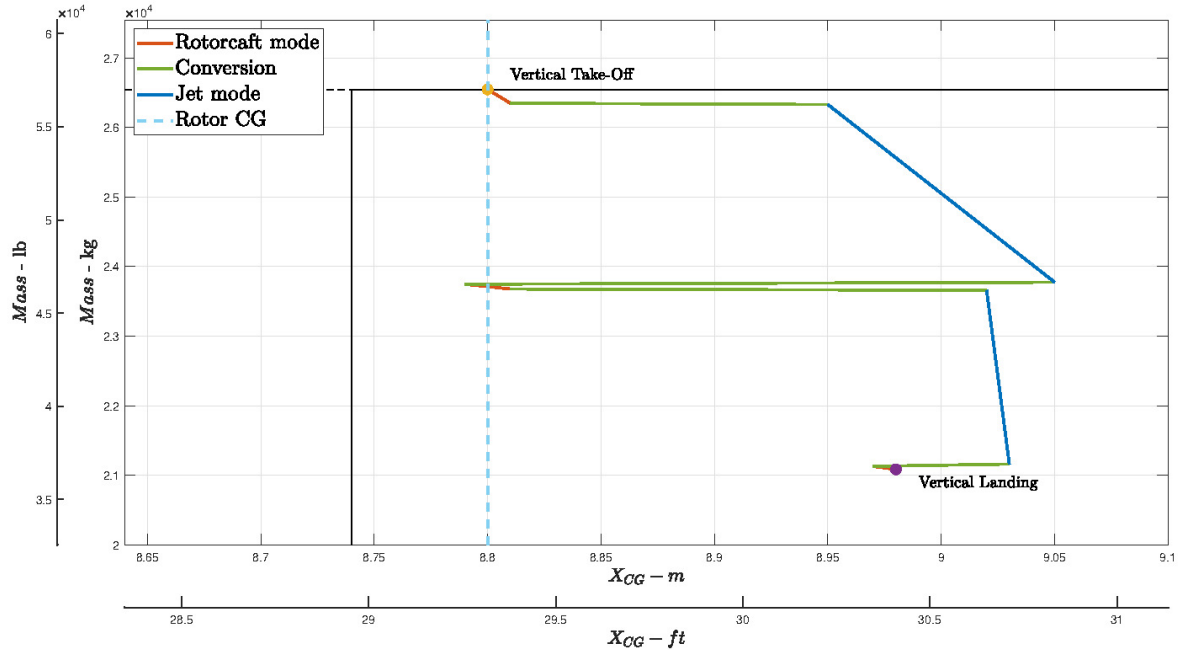


Figure 15.23: Longitudinal CG position travel during Primary Mission

During the phases in which the aircraft flies in jet configuration, it is always possible to decide the longitudinal position of the center of gravity. However, in the helicopter configuration, maintaining the center of gravity in the desired position is only possible if there is enough fuel. As can be seen in Figure 15.23, in the final hover phase of the mission, the center of gravity is 0.18 m rearward from the rotor axis. In the stability chapter, it will be shown how this remains an acceptable condition for the aircraft's flight, as it can still be trimmed.

Therefore, the minimum fuel weight necessary to obtain $X_{CG} = 8.80$ m has been computed. The center of gravity longitudinal position has been calculated for 5 different configuration with different fuel distribution, represented in Figure 15.24, where Tank 1 is the most forward fuselage tank.

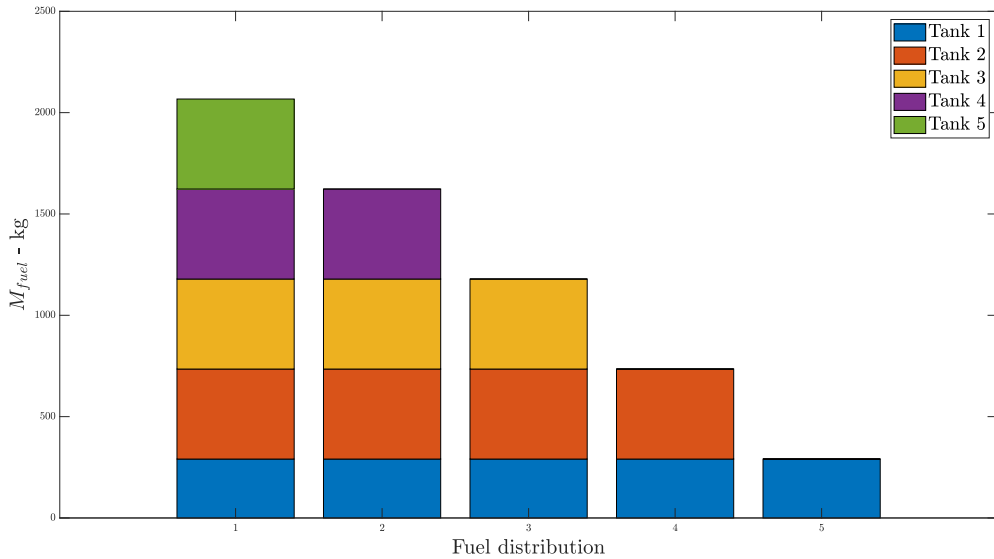


Figure 15.24: Fuel distribution in the forward tanks

In Figure 15.25 can be seen that the quantity of fuel sufficient to decide the longitudinal position of the CG is around 1600 kg.

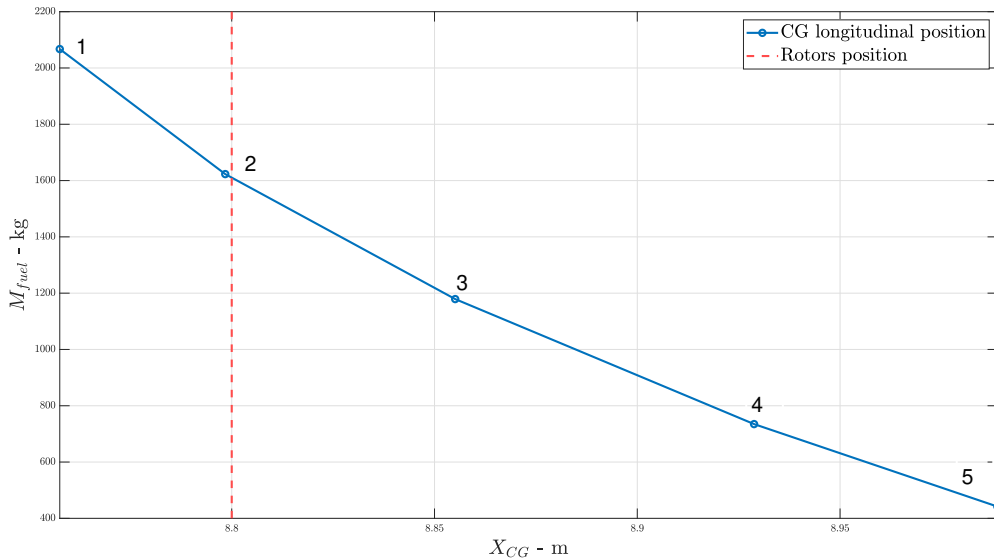


Figure 15.25: Caption

So, with slightly less than 4 full front tanks, there isn't enough fuel to maintain the center of gravity in the desired position.



15.5.4. CG location and landing gear

The final analysis to be conducted regarding the center of gravity concerns its relationship with the landing gear position. Indeed, for the aircraft to be stable on the ground and land safely, the center of gravity must always remain within the triangle formed by the ground contact points of the aircraft.

From Chapter 13, the main landing gear and the nose landing gear are respectively at 9.5 m and 2 m from the nose of the fuselage. Therefore, the center of gravity, whose range is [8.74 m - 9.41 m], is always within the required area.

16 | Controls

The Raven 4 concept offers huge operational advantages and flexibility; however the flight system capable of controlling an aircraft capable of conventional flight and helicopter like Vertical Take-Off and Landing (VTOL) and mastering the transitions between these modes necessitates a complex flight control system.

It should also be noted that, as mentioned in previous chapters, the Raven 4 concept is designed so that all jet mode phases can be performed with the flaperons used only as ailerons.

16.1. Jet-mode

The conventional flight modes depicted in Table 16.1 are controlled as follows:

- *Pitch*: Forward movement of the control stick causes the aircraft to pitch nose-down due to the operation of the elevators; altitude decrease and airspeed increases. Aft movement of the control stick causes the aircraft to pitch nose-up, altitude increases and airspeed decreases.
- *Roll*: Lateral movement of the control stick causes the aircraft to roll using the flaperons as ailerons. If rolling left, the left flaperon deflect up while right flaperon deflect down and the aircraft rolls left.
- *Yaw*: Movement of the rudder pedals cause the aircraft to yaw using the twin rudders in a conventional aircraft sense.
- *Thrust*: Operation of the throttle lever alters engine thrust.

Pitch			Ruddervator
Roll			Flaperons
Yaw			Ruddervator
Thrust			Throttle

Table 16.1: Aircraft flight control system modes

The aircraft control surfaces were sized following the guidelines presented by the Reference [29]. In the following calculations, the reference system adopted will always be the body-fixed coordinate system, and the sign convention used is shown in the Figure 16.1. Due to other constraints, such as vertical take-off and V-tail, the solution followed by the Team was to exploit a non-conventional configuration, i.e., ruddervator for the V-tail and flaperon for the outboard part of the wing, in order to reduce the download.

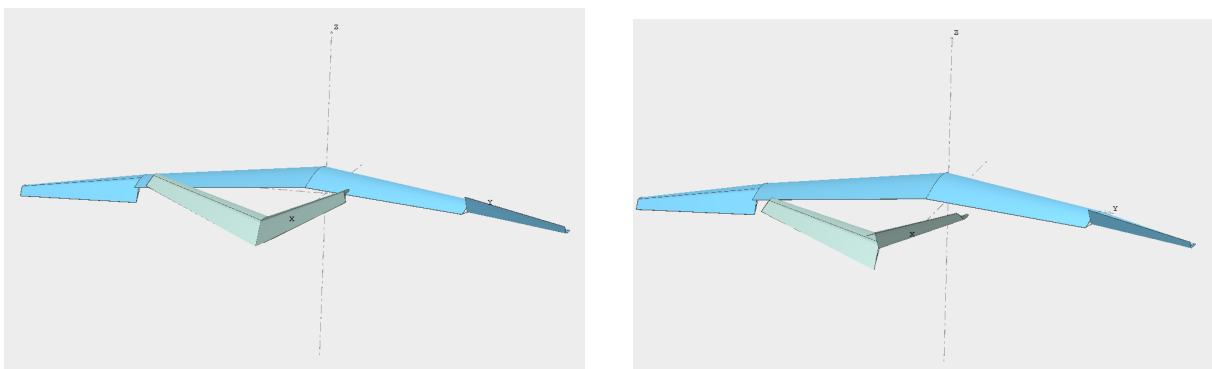


Figure 16.1: Positive sign convention for primary airplane controls (back view of the aircraft)



The control surfaces must be designed such that aircraft possess acceptable flying and handling qualities during the operational flight envelope, with allowable center of gravity range and aircraft weight. So, for these analysis are important both the inertia parameters from Chapter 15 and the handling qualities specifications from MIL-STD-1797.

For the purpose of handling qualities, Raven 4 is a Class II aircraft (MTOW between 13000 and 66000 lbf), with a level of acceptability equal to 1 (or pilot comfort between 1 and 3, on a scale of 1 to 10). In addition, specifications were considered for both phase B missions (e.g., conversion to airplane mode, climb, cruise and penetration), phase C missions (i.e., takeoff and landing), and phase A mission (i.e., in-flight refuelling).

16.1.1. Aileron design

A flaperon configuration was implemented only to ensure less download during hover phases, but the aircraft is able to perform all flight phases by exploiting only the internal flap (see Section 11.4). Thus, in the aileron design the location, chord and surface area are already defined, while $\pm 25^\circ$ was chosen as the maximum control excursion.

For a class II aircraft (Level 1) MIL-STD regulations requires 1.4 s (1.9 s for Level 2) to achieve a bank angle of 45° during a phase A mission, 1.8 s to achieve a bank angle of 45° during a phase B mission, or 1.9 s to achieve a bank angle of 30° during a phase C mission in low airspeed flight conditions.

The procedure proposed by Reference [29] is based on the computation of aircraft rate of roll rate produced by the aileron rolling moment until the aircraft reaches the steady-state roll rate, so that afterwards, through an integration, it's possible to derive the bank angle and the corresponding time to reach this angle. The results are displayed graphically in Figures 16.2 and 16.3, and it can be seen that aircraft reaches the military requirements in both phase B and phase C mission category, while during a phase A mission (i.e., in-flight refueling at 120% of the stall airspeed in clean configuration) is guaranteed only a Level 2 capability.

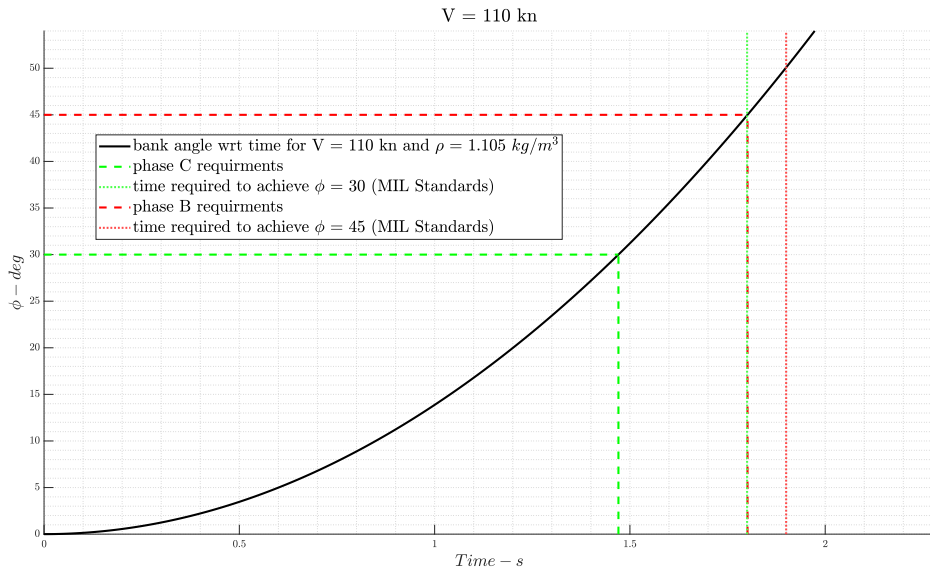


Figure 16.2: Aileron performance for phase B and C

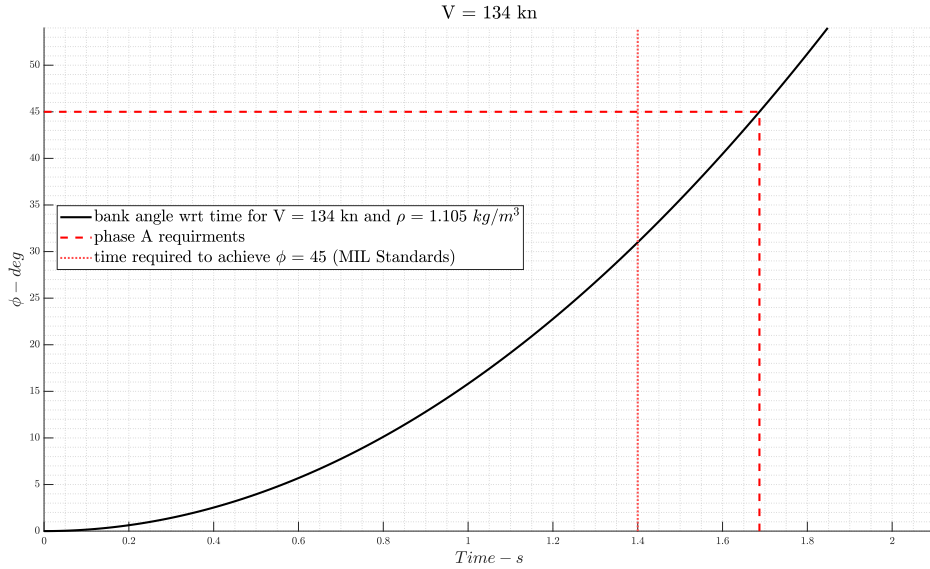


Figure 16.3: Aileron performance for phase A

This result is expected, and it is mainly due to the presence of the two heavy turboshafts in the middle of the wing. Thus, to improve controllability the simplest way is to design a flaperon also for the inner wing, without radically changing the structural characteristics. Figures 16.4 and 16.5 show the results for a flaperon all over the wing. It can be observed that the Level 1 requirement for a Phase A mission can also be met, remembering however



that in all phases of flight, except the in-flight refueling, Raven 4 would be Level 1 even with flaperons in the outer wing only.

As a future development, a more in-depth analysis could be performed on the actual usefulness of in-flight refueling for Raven 4, and if so, consideration could be given to moving the turboshafts into the fuselage; however, this modification would affect the structural analysis of the aircraft.

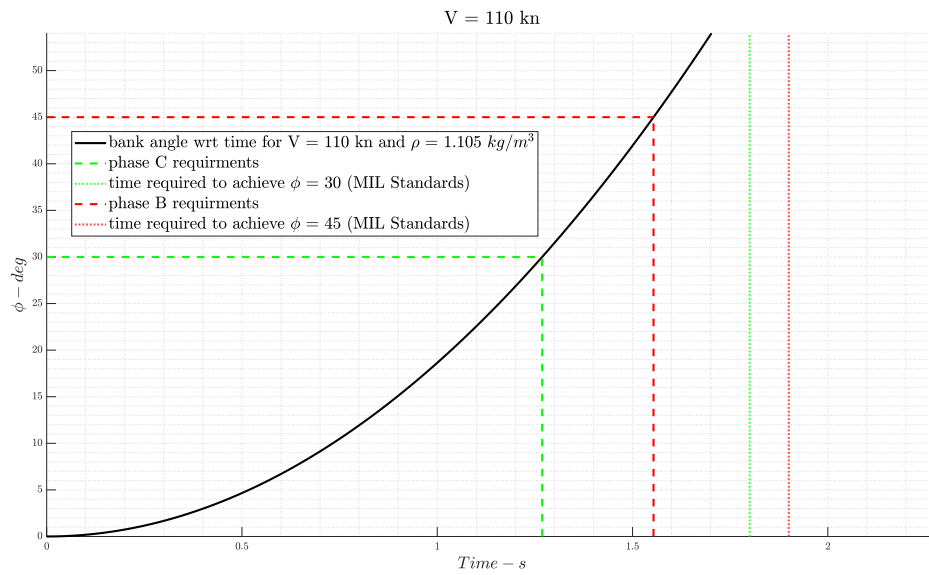


Figure 16.4: Aileron performance for phase B and C

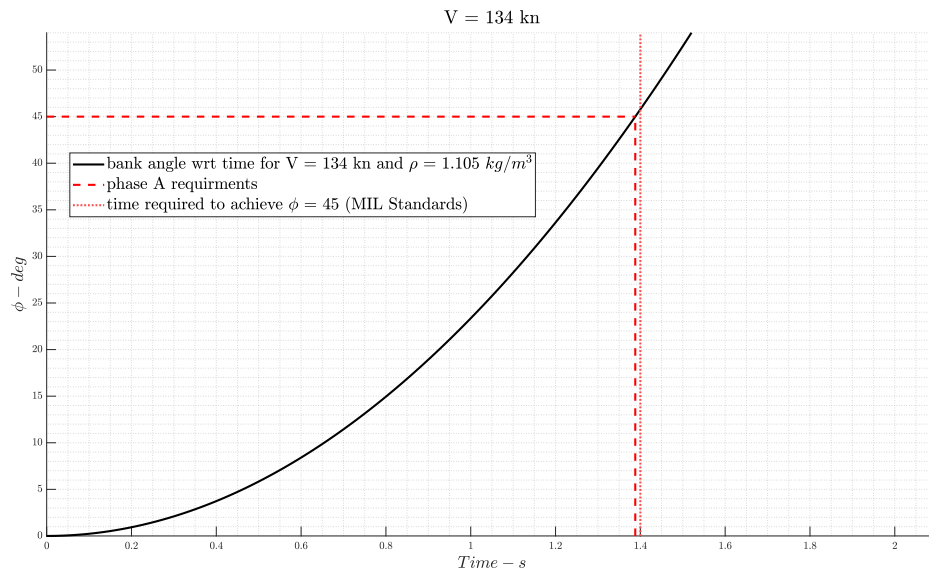


Figure 16.5: Aileron performance for phase A

In Tables 16.2 and 16.3 are presented the final geometric parameters of the aileron.

Location	C_a/C_{wing}	S_a	b_a	$\pm\delta_a$
Outboard wing	0.4	71.0 ft^2 (6.6 m^2)	13.1 ft (4.0 m)	$\pm 25^\circ$

Table 16.2: Outboard aileron parameters

Location	C_a/C_{wing}	S_a	b_a	$\pm\delta_a$
Inboard wing	0.4	120.1 ft^2 (11.2 m^2)	22.0 ft (6.7 m)	$\pm 25^\circ$

Table 16.3: Inboard aileron parameters

16.1.2. Rudder design

Note that for elevator and rudder all calculations were scaled to the horizontal or vertical projection of the V-tail, maintaining the same philosophy of Roskam, who treats V-tails as projected surfaces.

Since aircraft has only one engine, the worst condition is the cross-wind landing. From Reference [29] a class II aircraft must be able to be piloted during takeoff and landing in a 90-deg crosswind of at least 30 kn.

Through trial and error it was found that it is required a 30% of the tail and a maximum rudder deflection of $\pm 30^\circ$ to ensure this condition.

The results are displayed graphically in Figure 16.6, where it can be seen that the rudder is powerful enough to trim the airplane in a cross-wind of 31.5 kn at an airspeed of 110 kn. In Table 16.4 are presented main rudder parameters.



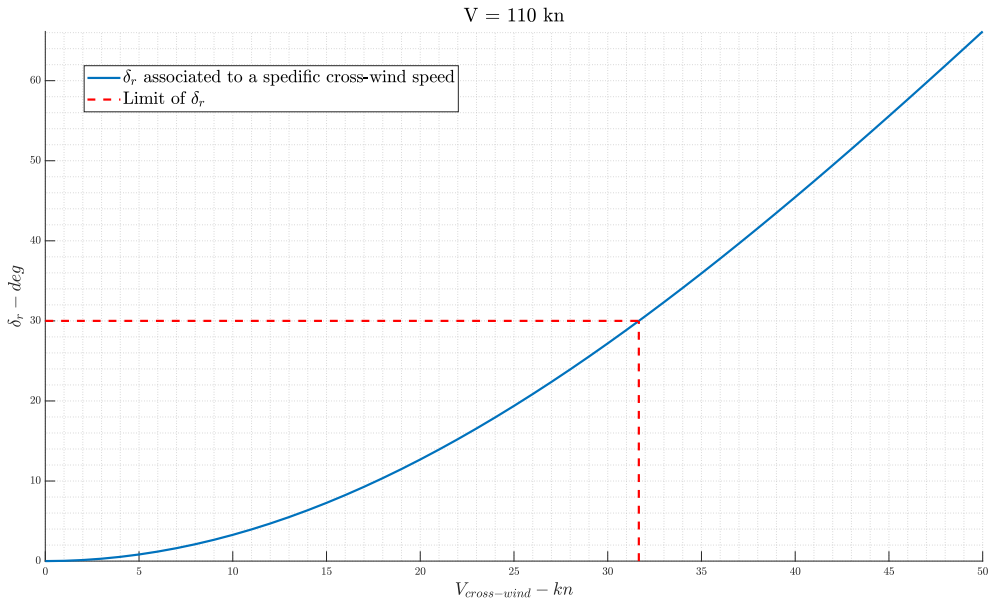


Figure 16.6: Rudder performance

C_r/C_{wing}	$S_r^{projected}$	$b_r^{projected}$	$\pm\delta_r$	Maximum Cross-wind
0.3	32.3 ft^2 (3.0 m^2)	15.0 ft (4.6 m)	$\pm 30^\circ$	31.5 kn (16.2 m/s)

Table 16.4: Rudder parameters

16.1.3. Elevator design

To design the elevator, a simple system of two equations (16.1) must be solved to prove that the aircraft can perform take-off with a certain minimum pitch angular acceleration ($\ddot{\theta}$).

$$\begin{aligned} \sum F_z &= 0 \\ \sum M_{y_{lg}} &= I_{yy} \ddot{\theta} \end{aligned} \tag{16.1}$$

So the conditions considered to size the elevator during the take-off are the most critical one: MTOW, center of gravity in forward longitudinal position, sea level, and rotational speed of 110 kn. In addition, Reference [29] states that an acceptable take-off acceleration for small transport aircraft is between 6 and 8 deg/s^2 , so the Team opted to size the horizontal control to ensure $\ddot{\theta} = 8 deg/s^2$.

It was also observed that parameters that most influence the elevator design are the longitudinal position of the landing gear relative to the center of gravity and the vertical

position of the jet engine.

Due to the V-tailed configuration, rudder and elevator are geometrically constrained. Thus, the idea is to verify that the elevator may guarantee $\ddot{\theta} = 8 \text{ deg}/\text{s}^2$ for a maximum (negative) elevator deflection of -30° starting from the values defined in the Table 16.4.

From the analyses, it was observed that -29.03° of deflection would be necessary to achieve $\ddot{\theta} = 8 \text{ deg}/\text{s}^2$; therefore, the ruddervator can guarantee both cross-wind and take-off requirements.

In Table 16.5 are presented main elevator parameters.

C_e/C_{wing}	$S_e^{projected}$	$b_e^{projected}$	$\min(\delta_e)$
0.3	$61.8 \text{ ft}^2 (5.7 \text{ m}^2)$	28.7 ft (8.7 m)	-30°

Table 16.5: Elevator parameters

16.2. Rotorcraft-mode

The manner in which the actions of the main rotors are combined to produce the required control moments and forces depends on the helicopter configuration.

In the side-by-side configuration chosen, control is as for the tandem helicopter configuration, but with the pitch and roll axes reversed.

To ensure the necessary forces and moments for rotorcraft mode, the following commands can be applied to the two rotors:

- *Torque balance*: since the two rotors rotate counter-rotating with respect to each other, the torque balance it is obtained by the two main rotor differential torque.
- *Pitch moment*: to guarantee longitudinal control, the pitch control is achieved by a symmetric variation on longitudinal cyclic pitch on both of the rotors.
- *Roll moment*: to guarantee lateral control, the roll moment is achieved by differential change of the main rotor thrust magnitude by differential collective pitch.
- *Yaw moment*: to guarantee directional control, the yaw control is achieved by differential cyclic on the rotors.
- *Vertical force*: it is obtained by the rotor collective to guarantee height control.



Similarly, we can explore the potential maneuvers achievable by leveraging the ability to act on both rotors through the cyclic and collective controls:

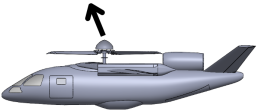
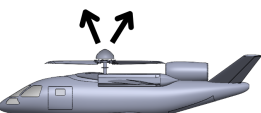
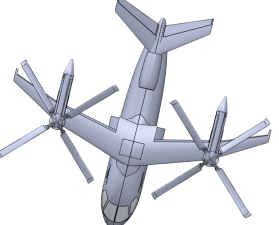
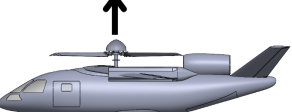
Pitch			Cyclic
Roll			Differential collective
Lateral			Cyclic
Yaw			Differential cyclic
Thrust			Collective

Table 16.6: VTOL flight control system modes

16.3. Conversion phase

In exemplifying how the controls are handled in both the jet and rotorcraft modes, appropriate insight must be made into how these two different worlds can interface with each other.

In the cockpit the controls present on which the pilot can act are:

- Stick bar
- Pedalboard
- Collective
- Jet throttle.

For such an aircraft, the pilot's workload may be too excessive without the necessary safety measures. For this reason, the pilot will never have control of all 4 controls at the same time also due to a human physiognomy problem so that control of all 4 simultaneously would be impossible. So, in rotorcraft-mode the pilot will have control of the stick bar, pedalboard and collective. On the other hand in jet-mode the pilot will have control of the stick bar, pedalboard and jet throttle.

It is therefore necessary to bring the development of a flight control system that in rotorcraft-mode in autonomy, depending on the airspeed and attitude of the aircraft, requires more or less power from the jet engine so that the pilot can control the aircraft like a helicopter but keeping guaranteed a correct and efficient distribution of forces and aerodynamic moments of the mechanics of flight. In fact, by doing so the attitude of the aircraft would be able to remain approximately edgewise since part of the longitudinal thrust would be provided by the jet engine instead by the rotors. For further details refer to chapter 19, rotorcraft sections.

At the time of the actual conversion from one configuration to another, the pilot would instead play only a supervisory role. In fact, because of its complexity related to attitude, speed, available thrust of the rotors and jet, would require too much load on the pilot. The aircraft would then switch from rotorcraft-mode to jet-mode and vice versa automatically as shown in Figure 16.8.

		<i>Rotorcraft mode</i>	<i>Jet mode</i>	<i>Conversion phase</i>
Raven 4 controls	Stick bar			Automated procedures: autopilot properly sets the jet thrust and trim the aircraft while the rotors slow down
	Pedalboard			
	Collective		Deactivate	
	Jet Throttle	Autothrottle		

Figure 16.7: Controls during all configurations



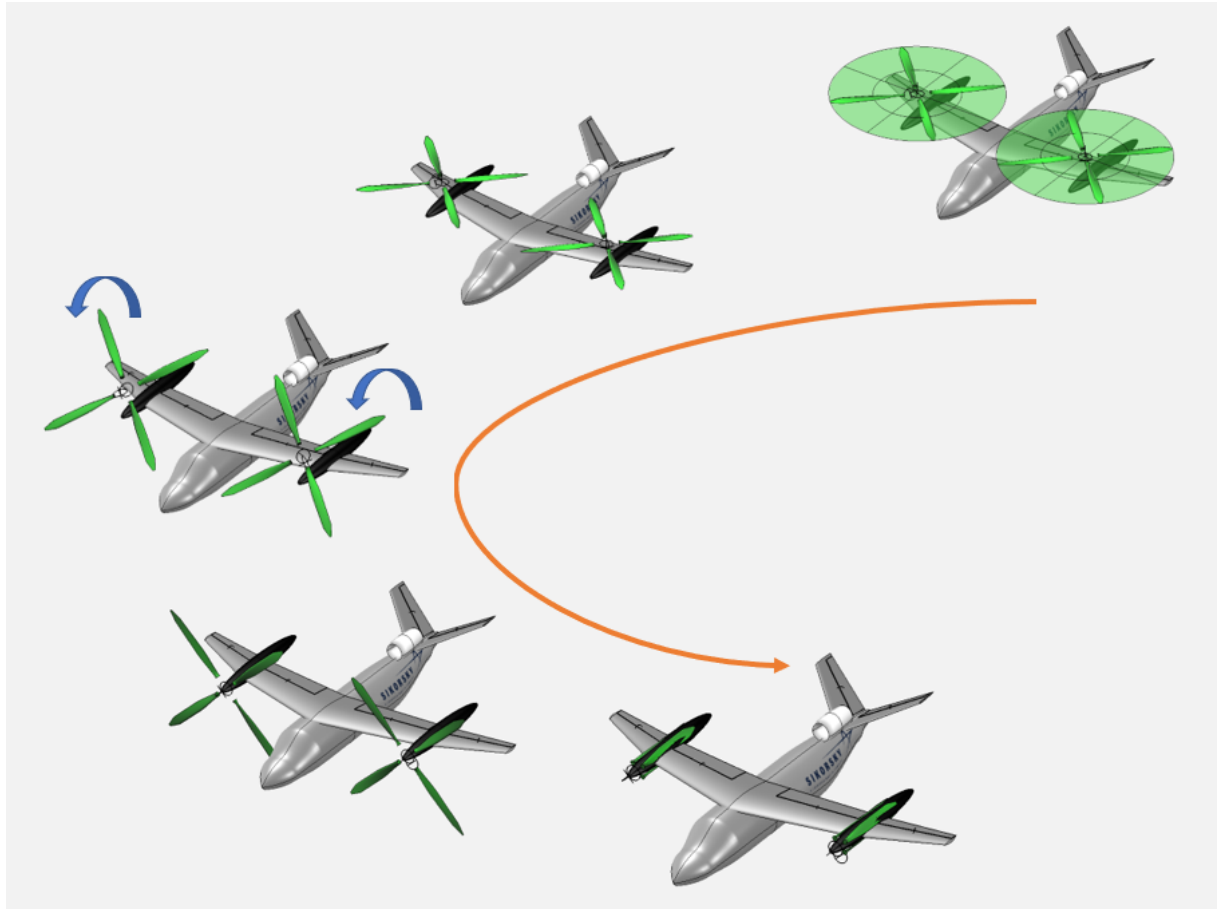


Figure 16.8: Conversion phase

Therefore, it must be emphasized that between before and after the conversion, the controls on which the pilot is going to act will have a different effect: for example, acting on the stick bar in the forward direction will no longer act on the swashplate but rather will act on the ruddervator.

17 | Aerodynamic characteristics

17.1. Drag build-up approach

For the preliminary design, Reference [26] describes two methods to estimate the aerodynamic polar of the aircraft:

1. Class I method, in which we start from some generic parameters (such as the aspect ratio, wing span, reference wing surface, ...) to derive the zero-lift drag coefficient (C_{d_0}) and the Oswald efficiency number (e) by historical-statistical analysis.
2. Class II method, in which all components of the aircraft, whose geometric parameters have been well defined in previous chapters, are analyzed separately.

A class I method has already been described in Chapter 9, whereas, the aim of this chapter is to present the class II method to estimate the aerodynamic polar of the whole aircraft. The main components considered in the total drag estimation are:

$$C_D = C_{D_{wing}} + C_{D_{fuselage}} + C_{D_{jet \ engine}} + C_{D_{rotors \ nacelles}} + C_{D_{V-tail}} + \dots \quad (17.1)$$

$$\dots + C_{D_{trim}} + C_{D_{landing \ gear}} + C_{D_{flap}} + C_{D_{rotors \ hub}}$$

In addition, boundary layer is considered mostly laminar on the wing thanks to the natural laminar flow airfoils selected. While, regarding roughness, considering the surfaces covered by "camouflage paint applied in the factory" as the worst case, it is observed that the cut-off Reynolds number is bigger than the actual Reynolds number, thus the effect of roughness may be neglected.

Given the fact that the airplane have to reach at least 450 kn at 20,000 ft (i.e., Mach number of 0.73), the transonic regime is considered during the following analysis.

The goal is to obtain a drag polar that can be expressed as the sum of a parasite contribution (due to skin-friction, pressure, waves, and so on) and an induced contribution due

to lift. Hence, the drag of the aircraft may be written as:

$$C_D = C_{D_0} + C_{D_{induced}} = C_{D_0} + \frac{1}{\pi AR e} (C_L - C_{L_{min}})^2 \quad (17.2)$$

Where C_{D_0} is the parasite drag coefficient, e is the Oswald's factor, and $C_{L_{min}}$ is the lift coefficient of minimum drag because drag is not minimum at zero lift.

17.1.1. Drag due to the wing

Drag coefficient of the wing may be defined from equation 17.3.

$$C_{D_{wing}} = C_{D_0}^{wing} + C_{D_L}^{wing} \quad (17.3)$$

Where $C_{D_L}^{wing}$ is the drag coefficient due to lift, while $C_{D_0}^{wing}$ the wing zero-lift drag coefficient, composed by the sum of drag coefficient due to friction ($C_{D_{0M=0.6}}^{wing}$) and wing wave drag coefficient ($C_{D_{wave}}^{wing}$).

Wing drag coefficient due to friction

This coefficient is assumed to stay constant with Mach number in the entire transonic speed range, so may be found from the following equation:

$$\begin{aligned} C_{D_{0M=0.6}}^{wing} = & R_{wf} R_{LS} (1 + L' (t/c) + 100(t/c)^4) [(C_{flaminar}^{wing} - C_{fturbulent}^{wing}) S_{wetlaminar}^{wing} + \dots \\ & \dots + C_{fturbulent}^{wing} S_{wet}^{wing}] / S_{ref} = 0.00172 \end{aligned}$$

In Table 17.1 are presented all useful data and results to compute this coefficient.



Parameter	Description and definition	Value
S_{ref}	Wing reference area	777.15 ft^2 (72.2 m^2)
S_{wet}^{wing}	Wetted area of the exposed wing	1254.0 ft^2 (116.50 m^2)
$S_{wet_{laminar}}^{wing}$	Wetted area of the laminar wing	996.65 ft^2 (92.59 m^2)
MGC	Mean geometric chord of the exposed wing	9.58 ft (2.92 m)
$MGC_{laminar}$	Laminar part of the mean geometric chord	7.18 ft (2.19 m)
t/c	Thickness ratio defined at the MGC	0.12
L'	Factor related to location of maximum airfoil thickness	1.2
$\Lambda_{(t/c)_{max}}$	Sweep angle at $(t/c)_{max} = 0.5 c$	14°
$l_{fuselage}$	Length of the fuselage	65.62 ft (20 m)
V	Steady state airspeed	450 kn (231.5 m/s)
Re	Reynolds number of the wing, $\frac{V \cdot MGC}{\nu}$	2.8 e+7
$Re_{laminar}$	Reynolds number of the laminar wing, $\frac{V \cdot MGC_{laminar}}{\nu}$	2.1 e+7
$Re_{fuselage}$	Reynolds number of the fuselage, $\frac{V \cdot l_{fuselage}}{\nu}$	1.9 e+8
R_{wf}	Wing - fuselage interference factor, related with $Re_{fuselage}$	1.02
R_{LS}	Lifting surface correction factor, related with $\Lambda_{(t/c)_{max}}$	1.22
$c_{f_{turbulent}}^{wing}$	Turbulent flat plate friction coefficient, related with Re	0.00245
$c_{f_{laminar}}^{wing}$	Laminar flat plate friction coefficient, $1.328/(Re_{laminar})^{0.5}$	0.00029

Table 17.1: Parameters for wing zero-lift friction drag

Wing wave drag coefficient

This coefficient depends on the wing sweep angle and the mach number. The idea is find the value of wave drag coefficient for an unswept wing from Reference [26] and then add a correction due to the sweep angle of the wing. So, the final solution can be found graphically from figure 17.1:

$$C_{D_{wave}}^{wing} = 0.0039$$

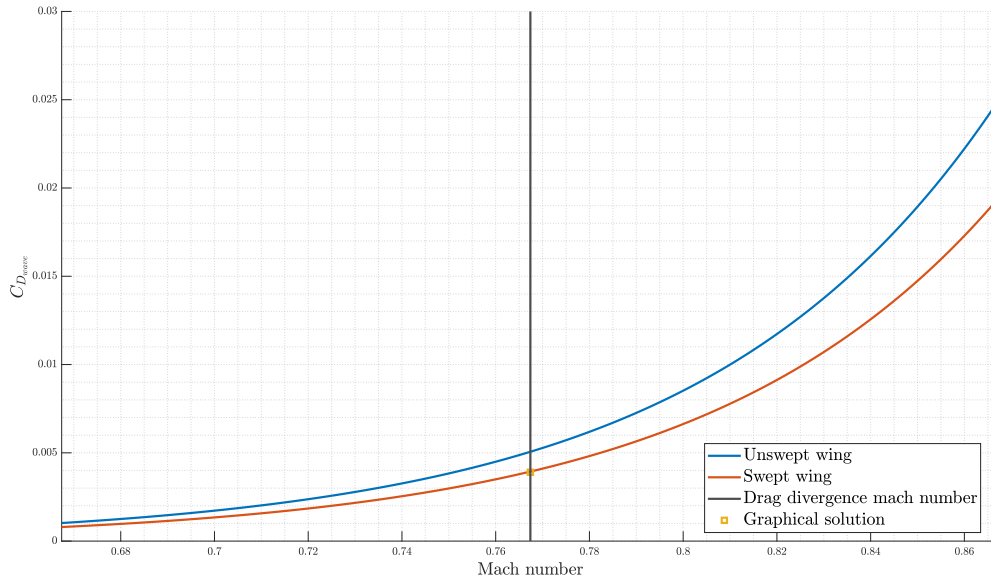


Figure 17.1: Graphical solution of wing wave drag coefficient

Hence, the complete wing zero-lift drag coefficient is $C_{D_0}^{\text{wing}} = C_{D_0M=0.6}^{\text{wing}} + C_{D_{wave}}^{\text{wing}} = 0.00562$

Wing drag coefficient due to lift

$$C_{D_L}^{\text{wing}} = (C_D/C_L^2) C_L^2 \quad (17.4)$$

Where the parameter (C_D/C_L^2) can be found graphically from Reference [26], knowing the aspect ratio, sweep angle at leading edge, steady state mach number, taper ratio, and thickness ratio.

Parameter	Description and definition	Value
Λ_{LE}	Sweep angle at leading edge	18.4°
λ	Global taper ratio of the wing	0.3
M	Mach number in cruise	0.73
AR	Aspect ratio of the wing	8.6
(C_D/C_L^2)	Slope of $C_{D_L}^{\text{wing}}$	0.011

Table 17.2: Parameters for wing drag coefficient due to lift



17.1.2. Drag due to the fuselage

Drag coefficient of the fuselage may be defined from equation 17.5.

$$C_{D_{fuselage}} = C_{D_0}^{fuselage} + C_{D_L}^{fuselage} \quad (17.5)$$

$$\text{With } C_{D_0}^{fuselage} = R_{wf} (C_{D_{friction}}^{fuselage} + C_{D_{pressure}}^{fuselage}) + C_{D_{base}}^{fuselage} + C_{D_{wave}}^{fuselage} \frac{S_{fuselage}}{S_{ref}}$$

In particular, $R_{wf} = 1.02$ is the wing/fuselage interference factor (already defined in table 17.1), $C_{D_{friction}}^{fuselage}$ is the fuselage skin-friction drag coefficient at $M = 0.6$ which is assumed to stay constant in the entire transonic range, $C_{D_{pressure}}^{fuselage}$ is the fuselage pressure drag coefficient which stay constant from $M = 0.6$ to $M = 1.0$, $C_{D_{base}}^{fuselage}$ is the fuselage base drag coefficient, and $C_{D_{wave}}^{fuselage}$ is the fuselage wave drag coefficient.

Figure 17.2 illustrates the build-up of the fuselage zero-lift drag coefficient.

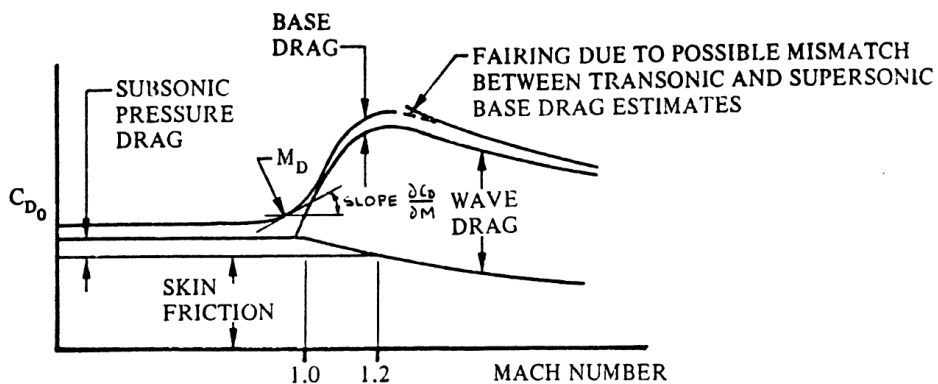


Figure 17.2: Build-up of transonic fuselage zero-lift drag coefficient from reference [26]

Fuselage skin-friction drag coefficient at $M = 0.6$

$$C_{D_{friction}}^{fuselage} = C_f^{fuselage} \frac{S_{wet}^{fuselage}}{S_{ref}} = 0.00459 \quad (17.6)$$

With: $C_f^{fuselage} = 0.0018$ and $S_{wet}^{fuselage} = 1,986 \text{ ft}^2$

Fuselage pressure drag coefficient

$$C_{D_{pressure}}^{fuselage} = (60/(l_f/d_f)^3 + 0.0025(l_f/d_f)) C_f^{fuselage} \frac{S_{wet}^{fuselage}}{S_{ref}} = 0.00110 \quad (17.7)$$

Fuselage base drag coefficient

The idea is to compute the base drag coefficient at $M = 0.6$ from equation 17.8 and then correct the solution exploiting plots from Reference [26]. However, due to the fact that the fuselage has no base (i.e., $d_{base} = 0.656\text{ ft} \cong 0$), this coefficient may be neglected.

$$C_{D_{base \text{ at } M=0.6}}^{fuselage} = \left[0.0029(d_{base}/d_f)^3 / \sqrt[2]{C_{D_0 \text{ fus-base}}(S_{ref}/S_{fus})} \right] \frac{S_{fus}}{S_{ref}} = 3.45e-6 \quad (17.8)$$

Fuselage wave drag coefficient

Wave drag coefficient is associated to mach number, but the projected speeds for the aircraft are well below $M = 1.0$, so also this coefficient may be neglected.

Hence, the fuselage zero-lift drag coefficient is: $C_{D_0}^{fuselage} = 0.0058$

Fuselage drag coefficient due to lift

Transonic fuselage drag coefficient due to lift is defined by equation 17.9.

$$C_{D_L}^{fuselage} = \alpha^2 \frac{S_{base}^{fuselage}}{S_{ref}} \quad (17.9)$$

Where $S_{base}^{fuselage}$ is the fuselage base area, and aircraft angle of attack can be estimated as
 $\alpha = \frac{W/(q S_{ref}) - C_{L_0}}{C_{L_\alpha}}$

Parameter	Description and definition	Value
d_{base}	Diameter of the base	0.656 ft (0.200 m)
$S_{base}^{fuselage}$	Fuselage base area, $\pi/4 d_{base}^2$	0.3380 ft^2 (0.0314 m^2)
C_{L_0}	Aircraft zero angle of attack lift coefficient	0.2

Table 17.3: Parameters for fuselage drag coefficient due to lift

17.1.3. Drag due to the jet engine

Jet engine is considered as a nacelle, so its drag is predicted from equation 17.10.

$$C_{D_{jet \text{ engine}}} = (C_{D_0}^{jet \text{ engine}} + C_{D_L}^{jet \text{ engine}}) + C_{D_{pylon}} + C_{D_{interference}}^{jet \text{ engine}} \quad (17.10)$$

Where, $(C_{D_0}^{jet \text{ engine}} + C_{D_L}^{jet \text{ engine}})$ are respectively the parasite and the induced drag of the jet engine isolated, $C_{D_{pylon}}$ is the drag coefficient related to the pylon of the engine, and $C_{D_{interference}}^{jet \text{ engine}}$ is associated to the interference between the jet engine and the fuselage.



However, jet engine is located overhead the aft fuselage with no pylon (tangent to the fuselage), so $C_{D_{pylon}} = 0$ and the induced drag may be neglected, $C_{D_L}^{jet\ engine} = 0$.

Isolated jet engine parasite drag coefficient (zero lift)

From Reference [26] the isolated engine can be seen as a small fuselage, so this coefficient is calculated as:

$$\begin{aligned} C_{D_0}^{jet\ engine} &= R_{wf}^{engine} c_f^{engine} \left(1 + \frac{60}{(l_{engine}/d_{engine})^3} + 0.0025 l_{engine}/d_{engine} \right) \frac{S_{wet}^{engine}}{S_{ref}} + \dots \\ &\dots + C_{D_{base}} + C_{D_{wave}} * S_{engine}/S_{ref} = 0.0030 \end{aligned} \quad (17.11)$$

Where S_{ref} is the reference surface, i.e. the wing surface.

Parameter	Description and definition	Value
d_{engine}	Diameter of jet engine	4.20 ft (1.28 m)
d_{inlet}	Diameter of the inlet	3.87 ft (1.18 m)
d_{nozzle}	Diameter of the nozzle	3.22 ft (0.98 m)
l_{engine}	Length of jet engine	8.37 ft (2.55 m)
S_{engine}	Maximum frontal area of the engine, $\frac{\pi}{4} d_{engine}^2$	13.85 ft^2 (1.29 m^2)
S_{wet}^{engine}	Wetted area of the engine, $\pi d_{engine} l_{engine}$	110.37 ft^2 (10.50 m^2)
Re_{engine}	Reynolds number of the jet engine, $\frac{V l_{engine}}{\nu}$	2.4 e+7
R_{wf}^{engine}	Jet engine - fuselage interference factor, related with Re_{engine}	1.01
c_f^{engine}	Skin friction coefficient of the jet engine, related with Re_{engine}	0.0024
$C_{D_{base}}$	Jet engine base-drag coefficient, from reference [26]	5.69 e-5
$C_{D_{wave}}$	Jet engine wave-drag coefficient, related with the Mach number	0

Table 17.4: Parameters for jet engine parasite (zero-lift) drag

Jet engine drag coefficient due to the interference with the fuselage

$$C_{D_{interference}}^{jet\ engine} = F_a (C'_{D_{engine}} - 0.05) \frac{S_{engine}}{S_{ref}} = 0.0013 \quad (17.12)$$

Parameter	Description and definition	Value
F_a	Parameter related to local area ruling	1
$C'_{D_{engine}}$	Parameter related to engine location	0.125

Table 17.5: Parameters for the jet engine-fuselage interference drag

Jet engine drag coefficient due to windmilling (only in case of failure)

In case of a failure that would stop the jet engine, the effect of windmilling must also be considered in the estimation of jet engine drag coefficient. So, the drag coefficient due to windmilling may be computed from equation 17.1.3:

$$C_{D_{windmilling}}^{jet \ engine} = 0.0785 \frac{d_{inlet}^2}{S_{ref}} + \frac{2}{1 + 0.16 * M^2} V_{noz}/V (1 - V_{noz}/V) \frac{S_{nozzle}}{S_{ref}} = 0.0062 \quad (17.13)$$

Parameter	Description and definition	Value
M	Mach in cruise (at 450 kn and 20000 ft)	0.73
V_{noz}/V	Ratio of flow velocity in the nozzle to the steady flight speed	0.42
S_{nozzle}	Nozzle cross section area, $\pi/4 d_{nozzle}$	8.12 ft^2 (0.75 m^2)

Table 17.6: Parameters for jet engine drag due to the windmilling

Hence, the final result is $C_{D_{jet \ engine}} = 0.0051$ without considering the windmilling, while in the case inoperative jet engine, drag coefficient is $C_{D_{jet \ engine}}^{inoperative} = 0.0113$

17.1.4. Drag due to the nacelles on the wing

Similarly to the jet engine, nacelles containing turboshaft engines and folded blades are considered as small fuselages inside the wing, so their contribution to the aircraft drag is predicted from equation 17.14.

$$C_{D_{nacelles}} = n_{nacelle} (C_{D_0}^{nacelle} + C_{D_L}^{nacelle} + C_{D_{interference}}^{nacelle}) * K_{blade} \quad (17.14)$$

Where, $n_{nacelle} = 2$ is the number of the nacelle and $K_{blade} = 1.2$ is a correction factor is a correction factor to account for the presence of fold blades along the nacelle; $C_{D_0}^{nacelle}$ and $C_{D_L}^{nacelle}$ are calculated with the same procedure of subsection 17.1.2.



Nacelle parasite drag coefficient (zero lift)

$$\begin{aligned}
 C_{D_0}^{nacelle} &= R_{wf}^{nacelle} c_f^{nacelle} \left(1 + \frac{60}{(l_{nacelle}/d_{nacelle})^3} + 0.0025 l_{nacelle}/d_{nacelle} \right) \frac{S_{wet}^{nacelle}}{S_{ref}} + \dots \\
 \dots + C_{D_{base}}^{nacelle} + C_{D_{wave}}^{nacelle} * S_{nacelle}/S_{ref} &= 0.000813
 \end{aligned} \tag{17.15}$$

Parameter	Description and definition	Value
$d_{nacelle}$	Diameter of the nacelle	3.28 ft (1.00 m)
$l_{nacelle}$	Length of the nacelle	26.25 ft (8.00 m)
$S_{nacelle}$	Maximum frontal area of the nacelle, $\frac{\pi}{4} d_{nacelle}^2$	8.45 ft^2 (0.79 m^2)
$S_{wet}^{nacelle}$	Wetted area of the nacelle, from reference [26]	259.39 ft^2 (24.10 m^2)
$Re_{nacelle}$	Reynolds number of the nacelle, $\frac{V l_{nacelle}}{\nu}$	7.6 e+7
$R_{wf}^{nacelle}$	Nacelle - fuselage interference factor, related to $Re_{nacelle}$	1.02
$c_f^{nacelle}$	Skin friction coefficient of the nacelle, related to $Re_{nacelle}$	0.0021
$C_{D_{base}}^{nacelle}$	Nacelle base-drag coefficient, from reference [26]	Negligible (no base)
$C_{D_{wave}}^{nacelle}$	Nacelle wave-drag coefficient, related to the Mach number	0

Table 17.7: Parameters for the nacelle parasite (zero-lift) drag

Nacelle drag coefficient due to lift

$$C_{D_L}^{nacelle} = \alpha_{nacelle}^2 \frac{S_{base}^{nacelle}}{S_{ref}} \cong 0 \tag{17.16}$$

Where $\alpha_{nacelle} = \alpha_{wing} (1 + d\epsilon_{nacelle}/d\alpha) + i_{nacelle}$.

This contribution may be neglected because the nacelles are designed to be without the base, so $S_{base}^{nacelle} \cong 0$.

Nacelle drag coefficient due to the interference with the wing

$$C_{D_{interference}}^{nacelle} = 0.036 \frac{c_{nacelle} b_{nacelle}}{S_{ref}} (\Delta C_{l_1} + \Delta C_{l_2})^2 = 5.73e-5 \tag{17.17}$$

Parameter	Description and definition	Value
$c_{nacelle}$	Wing chord at nacelle	9.43 ft (2.87 m)
$b_{nacelle}$	Diameter of the nacelle	3.28 ft (1.00 m)
$i_{nacelle}$	Nacelle incidence in cruise	0 °
ΔC_{l_1}	Factor related to nacelle location	0.2
ΔC_{l_2}	Proportional to nacelle incidence	0

Table 17.8: Parameters for the nacelle-wing interference drag

The final result is $C_{D_{nacelles}} = 0.0017 + C_{D_L}^{nacelle} \cong 0.0017$

17.1.5. Drag due to the empennage

To estimate the aerodynamic drag of the V-tail, the team decided to analyze the projections in the vertical and horizontal planes separately as if they were two tails. This approach is inspired by the same V-tail design philosophy proposed by the Reference [24] and developed in Chapter 12.

$$C_{D_{empennage}} = \sum_{n=1}^2 [(C_{D_0}^{empennage})_n + (C_{D_L}^{empennage})_n] \quad (17.18)$$

Where n is the number of the empennage, so in this case the horizontal and vertical projection, and the zero-lift drag coefficient is defined by equation 17.19.

$$(C_{D_0}^{empennage})_n = (C_{D_{0M=0.6}}^{empennage})_n + (C_{D_{wave}}^{empennage})_n \frac{S_n}{S_{ref}} \quad (17.19)$$

Empennage drag coefficient due to friction of horizontal and vertical surface

$$(C_{D_{0M=0.6}}^{empennage})_{horizontal} = R_{wf} R_{LS} C_f (1 + L'(t/c) + 100(t/c)^4) \frac{S_{wet}^{horizontal}}{S_{ref}} = 0.001859 \quad (17.20)$$

Similarly for vertical projection: $(C_{D_{0M=0.6}}^{empennage})_{vertical} = 0.000924$



Parameter	Description and definition	Value
R_{wf}	Empennage - fuselage interference factor	1.0
$\Lambda_{(t/c)_{max}}$	Sweep angle at maximum thickness	30 °
R_{LS}	Lifting surface correction factor	1.16
MGC	Mean geometric chord of empennage	7.74 ft (2.36 m)
$Re_{empennage}$	Reynolds number of empennage	2.2 e+7
C_f	Turbulent flat plate friction coefficient	0.00255
(t/c)	Maximum thickness at MGC	0.1
L'	Factor related to location of maximum airfoil thickness	1.2
S_{wet}^{V-tail}	Wetted area of V-tail	387.07 ft^2 (35.96 m^2)
$S_{wet}^{horizontal}$	Wetted area of horizontal projection	432.28 ft^2 (40.16 m^2)
$S_{wet}^{vertical}$	Wetted area of vertical projection	214.85 ft^2 (19.96 m^2)

Table 17.9: Parameters for empennage drag coefficient due to friction

Empennage zero-lift wave drag coefficient

The same procedure as used for the wing is applied (see Subsection 17.1.1). From Figure 17.3 we get the graphical solution: $C_{D_{wave}}^{empennage} = 0.00154$.

So, for the horizontal projection $C_{D_{wave}}^{empennage} \frac{S_{horizontal}}{S_{ref}} = 0.000857$, and for the vertical projection $C_{D_{wave}}^{empennage} \frac{S_{vertical}}{S_{ref}} = 0.000426$

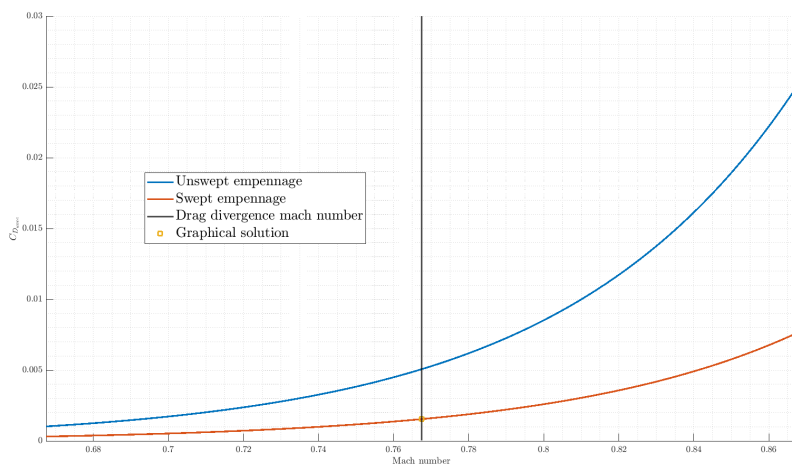


Figure 17.3: Graphical solution of empennage wave drag coefficient

Hence, the empennage zero-lift drag coefficient is equal to: $C_{D_0}^{empennage} = 0.00407$

Empennage drag coefficient due to lift

$$(C_{D_L}^{empennage})_{horizontal} = (C_D/C_L^2)_{horizontal} C_{L_{horizontal}} \quad (17.21)$$

With:

- $C_{L_{horizontal}} = C_{L/\alpha}^{horizontal} (\alpha_{horizontal} - \alpha_0^{horizontal})$
- $\alpha_{horizontal} = \alpha (1 - d\epsilon/d\alpha) + i_{horizontal}$
- $d\epsilon/d\alpha = 4.44 \left[(K_A K_\lambda K_h \sqrt{\cos(\Lambda_c/4)}) (1.19) (C_{L/\alpha_{at M}}^{wing}/C_{L/\alpha_{at M=0}}^{wing}) \right]$

Parameter	Description and definition	Value
$\Lambda_{LE}^{horizontal}$	Sweep angle at leading edge	30°
λ	Global taper ratio of the empennage	0.5
$C_{L_0}^{horizontal}$	Lift coefficient of empennage at $\alpha = 0^\circ$	0
$\alpha_0^{horizontal}$	Angle of attack of empennage at zero-lift	0°
$i_{horizontal}$	Incidence of empennage	-1.5 °
M	Mach number in cruise	0.73
$AR_{horizontal}$	Aspect ratio of the horizontal tail	3.61
K_A	-	0.0878
K_λ	-	1.3
K_h	-	1.0336
$(C_D/C_L^2)_{horizontal}$	Slope of $(C_{D_L}^{empennage})_{horizontal}$	0.089

Table 17.10: Parameters for empennage drag coefficient due to lift

For the vertical tail $(C_{D_L}^{empennage})_{vertical} = 0$ due to symmetry.

17.1.6. Drag due to the flap

The drag coefficient due to flap deflection may be estimated from the sum of three contributions: the flap profile drag increment, induced drag increment, and the interference drag increment due to the flap.

$$C_{D_{flap}} = \Delta C_{D_{profile}}^{flap} + \Delta C_{D_{induced}}^{flap} + \Delta C_{D_{interference}}^{flap} \quad (17.22)$$



Profile drag increment due to flaps

$$\Delta C_{D_{profile}}^{flap} = \Delta C_{D_{p\Lambda_{0.25c}=0}} \cos(\Lambda_{0.25c}) S_{wf}/S_{ref} \quad (17.23)$$

Where S_{wf} is the flapped wing area, while $\Delta C_{D_{p\Lambda_{0.25c}=0}}$ is the two-dimensional profile drag increment due to flaps and depends by the flap type, the ratio of wing chord flapped, and it has an exponential trend with respect to the flap deflection.

Induced drag increment due to flaps

$$\Delta C_{D_{induced}}^{flap} = K^2 \Delta C_{L_{flap}}^2 \cos(\Lambda_{0.25c}) \quad (17.24)$$

Where $\Delta C_{L_{flap}}$ is the incremental lift coefficient due to the flap (see Figure 11.15), while $K = 0.15$ is an empirical constant associated with the wing aspect ratio and the length of the flap. Note that, as anticipated earlier in other parts of the report, external flaps will only be used in hover phase to reduce the download, so only the contribution of the internal flap will be considered in this analysis.

Interference drag increment due to flaps

$$\Delta C_{D_{interference}}^{flap} = K_{int} \Delta C_{L_{prof}}^{flap} \quad (17.25)$$

Where $K_{int} = 0.4$ for slotted flaps, and $\Delta C_{L_{prof}}^{flap}$ comes from equation 17.23.

17.1.7. Drag due to the trim

Trim drag is caused by lift generated on the tail as a result of the requirement to trim the airplane. There are two types of trim drag: a trim drag due-to-lift and a profile drag due to the control surfaces deflection.

$$C_{D_{trim}} = \Delta C_{D_{trim_lift}} + \Delta C_{D_{trim_profile}} \quad (17.26)$$

Trim parasite drag coefficient

$$\Delta C_{D_{trim_parasite}} = \Delta C_{p\Lambda_{0.25}=0} \cos(\Lambda_{0.25_h}) (S_{ef}/S_h) (S_h/S_{ref}) \quad (17.27)$$

Where $\Delta C_{p\Lambda_{0.25}=0}$ is the parasite drag coefficient due to the elevator (or better the contribution of the ruddervator on the horizontal plane); this coefficient can be found with the same method used for the flap, but considering the elevator deflection instead of the flap deflection.

Parameter	Description and definition	Value
$\Lambda_{0.25_h}$	Sweep angle at 25% of the tail	33.8°
S_{ef}	Flapped horizontal tail area	183.7 ft ² (17.1 m ²)

Table 17.11: Parameters for parasite trim drag

Trim drag coefficient due to lift

$$\Delta C_{D_{trim_lift}} = (\Delta C_{L_h}^2 / (\pi A_h e_h)) S_{ref}/S_h \quad (17.28)$$

Where ΔC_{L_h} is the horizontal tail incremental lift coefficient required for trim.

17.1.8. Drag due to the landing gear

Reference [26] presents a method for calculating landing gear drag, valid only at low speeds:

$$C_{D_{LG}} = \sum_{i=1}^3 [(C_{D_0}^{LG})_i + p_i C_L) S_{LG_i}/S_{ref}] \quad (17.29)$$

Where factor p_i is negligible due to the fact that all landing gear are located on the fuselage (and not under the wing).

Parameter	Description and definition	Value
$C_{D_0}^{LG}$	Zero-lift LG drag coefficient	1.0
w_{tire}	Tire width	1.6 ft (0.5 m)
d_{tire}	Tire diameter	4.3 ft (1.3 m)
S_{LG}	Tire width	7.0 ft ² (0.65 m ²)

Table 17.12: Parameters for landing gear drag

17.1.9. Drag due to the rotor hub and unfolded rotors

With no advanced software available, the drag due to the rotor hub was chosen through Reference [9], and then increased by a 30% to account the stopped unfolded rotors as well. Thus, from Reference [9] a $C_{D_{hub}} = 0.014$ is acceptable (for a single hub).



17.1.10. Final results for drag estimation

Regarding the induced drag coefficient, the lift coefficient of minimum drag has been both calculated and estimated from XFLR5 to be 0.21 in cruise (Mach = 0.73), the Oswald's factor is equal to 0.815, and the lift coefficient slope of the whole aircraft is defined in equation 17.30. Note that this value of $C_{L/\alpha}$ is very similar to the one estimated with VLM simulations on XFLR5 (see Table 12.3).

$$C_{L/\alpha} = C_{L/\alpha}^{wing-fus} + C_{L/\alpha}^{tail} \eta_{tail} (1 - d\epsilon/d\alpha) \frac{S_{tail}}{S} = 5.18 \text{ rad}^{-1} \quad (17.30)$$

In Figures 17.4 and 17.5 are plotted respectively the drag polar of the whole aircraft and the drag polars of each components considered (at Mach = 0). While, Figures 17.6 and 17.7 show the aircraft polar in conversion/landing phase and in cruise phase.

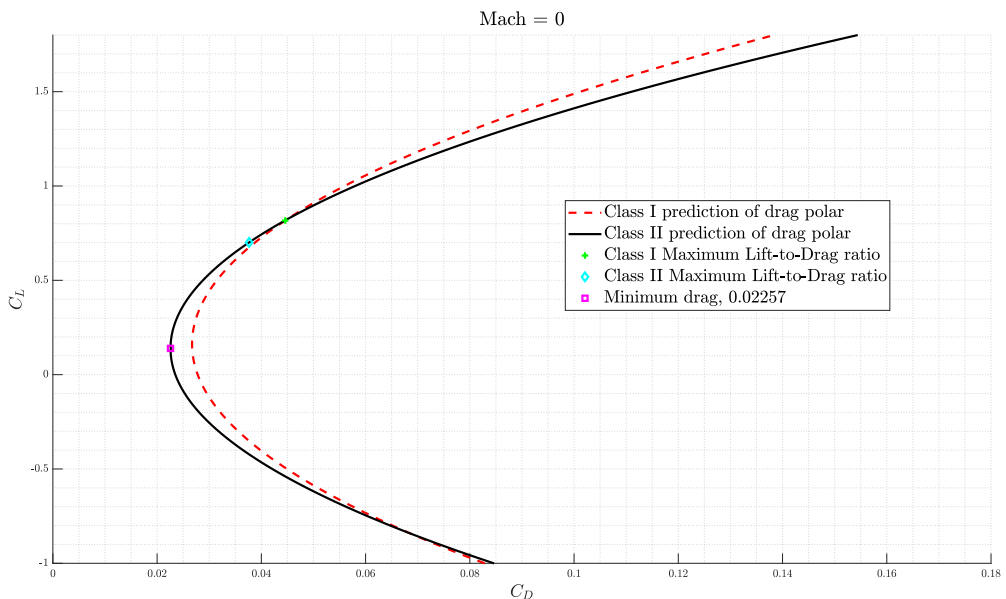


Figure 17.4: Polar curve predicted with Class II method of Roskam in clean configuration

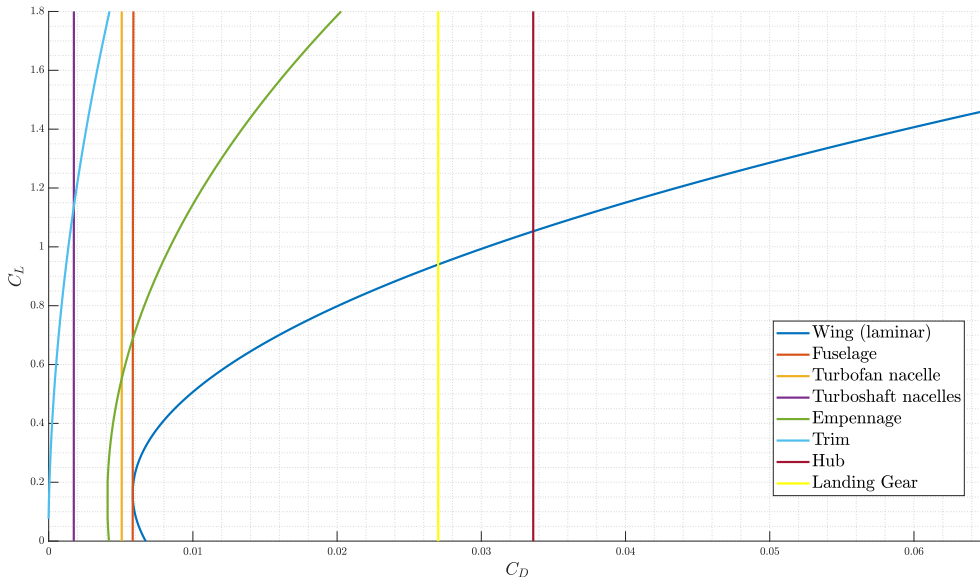


Figure 17.5: Contribution of each component on the drag polar

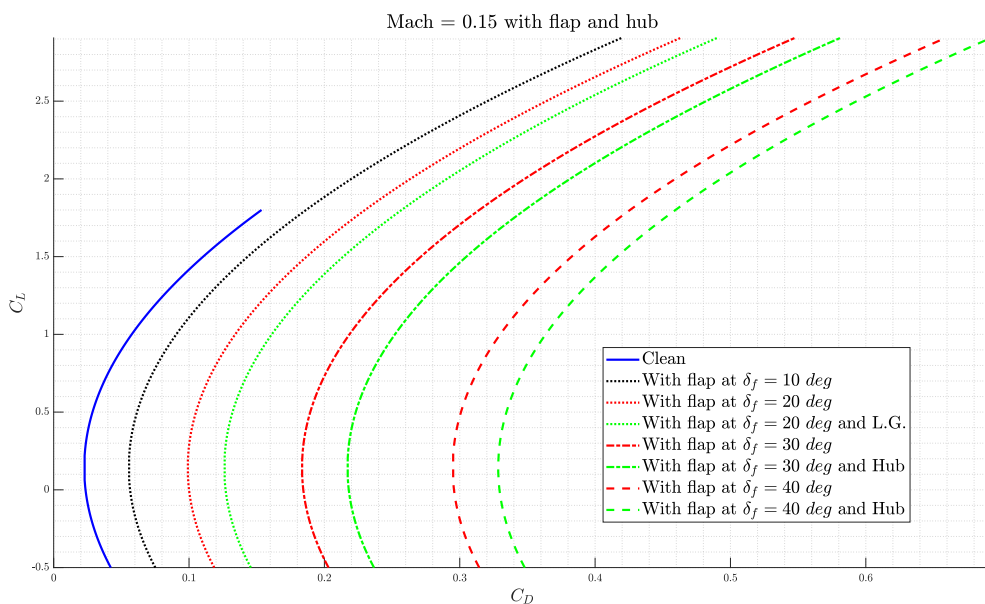


Figure 17.6: Polar curve predicted in conversion phase (with flap and unfold rotors)



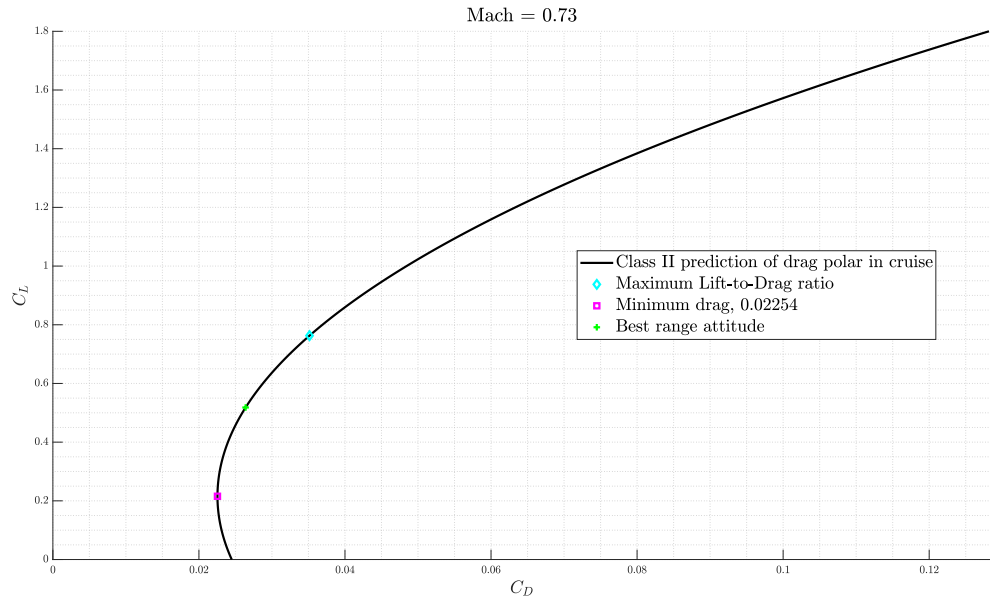


Figure 17.7: Polar curve predicted in cruise phase

Equivalent flat-plate parasite drag area :

From Reference [26] the equivalent parasite area (f) is computed as:

$$f = C_{D_0} S_{wing} = 18.6 \text{ } ft^2 = 1.7 \text{ } m^2 \quad (17.31)$$

So, considering that $S_{wet}^{aircraft} \cong 4,250 \text{ } ft^2$, the equivalent skin friction coefficient is $C_f = f/S_{wet}^{aircraft} = 0.0044$.

18 | Performance

18.1. Jet mode

For the case of Raven 4 engine (i.e., the F118-GE-100) it is available from manufacturer data only the maximum thrust at static sea level. For this purpose it was adopted a simplified jet engine regression model [13] so that it can conservatively approximate the performance of the engine. This model defines a variation of thrust with respect to both altitude and airspeed.

Thus, thrust available trends is plotted in Figure 18.1, in which the effect of airspeed on thrust can be neglected over 25,000 ft.

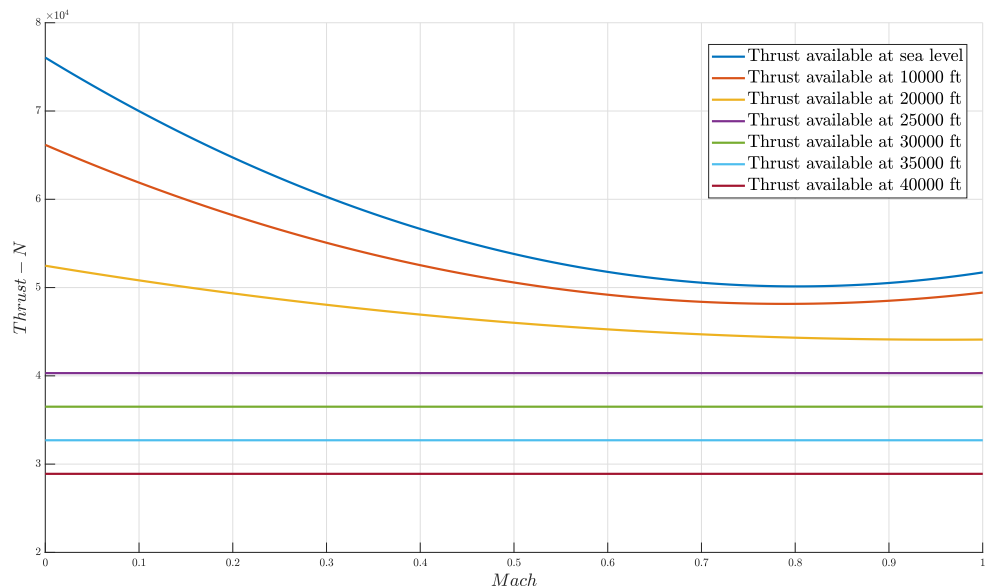


Figure 18.1: Thrust available trends

On the other hand, with regard to the required thrust, equation 18.1 is used in the different phases of flight.

$$T = \frac{1}{2} \rho V^2 S C_D \quad (18.1)$$

Where C_D is the drag coefficient defined in Chapter 17 for different flight conditions.

Below are listed the available and required thrusts for the most important flight phases:

- I. Conversion from rotorcraft to jet mode at 2,000 ft (610 m) and MTOM (26,544 kg or 58,520 lb), with stopped unfold rotors and flap down deflected by 30°. In this case, the flaps are deflected only on the inner wing.

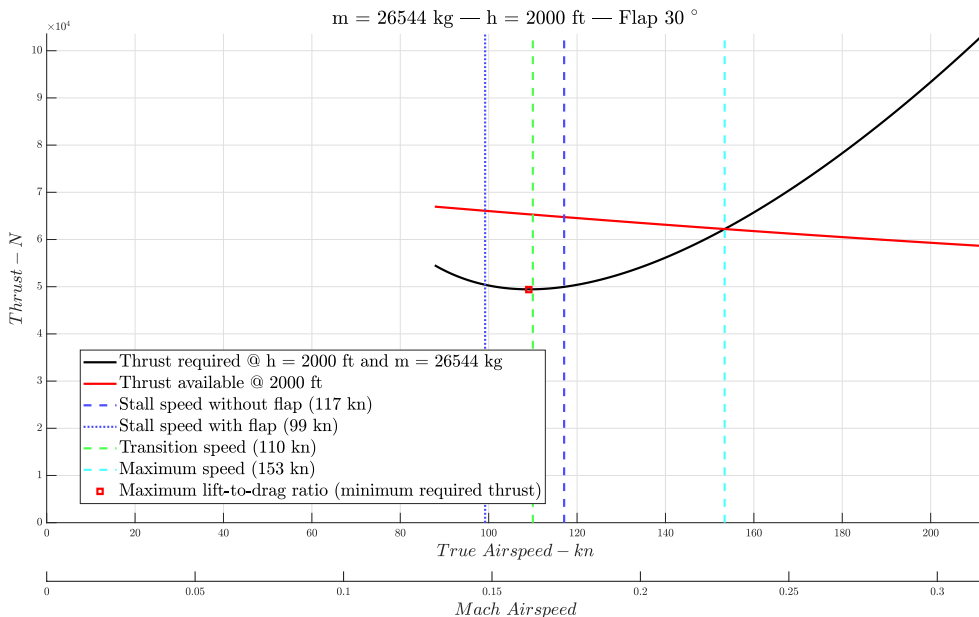


Figure 18.2: Conversion phase with $\delta_f = 30^\circ$

This flap configuration allows for a wide speed range (from 99 kn to 153 kn). The main disadvantage is that the AoA required to maintain a conversion speed of 110 kn in this condition is 13.5°. Hence, two possible alternatives are: perform the conversion phase with flaps deflected by 40°, which would lower the AoA to 10.5°, but would greatly reduce the airspeed range due to the drag increment (see Figure 18.3), or deflect the flaps on the whole wing (also on the outer wing) by 20°; this latter solution remains the least favored, because it could lead to an excessive reduction in roll controllability (see Figure 18.4).



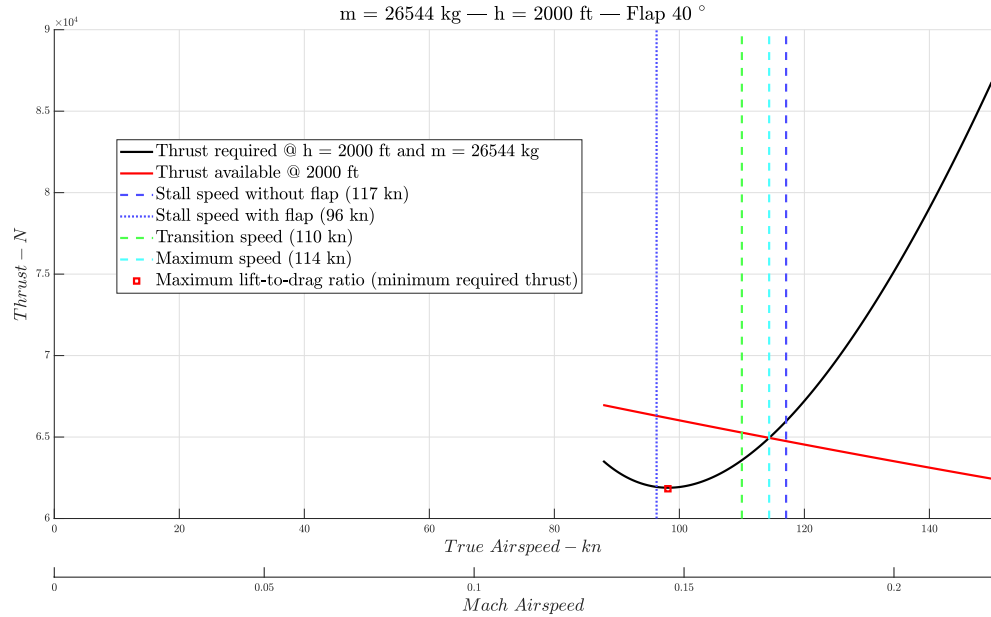


Figure 18.3: Conversion phase with $\delta_f = 40^\circ$ (only on the inboard wing)

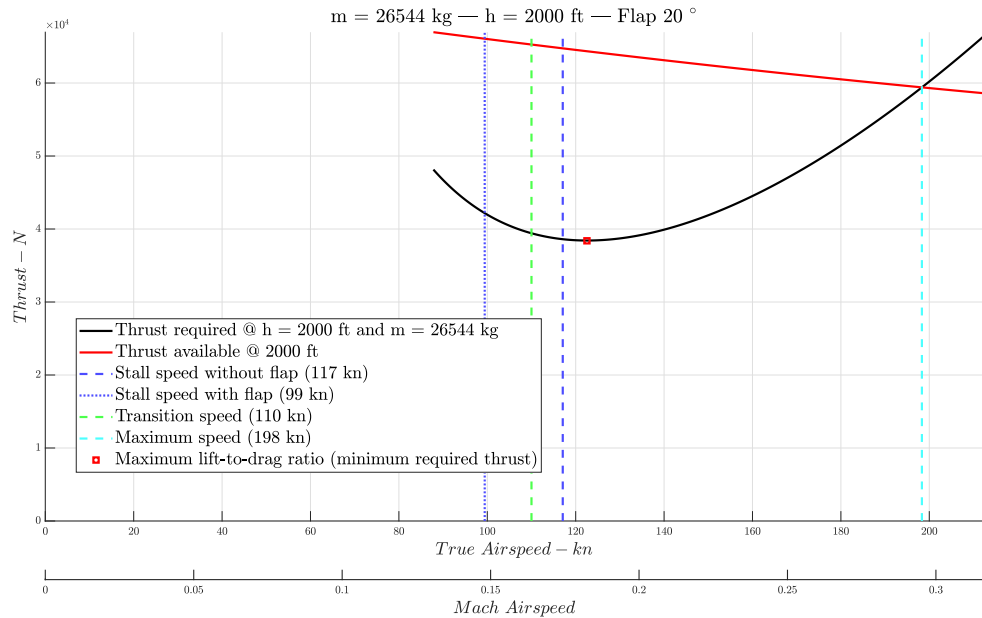


Figure 18.4: Conversion phase with $\delta_f = 20^\circ$ all over the wing

II. Cruise at 20,000 ft (6,096 m) and $M_{average}^{1st\ cruise} = 24,753\ kg = 54,571\ lb$

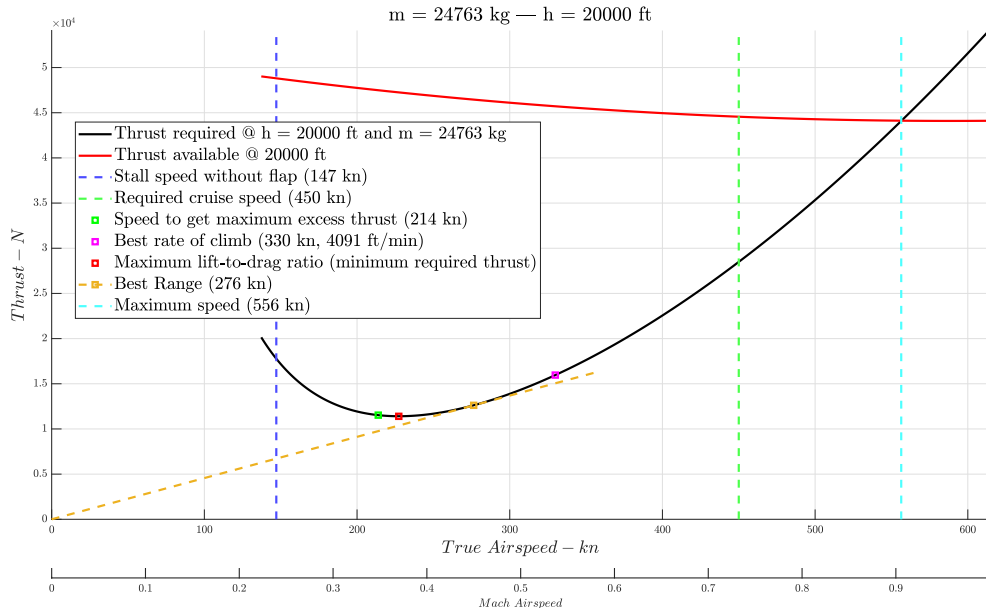


Figure 18.5: Cruise phase

From this graph, it can be seen that the aircraft is able to perform a cruise at 450 kn and 20,000 ft, as required by the RFP. However, at this altitude the best range airspeed corresponds to about 275 kn. In fact, best-range attitude is a characteristic of the drag polar, and the airspeed of best range depends mainly on weight and altitude. Thus, to have a constant best-range speed at 450 kn, the aircraft must increase altitude as the mass changes. Figure 18.6 shows how best range altitude varies as mass varies.



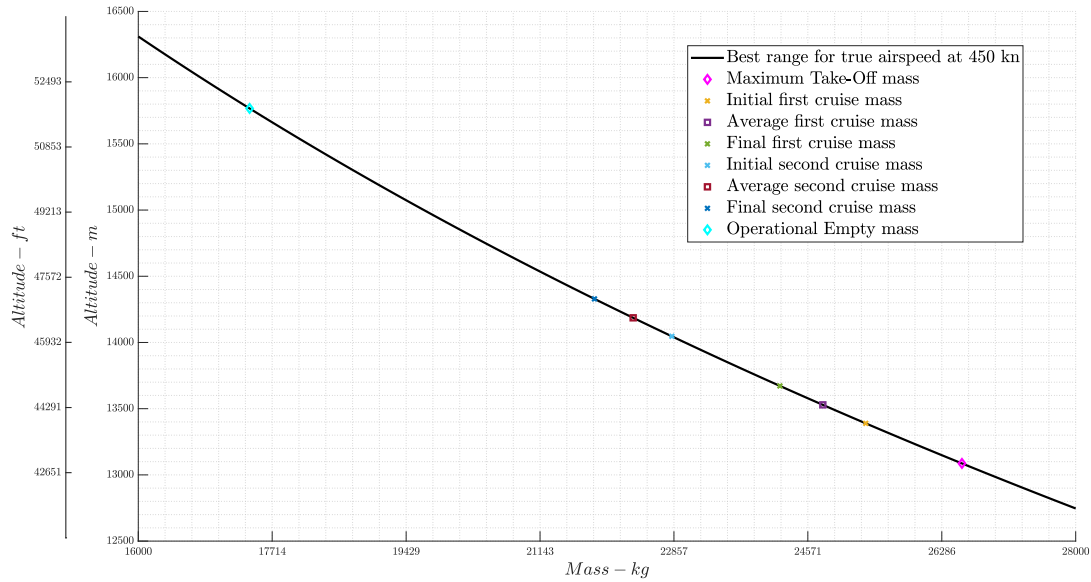


Figure 18.6: Best range altitude for constant speed and weight

For example, in order to perform the first cruise ($M_{average}^{1st\,cruise} = 24,753\,kg = 54,571\,lb$) at 450 kn (231.5 m/s) as best range airspeed, it will be required an (average) altitude of 45,250 ft (13,792 m).

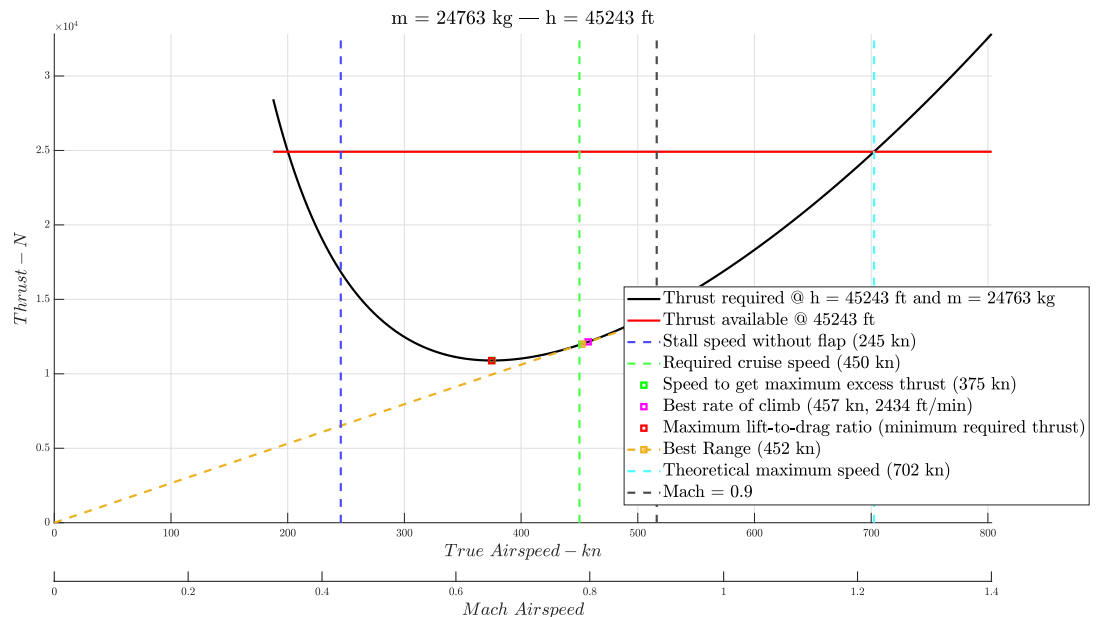


Figure 18.7: Best range cruise at 450 kn

III. Penetration at 2,000 ft (610 m), flap up, and a mass of 24,345 kg (53,672 lb). It has been shown that at Maximum Continuous Power it's possible to maintain an airspeed of 450 kn at 2,000 ft.

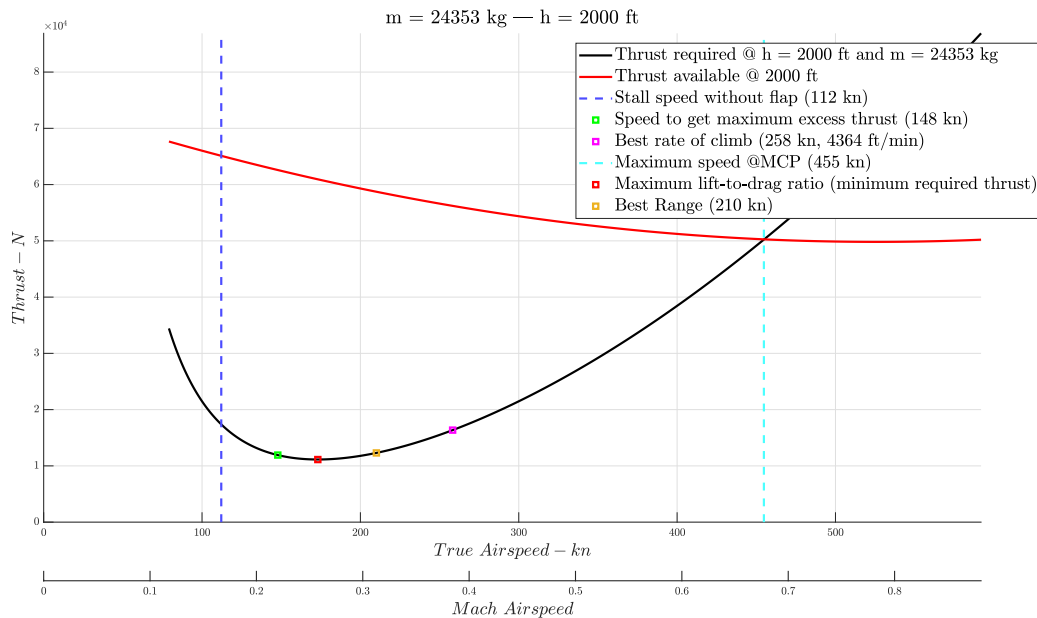


Figure 18.8: Penetration phase

In addition, note that in some diagrams above, increasing the altitude shows that the aircraft would be at mach greater than one, but the calculations may not be reliable for mach values close to 1 because drag rise was not considered in these analysis, and the aircraft isn't designed for supersonic flight.

18.1.1. Take-Off performance

The vehicle is capable of taking off vertically, but it will also be able to take off in airplane mode (i.e., with the rotors folded and using only the power of the jet engine). For this reason, take-off and landing performance was analyzed.

First of all, the following military regulations were considered: *MIL-C-005011B, par. 3.4.2.4 and 3.4.5*

From these regulations, it was defined that the aircraft must have a lift-off speed (V_{LOF}) equal to the 110% of the power-off stall speed in take-off configuration, should be considered 50 ft as the height of the obstacle at the end of the runway, and the climb speed at the 50-foot obstacle shall not be less than the 115% of the power off stall speed.



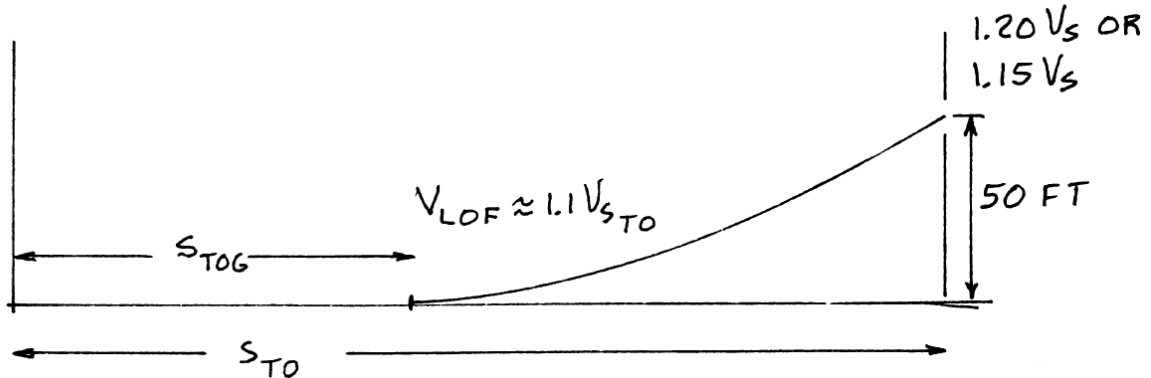


Figure 18.9: Definition of military take-off distance

To calculate the take-off distance, the method proposed by Roskam (Reference [27]) is used, according to which:

$$S_{TO} = f_{TO} h_{TO} \left[\frac{1}{\gamma_{LOF}} + \frac{(V_3/V_{S_{TO}})^2 (W/S)_{TO} (((\bar{T}/W)_{TO} - \mu')^{-1} + 1.414)}{(h_{TO}\rho g C_{L_{max}}^{TO})(1 + 1.414\gamma_{LOF})} \right] \quad (18.2)$$

$$S_{TO_{ground}} = \frac{V_{LOF}^2}{2g ((\bar{T}/W)_{TO} - \mu')} \quad (18.3)$$

Where:

- $V_{LOF} = 1.10 V_{S_{TO}}$
- $V_3 = 1.15 V_{S_{TO}}$
- $f_{TO} = 1.0$
- $(W/S)_{TO}$ is the take-off wing loading
- $(\bar{T}/W)_{TO}$ is the mean thrust-to-weight ratio at the speed of $0.707 V_{LOF}$; from Reference [27]: $\bar{T} = 0.75 T_{static} \frac{5+BPR}{4+BPR}$
- $\mu' = \mu_g + 0.72 \frac{C_{D_0}}{C_{L_{max}}^{TO}}$; with $\mu_g = 0.02$, considering a concrete/asphalt runway.
- $\gamma_{LOF} = \left(\frac{T-D}{W} \right)_{LOF}$, but it may be approximated by $\gamma_{LOF} \cong 0.9 (\bar{T}/W)_{TO} - \frac{0.3}{\sqrt{AR}}$

Take-off performance under different conditions was then analyzed. The first analysis was implemented to observe how take-off performance varies with respect to the maximum thrust considered, maintaining a 20° angle for the flaps and the runway at sea level. The results of this analysis can be seen in Table 18.1 and Figure 18.10.

Static Thrust	S_{TO} [m]	$S_{TO_{ground}}$ [m]
Maximum Thrust	876	655
Maximum Continous Thrust	1010	752

Table 18.1: Take-off distance for different thrust

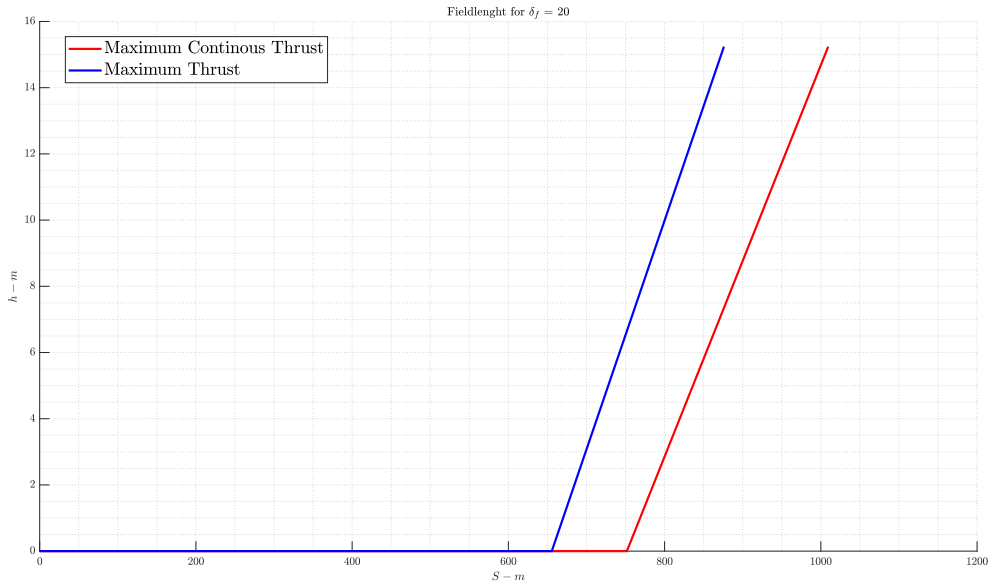


Figure 18.10: Take-off distance for different thrust



The second analysis concerns the study of take-off performance varying the flap deflection angle, from 0° to 20° , considering the maximum thrust and the runway at sea level. The results are shown in the Table 18.2 and Figure 18.11.

δ_f°	S_{TO} [m]	$S_{TO_{ground}}$ [m]	V_{LOF} [kn]
0	1,041	776	122
10	942	702	114
20	876	655	108

Table 18.2: Take-off distance for different flap deflections

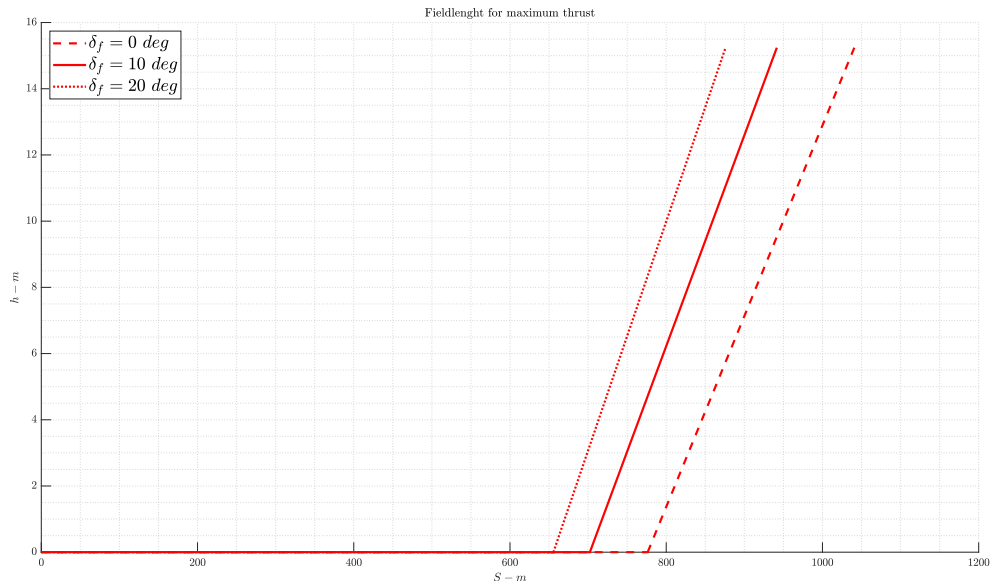


Figure 18.11: Take-off distance for different flap deflections

The third and final analysis consists of varying the altitude, maintaining the maximum thrust and 20° as flap deflection angle. The results are shown in the Table 18.3 and Figure 18.12.

Runway elevation [m]	S_{TO} [m]	$S_{TO_{ground}}$ [m]
0	876	656
500	915	688
1,000	956	722
2,000	1,045	798

Table 18.3: Take-off distance for different runway elevation

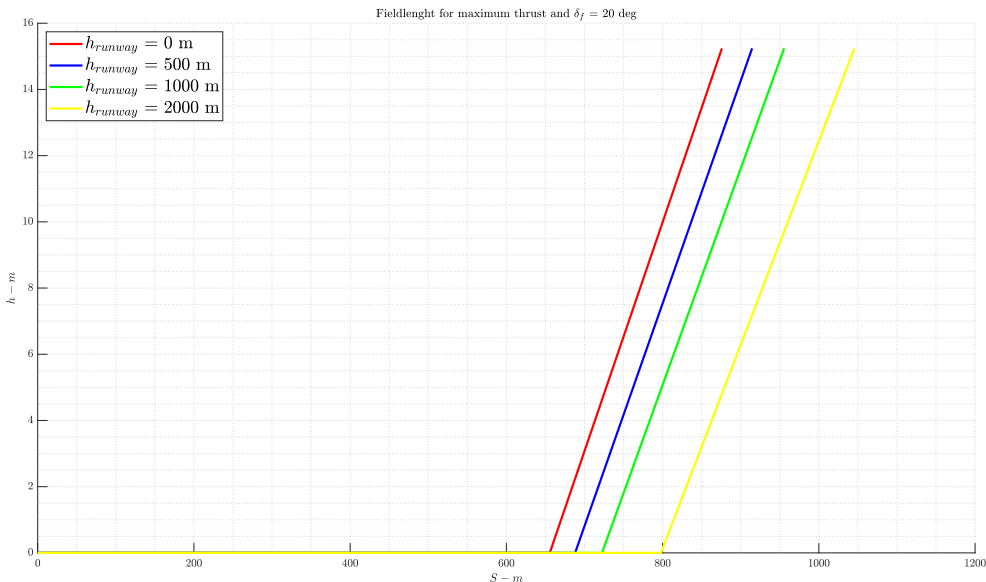


Figure 18.12: Take-off distance for different runway elevation

18.1.2. Landing performance

The following military regulations were considered: *MIL-C-005011B, par. 3.4.2.11, 3.4.2.12 and 3.4.7*

From these regulations, it was defined that the aircraft must have an approach speed down to the 50-foot obstacle shall be 120% of 1.0g power-off stall speed (in approach configuration), the landing speed shall be 115% of 1.0g power-off stall speed (in landing configuration), and the landing distance must include the landing ground roll (S_{LG}) and the distance over a 50-foot obstacle (S_{AIR}). In addition, the max take-off weight is con-



sidered in order to simulate the most critical condition.

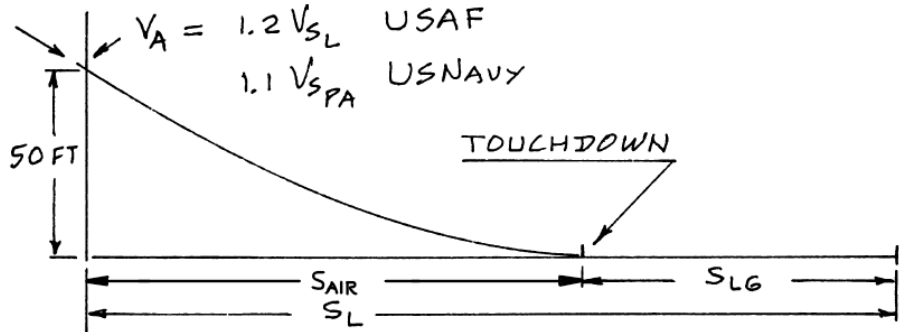


Figure 18.13: Definition of military landing distance

Hence, the landing distance is defined as:

$$S_L = S_{AIR} + S_{LG}$$

With:

$$S_{AIR} = \frac{1}{\bar{\gamma}} \left(\frac{V_A^2 - V_{TD}^2}{2g} + h_L \right) \quad (18.4)$$

$$S_{LG} = \frac{V_{TD}^2}{2 \left(\frac{D+\mu m g}{m} \right)} \quad (18.5)$$

Where:

- $\bar{\gamma} = \left(\frac{D-T}{W} \right)_{average}$
- The approach speed is $V_A = 1.2 V_{S_L}$
- The touchdown speed can be defined as $V_{TD} = V_A \sqrt{(1 - \bar{\gamma}^2 / \Delta n)}$
- Δn is related to the pilot technique and on airplane handling qualities. From Reference [27] an acceptable value is $\Delta n = 0.10$
- $\mu = 0.3$ from *MIL-C-005011B, par. 3.4.5.5.2*

Firstly, it was calculated the landing distance with different aircraft weight, considering both the most critical case (i.e., MTOW) and the weight that the aircraft will actually have during the typical mission (see Figure 18.39); the runway at sea level and flaps deflected by 30° were considered in this analysis. The results are shown in the Table 18.4 and Figure 18.15

Landing Weight	S_L [m]	$S_{L_{ground}}$ [m]
Maximum Take-Off Weight	708	385
Mission Landing Weight	629	334

Table 18.4: Landing distance for different weight

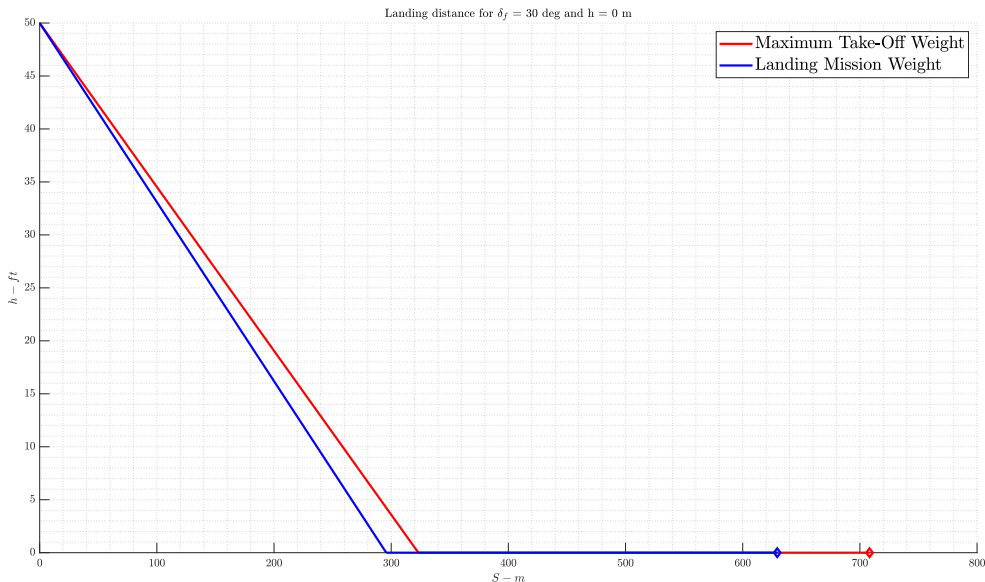


Figure 18.14: Landing distance for different weight

In addition, as also done for take-off, the effects of flap deflection and runway elevation on landing performance were analyzed. The results can be seen in Tables 18.5 and 18.6, respectively, and Figures 18.15 and 18.16

δ_f °	S_L [m]	$S_{L_{ground}}$ [m]	$V_{touchdown}$ [kn]
0	1,607	751	133
30	708	385	106
40	636	288	94

Table 18.5: Landing distance for different flap deflections



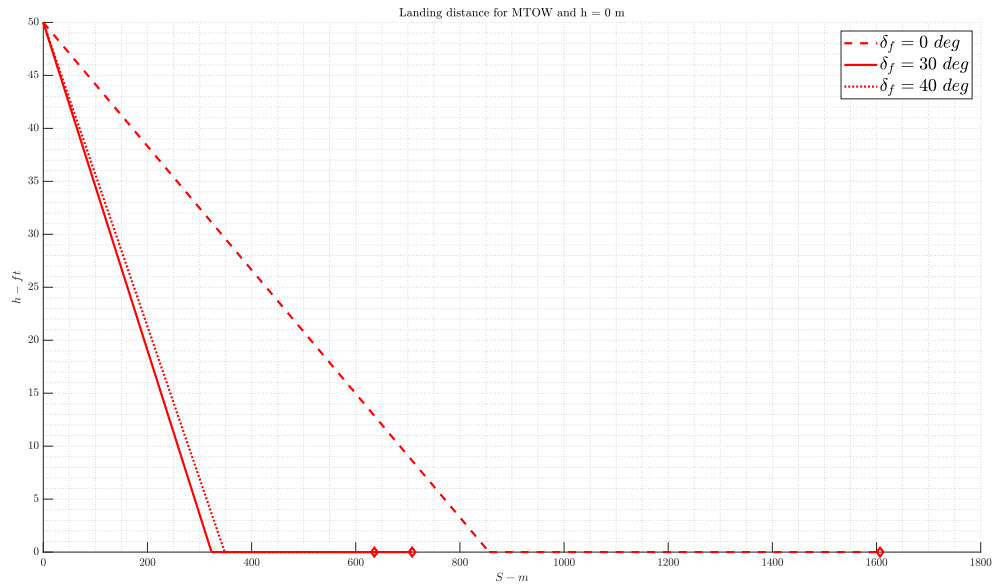


Figure 18.15: Landing distance for different flap deflections

Runway elevation [m]	S_L [m]	$S_{L_{ground}}$ [m]
0	708	385
500	736	404
1,000	765	424
2,000	830	468

Table 18.6: Landing distance for different runway elevation

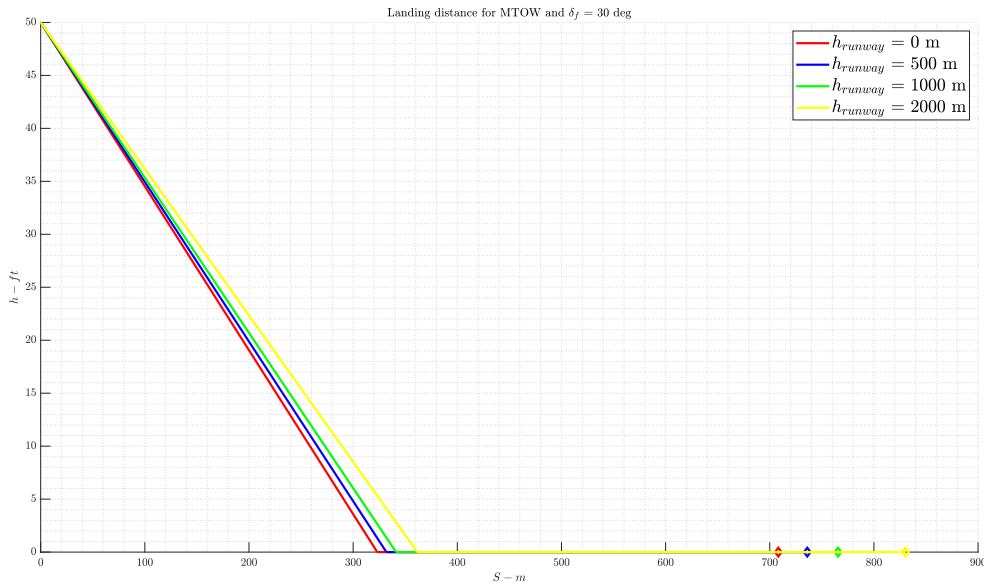


Figure 18.16: Landing distance for different runway elevation

Finally, no limits on maximum take-off length are imposed by the regulations, but below it is presented a comparison with respect to other competitors, and a study of some strategical NATO or U.S. airports.

Aircraft name	Take-Off run	Landing run	Maximum Take-Off Mass
ATR 42	1,165 m (3,822 ft)	1,040 m (3,412 ft)	18,600 kg (41,006 lb)
ATR 72	1,290 m (4,232 ft)	1,067 m (3,500 ft)	22,500 kg (49,604 lb)
C27-J Spartan	580 m (1,903 ft)	340 m (1,115 ft)	31,800 kg (70,107 lb)
An 72	620 m (2,034 ft)	420 m (1,378 ft)	31,200 kg (68,784 lb)
V-22 (STO)	152 m (499 ft)	-	27,442 kg (60,499 lb)
C-130J	930 m (3,051 ft)	427 m (1,401 ft)	74,389 kg (164,000 lb)
C-130J (max effort)	549 m (1,801 ft)	427 m (1,401 ft)	74,389 kg (164,000 lb)
Raven 4	655 m (2,149 ft)	385 m (1,263 ft)	26,544 kg (58,519 lb)

Table 18.7: Take-off distance for some competitor (Reference [7])



Airport	Runway length	Runway elevation
Sigonella [LICZ]	2,450 m (8,038 ft)	22 m (72 ft)
Ghedi Air Base [LIPL]	2,987 m (9,800 ft)	98 m (322 ft)
Morón Air Base [LEMO]	3,597 m (11,801 ft)	87 m (285 ft)
Geilenkirchen [ETNG]	3,050 m (10,007 ft)	82 m (269 ft)
Lajes AB, Lajes [LPLA]	3,294 m (10,807 ft)	52 m (171 ft)
Izmir Air Station [LTBL]	2,988 m (9,803 ft)	4 m (13 ft)
Osan Air Base [RKS0]	2,743 m (9,000 ft)	12 m (39 ft)
Edwards [KEDW]	4,572 m (15,000 ft)	700 m (2,297 ft)
Langley AFB, Hampton [KLFI]	3,048 m (10,000 ft)	2 m (7 ft)

Table 18.8: Runway length of some strategic air base located on NATO countries

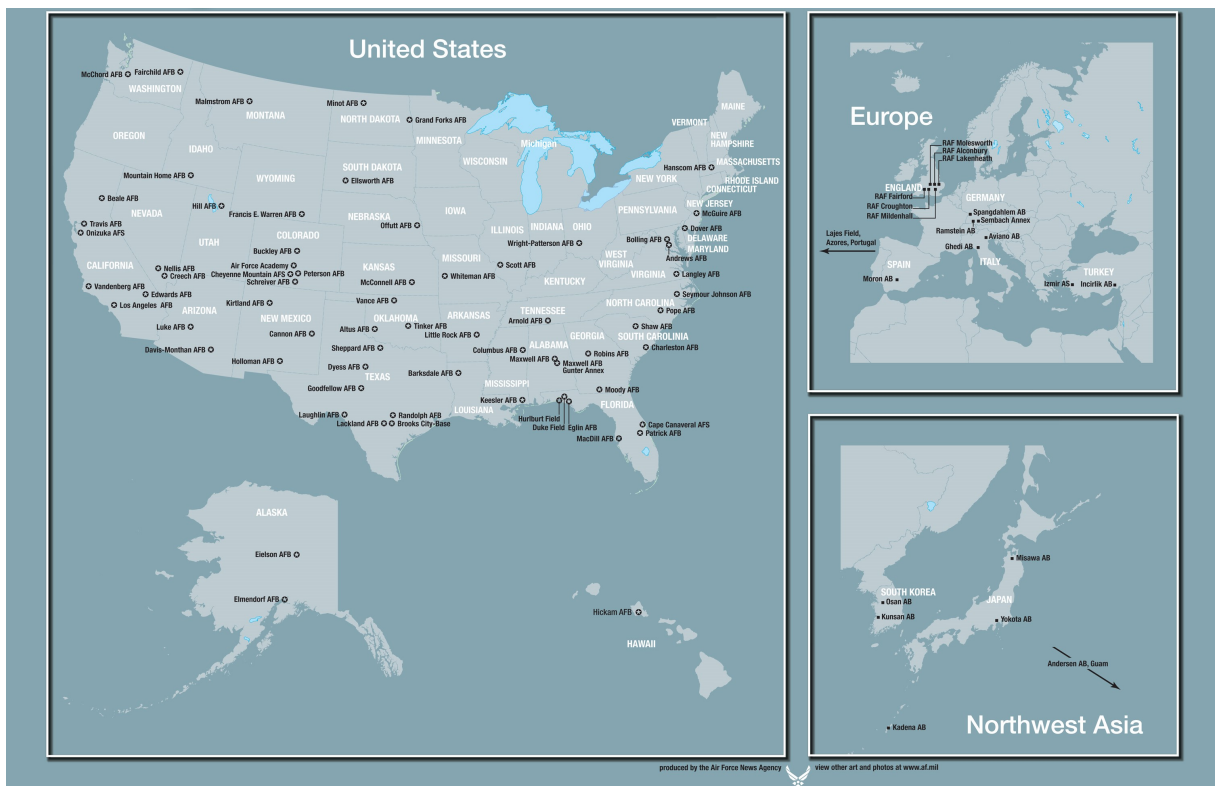


Figure 18.17: Major US and NATO air force facilities

These comparisons show that the Raven 4 aircraft is in line with military competitors, and will certainly be able to take-off and land from very strategic U.S. air bases.

18.1.3. Climb performance

There are no specific requirements from military regulations for climb, except that the aircraft must perform this maneuver in Best-Rate-of-Climb attitude. The behavior of the rate of climb with increasing airspeed at sea level is presented in Figure 18.18, and it is noted that the aircraft may perform a maximum rate of climb of 3,900 ft/min (19.8 m/s) at 250 kn in MCP.

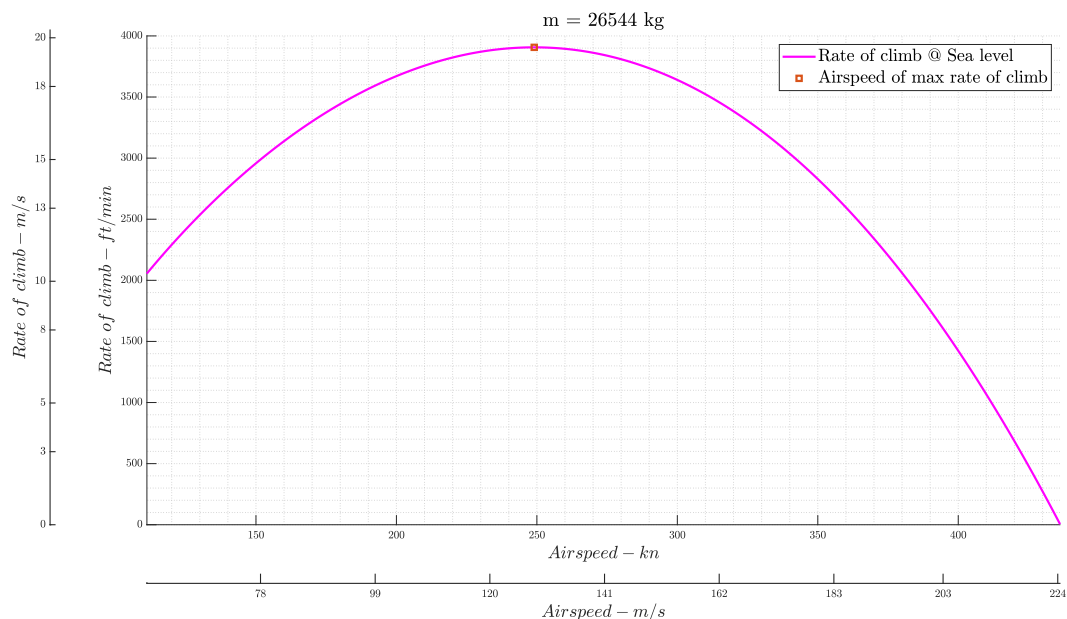


Figure 18.18: Rate of climb at sea level (and MTOW)

It's also interesting to observe how the maximum rate of climb and the corresponding airspeed varies with altitude; Figures 18.19 and 18.20 shows these trends, which were obtained by fitting the data obtained from the available thrust model (Figure 18.1). It is also observed that the absolute ceiling altitude is 62,250 ft (18,974 m).



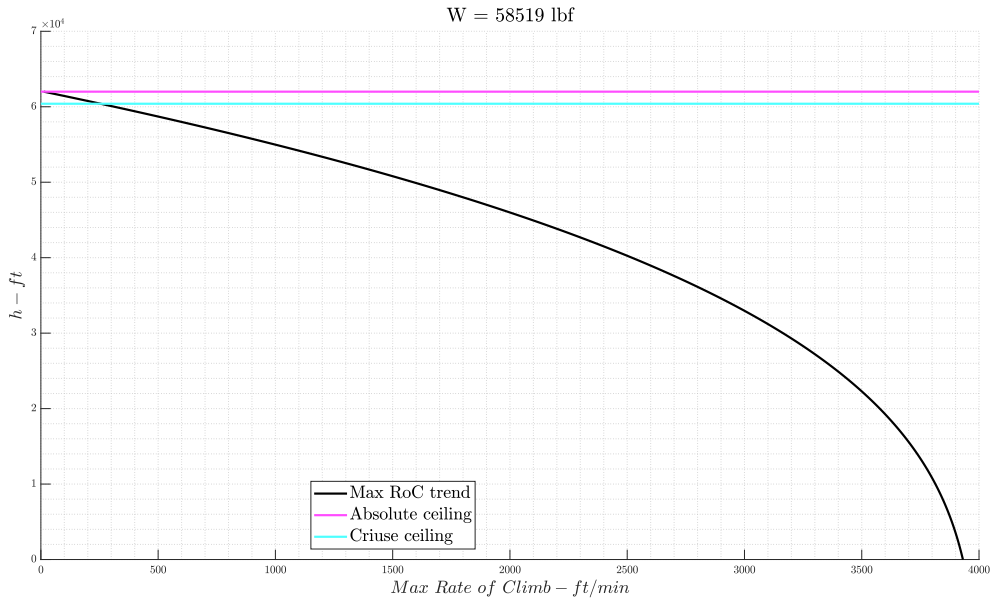


Figure 18.19: Best rate of climb with respect to altitude

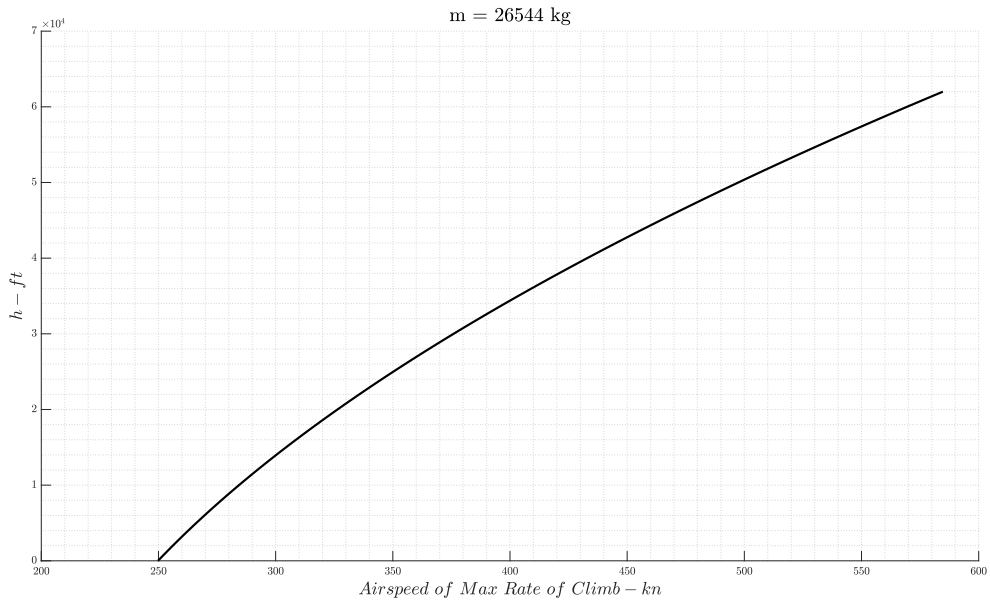


Figure 18.20: Airspeed of BROC with respect to altitude

Finally, by integrating the rate of climb of the Figure 18.19, it's possible to derive the Time-to-Climb performance. For example, it takes about 5.5 minutes to climb to 20,000 ft (in BROC), and about 14 minutes to reach the best range altitude.

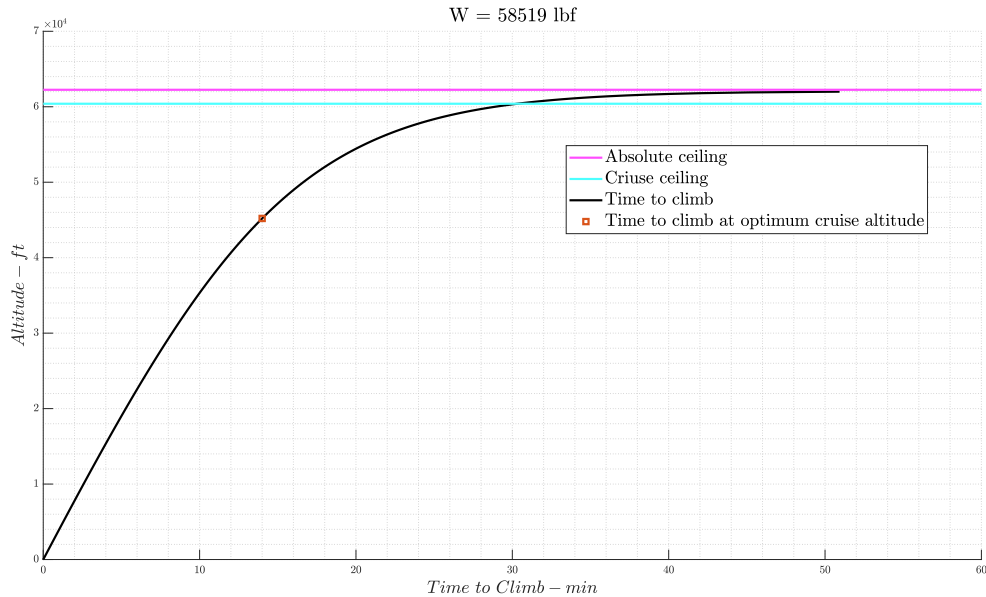


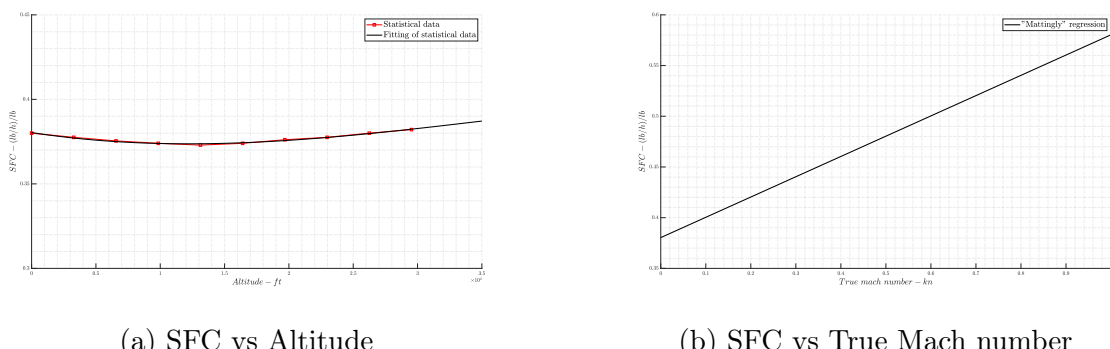
Figure 18.21: Time to Climb

18.1.4. Range performance and operational flight envelope

Breguet's formulas at constant-speed (equation 18.6) were used to calculate the aircraft range in cruise and penetration phases.

$$R = \frac{V}{SFC} \frac{L}{D} \ln \left(\frac{W_{initial}}{W_{final}} \right) \quad (18.6)$$

To account for variations in SFC with altitude and airspeed, two models based on historical-statistical regressions of typical turbofan low-by-pass ratios were implemented. Figure 18.22 shows these regressions.



(a) SFC vs Altitude

(b) SFC vs True Mach number

Figure 18.22: Effect of altitude and mach number on turbofan SFC



Specifically, it was shown that to ensure the RFP requirements (i.e., cruise at 450 kn, and penetration at MCP and low altitude) without consuming more fuel than preliminary planned, it's sufficient to execute the cruise at 31,000 ft. In this way, a range of 450 nm in climb and cruise, and a range of 50 nm in penetration can be guaranteed.

1st climb	1st cruise	1st penetration	2nd climb	2nd cruise	2nd penetration
46 nm	410 nm	50 nm	41 nm	421 nm	50 nm

Table 18.9: Taper ratio and wing chords

Furthermore, regarding the payload-range diagram, calculated considering the best cruise condition (i.e., best range attitude), it was found that the aircraft would be able to fly for about 3,400 nm, extendable up to 4,200 nm by unloading all the payload and filling the tanks to maximum volumetric capacity (i.e., $1.24 m^3$ more fuel, about 1,000 kg). This allows for ferry range flights from North America to Europe (Figure 18.24).

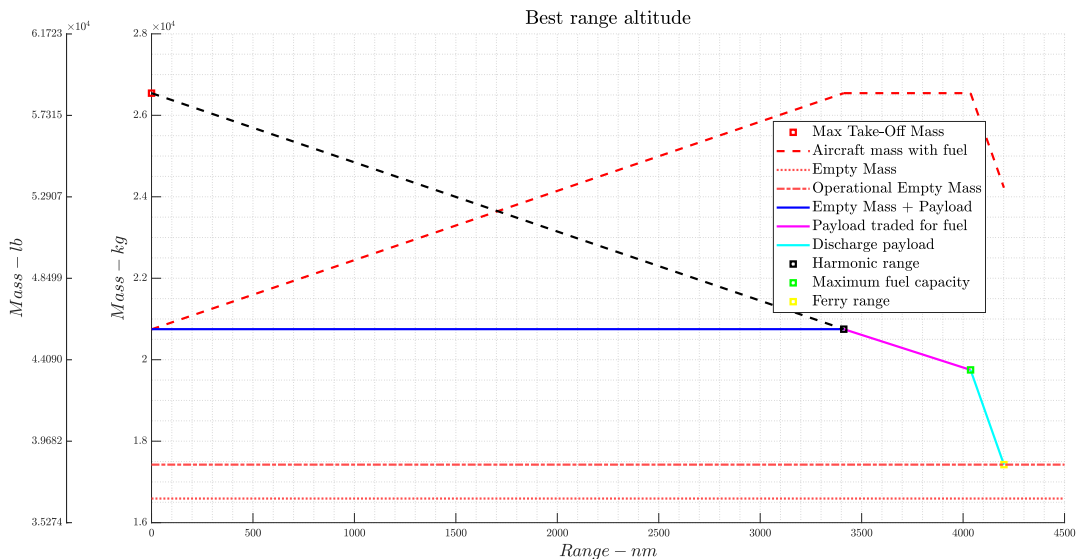


Figure 18.23: Payload range diagram



Figure 18.24: Ferry range capability

Operational flight envelope

Finally, by calculating the excess power at various altitudes at MTOW, it was possible to plot the operational flight envelope combined with the rates of climb relative to each altitude, limiting the plots to mach numbers less than one.

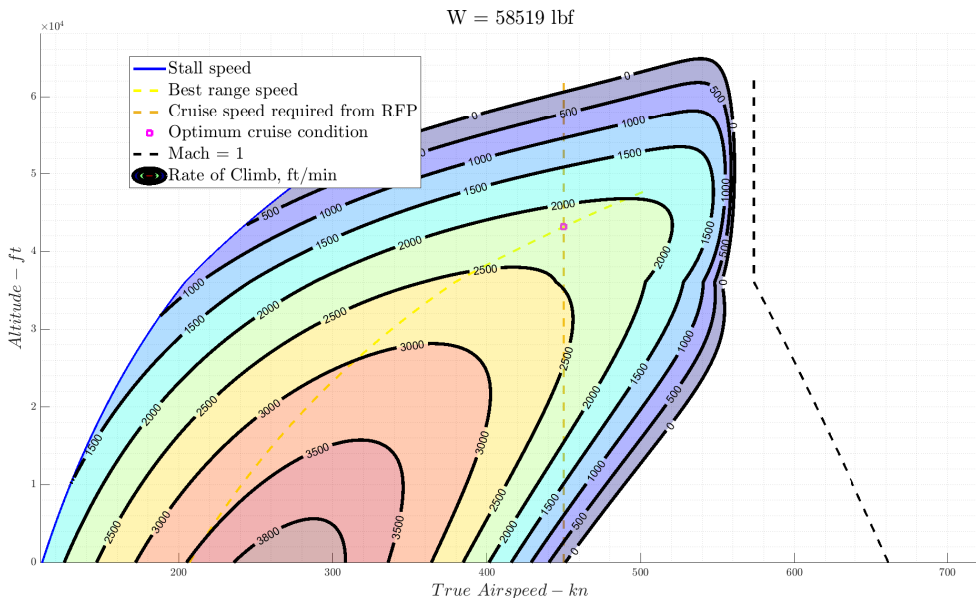


Figure 18.25: Operational Flight Envelope



18.2. Rotorcraft mode

The calculation of rotorcraft performance is largely a matter of determining the power required and power available over a range of flight conditions. The power information can then be translated into quantities such as payload, range, ceiling, speed, and climb rate, which define the operational capabilities of the aircraft. The rotor power required is divided into four parts: the induced power, required to produce the rotor thrust; the profile power, required to turn the rotor through the air; the parasite power, required to move the aircraft through the air; and the climb power, required to change the gravitational potential energy. In addition, all losses caused by transmission, rotor downloading to the fuselage, and similar are considered through a coefficient $\eta = 0.85$

18.2.1. Hover performance

Hover performance can be treated with the same mathematical model introduced in the section 9.3

Figure 18.26 is called hover polar and expresses the link between C_P and C_T in hover.

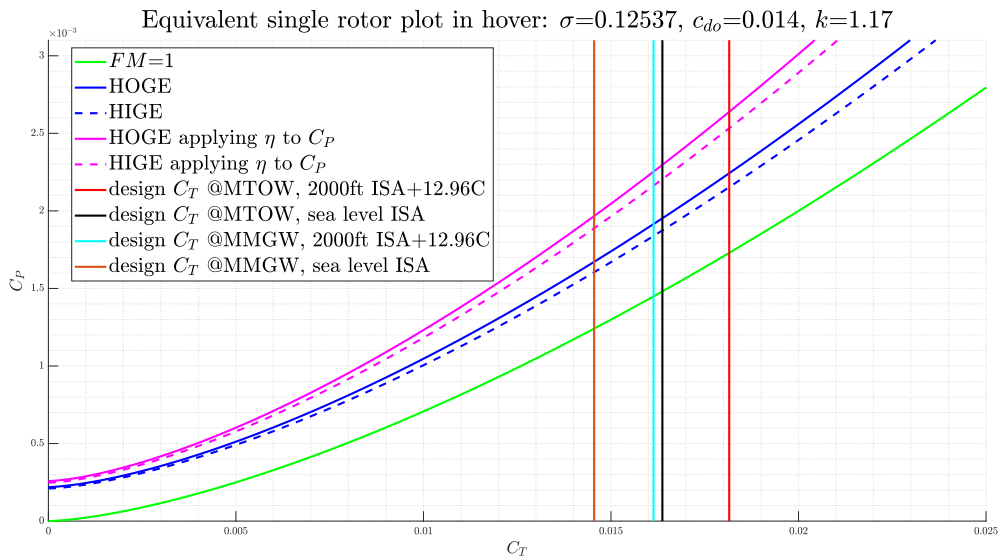


Figure 18.26: Hover polar

Figures 18.27 and 18.28 concern about the figure of merit. The figure of merit is a measure of rotor hovering efficiency, defined as the ratio of the minimum possible power required to hover to the actual power required to hover. Thus the figure of merit compares the actual rotor performance with the performance of an ideal rotor, which has only the inescapable induced power. However, the figure of merit can be misleading, since M is

not directly concerned with the total hover power. By increasing the disk loading, the induced power is increased relative to the profile power, resulting in a higher figure of merit. However, the total power required also then increases, which is unlikely to be considered an improvement in the rotor efficiency. The use of the figure of merit to compare rotors is thus best restricted to constant disk loading. In the figure 18.26 it can be seen that for zero thrust, the rotor with $FM=1$ requires no power, considering only the induced power, while the real rotor while producing no thrust must expend energy to keep itself rotating through the air.

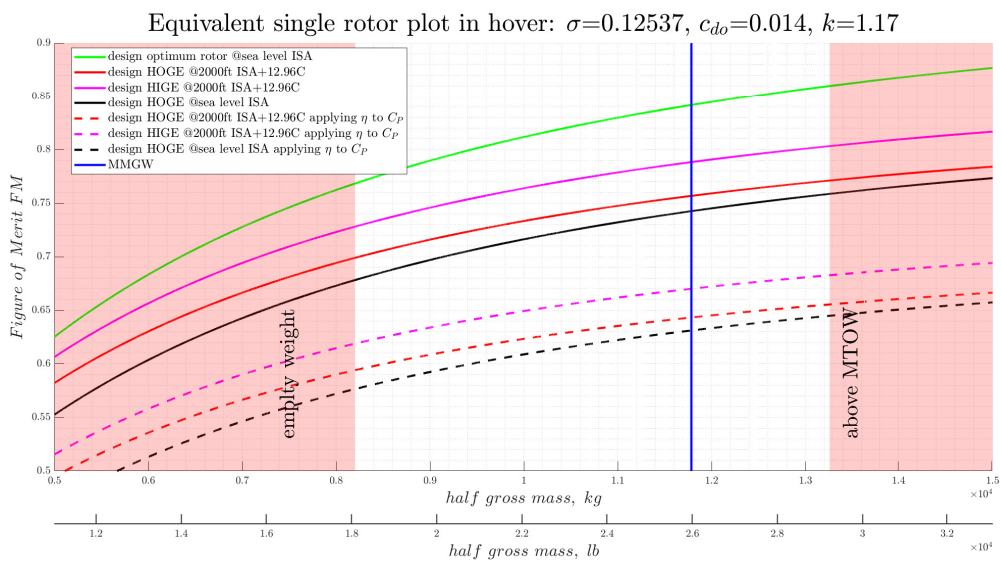
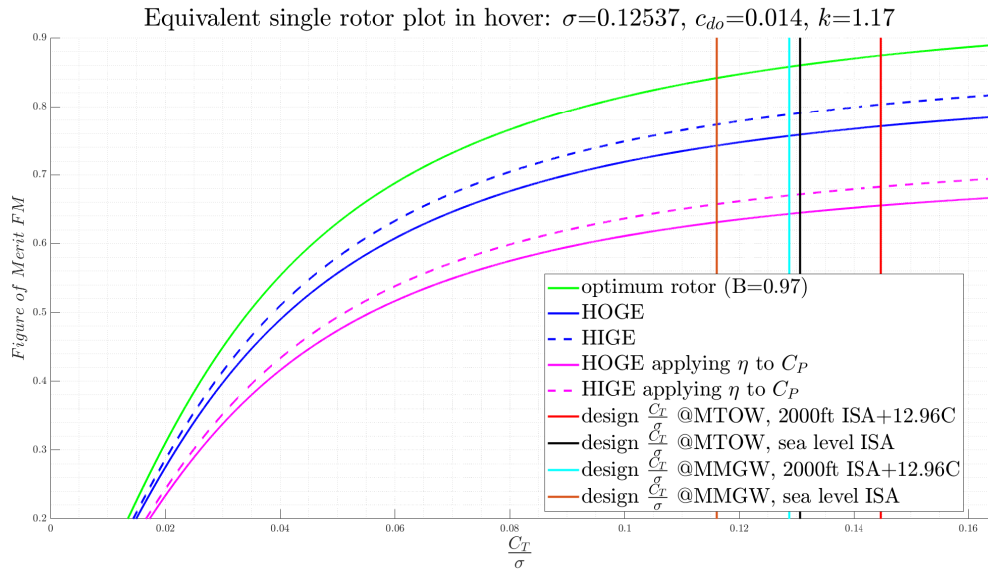


Figure 18.27: FM vs gross weight





18.2.2. Rotor download

The rotor downwash acting on the fuselage produces a vertical drag force or download on the helicopter in hover and vertical flight. This drag force requires an increase in the rotor thrust for a given gross weight and hence degrades the helicopter performance.

Exploiting the momentum theory in hover, the download can be expressed as [9]:

$$\frac{\Delta T}{T} = \frac{\Delta W}{W} = \frac{S}{A} \left(\frac{n^2 C_D}{4} \right) \quad (18.7)$$

where A is the rotor area, S is the wing area under the rotor projection, C_D has been selected pretending the wing effect to be the same of a flat plate in terms of drag, and n accounts for the distance between wing and rotor z as follows:

$$n = 1 + \frac{z/R}{\sqrt{1 + (z/R)^2}} \quad (18.8)$$

Figure 18.29 shows the download effect varying the wing surface under the rotor and the distance of the rotor from the wing. In particular, this plot can be exploited to chose an appropriate flap surface, as they can be rotated 90 degrees in hover reducing the area subtended by the rotor. The red dot shows the design point chosen resulting in a tolerable download of 7.89%.

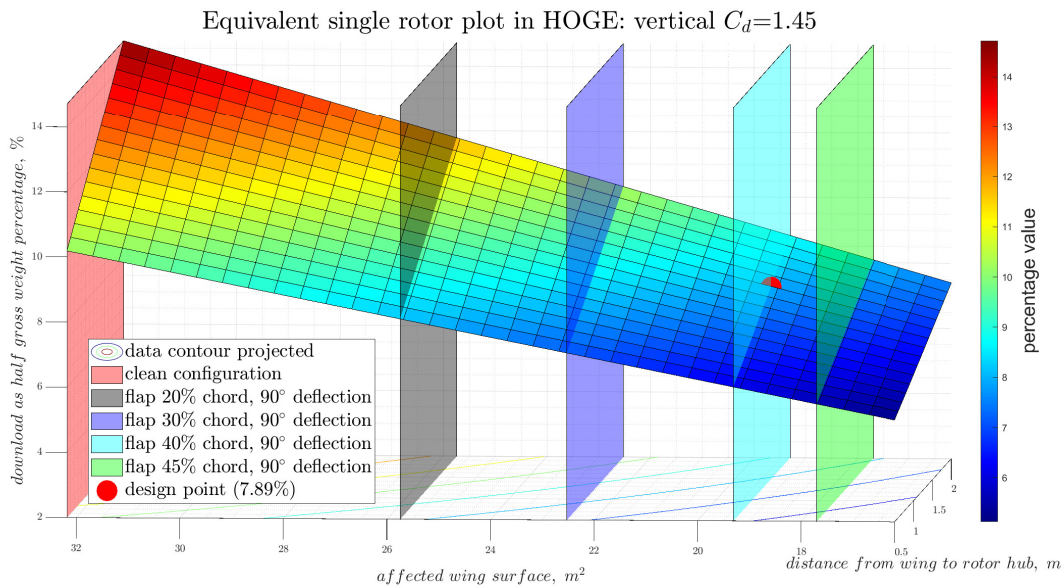


Figure 18.29: Equivalent single rotor download effect

The Raven 4 fell between helicopter and tiltrotor in this parameter, since the typical download value for that categories are respectively 5% and 10%.

In addition, downloading can have adverse aeroelastic effects on the wing, called whirl flutter, that must be taken into account in advanced design phase.

18.2.2.1. Download model validation

This simple model, presented in reference [9] chapter 4, has been validated with known download percentage of some helicopters and tiltrotor, yielding good consistency. Here, figure 18.30, is the case of V22 Osprey, the result of which aligns perfectly with the known data on the tiltrotor class.



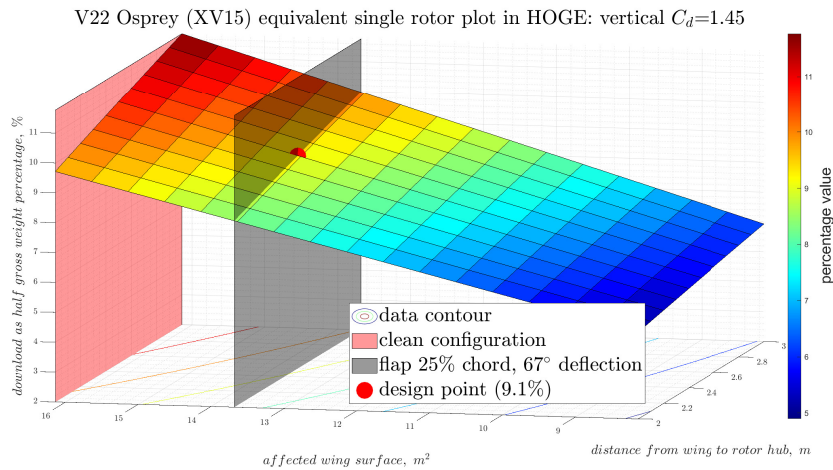


Figure 18.30: Equivalent single rotor download effect, V22 Osprey validation

The 67-degree deflection value was found in a paper reporting on the advanced study of V22 [21], where it was found that this angle was able to reduce unfavorable interference between rotor and wing more than a 90-degree deflection.

18.2.3. Edgewise forward flight

The estimation of helicopter parasite drag is an important aspect of performance calculation because it establishes the propulsive force and power requirement at high speed. A major contributor to the helicopter drag is the rotor hub, which typically accounts for 25% to 50% of the total parasite drag area.

Taking advantage of the statistical work of Keys and Rosenstein (1978 in the figure 18.31, a single hub drag drag of $f_{hub} = 12.6 \text{ ft}^2$ has been estimated. Using the same reference surface used in the chapter 17 for homogeneity, yields $C_{D_{HUB}} = 0.014$.

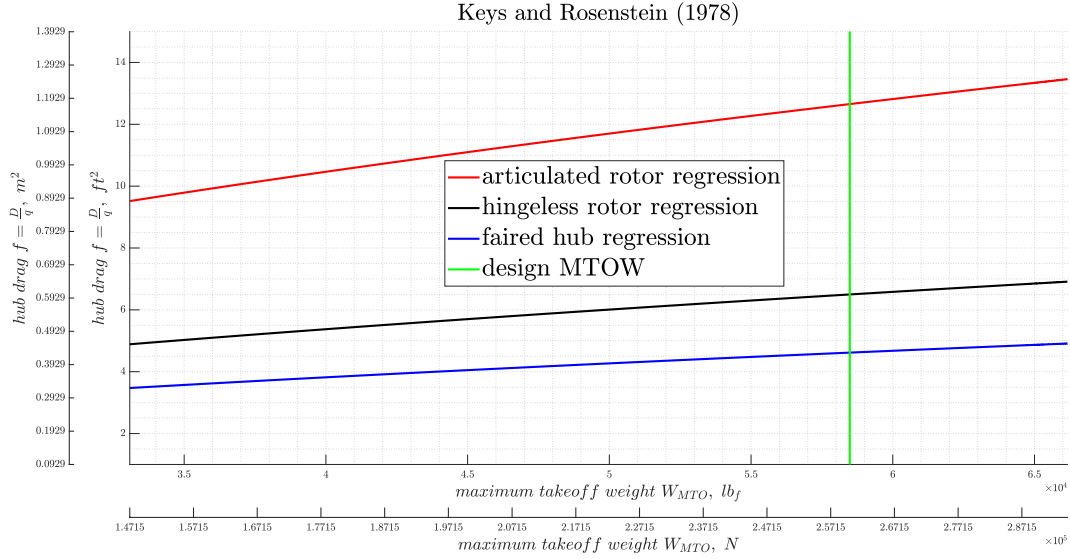


Figure 18.31: Statistical hub drag

In general, the power required in forward edgewise flight can be expressed as:

$$C_P = \frac{\kappa C_T^2}{2\mu} + \frac{\sigma c_{d0}}{8}(1 + 4.65\mu^2) + \frac{1}{2}\mu^3 \frac{f}{A} + \lambda_C C_T \quad (18.9)$$

accounting respectively for induced, profile, parasite and climb power, where μ is the advance ratio defined as:

$$\mu = \frac{V}{\Omega R} \quad (18.10)$$

and f can be roughly estimated as $f = f_{hub} + \frac{f_{wb}}{2}$ to account for wing, fuselage, and similar sources of drag. Recall that the analysis concern an equivalent single rotor, so the drag coefficient of the wing body has been brutally divided by two in this very first analysis (the limit of this assumption are well known, since it is not true that the drag coefficient of a halved body is the coefficient of drag halved, however, a small change is assumed and the only effect can be modeled as a halving of the surface area).

Also note that the expression of induced power reported in equation 18.9 is valid only at high speeds, i.e. $\mu > 0.1$. At lower speeds it is possible to write:

$$C_{P_i} = \frac{k C_T^2}{2\sqrt{\mu^2 + \lambda^2}} \quad (18.11)$$

where the Glauert inflow ratio formula states:



$$\lambda_i = \frac{C_T}{2\sqrt{\mu^2 + \lambda^2}} \quad (18.12)$$

$$\lambda = \lambda_i + \mu \tan i \quad (18.13)$$

from the latter two equations it is possible to obtain λ by an iterative method for each flight condition. For further details refer to reference [9], chapters 5, 7.

On the other hand, the model used to estimate profile power holds well up to $\mu = 0.5$, well sufficient for this work.

However, this configuration does not correspond exactly to a helicopter: the presence of the jet engine can be modeled as a reduction in drag and thus, in the equation 18.9, as a decrease in f . Also, the presence of the wing can be modeled, in the equation 18.9, as an aggravation or a relief on C_T depending on whether it generates downforce or lift. However, at this stage the estimation of wing C_L is complicated, since the trim condition in forward flight and thus the angle of attack is not yet known (regarding this refer to chapter 19). Moreover, for the jet, it is chosen, to stay conservative, thus to consider the thrust to be zero, simulating, for example, a failure of the latter. While considering the wing, a further study of the effect of the rotor downwash on it must be performed. However, while velocity increases the rotor wake is dragged posterior to the wing and the interaction should vanish or at least reduce. Results are reported, for different weights and turboshaft power conditions. Namely combination of MMGW,MTOW,MCP,MRT.

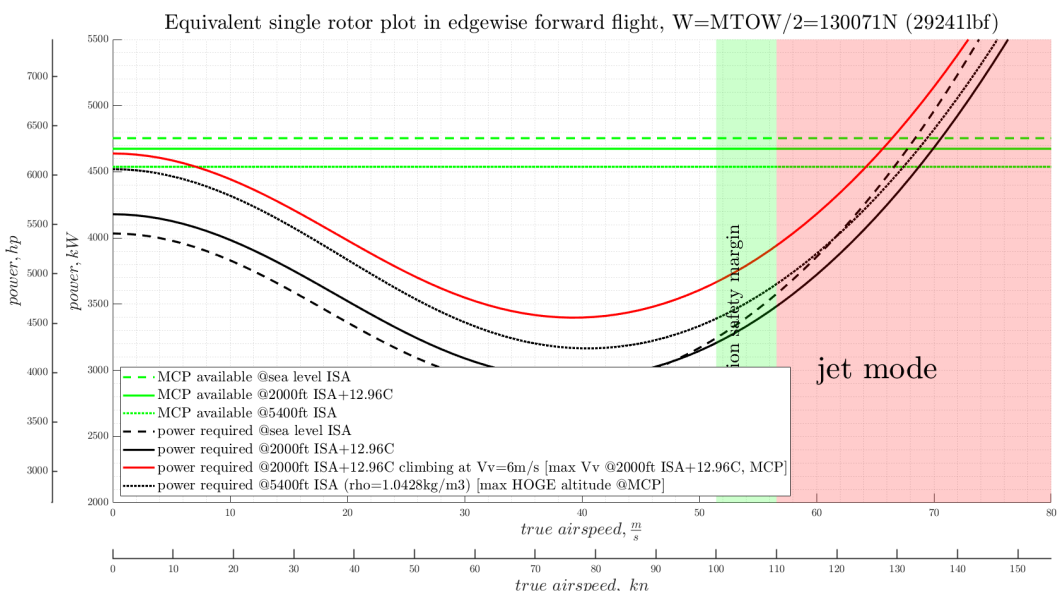


Figure 18.32: Edgewise forward flight (MTOW vs MCP)

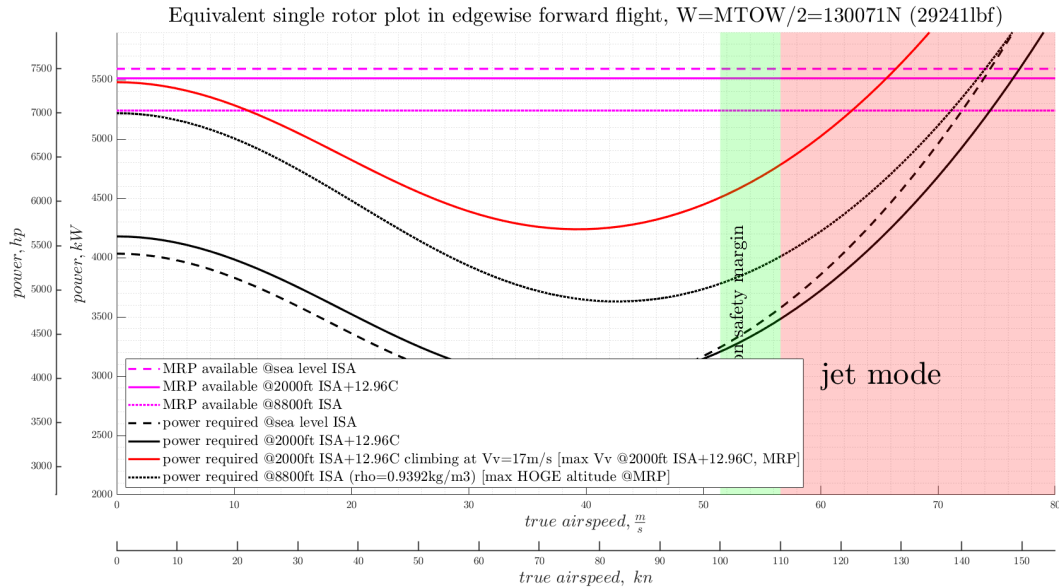


Figure 18.33: Edgewise forward flight (MTOW vs MRP)

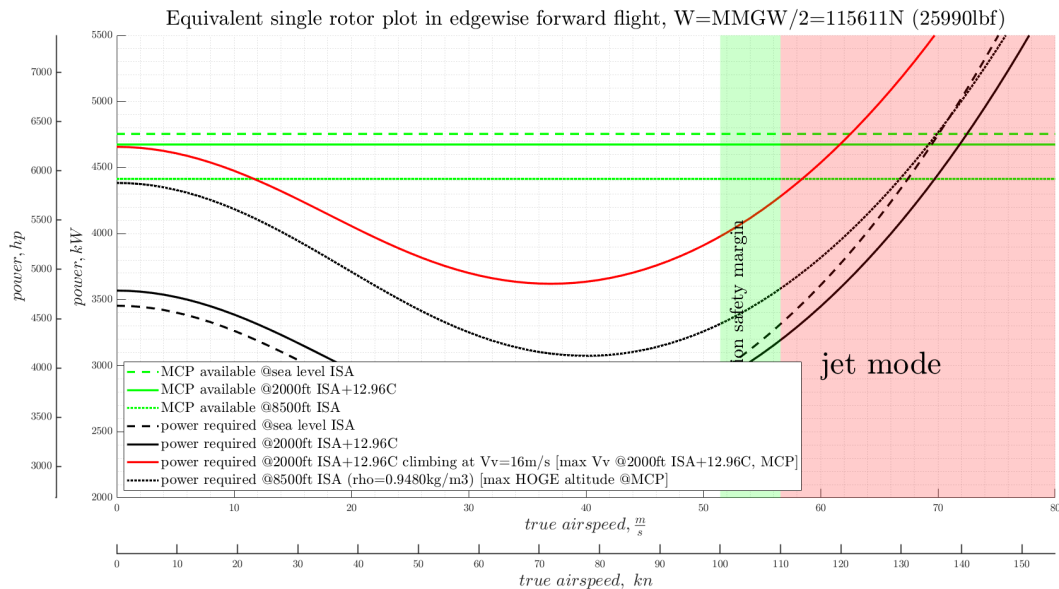


Figure 18.34: Edgewise forward flight (MMGW vs MCP)



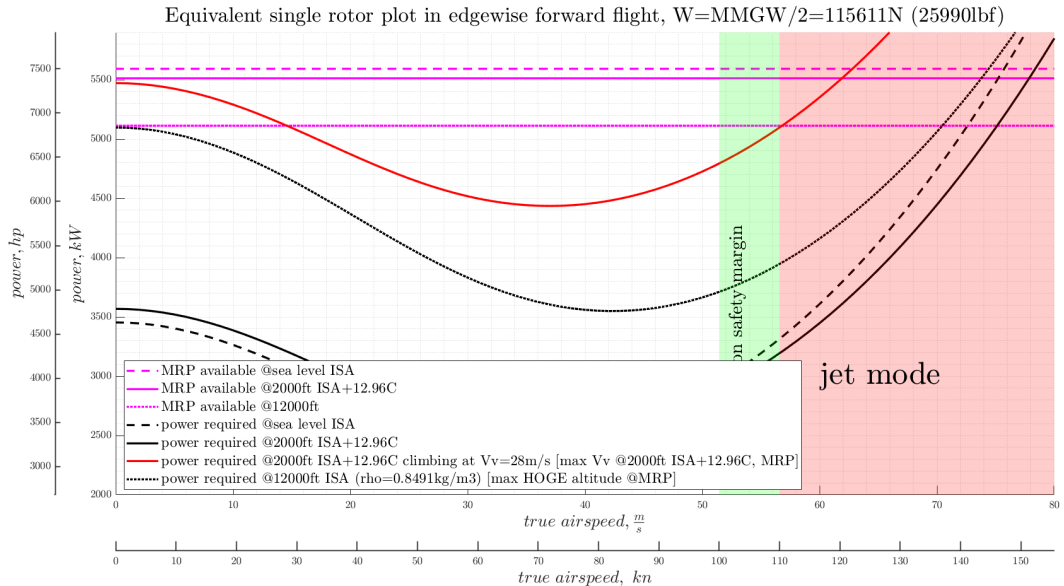


Figure 18.35: Edgewise forward flight (MMGW vs MRP)

Note that the hover condition is always the most critical in terms of power. In the graphs for the respective weights, it was also possible to find the maximum performance of the vehicle in hover and vertical flight. The classic rising of the curve due to parasite drag determine the maximum velocity in forward flight.

18.2.3.1. Equivalent lift-to-drag

The rotor equivalent drag-to-lift ratio is defined as:

$$\left(\frac{D}{L}\right)_e = \left(\frac{D}{L}\right)_i + \left(\frac{D}{L}\right)_o \quad (18.14)$$

where the two terms accounts for induced and profile drag-to-lift ratio. Results are reported in figure 18.36.

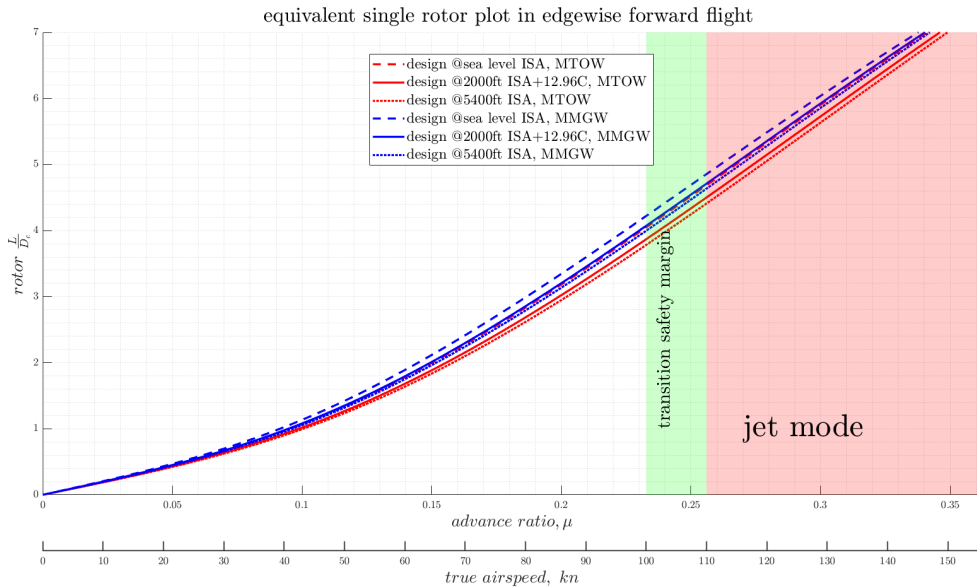


Figure 18.36: rotor lift-to-equivalent drag

As a last consideration, since the two rotors are not excessively close laterally, the beneficial mutual interaction between the two was neglected at this stage. This does not generate concern because a potentially worse situation has been analyzed.

18.2.4. Summary of rotorcraft performance

HOGE: MCP, MTOW	up to 5400 ft ISA
HOGE: MCP, MMGW	up to 8500ft ISA
HOGE: MRP, MTOW	up to 8800 ft ISA
HOGE: MRP, MMGW	up to 12000 ft ISA
V _V @2000 ft ISA, MCP, MTOW	6 m/s
V _V @2000 ft ISA, MCP, MMGW	16 m/s
V _V @2000 ft ISA, MRP, MTOW	17 m/s
V _V @2000 ft ISA, MRP, MMGW	28 m/s
V _H @2000 ft ISA, MCP, MTOW	136 KTAS
V _H @2000 ft ISA, MCP, MMGW	140 KTAS
V _H @2000 ft ISA, MRP, MTOW	148 KTAS
V _H @2000 ft ISA, MRP, MMGW	149 KTAS

Table 18.10: Summary of rotorcraft performance obtained



18.2.5. Conversion and jet thrust

The thrust to go from hover to conversion could be ideally provided by the jet only. As already stated, the way to arrive at the conversion phase will be discussed in Chapter 19. However, here the purpose is to demonstrate that all the thrust to balance the drag can be provided by the jet only, i.e. the rotor provides only vertical sustenance.

The zoom in the graph expand the zone when the AoA is increased and the rotor slowed down, which is obviously the worst from the jet point of view. The drag coefficient to build this graph are taken from Chapter 17. The figure 18.37 shows the required versus the available thrust of the jet engine. Since the available thrust of the jet is dependent with velocity, the available thrust was linearized around the the conversion velocity.

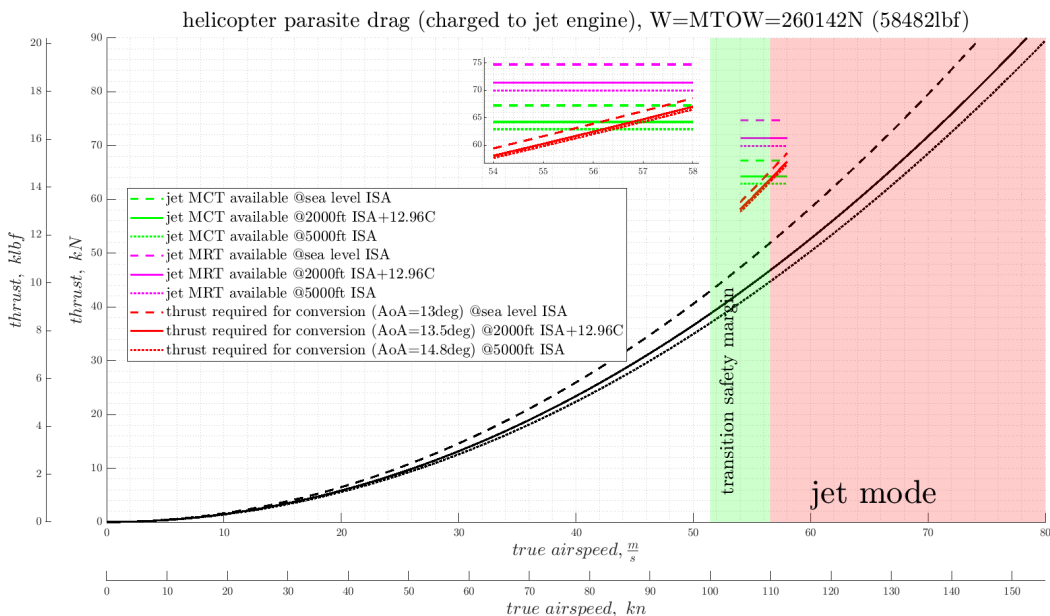


Figure 18.37: Required vs available jet thrust in conversion

18.3. Mission performance data

Table 18.11 lists the performance of the aircraft during the mission profile provided by RFP. In addition, Figures 18.38 and 18.39 show the actual mission profile with the corresponding fuel consumed during the flight phases. In particular, since the turboshaft engines remain active during all flight phases, fuel consumption of them was considered as if they were in idle during all jet-mode phases. However, even considering this additional fuel consumption of the engines in idle, it remains a small margin of fuel (approximately 7% of the total fuel) that could be used for additional safety in reserve, or to improve

mission performances, such as increasing mission duration and range, reducing cruise altitude (moving further away from the best-range condition), and so on.

Mission	Altitude	Average mass	Airspeed (average)	Distance or Time	Fuel flow	Power required	Power available
Idle	0 ft	58520 lb	0 kn	10 min	-	0	idle
HIGE (take-off)	2000 ft	58449 lb	0 kn	2 min	$70.7 \frac{lb}{min}$	5379 hp	5379 hp
1st climb	-	57532 lb	313 kn	46 nm	$158.1 \frac{lb}{min}$	3665 lbf	12640 lbf
1st cruise	31000 ft	55803 lb	450 kn	410 nm	$39.0 \frac{lb}{min}$	4366 lbf	4366 lbf
1st descent	-	54463 lb	226 kn	94 nm	$21.9 \frac{lb}{min}$	2845 lbf	1280 lbf
1st penetration	2000 ft	53863 lb	456 kn	50 nm	$98.7 \frac{lb}{min}$	11295 lbf	11295 lbf
HOGE	2000 ft	53451 lb	0 kn	2 min	$65.5 \frac{lb}{min}$	4977 hp	4977 hp
2nd climb	-	52752 lb	310 kn	41 nm	$157.8 \frac{lb}{min}$	5124 lbf	12142 lbf
2nd cruise	31000 ft	51048 lb	450 kn	421 nm	$38.9 \frac{lb}{min}$	4345 lbf	4345 lbf
2nd descent	-	49705 lb	221 kn	96 nm	$21.5 \frac{lb}{min}$	2481 lbf	1116 lbf
2nd penetration	2000 ft	49130 lb	455 kn	50 nm	$98.8 \frac{lb}{min}$	11300 lbf	11300 lbf
Landing	0	48718 lb	0 kn	2 min	$62.9 \frac{lb}{min}$	4785 hp	4785 hp
Reserve	2000 ft	48576 lb	210 kn	20 min	$7.8 \frac{lb}{min}$	2845 lbf	2845 lbf

Table 18.11: Mission profile parameters

Note that the distance traveled in the descent phases should not be considered in the mission profile according to military regulations.



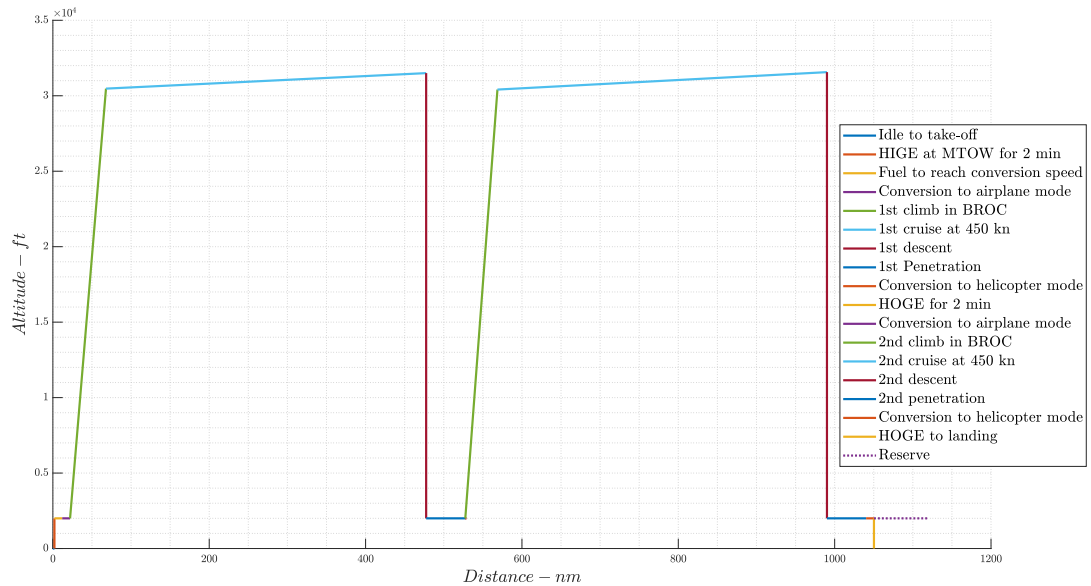


Figure 18.38: Typical mission profile

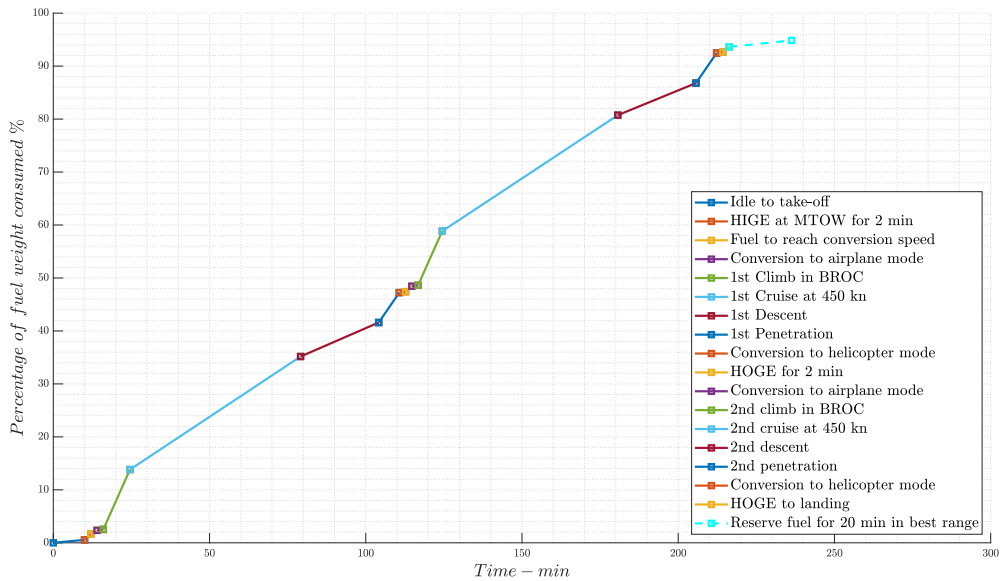


Figure 18.39: Fuel consumed during primary mission profile

19 | Equilibrium, control and static stability

19.1. Longitudinal equilibrium, control and static stability in jet-mode

Assume steady, level ($\gamma = 0$), symmetric ($\beta = 0$), maneuver in the plane of symmetry ($p = r = 0$), non-rotating flight ($q = 0$) and neglect the propulsive component of force and moment ($T \sin(\varepsilon) = 0$, $\Gamma_{CG_y}^b = 0$). The longitudinal equilibrium can be written as:

$$\begin{cases} L = W \\ M_{CG} = 0 \end{cases} \quad (19.1)$$

Recalling the constitutive relations:

$$\begin{cases} L = L(\alpha, \delta_e, M, Re, q_d) = L_{|\alpha}\alpha + L_{|\delta_e}\delta_e + L_0 = L_{|\alpha}(\alpha - \alpha_0) + L_{|\delta_e}(\delta_e - \delta_{e0}) \\ M_p = M_p(\alpha, \delta_e, M, Re, q_d) = M_{p|\alpha}\alpha + M_{p|\delta_e}\delta_e + M_{p0} = M_{p|\alpha}(\alpha - \alpha_0) + M_{p|\delta_e}(\delta_e - \delta_{e0}) \end{cases} \quad (19.2)$$

the first step is possible because a linear dependency is observed in wind tunnel testing, then the system can be written in homogeneous form through α_0 and δ_{e0} , that can be obtained imposing:

$$\begin{cases} L_{|\alpha}\alpha_0 + L_{|\delta_e}\delta_{e0} + L_0 = 0 \\ M_{p|\alpha}\alpha_0 + M_{p|\delta_e}\delta_{e0} + M_{p0} = 0 \end{cases} \quad (19.3)$$

this is always possible since the system is always determined (the coefficients are independent).

Then to solve the problem quantitative knowledge of $L_{|\alpha}$, $L_{|\delta_e}$, L_0 , $M_{p|\alpha}$, $M_{p|\delta_e}$, M_{p0} is

required.

However, as shown in subsection 19.1.2, thanks to Borri's formulation, the problem can be shifted to the knowledge of $L_{|\alpha}$, $L_{|\delta_e}$, α_0 , δ_{e_0} , x_A , x_C , where A and C are the neutral and control points of the aircraft, respectively.

19.1.1. Two surface model

The quantitative of $L_{|\alpha}$, $L_{|\delta_e}$, L_0 , $M_{p|\alpha}$, $M_{p|\delta_e}$, M_{p0} , x_A , x_C is gained through a classical two-surface model as follow:

$$\begin{aligned} L_{|\alpha} &= q_d S(a^{wb} + \eta \sigma a^{ht}(1 - \varepsilon_\alpha)) \\ L_{|\delta_e} &= q_d S \eta \sigma b^{ht} \\ L_0 &= q_d S(a^{wb} i^{wb} + \eta \sigma a^{ht}(i^{ht} - \varepsilon_0)) \\ M_{p|\alpha} &= q_d S((x_{A^{wb}} - x_P)a^{wb} + \eta \sigma a^{ht}(x_{A^{ht}} - x_P)(1 - \varepsilon_\alpha)) \\ M_{p|\delta_e} &= M_{A^{ht}, \delta_e}^{ht} + q_d S \eta \sigma (x_{A^{ht}} - x_P) b^{ht} \\ M_{p0} &= q_d S((x_{A^{wb}} - x_P)a^{wb} i^{wb} + \eta \sigma (x_{A^{ht}} - x_P)a^{ht}(i^{ht} - \varepsilon_0)) + M_{A^{wb}}^{wb} + M_{A^{ht}}^{ht} \end{aligned} \quad (19.4)$$

Note that b^w is set to zero (no effect of elevator deflection on the wing) and $M_{A^{ht}|\delta_e}^{ht}$ can be set to zero for a symmetric tail, this implies $x_C = x_A^{ht}$ as proven in equation 19.5. Again the symmetry of the tail implies $M_{A^{ht}}^{ht} = 0$.

Moreover, note that the slope's coefficient were appropriately corrected with Prandtl-Glauert for each EAS condition (and thus its associated Mach).

The numerical values to be inserted in equation 19.4 can be found in wing and tail design chapters (11,12).

Furthermore:

$$\begin{aligned} x_A &= \frac{M_{p|\alpha}}{L_{|\alpha}} + x_P \\ x_C &= \frac{M_{p|\delta_e}}{L_{|\delta_e}} + x_P \end{aligned} \quad (19.5)$$

It is possible to note that the effect of the tail is to move the aerodynamic center backward compared to the case of the wing alone.

From the point of view of notation, The aerodynamic center of the aircraft, x_A , and the neutral point of the aircraft, x_N , are used interchangeably.

19.1.2. Borri's formulation

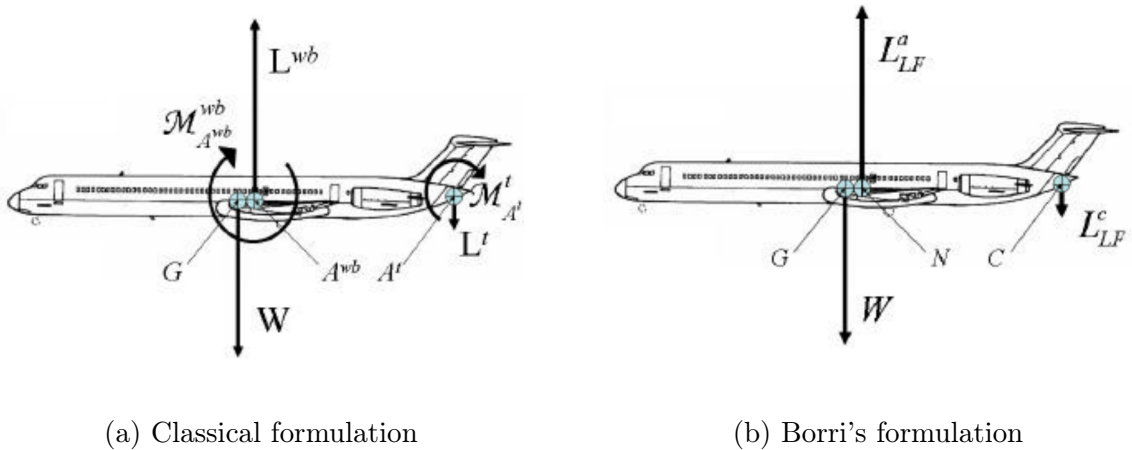
Borri's formulation, developed by Professors of the Politecnico di Milano Marco Borri and Lorenzo Trainelli with the aim of simplifying the system of aerodynamic forces acting on



the aircraft without assuming a particular aircraft configuration, was used to solve the equilibrium problem and study the static stability of the aircraft (Reference [1]).

In more details, starting by stating the ‘constitutive laws’ for lift and pitching moment under hypotheses of linear, low subsonic, steady-state aerodynamics in symmetric flight, we are naturally drawn to introduce the neutral and control points. These quantities allow to reduce the complex system of aerodynamic forces acting on the airplane to an equivalent one consisting in only two single applied forces. This considerably simplifies the form of the expressions relevant to trim and static stability analysis, leading to simple, intuitive reasoning on basic trim and stability issues.

Figure 19.1a and 19.1b show, respectively, the system of forces and moments used in the “classical” formulation and those used in the Borri’s model for level flight; the problem does not contain moments anymore making it much more intuitive.



Thus, firstly the static margin was calculated for different center of gravity position with the equation 19.6

$$SM = \frac{x_{CG} - x_N}{MAC} \quad (19.6)$$

where, MAC is the Mean Aerodynamic Chord, x_{CG} is the center of gravity position, and x_N is the neutral point position (or aerodynamic center of the airplane), considering the body axes (i.e., x-axis from nose to tail) as reference system.

The CG positions considered are the following one:

- CG aft position: ($x_{CG}^{aft} = -9.41\text{ m}$): $SM_{aft} = 1.5\%$
- CG fwd position: ($x_{CG}^{fwd} = -8.75\text{ m}$): $SM_{fwd} = 22.5\%$
- Nominal CG position in cruise: ($x_{CG}^{cruise} = -9.01\text{ m}$): $SM_{fwd} = 14.3\%$

In addition, these three conditions are shown in Figure 19.2. The typical range of static

margin should vary from 5% to 15%, while from the results obtained, Raven 4 could theoretically be in a near-neutral stability or too much stability condition. However, as already explained in detail in chapter 15, this center of gravity excursion is forced in order to ensure trim conditions in rotorcraft mode. It should also be noted both that the aircraft is equipped with a fuel-pump system that allows the static margin to be limited between 5% and 15% in all flight phases (in jet mode), details in chapter 15, and that the aircraft will be equipped with a SAS+CAS, details in chapter 21, which would allow controlled flight even in conditions of neutral stability or instability.

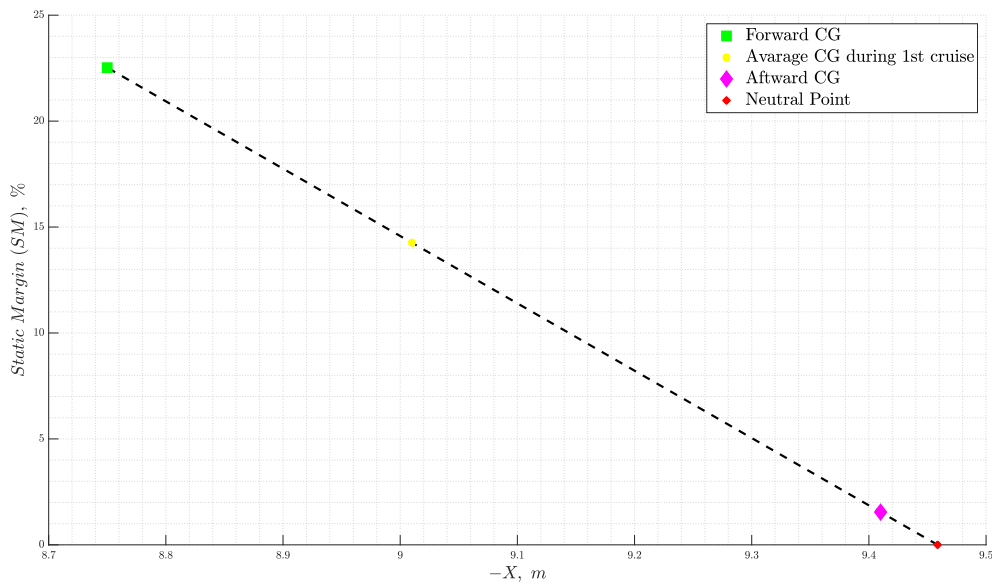


Figure 19.2: Static Margin for different position of center of gravity

Static stability concerns about the initial tendency of a given system when perturbed from an equilibrium condition. The word "initial" is critical in that it only pertains to the tendency at the first instant and nothing guarantees regarding the return to equilibrium after a perturbation, which must be analyzed through the dynamics of the aircraft. However static stability is a necessary condition for dynamic stability. In other words, it's a reduced form of the stability.

For an aircraft, the condition for static stability, also called pitch stiffness, is:

$$C_{m_{CG}|\alpha} < 0 \quad (19.7)$$

In general $C_{m_{CG}} = C_{m_{CG}}(\alpha, \delta_e)$. However δ_e in this discussion is considered fixed, which leads to a "stick-fixed" static stability condition. Otherwise it would be possible to define



a "stick-free" static stability condition. However, since the kinematic chain of the Raven 4 is non-reversible, the actuators controlling the control surfaces always impose a position on them, so the "stick-free" case is meaningless under these circumstances and will therefore not be analyzed. Starting from here and exploiting Borri's formulation it is possible to obtain a "practical" criterion for static stability by means of "Borri's parameter", defined in Equation 19.8

$$\varepsilon = \frac{x_{CG} - x_N}{x_N - x_C} \quad (19.8)$$

Where x_C is the control point (where the control lift is applied).

For a traditional tailed aircraft (i.e., $X_N > X_C$), Borri's parameter must be positive in order to ensure static stability.

The following results were obtained for Raven 4:

- $\varepsilon_{fwd} = 0.0767$
- $\varepsilon_{cruise} = 0.0486$
- $\varepsilon_{aft} = 0.0053$

Finally, the angle of attack and the elevator deflection to satisfy the equilibrium in level flight condition as function of EAS were calculated. Imposing equilibrium:

$$\begin{cases} L = L^a(\alpha) + L^c(\delta_e) = W \\ M_{CG} = L^a(\alpha) (x_N - x_{CG}) + L^c(\delta_e) (x_C - x_{CG}) = 0 \end{cases} \quad (19.9)$$

Where $L^a = L_{|\alpha}(\alpha - \alpha_0)$, $L^c = L_{|\delta_e}(\delta_e - \delta_{e0})$, and α_0 and δ_{e0} are the angles to ensure $L(\alpha, \delta_e) = 0$ and $M_{CG}(\alpha, \delta_e) = 0$, as already seen before.

Then, the solution to the equilibrium or trim problem is:

$$\begin{cases} \alpha - \alpha_0 = (1 + \varepsilon) \frac{W}{L_{|\alpha}} \\ \delta_e - \delta_{e0} = -\varepsilon \frac{W}{L_{|\delta_e}} \end{cases} \quad (19.10)$$

Hence, fixed a dynamic pressure, there is only a couple (α, δ_e) which satisfy the equilibrium equation 19.9. Note that α_0, δ_{e0} do not depends on dynamic pressure.

Figure 19.3 shows the angle of attack of the aircraft in level flight for different values of equivalent airspeed.

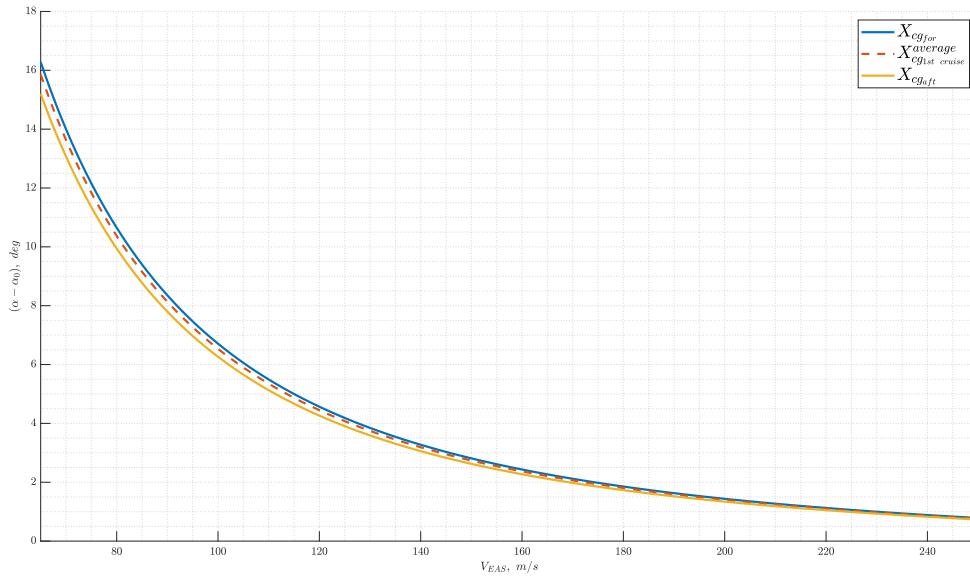


Figure 19.3: Angle of attack in level flight

Figure 19.4 shows the elevator deflection in level flight for different values of equivalent airspeed.

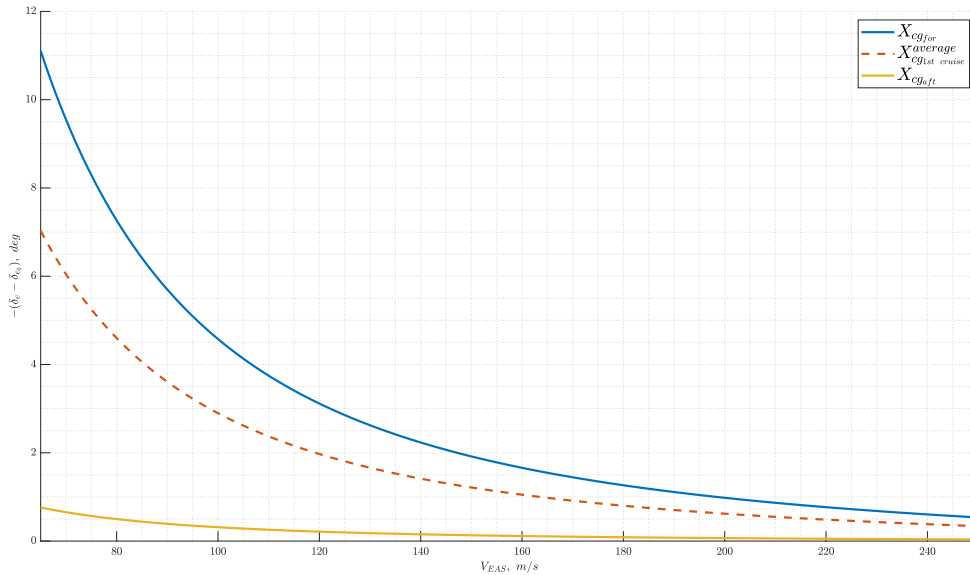


Figure 19.4: Elevator deflection angle in level flight

The trend of decreasing δ_e with increasing EAS is a clear indication of static stability, consistent with previous results.



19.1.3. Crocco's diagram

Crocco's diagram is a tool that provides a graphical representation of the solution to the stability and control problem of an aircraft in a single diagram. It was developed by Gaetano Arturo Crocco (Napoli, 1877-Roma, 1968), an aeronautical engineer and General of the former Royal Italian Air Force (Regia Aeronautica Italiana).

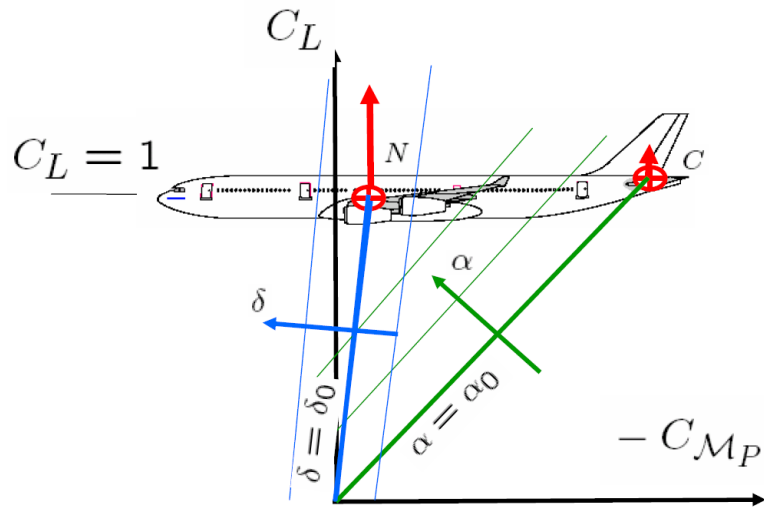


Figure 19.5: Example of Crocco's diagram

This approach visualise the (C_l, C_m) bond, which is analogous to the bond (α, δ_e) . For each couple (α, δ_e) a point on the diagram exist, however, as we shall see, only one pair satisfies the equilibrium equations.

According to Crocco's original development, the reference point P for the computation of the moment is the leading edge of the mean aerodynamic chord location, and so this reference has been retained in this discussion. The tool comprises two bundles of parallel lines: the green ones that are plotted each for a constant value of α are called isoclinic lines. On the other hand, the blue ones, plotted each for a constant value of δ_e are called stick lines. In order to define the lines equations, recall that is possible to write:

$$\begin{cases} C_L = C_{L|\alpha}(\alpha - \alpha_0) + C_{L|\delta_e}(\delta_e - \delta_{e0}) \\ C_{m_P} = (\xi_N - \xi_P)C_{L|\alpha}(\alpha - \alpha_0) + (\xi_C - \xi_P)C_{L|\delta_e}(\delta_e - \delta_{e0}) \end{cases} \quad (19.11)$$

where ξ is the dimensionless form of the position x , N the neutral point, C the control point, P the reference point.

For isoclinic lines, setting $\alpha = \alpha_0$, equation 19.11 turns in:

$$\begin{cases} C_L = C_{L|\delta_e}(\delta_e - \delta_{e_0}) \\ C_{m_P} = (\xi_C - \xi_P)C_{L|\delta_e}(\delta_e - \delta_{e_0}) = (\xi_C - \xi_P)C_L \end{cases} \quad (19.12)$$

Doing the same setting a different value for α , e.g. $\alpha = \alpha_1$:

$$\begin{aligned} C_{m_P} &= (\xi_N - \xi_P)C_{L|\alpha}(\alpha_1 - \alpha_0) + (\xi_C - \xi_P)C_{L|\delta_e}(\delta_e - \delta_{e_0}) \\ &= (\xi_N - \xi_P)C_{L|\alpha}(\alpha_1 - \alpha_0) + (\xi_C - \xi_P)(C_L - C_{L|\alpha}(\alpha_1 - \alpha_0)) \\ &= (\xi_C - \xi_P)C_L + (\xi_N - \xi_C)C_{L|\alpha}(\alpha_1 - \alpha_0) \end{aligned} \quad (19.13)$$

Inverting equation 19.13 it is possible to obtain C_L as a function of C_{m_P} , parameterized for different constant α_i :

$$C_L = \frac{C_{m_P} - (\xi_N - \xi_C)C_{L|\alpha}(\alpha_i - \alpha_0)}{(\xi_C - \xi_P)} \quad (19.14)$$

that is the equation for the isoclinic lines, where the subscript i indicates the general constant value of α . According to equation 19.12, the intersection between the isoclinic line $\alpha = \alpha_0$ and the horizontal lines $C_L = 1$ returns the dimensionless control point.

It is possible to use the same machinery to obtain the stick lines equation. Considering $\delta = \delta_{e_0}$ constant, equation 19.11 turns in:

$$\begin{cases} C_L = C_{L|\alpha}(\alpha - \alpha_0) \\ C_{m_P} = (\xi_N - \xi_P)C_{L|\alpha}(\alpha - \alpha_0) = (\xi_N - \xi_P)C_L \end{cases} \quad (19.15)$$

Doing the same but setting a different value for δ_e , e.g. $\delta = \delta_{e_1}$:

$$\begin{aligned} C_{m_P} &= (\xi_N - \xi_P)C_{L|\alpha}(\alpha - \alpha_0) + (\xi_C - \xi_P)C_{L|\delta_e}(\delta_{e_1} - \delta_{e_0}) \\ &= (\xi_N - \xi_P)(C_L - C_{L|\delta_e}(\delta_{e_1} - \delta_{e_0})) + (\xi_C - \xi_P)C_{L|\delta_e}(\delta_{e_1} - \delta_{e_0}) \\ &= (\xi_N - \xi_P)C_L + (\xi_C - \xi_N)C_{L|\delta_e}(\delta_{e_1} - \delta_{e_0}) \end{aligned} \quad (19.16)$$

Inverting equation 19.16 it is possible to obtain C_L as a function of C_{m_P} , parameterized for different constant δ_{e_i} :

$$C_L = \frac{C_{m_P} - (\xi_C - \xi_N)C_{L|\delta_e}(\delta_{e_i} - \delta_{e_0})}{(\xi_N - \xi_P)} \quad (19.17)$$



that is the equation for the stick lines, where the subscript i indicates the general constant value of δ_e . According to equation 19.15, the intersection between the stick line $\delta = \delta_{e_0}$ and the horizontal lines $C_L = 1$ returns the dimensionless neutral point.

Finally, the line that represent the relationship between C_L and C_{m_P} at trim condition, called barycentric line, must be computed. In analogy to the previous cases, it intercepts the dimensionless position of the center of gravity with respect to P along the line $C_L = 1$. To do so consider the condition at trim:

$$\begin{cases} C_L = C_L^* \\ C_{m_{CG}} = 0 \end{cases} \quad (19.18)$$

By applying the transportation of moment between G and P, the expression for the moment coefficient with respect to the leading edge of the MAC is:

$$C_{m_P} = C_{m_{CG}} - (\xi_P - \xi_G)C_L \quad (19.19)$$

Imposing the trim condition; i.e. $C_{m_{CG}} = 0$:

$$C_{m_P} = (\xi_G - \xi_P)C_L \quad (19.20)$$

and inverting the equation 19.20, the equation for the barycentric line is:

$$C_{m_P} = \frac{C_{m_P}}{(\xi_G - \xi_P)} \quad (19.21)$$

In conclusion there is a single isoclinic line and a single stick line for each trim point (so a single (α, δ_e) couple). To identify the trim condition, search for the couple of isoclinic and stick intersecting lines whose intersection lies on the barycentric line. Note that only the barycentric line depends on the center of gravity position. Hence, for a different CG condition corresponds a different barycentric line.

Figure 19.6 shows Crocco's diagram in cruise configuration, where the reference point (x_p) is the leading edge of the wing, and the black dashed lines are the barycentric lines for the center of gravity in forward position and aft position. The limits of this graph are the stall AoA for the isoclinic lines and the maximum deflection for the stick lines, and it is immediately observed that the aircraft is within these limits, so it can be trimmed, in all flight conditions. Furthermore, the center of gravity could be moved even further forward, up to the intersection of the α_{stall} and $\delta_{e_{max}}$ lines.

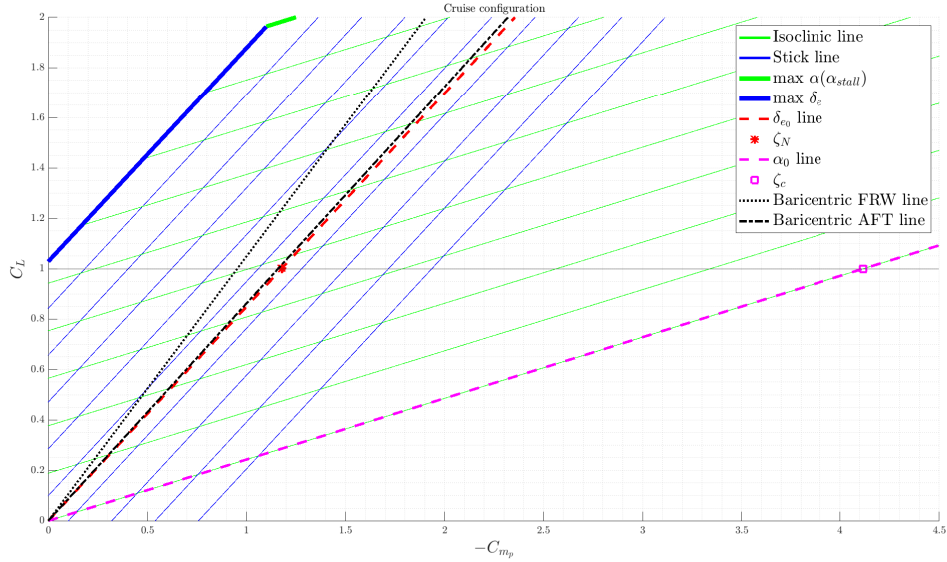


Figure 19.6: Crocco's diagram in cruise configuration

Crocco's diagram is also obtained for other important configurations, such as the rotorcraft-to-jet conversion phase (Figure 19.7), landing (Figure 19.8), and take-off (Figure 19.9). Specifically, the conversion phase occurs at 110 kn, 2,000 ft and flaps deflected by 30°, landing occurs at 105 kn, sea level and flaps deflected by 30°, and finally take-off occurs at 115 kn, sea level and flaps deflected by 10°.

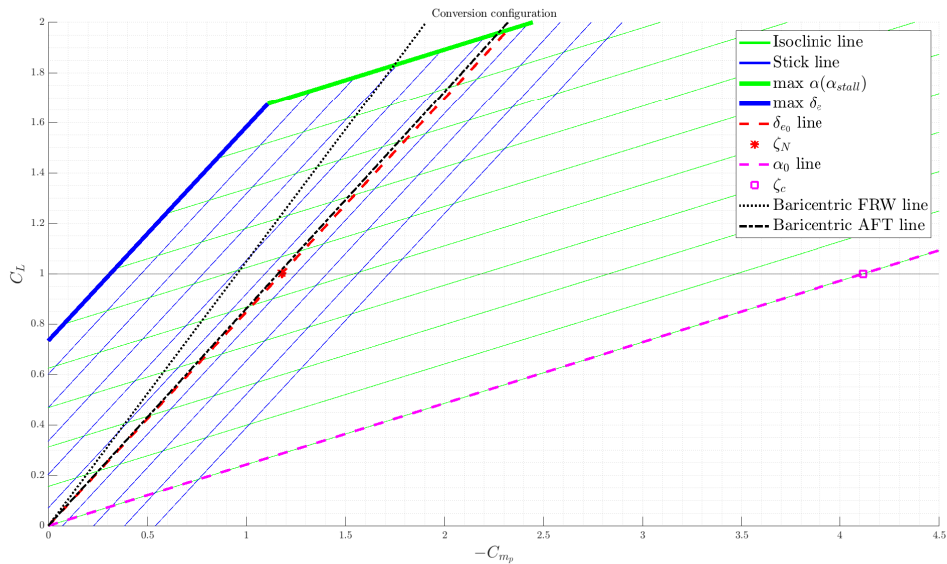


Figure 19.7: Crocco's diagram in conversion configuration



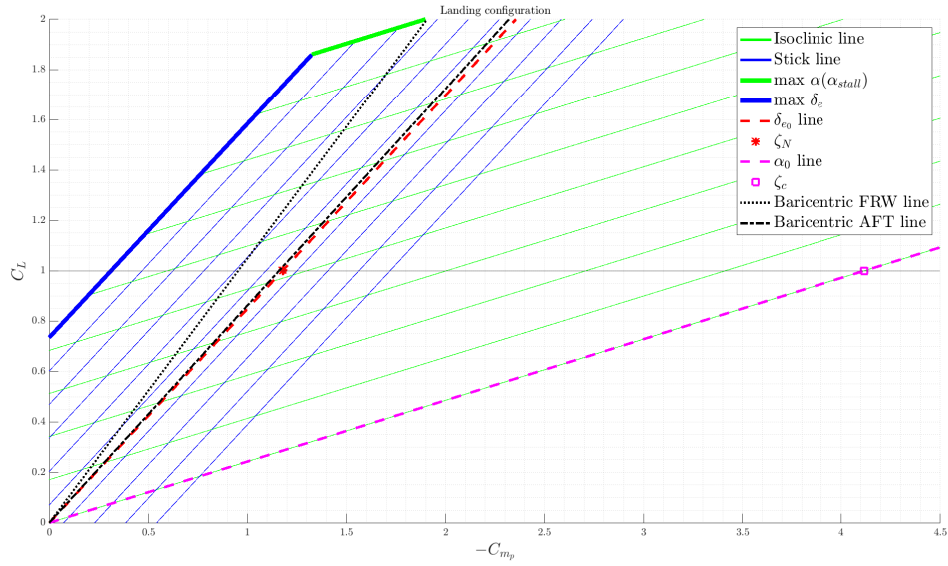


Figure 19.8: Crocco's diagram in landing configuration

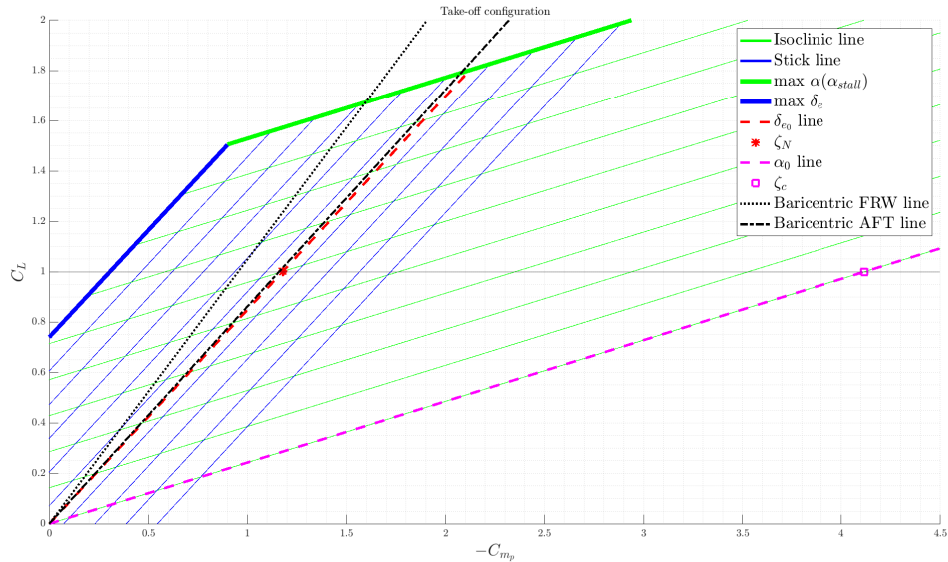


Figure 19.9: Crocco's diagram in take-off configuration

19.1.4. Maneuvering stability

From Borri's formulation it is possible to compute easily the neutral maneuver point (X_M) and consequently the Borri's parameter (e_M) in maneuvered flight (see Equation 19.22).

$$\begin{aligned} x_M &= x_N + \frac{M_{N_q}}{(n - 1) W} q \\ e_M &= \frac{x_{cg} - x_M}{x_N - x_C} \end{aligned} \quad (19.22)$$

The two main maneuvers were analyzed: pull-up and coordinated turn.

19.1.4.1. Pull-up and Pull-down

For a pull-up maneuver the pitch rate can be defined as:

$$q = (n - 1) \frac{g}{V} \quad (19.23)$$

Hence, static stability in pull-up is not influenced by the load factor. Borri's pull-up parameters for the three center of gravity conditions used for the level flight case are listed below:

- $e_M^{fwd} = 0.7937$
- $e_M^{cruise} = 0.7655$
- $e_M^{aft} = 0.7222$

As expected, static stability in pull-up has increased significantly. This phenomenon is probably due to the fact that the elevator instantly perceives a high angle of attack, producing a moment in favor of stability.

19.1.4.2. Coordinated turn

For a coordinated turn maneuver the pitch rate can be defined as:

$$q = \frac{n^2 - 1}{n} \frac{g}{V} \quad (19.24)$$

Therefore, the static stability in turn is affected by the load factor, and it is also observed that for an infinite load factor, the stability in coordinated turn will lean toward that of the pull-up maneuver. Figure 19.10 and 19.11 shows the Borri's parameters and static margin in the three center of gravity configurations with respect to the load factor.



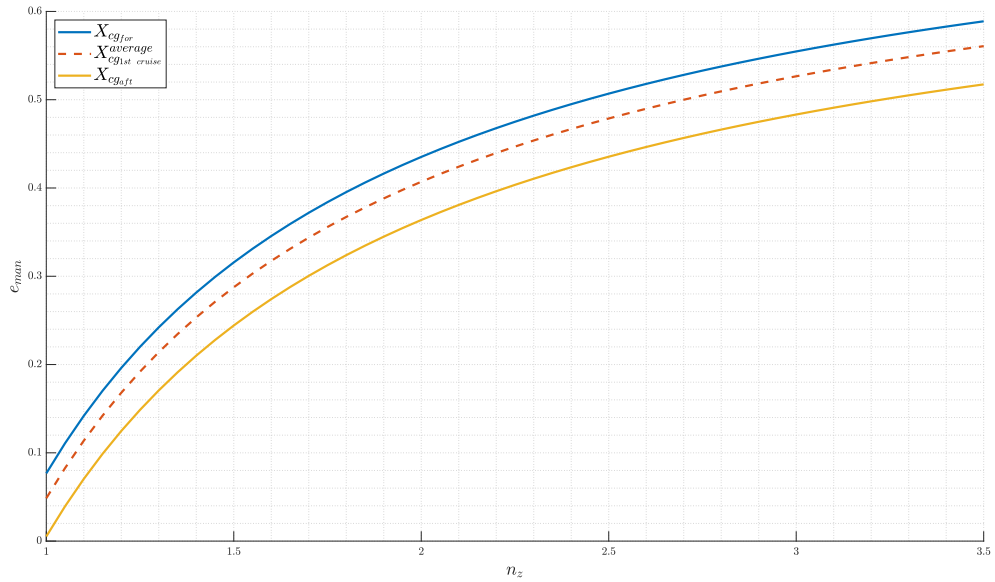


Figure 19.10: Borri's parameters in coordinated turn

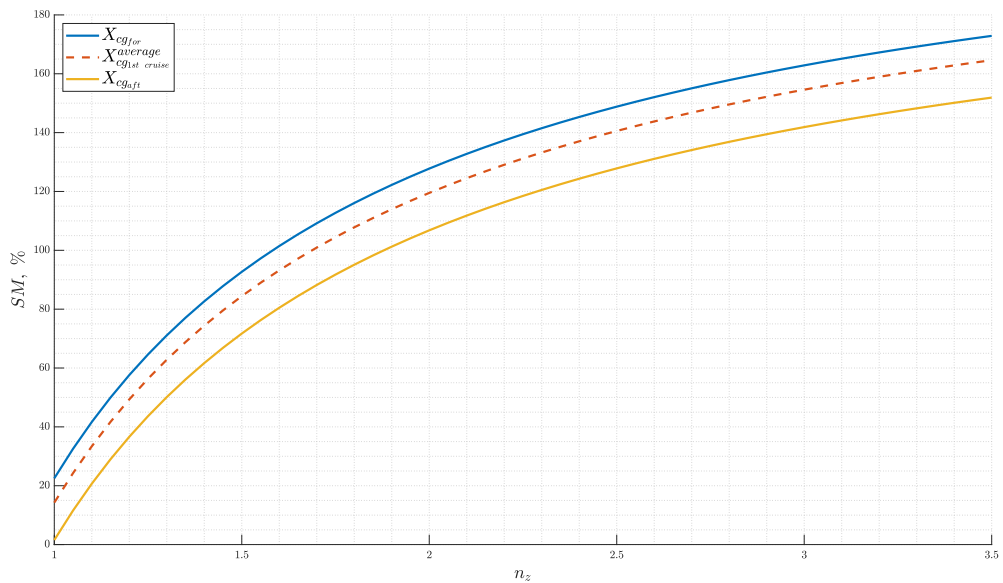


Figure 19.11: Static margins of coordinated turn

19.2. Trimmed lift and polar for Take-off, Conversion, Cruise, and Landing configurations in jet-mode

Typically, for a conventional aft-tailed aircraft, the trim condition is achieved with a combination of positive lift produced by the wing and a negative contribution from the tail, which is necessary to achieve momentum balance to get equilibrium. Consequently, the angle of attack must be greater than that of an isolated wing.

Therefore, the trimmed polars of the aircraft in the most important or most critical configurations were defined for different longitudinal position of the center of gravity.

19.2.1. Trim in cruise

Wing and tail are designed primarily to reduce drag in cruise. As might be expected, in a clean configuration in cruise, it is required just a small contribution of the tail to balance the aircraft. Furthermore, the changes in the angle of attack required for trim are very little as the center of gravity changes (Figure 19.12); similarly, for the trimmed drag (Figure 19.13).

In all the graphs below, zooms have been made for more clarity

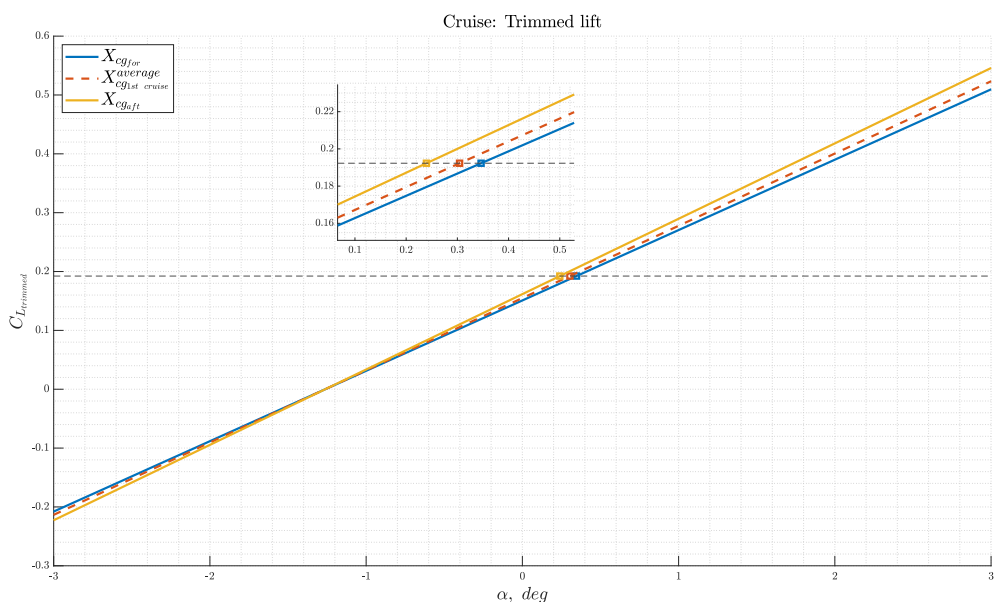


Figure 19.12: Trimmed lift in cruise configuration



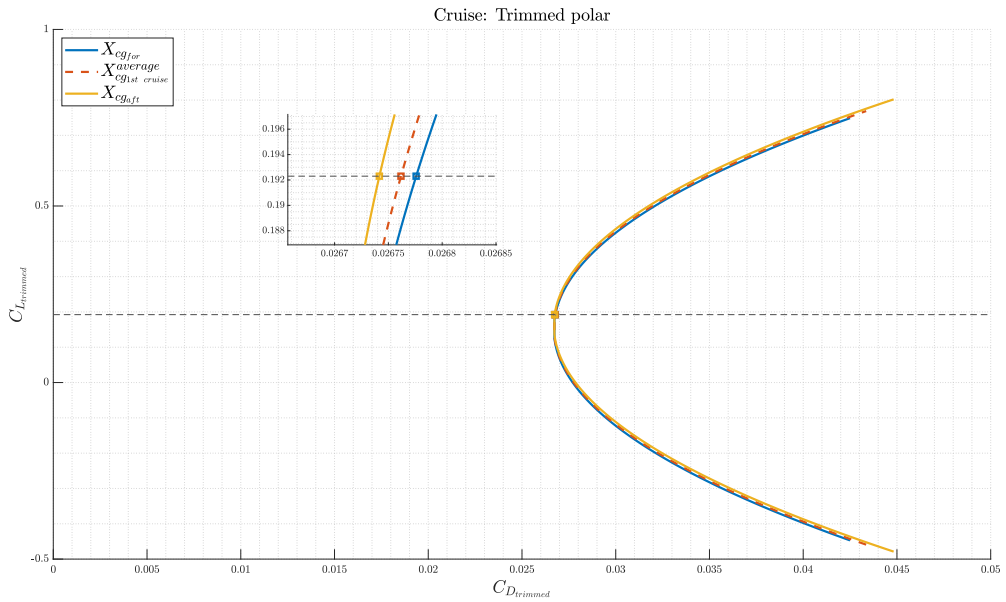


Figure 19.13: Trimmed polar in cruise configuration

19.2.2. Trim in conversion

The rotorcraft-to-jet conversion phase is another very critical configuration, as it is performed at low altitude and high angle of attack. From Penaud diagrams (Chapter 18), an angle of 13.5° was selected for this phase. Again, there are little changes from the position of the center of gravity; Figures 19.14 and 19.15 show the trimmed lift and trimmed polar in conversion configuration.

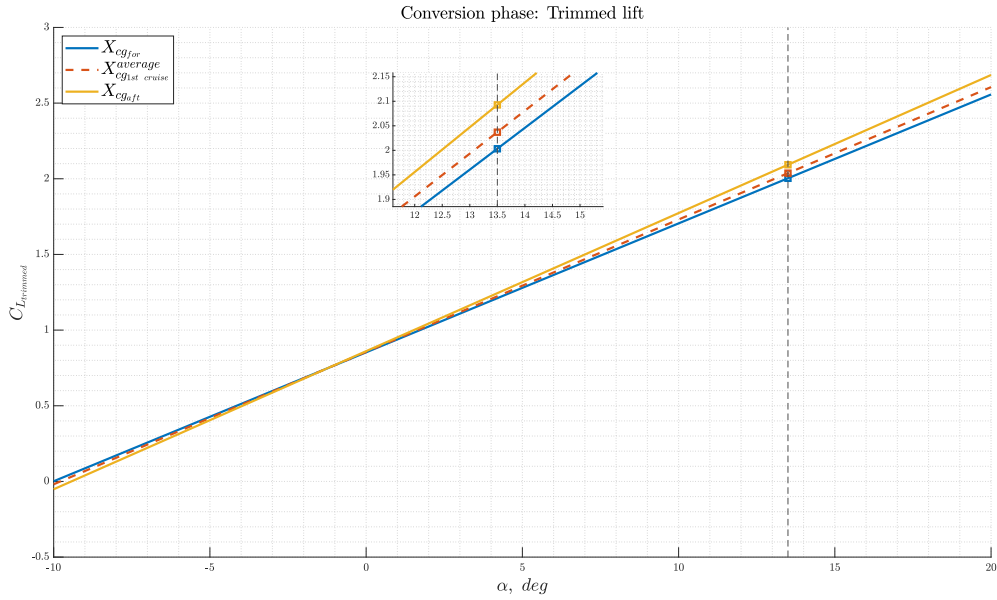


Figure 19.14: Trimmed lift in conversion configuration

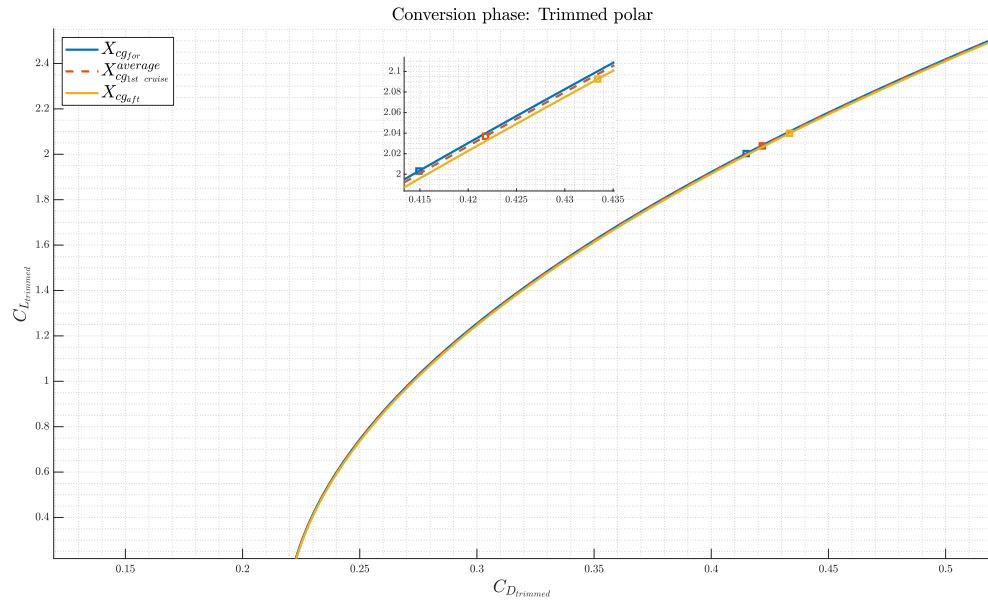


Figure 19.15: Trimmed polar in conversion configuration

19.2.3. Trim in take-off and landing

Typically take-off and landing are other critical configurations for a conventional aircraft. On the other hand, for Raven 4, vertical take-off/landing is the standard, however, the



Team decided to demonstrate the feasibility of take-off and landing even with closed rotors, seeing this as a strength not to be overlooked. Therefore, the polar and trimmed lift are graphed below for a typical takeoff and landing configuration.

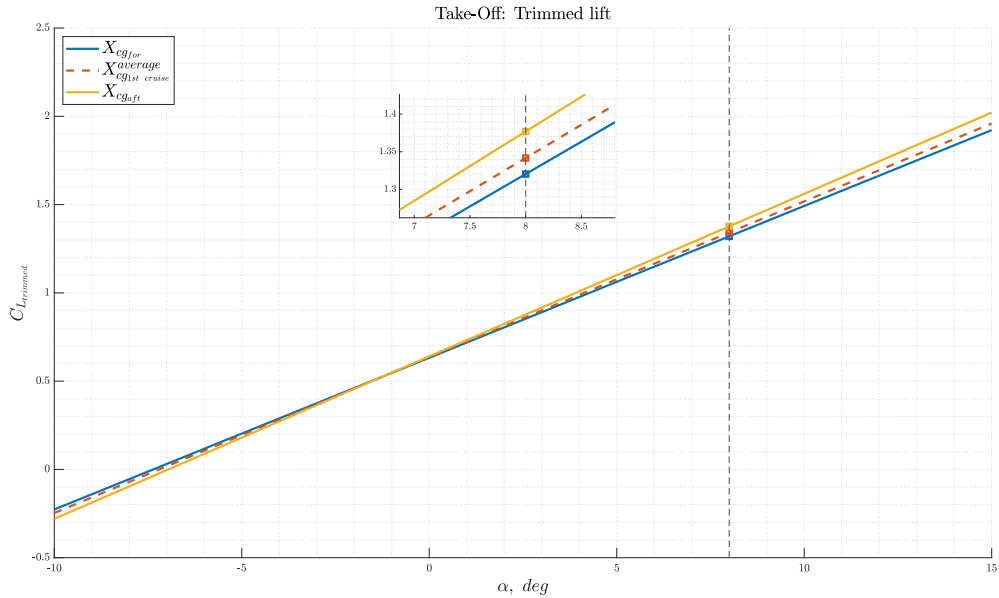


Figure 19.16: Trimmed lift in take-off configuration

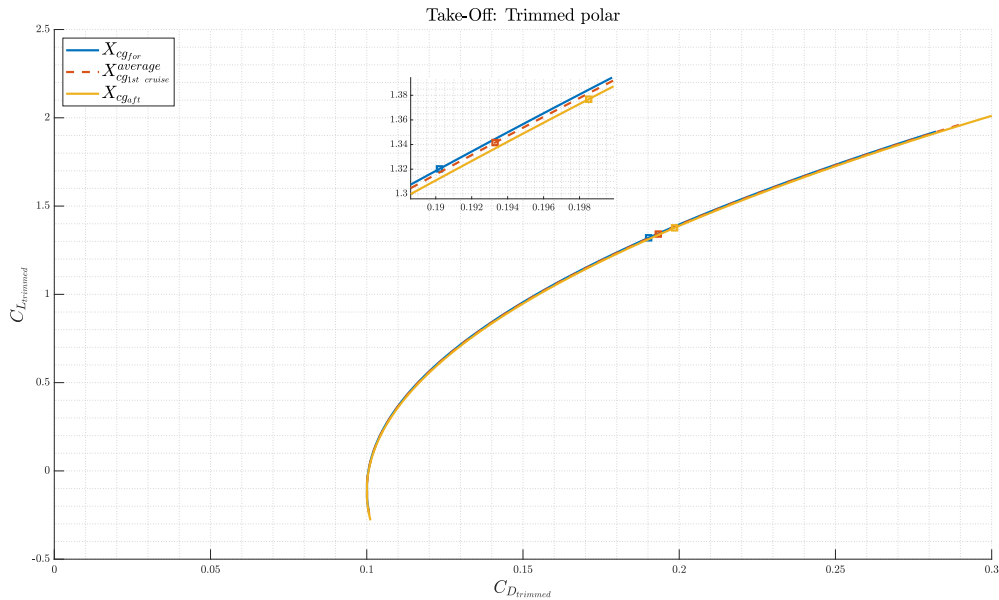


Figure 19.17: Trimmed polar in take-off configuration

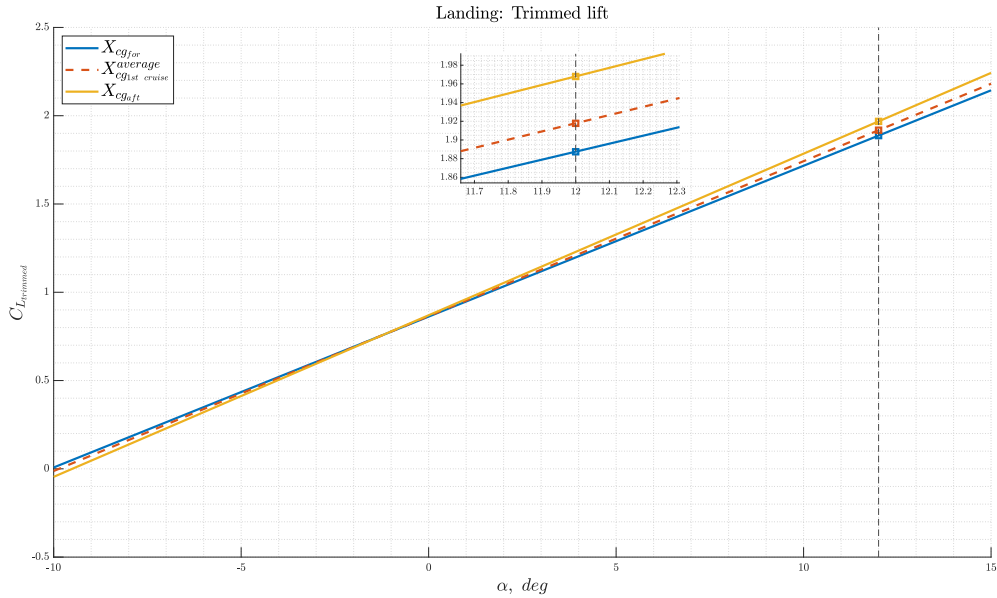


Figure 19.18: Trimmed lift in landing configuration

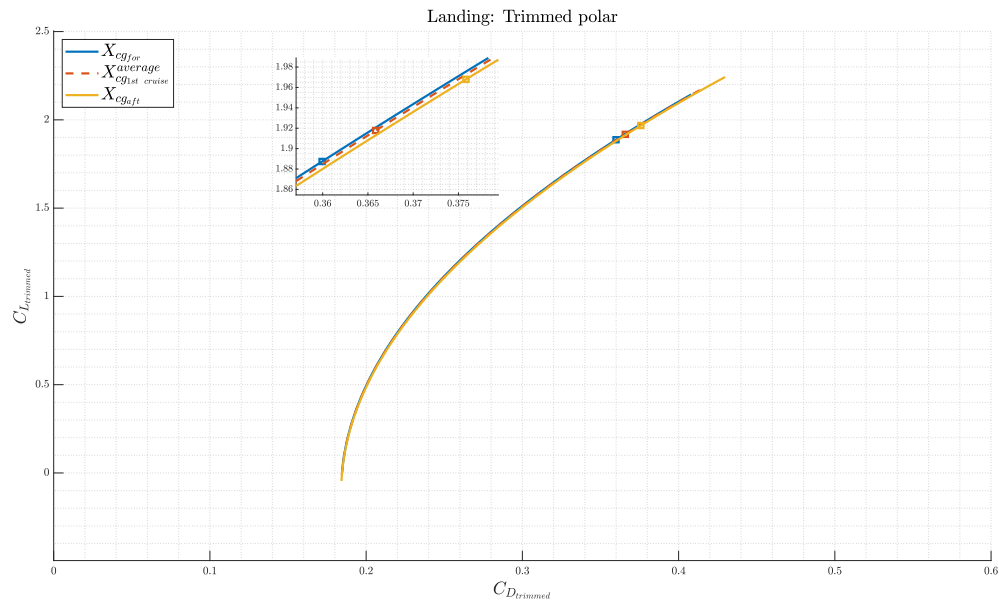


Figure 19.19: Trimmed polar in landing configuration



19.3. Equilibrium and control in rotorcraft-mode

19.3.1. Hover condition

Consider a helicopter in hover condition. The equilibrium can be imposed as:

$$\begin{cases} T = W \\ M_G = 0 \end{cases} \quad (19.25)$$

The rotor thrust must be necessarily aligned with the local vertical, otherwise there would be no way to impose horizontal equilibrium since only the rotor is able to generate forces and therefore the hover condition would not be met. Moreover, as already discussed in chapter 10, it can be assumed that the rotor can only generate forces (otherwise, to assess the moment it would be necessary to solve the flapping equations); the impact of this assumption in this framework will be taken up later, Where it will be shown to be a conservative situation (worst case scenario).

Having made these considerations, it is evident that the only way to achieve the trim condition is for the rotor thrust to pass through the center of gravity, so that no moment is generated. But since the rotor must as mentioned be horizontal, the trim condition implies that the fuselage is tilted appropriately from the local horizontal so that the center of mass is on the line of action of the thrust. The only case where the fuselage can be kept horizontal is where the center of mass is exactly on the axis of the rotor, a desirable condition and thus defined as nominal. However, a fluctuation in the position of the center of gravity during flight is unavoidable: the purpose of this section is to ensure that the aircraft can be trimmed in hover for extreme conditions of center of gravity, without implying angles of fuselage tilt with respect to the local horizon hat would impede the operational capability of the aircraft or crew.

In this analysis the case of lateral trim is trivial: by symmetry of the aircraft the resultant of the force of the rotors will lie on the plane of symmetry, as will the center of gravity. Even if there were load asymmetries a difference of collective between the two rotors is able to balance without problems the moment.

Otherwise, the longitudinal case must be investigated further. For Raven 4, the longitudinal distance between nose and rotor axis is known, i.e. $d_r = -8.8m$ (reference system points from tail toward nose). In addition, both the vertical distance between rotor hub and nominal center of gravity (i.e. $x_{CG}^{nom} = -8.8m$) and the boundary positions of the center of gravity in rotorcraft-mode w.r.t aircraft node are known; respectively $h = 1.66m$, $x_{CG}^{fwd} = -8.74m$, $x_{CG}^{aft} = -9.33m$. Defined $d = x_{CG} - d_r$, the fuselage angle with respect to

the local horizontal plane (positive nose up) to achieve equilibrium can be written as:

$$\theta_{fuselage} = \arctan\left(\frac{d}{h}\right) \quad (19.26)$$

Note figure 19.20 for clarifications.

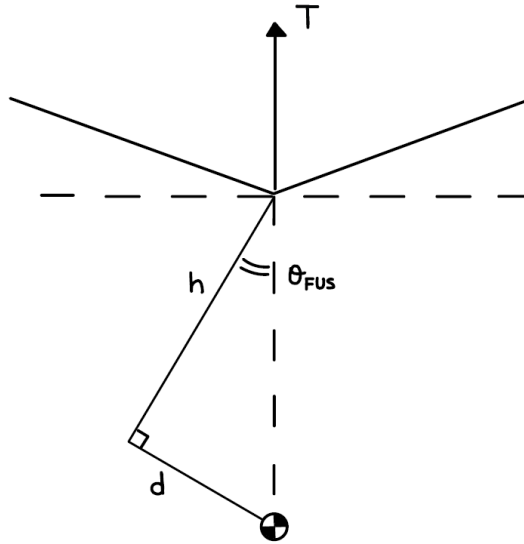


Figure 19.20: Hover trim non-linear model

Numerical results are reported in figure 19.21

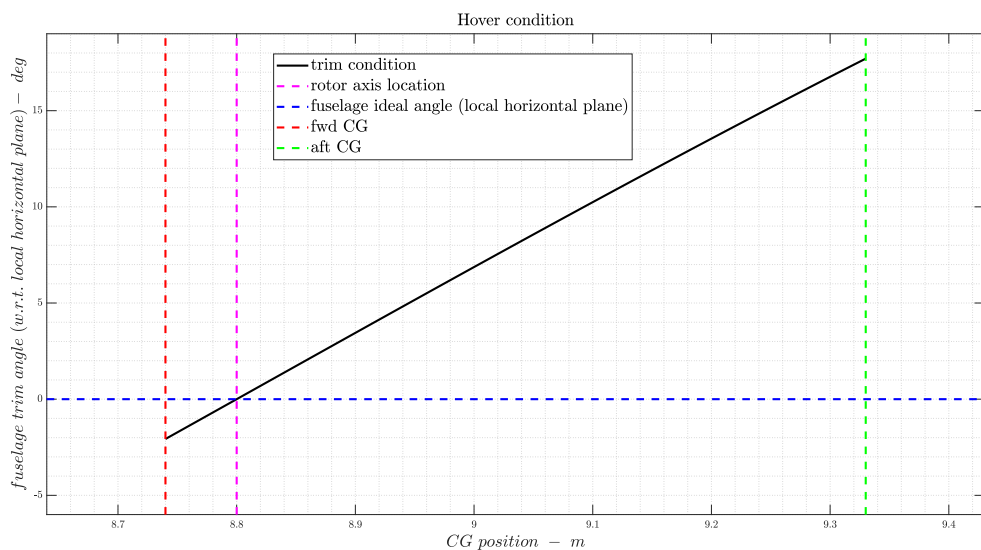


Figure 19.21: Hover trim condition



Note that even in extreme cases, which should not occur in the case of an active fuel pumping system, see chapter 15 for details, the angles remain within reasonable operational limits. It is also important to note that the assumption that the rotor only generates forces in this context is conservative: in fact, the moment generated by the rotor would oppose the moment generated by the weight of the aircraft, reducing the angle of the fuselage necessary for equilibrium. From the longitudinal tip-path-plane tilt, $\beta_{1cHP} = \theta_{fuselage}$, the flapping solution gives the longitudinal cyclic control required, θ_{1sHP} . The solution can be found in Johnson's book, chapter 6 [9], using rotor characteristics reported in chapter 10 of this document, and it is not reported here since it is well beyond the purpose of this section. Finally, note that the angle of the rotor shaft with respect to the fuselage is considered 90°, but at an advanced stage of the project it can be adjusted appropriately if necessary.

19.3.2. Edgewise forward flight condition

As showed in Johnson's book, chapter 6 [9], the problem of trim in edgewise forward flight can be addressed by first imposing force equilibrium on the rotor and then moment equilibrium on the helicopter.

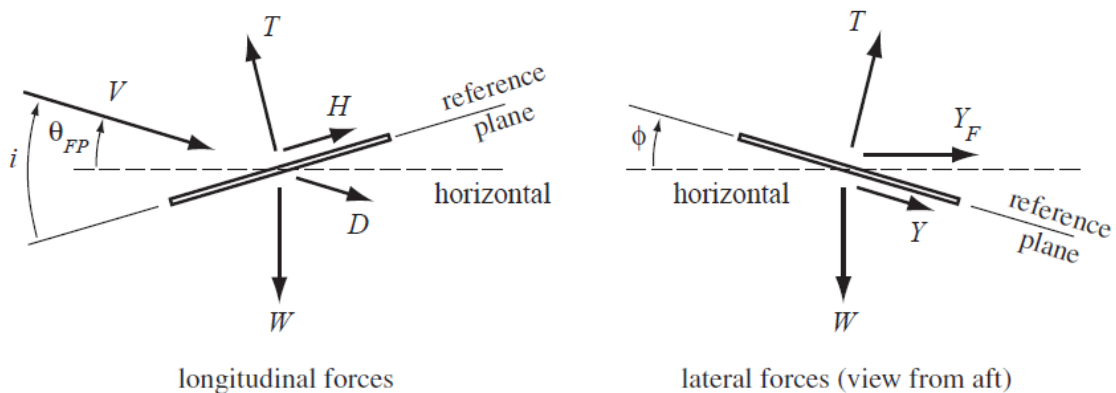


Figure 19.22: Helicopter force equilibrium

Starting from the forces, with reference to the figure 19.22, the solution can be expressed in the longitudinal and lateral cases respectively as:

$$i = \arctan \left(\tan(\theta_{FP}) + \frac{D}{W \cos \theta_{FP}} \right) + \arctan \frac{H}{T} = i_{|H=0} + \arctan \frac{H}{T} \quad (19.27)$$

$$\phi = \arctan \frac{Y_F}{W} - \arctan \frac{Y}{T} \quad (19.28)$$

where V is the helicopter speed, θ_{FP} is the flight path angle, T and D the rotor thrust and drag, W the weight and D the aerodynamic drag.

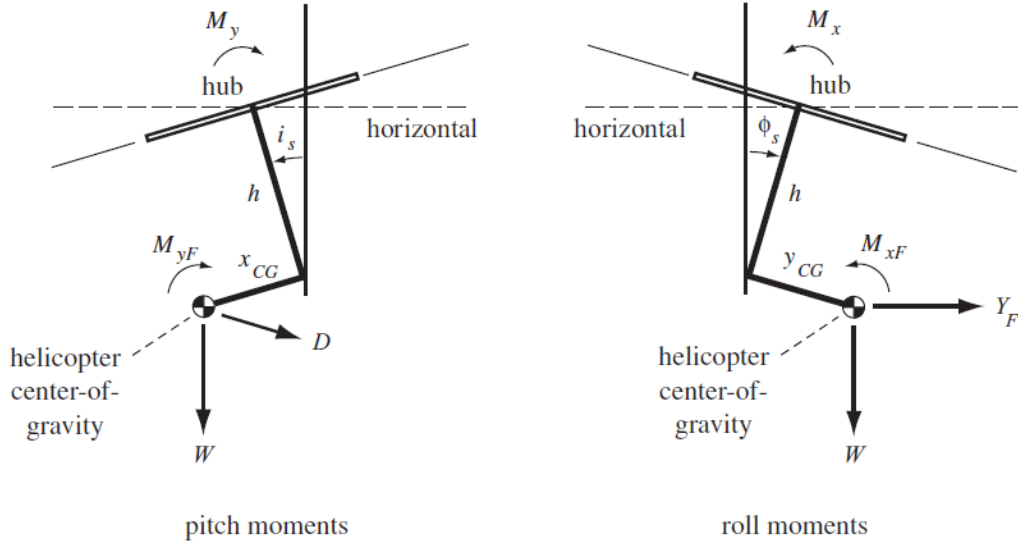


Figure 19.23: Helicopter moment equilibrium

Next consider the equilibrium of pitch moments on the helicopter, figure 19.23, which determines the angle-of-attack of the rotor shaft relative to the vertical, i_s . Moments are taken about the rotor hub so that the rotor forces are not involved and the rotor reference plane does not enter the problem. The rotor hub moment M_y must be included, however. The solution can be obtained, also taking advantage of the above balance of forces, as:

$$\begin{cases} i_s = i_{HP} - \theta_{FP} \\ i_{HP} = \frac{D}{W} + \frac{1}{1 + \frac{(\nu^2 - 1)/\gamma}{h^2 C_T/\sigma a}} \left(\frac{x_{CG}}{h} - \frac{M_{yF}}{hW} + \frac{(\nu^2 - 1)/\gamma}{h^2 C_T/\sigma a} \frac{C_{HTPP}}{C_T} \right) \end{cases} \quad (19.29)$$

and so:

$$i_s = \frac{D}{W} + \frac{1}{1 + \frac{(\nu^2 - 1)/\gamma}{h^2 C_T/\sigma a}} \left(\frac{x_{CG}}{h} - \frac{M_{yF}}{hW} + \frac{(\nu^2 - 1)/\gamma}{h^2 C_T/\sigma a} \frac{C_{HTPP}}{C_T} \right) - \theta_{FP} \quad (19.30)$$

while for the lateral:

$$\phi_s = -\frac{Y_F}{W} + \frac{1}{1 + \frac{(\nu^2 - 1)/\gamma}{h^2 C_T/\sigma a}} \left(\frac{y_{CG}}{h} - \frac{M_{xF}}{hW} - \frac{(\nu^2 - 1)/\gamma}{h^2 C_T/\sigma a} \frac{C_{YTPP}}{C_T} \right) \quad (19.31)$$

They are all known parameters for the rotor design in chapter 10, exploiting flapping



equations reported in chapter 6 of reference [9]. Note that the longitudinal cyclic is not a variable, as at equilibrium it can be related to i_s ; for further details refer to reference [9] section 6.21.

Always as suggested by reference [9], auxiliary propulsion or lifting devices can be accounted for by including their forces in \mathbf{W} and \mathbf{D} .

Assuming that the angle of the rotor shaft with respect to the fuselage is considered 90° :

$$\theta = \alpha + \gamma = i_s \quad (19.32)$$

note that in this framework γ and θ_{FP} are used interchangeably.

Assuming $\alpha \ll 1\text{rad}$ it is possible to introduce the effect of the lift on the weight as an "apparent weight", W^* , which replaces W in the figure 19.23, and the effect of the jet engine on the aerodynamic drag as an "apparent drag", D^* , which replaces D in the figure 19.23 as follow:

$$W^* = W - L(\alpha, \delta_e) = W - L(i_s, \delta_e) \quad (19.33)$$

$$D^* = D - T_{jet} \quad (19.34)$$

Moreover, seems reasonable to consider also the effect of aerodynamics moment, in the same fashioned way as:

$$M_{yF}^* = M_{yF} + M(\alpha, \delta_e) = M_{yF} + M(i_s, \delta_e) \quad (19.35)$$

At this point the equation 19.30 has three unknowns: i_s , δ_e , T_{jet} . recalling that:

$$T_{jet} = T_{jet}(\delta_T, V, h) \quad (19.36)$$

Assuming that in rotorcraft-mode V and h are small, and so its effects on $T_{jet,nominal}$ can be neglected, the problem can be solved for i_s parameterizing δ_T and δ_e . Now, the analytical solution of this system goes beyond the needs of this project; however it is possible to ask (ignore for the moment δ_e): what are the two extreme cases?

19.3.2.1. Condition $T_{jet}(\delta_T) = 0$

In this condition, the jet engine is idle, so the thrust needed to overcome drag must come entirely from the rotor as a classical helicopter; this will involve tilting the rotor axis forward to generate a proper force component opposite to the drag. However, the

presence of the wing should not be forgotten; in fact, during this maneuver it could assume strongly negative angles of attack, generating a considerable workload on the rotor.

19.3.2.2. Condition $T_{jet}(\delta_T) = \mathbf{D}$

In this condition, the jet engine provides all the thrust needed to overcome aerodynamic drag. It was proven in the chapter 18 that the thrust of the jet is sufficient to accomplish this up to the conversion speed.

In this type of maneuvering the rotor and so the fuselage, remains parallel to the local horizontal, having no need to generate forces other than on the local vertical.

19.3.3. Conclusions about trim in edgewise forward flight

Where is the truth? Among all the possible couples (or triplets if considering also δ_e) that satisfies the equation 19.30 as well as the power limitations, some sort of optimization process must be performed, minimizing a figure of merit that could be, for instance, the fuel consumption. Obviously this type of algorithm will be contained in the FMS, whose development is totally outside the scope of this discussion.

Another approach that seems reasonable is to keep the jet idle for low forward velocities, e.g. $V < 50 \text{ kn}$, where in any case the tilt of the rotor axis remains limited. On the other hand the jet may take action for velocities close to the conversion speed to limit the vehicle tilt angle.

Or again, given the type of aircraft, it would be appropriate to assess how different solutions impact, for example, maneuverability, and create different scheduled plans that can be selected appropriately by the pilot depending on contingent operational need.



20 | Dynamic stability and flying qualities

20.1. Aircraft dynamics linearized framework

The aircraft first order non-linear equations of motion are very general but also very complex to manage. Linearization of the equations is a process that is possible to deploy in order to:

- Provide a description of the local behavior of the aircraft, around a reference condition
- Have a description much easier to manage, where it is possible to analyze the eigen-dynamics and the integration is possible. The eigendynamics is the analysis of the free response of the system, (i.e. null control input variation or $\Delta = 0$)
- Enable the ability to perform a time-marching simulation
- Enable the ability to deploy model-based control design technique, such as LQR, to implement some augmentation system (see Chapter 21)
- Enable the ability to evaluate the performance of some tuned controllers (again, see Chapter 21)
- In this framework with proper simplifications, for a conventional configuration aircraft, the longitudinal and lateral-directional dynamics can be decoupled and studied independently.

20.1.1. Longitudinal dynamics model

Longitudinal dynamics model can be expressed as a first order linear differential equation:

$$M_{Lon} \dot{x}_{Lon} + K_{Lon} x_{Lon} = \Delta_{Lon} \delta_{Lon} \quad (20.1)$$

With:

$$x_{Lon} = \begin{pmatrix} u \\ \Delta\alpha \\ \Delta q \\ \Delta\theta \end{pmatrix}; \delta_{Lon} = \begin{pmatrix} \delta_e \\ \delta_T \end{pmatrix}$$

$$M_{Lon} = \begin{bmatrix} m_1 & -c_1 C_{X_{\dot{\alpha}}} & 0 & 0 \\ -C_{Z_{\dot{u}}} & m_1 - c_1 C_{Z_{\dot{\alpha}}} & 0 & 0 \\ -c_1 - C_{m_{\dot{u}}} & -c_1 C_{m_{\dot{\alpha}}} & J_{y_1} & 0 \\ 0 & 0 & 0 & 1 \end{bmatrix}; \Delta_{Lon} = \begin{bmatrix} C_{X_{\delta_T}} & C_{X_{\delta_e}} \\ C_{Z_{\delta_T}} & C_{Z_{\delta_e}} \\ C_{m_{\delta_T}} & C_{m_{\delta_e}} \\ 0 & 0 \end{bmatrix}$$

$$K_{Lon} = \begin{bmatrix} -C_{X_u} - 2C_{X_0} & -C_{X_\alpha} + m_1 q_0 & -c_1 C_{Y_q} + \frac{m_1 w_0}{U_0} & \frac{m_1 g \cos(\theta_0)}{U_0} \\ -C_{Z_u} - 2C_{Z_0} - m_1 q_0 & -C_{Z_\alpha} & -c_1 C_{Z_q} - m_1 & \frac{m_1 g \sin(\theta_0)}{U_0} \\ -C_{m_u} - 2C_{M_0} & -C_{m_\alpha} & -c_1 C_{m_q} & 0 \\ 0 & 0 & -1 & 0 \end{bmatrix}$$

And the inertia parameters are:

$$m_1 = \frac{m U_0}{0.5 \rho U_0^2 S}$$

$$c_1 = \frac{MAC}{2U_0}$$

$$J_{y_1} = \frac{J_{yy}}{0.5 \rho U_0^2 S MAC}$$

Alternatively, this linear system can be expressed as a state-space system where the state matrix has 4x4 dimension:

$$\dot{x}_{Long} = A_{Long} x_{Long} + B_{Long} \delta_{Long} \quad (20.2)$$

With:

$$A_{Long} = -M_{Long}^{-1} K_{Long}$$

$$B_{Long} = M_{Long}^{-1} \Delta_{Long}$$



20.1.2. Lateral-directional dynamics model

Lateral-directional dynamics model can be expressed as a first order linear differential equation:

$$M_{Lat} \dot{x}_{Lat} + K_{Lat} x_{Lat} = \Delta_{Lat} \delta_{Lat} \quad (20.3)$$

With:

$$x_{Lat} = \begin{pmatrix} \Delta p \\ \Delta r \\ \Delta \phi \\ \Delta \psi \end{pmatrix}; \delta_{Lat} = \begin{pmatrix} \delta_a \\ \delta_r \end{pmatrix}$$

$$M_{Lat} = \begin{bmatrix} m_1 - b_1 C_{Y_\beta} & 0 & 0 & 0 & 0 \\ -b_1 C_{l_\beta} & J_{x_1} & -J_{xz_1} & 0 & 0 \\ -b_1 C_{n_\beta} & -J_{xz_1} & J_{z_1} & 0 & 0 \\ 0 & 0 & 0 & 1 & 0 \\ 0 & 0 & 0 & 0 & 1 \end{bmatrix}; \Delta_{Lat} = \begin{bmatrix} C_{Y_{\delta_a}} & C_{Y_{\delta_r}} \\ C_{l_{\delta_a}} & C_{l_{\delta_r}} \\ C_{n_{\delta_a}} & C_{n_{\delta_r}} \\ 0 & 0 \\ 0 & 0 \end{bmatrix}$$

$$K_{Lat} = \begin{bmatrix} -C_{Y_\beta} & -b_1 C_{Y_p} - m_1 \frac{w_0}{U_0} & m_1 - b_1 C_{Y_r} & -\frac{m_1 g \cos(\theta_0)}{U_0} & 0 \\ -C_{l_\beta} & -b_1 C_{l_p} - q_0 J_{xz_1} & -b_1 C_{l_r} + q_0 (J_{z_1} - J_{z_2}) & 0 & 0 \\ -C_{n_\beta} & -b_1 C_{n_p} + q_0 (J_{y_2} - J_{x_1}) & -b_1 C_{n_r} + q_0 J_{xz_1} & 0 & 0 \\ 0 & -1 & -\tan(\theta_0) & -q_0 \tan(\theta_0) & 0 \\ 0 & 0 & -\frac{1}{\cos(\theta_0)} & -\frac{q_0}{\cos(\theta_0)} & 0 \end{bmatrix}$$

And the inertia parameters are:

$$m_1 = \frac{m U_0}{0.5 \rho U_0^2 S}$$

$$b_1 = \frac{b}{2U_0}$$

$$J_{x_1} = \frac{J_{xx}}{0.5 \rho U_0^2 S b}$$

$$J_{z_1} = \frac{J_{zz}}{0.5 \rho U_0^2 S b}$$

$$J_{y_2} = \frac{J_{yy}}{0.5 \rho U_0^2 S b}$$

$$J_{xz_1} = \frac{J_{xz}}{0.5 \rho U_0^2 S b}$$

Alternatively, this linear system can be expressed as a state-space system where the state matrix has 5×5 dimension:

$$\dot{x}_{Lat} = A_{Lat} x_{Lat} + B_{Lat} \delta_{Lat} \quad (20.4)$$

With:

$$A_{Lat} = -M_{Lat}^{-1} K_{Lat}$$

$$B_{Lat} = M_{Lat}^{-1} \Delta_{Lat}$$

20.2. Stability and control derivatives

The stability and control derivatives were derived at various points in the typical mission from both the *VSPAERO - OpenVSP* software and analytical calculations from the References [27] and [29]. Figure 20.1 shows the model that was implemented to study the stability characteristics, while Figures 20.2 and 20.3 lists the stability derivatives respectively for the conversion phase and cruise condition; the same method is reapplied also for other typical flight phases.

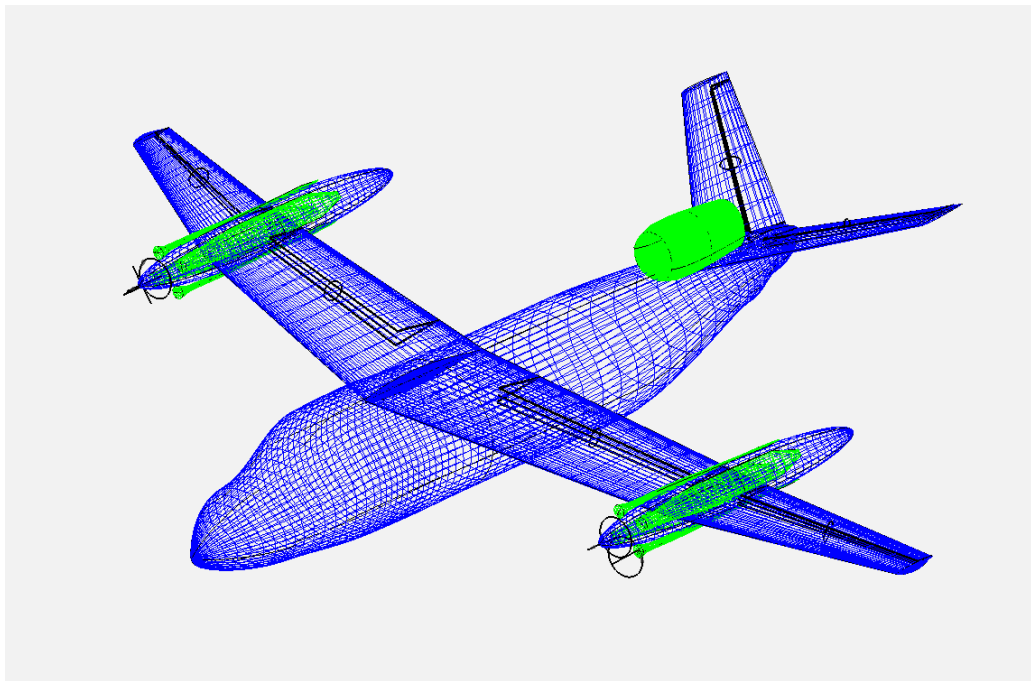


Figure 20.1: Aircraft model in OpenVSP



CONVERSION Conditions : V = 57 m/s, alpha = 15°, rho = 1.105 kg/m³, M = 0.15, Re = 1.5e7											
	ref	/α	/β	/p	/q	/r	/Mach	/u	/δ_a	/δ_e	/δ_r
C_{Fx}	-0.0270000	2.1471470	-0.0019065	0.1500689	3.7789683	0.0223321	-0.0296745	-0.0014451	-0.0029205	-0.0518747	-0.0018923
C_{Fy}	0.0000000	0.0000000	-0.3114560	0.0042887	0.0000000	0.0497720	0.0000000	0.0000000	-0.0568510	0.0000000	-0.1446362
C_{Fz}	-0.1921000	-4.6971705	0.0168684	0.0025442	-15.5192428	-0.0650456	0.1010855	0.0351628	0.0031719	0.5420228	0.0044362
C_{Mx}	0.0000000	0.0000000	0.0011745	-0.4937194	0.0000000	0.0604427	0.0000000	0.0000000	0.2482213	0.0000000	-0.0167952
C_{My}	-0.0388546	-1.8025074	-0.0574286	0.1128038	-30.7300658	-0.0767763	0.0270735	0.0406100	0.0006602	2.0636359	0.0171967
C_{Mz}	0.0000000	0.0000000	0.2959518	-0.0022844	0.0000000	-0.0978465	0.0000000	0.0000000	0.0350972	0.0000000	0.0673907

Figure 20.2: Stability and control derivatives for the conversion phase

CRUISE Conditions : V = 230 m/s, alpha = 0°, rho = 0.44 kg/m³, M = 0.77, Re = 4e7											
	ref	/α	/β	/p	/q	/r	/Mach	/u	/δ_a	/δ_e	/δ_r
C_{Fx}	-0.0270000	0.1275486	0.0007989	0.0390459	0.9916847	0.0038761	-0.0000212	-0.0000140	-0.0030741	-0.0054691	-0.0022431
C_{Fy}	0.0000000	0.0000000	-0.3987150	0.1296530	0.0000000	0.1378942	0.0000000	0.0000000	-0.0483636	0.0000000	-0.1920506
C_{Fz}	-0.1921000	-6.7017960	-0.0615201	-0.0226516	-16.1378965	-0.0337450	0.0610597	0.0557902	-0.0013559	0.7051028	0.0025273
C_{Mx}	0.0000000	0.0000000	0.0044785	-0.5813865	0.0000000	0.0773476	0.0000000	0.0000000	0.3054037	0.0000000	-0.0232357
C_{My}	-0.0361601	-1.2075230	-0.1490170	-0.0510284	-32.9878562	-0.1045692	0.0458789	0.0374600	-0.0031752	2.7898888	0.0107352
C_{Mz}	0.0000000	0.0000000	0.1304063	-0.0110480	0.0000000	-0.1186512	0.0000000	0.0000000	0.0067355	0.0000000	0.0919859

Figure 20.3: Stability and control derivatives in cruise

20.3. Free dynamic response

As already discussed the free response concern the evolution of the system at null input variation.

The free response can be observed by means of two equivalent ways:

1. apply a control input variation then fix it and observe the evolution of the states.
2. apply the perturbation directly on the states and then observe their evolution.

The first approach, differently from the second, involves also the control derivatives. Remark that this is not necessary, being the free response associated only to the state matrix. However, being almost all the control derivatives available, following results was obtained pursuing the first option. Hence, Raven 4 dynamics equations is integrated by exploiting the *MATLAB* command *ODE45*.

Only the two most typical flight conditions, which also extend over a wide airspeed range, namely cruise and conversion, have been analyzed below. The same procedure can be applied to the other flight phases.

20.3.1. Free longitudinal response and eigenanalysis

To analyze the longitudinal response, the system is perturbed with a 4° elevator singlet for 4 seconds; instead, δ_T is kept equal to zero since the respective control derivatives is not available. Figure 20.4 shows this elevator control input.

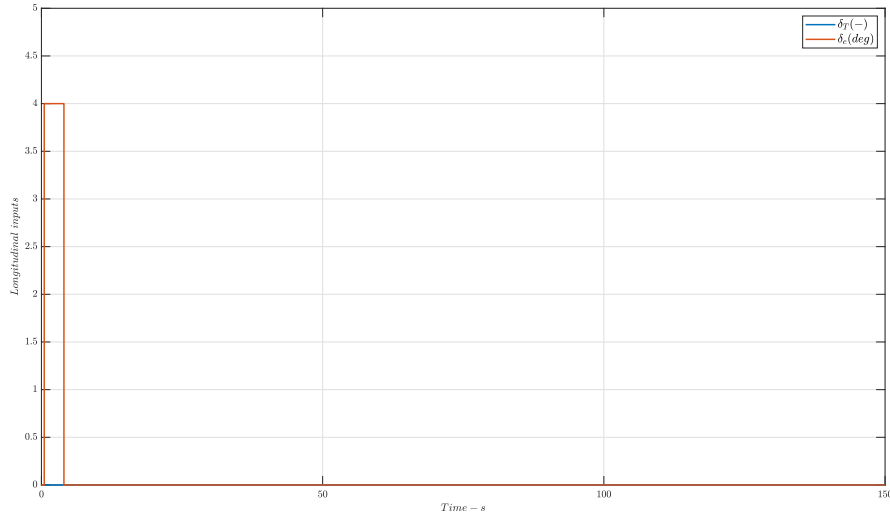


Figure 20.4: Longitudinal input

Longitudinal response in conversion (low speed)

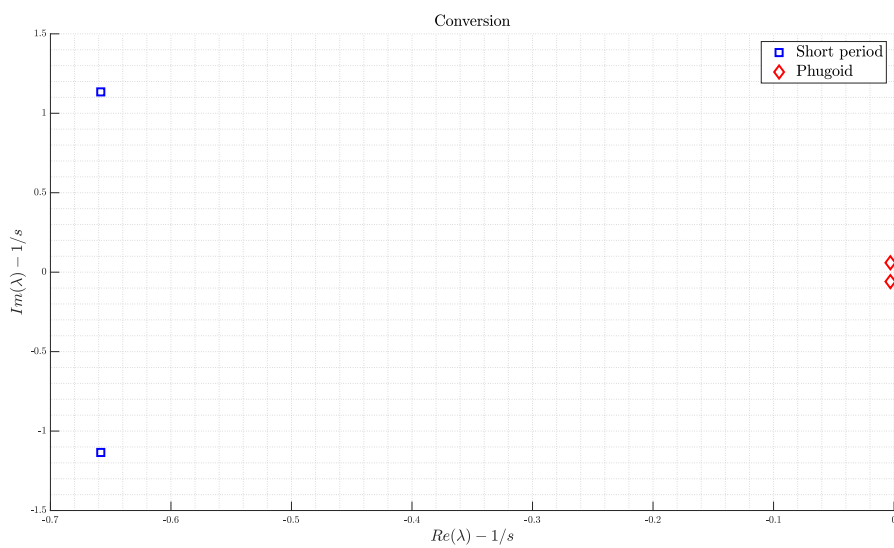


Figure 20.5: Longitudinal mode eigenvalues (conversion configuration)



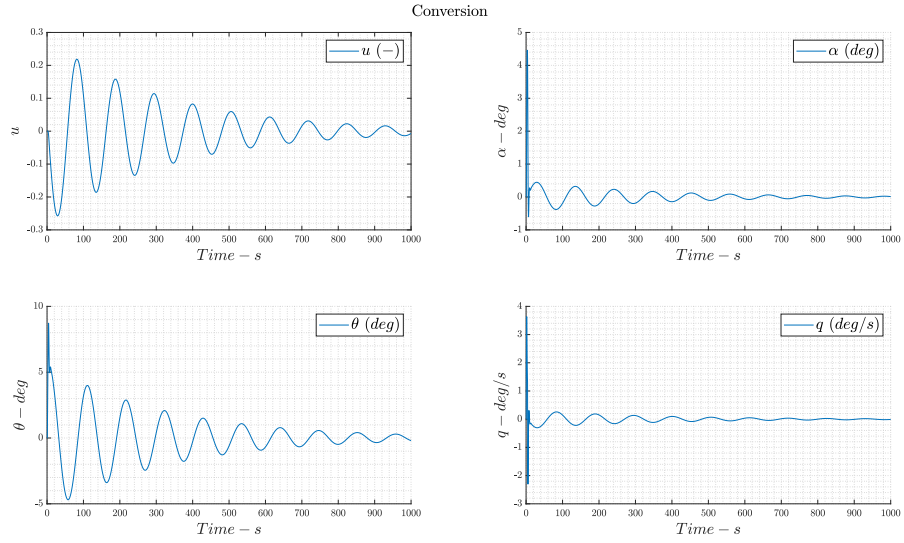


Figure 20.6: Longitudinal response (conversion configuration)

Mode	Eigenvalues [rad/s]	ω_n [rad/s]	ζ
Short period	$-0.6582 \pm i1.1346$	1.312	0.502
Phugoid	$-0.0031 \pm i0.0593$	0.059	0.052

Table 20.1: Longitudinal modes (conversion configuration)

Longitudinal response in cruise (high speed)

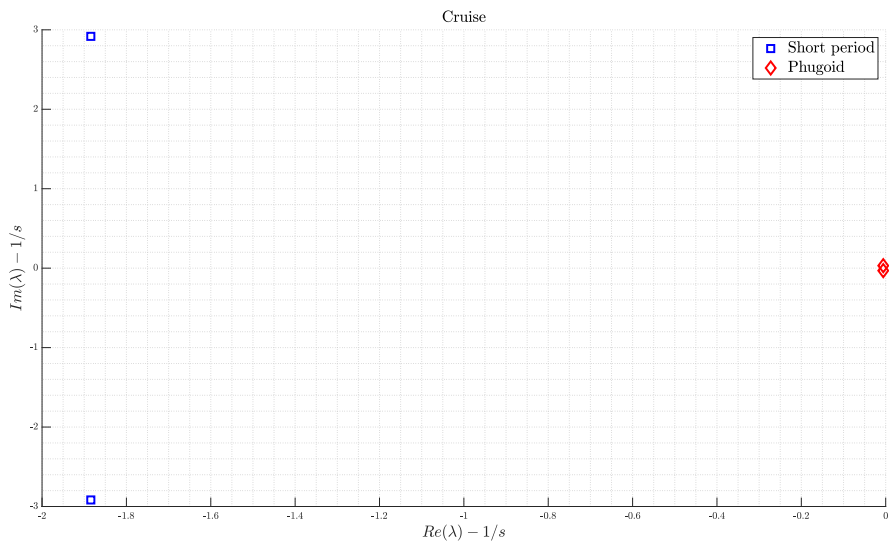


Figure 20.7: Longitudinal mode eigenvalues (cruise configuration)

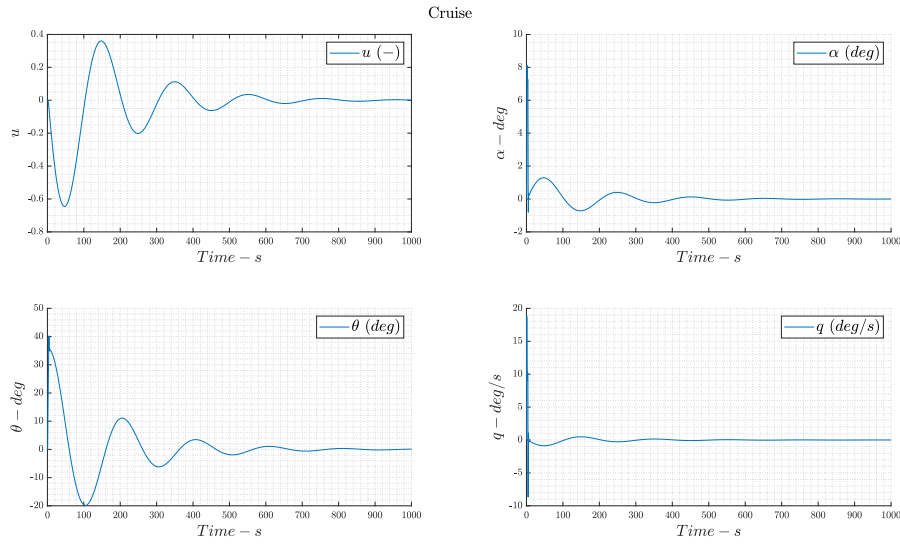


Figure 20.8: Longitudinal response (cruise configuration)

Mode	Eigenvalues [rad/s]	ω_n [rad/s]	ζ
Short period	$-1.8844 \pm i2.9176$	3.473	0.543
Phugoid	$-0.0058 \pm i0.0311$	0.032	0.182

Table 20.2: Longitudinal modes (cruise configuration)

Where:

$$\omega_n = \frac{-Re(\lambda)}{\zeta}$$

$$\zeta = \sqrt{\frac{1}{1 + (Im(\lambda)/Re(\lambda))^2}}$$



20.3.2. Free Lateral-directional response and eigenanalysis

To analyze the lateral-directional free response, the system is perturbed with a combination of two singlets of aileron (2°) and rudder (1.5°) for 3 seconds; Figure 20.9 shows these control inputs.

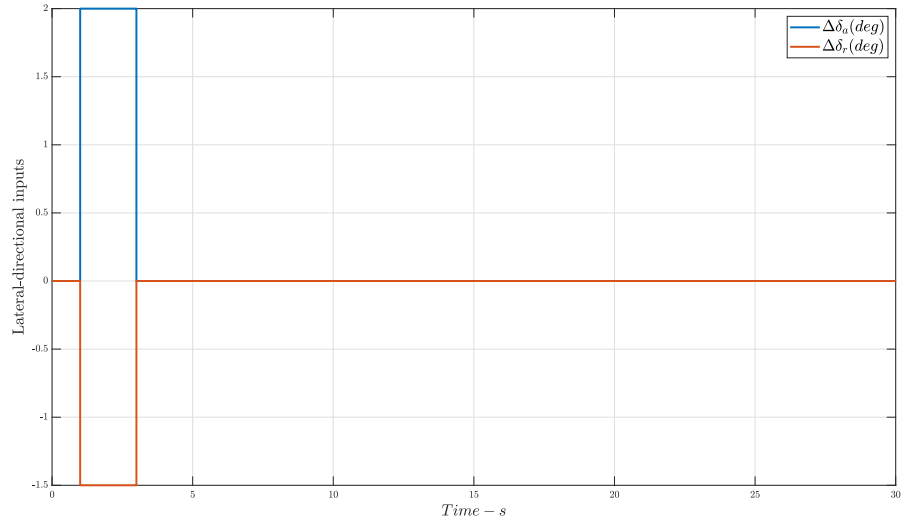


Figure 20.9: Lateral-directional inputs

Lateral-directional response in conversion (low speed)

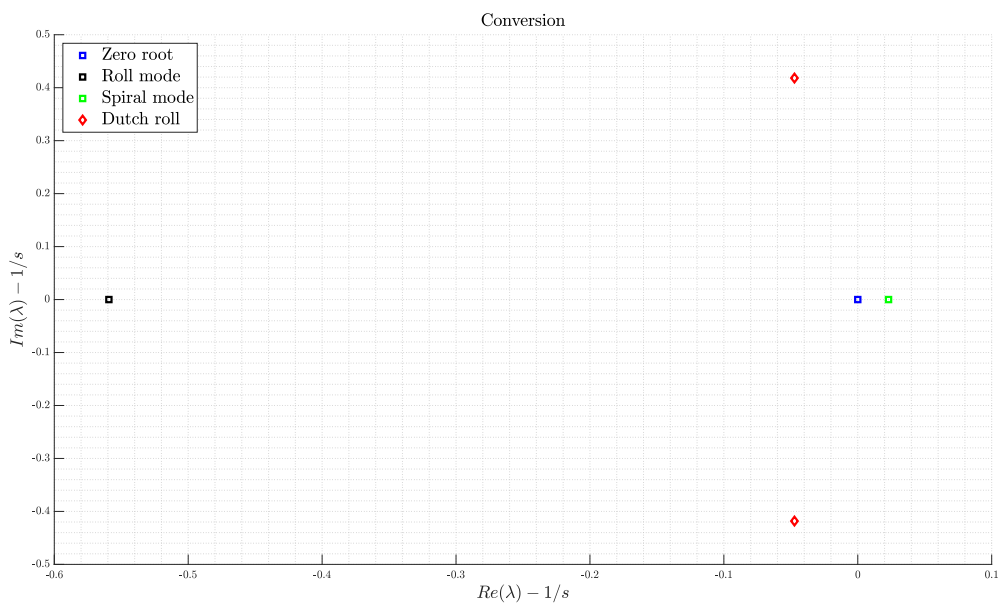


Figure 20.10: Lateral-directional mode eigenvalues (conversion configuration)

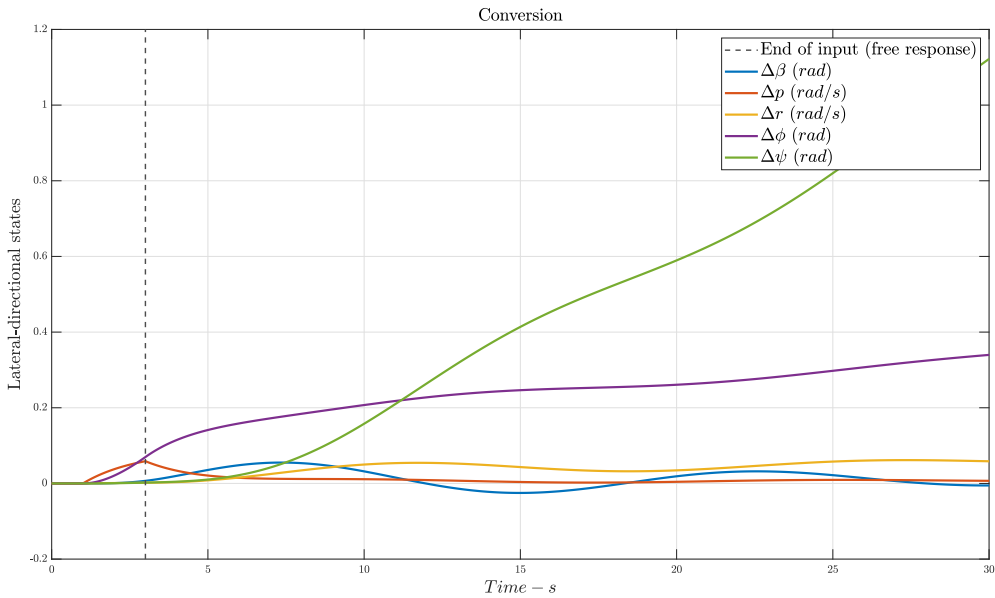


Figure 20.11: Lateral-directional response (conversion configuration)

Mode	Eigenvalues [rad/s]	ω_n [rad/s]	ζ	T [s]	$T_{1/2}$ [s]	T_2 [s]
Roll	-0.5592	-	-	1.788	1.240	-
Spiral	+0.0230	-	-	43.521	-	30.167
Dutch roll	$-0.0473 \pm i0.4182$	0.421	0.112	15.024	-	-

Table 20.3: Lateral-directional modes (conversion configuration)

Where:

$$T = \frac{2\pi}{\omega_n \sqrt{1 - \zeta^2}} \text{ (for complex mode)}$$

$$T = \frac{1}{|\lambda|} \text{ (for real mode)}$$

$$T_{1/2} = \frac{\ln(2)}{|Re(\lambda)|} \text{ (for stable mode)}$$

$$T_2 = \frac{\ln(2)}{|Re(\lambda)|} \text{ (for unstable mode)}$$



Lateral-directional response in cruise (high speed)

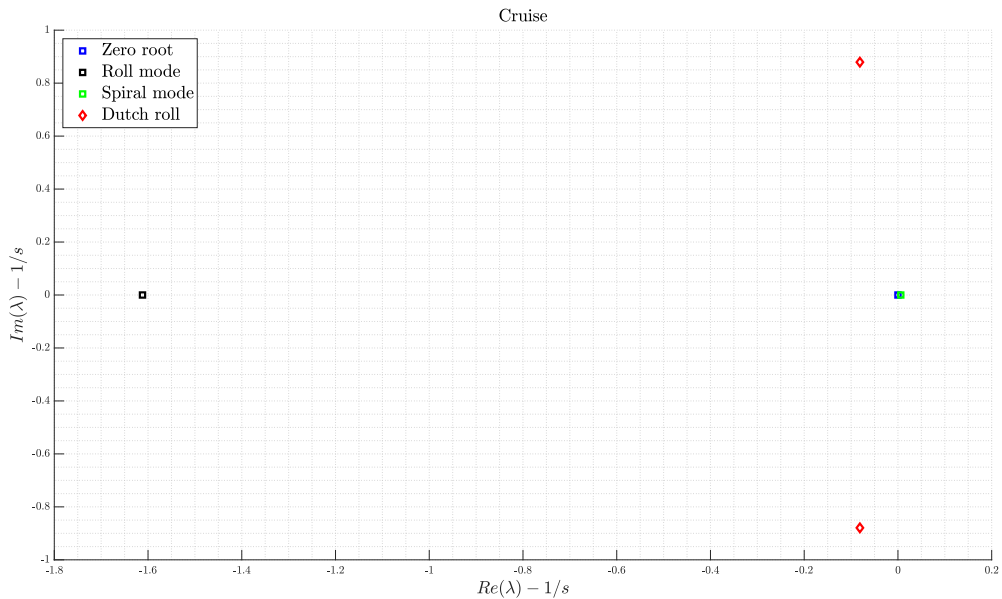


Figure 20.12: Lateral-directional mode eigenvalues (cruise configuration)

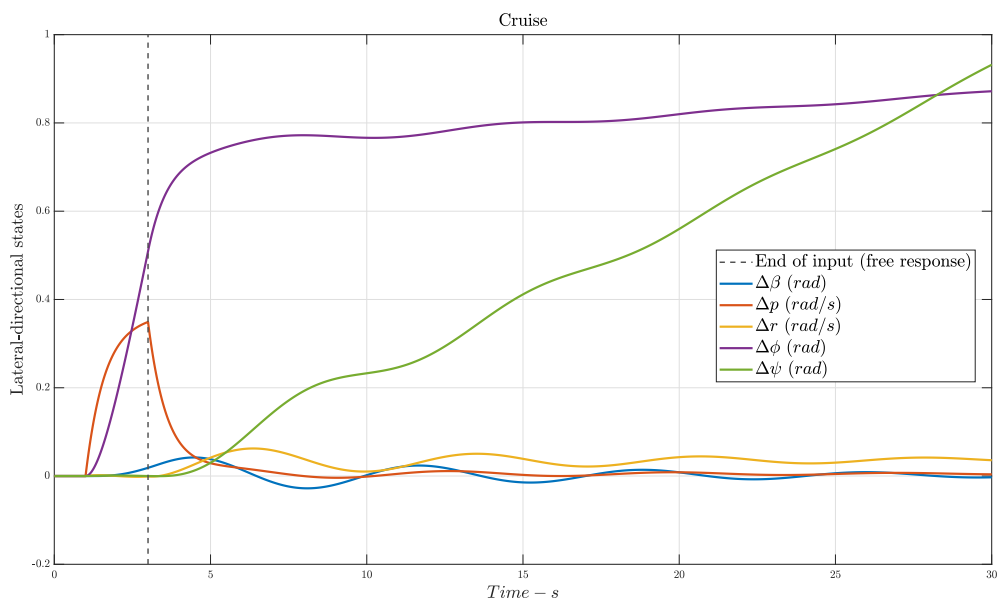


Figure 20.13: Lateral-directional response (cruise configuration)

Mode	Eigenvalues [rad/s]	ω_n [rad/s]	ζ	T [s]	$T_{1/2}$ [s]	T_2 [s]
Roll	-1.6118	-	-	0.620	0.430	-
Spiral	+0.0060	-	-	165.823	-	114.940
Dutch roll	$-0.0812 \pm i0.8792$	0.883	0.092	7.146	-	-

Table 20.4: Lateral-directional modes (cruise configuration)

20.4. Flying qualities

MIL-F-8785C specification is used to analyze the flying qualities of the aircraft. This specification is intended to assure flying qualities that provide adequate mission performance and flight safety. The useful paragraphs of MIL-F-8785C for this project are as follows:

- 3.2.1.2) Phugoid stability
- 3.2.2) Short-period response
- 3.3.1.1) Lateral-directional oscillations (Dutch-roll)
- 3.3.1.2) Roll mode
- 3.3.1.3) Spiral mode

This specification define also three levels of flying qualities:

- Level 1: Flying qualities clearly adequate for the mission Flight Phase, which in turn can be divided into three categories based on the type and difficulty of the mission.
- Level 2: Flying qualities adequate to accomplish the mission Flight Phase, but some increase in pilot workload or degradation in mission effectiveness, or both, exists.
- Level 3: Flying qualities such that the airplane can be controlled safely, but pilot workload is excessive or mission effectiveness is inadequate, or both. Category B and C Flight Phases can be completed anyway.

In addition, Raven 4 can be considered as a Class II Land-based aircraft, abbreviated as "II-L" from here on in the report.



20.4.1. Phugoid

From *MIL-F-8785C par. 3.2.1.2*, the long-period airspeed oscillations (or phugoid) which occur when the airplane seeks a stabilized airspeed following a disturbance shall meet the following requirements:

Level	Requirement
1	$\zeta_p > 0.04$
2	$\zeta_p \geq 0$
3	$T_2 > 55 \text{ s}$

Table 20.5: Phugoid damping ratio requirements

Based on the results obtained in Section 20.3.1, it can be said that at both high speed ($\zeta_p = 0.182$) and low speed ($\zeta_p = 0.052$) the **Level 1** requirement is met.

20.4.2. Short period

For the short period, there are requirements on both frequency and damping.

Short period damping The equivalent short-period damping ratio (ζ_{sp}) shall be within the limits of Table 20.6:

Level	Category A and C Flight phases	Category B Flight phase
1	$0.35 < \zeta_{sp} < 1.30$	$0.30 < \zeta_{sp} < 2.00$
2	$0.25 < \zeta_{sp} < 2.00$	$0.30 < \zeta_{sp} < 2.00$
3	$\zeta_{sp} > 0.15$	$\zeta_{sp} > 0.15$

Table 20.6: Short period damping ratio requirements

Short period frequency The equivalent short-period undamped natural frequency ($\omega_{n_{sp}}$) shall be within the limits imposed by *MIL-F-8785C par. 3.2.2.1.1*; these limits are a function of the load factor divided by the angle of attack:

$$\frac{n}{\alpha} = \frac{1/2 \rho V^2 S C_L}{W} \quad \frac{1}{\alpha} = \frac{1/2 \rho V^2 S C_{L/\alpha}}{W} \quad (20.5)$$

More precisely, the aircraft shall respect the limits in Table 20.7, where $f = \frac{\omega_{n_{sp}}^2}{n/\alpha} \left[\frac{rad^2}{s^2 g} \right]$.

Level	Category A	Category B	Category C
1	$0.23 < f < 3.6$	$0.085 < f < 3.6$	$0.15 < f < 3.6$
2	$0.15 < f < 10.0$	$0.036 < f < 10.0$	$0.096 < f < 10.0$
3	$f > 0.15$	$f > 0.036$	$f > 0.096$

Table 20.7: Short period natural frequency requirements

For the cruise phase (at high speed), $\frac{n}{\alpha} = 37.274 \frac{1}{rad}$ and $f = 0.323 \frac{rad^2}{s^2 g}$, while for the conversion phase (at low speed) $\frac{n}{\alpha} = 2.513 \frac{1}{rad}$ and $f = 0.683 \frac{rad^2}{s^2 g}$.

Thus, at both high speed ($\omega_{n_{sp}} = 3.47 rad/s$ and $\zeta_p = 0.543$) and low speed ($\omega_{n_{sp}} = 1.31 rad/s$ and $\zeta_p = 0.502$) the **Level 1** requirement is met for all Flight Phases Category.

20.4.3. Roll

From *MIL-F-8785C par. 3.3.1.2* the roll-mode time constant (T_r) shall be no greater than the appropriate value in Table 20.8.

Flight Phase Category	Class	Level 1	Level 2	Level 3
A	I,IV	1.0 s	1.4 s	-
	II,III	1.4 s	3.0 s	-
B	All	1.4 s	3.0 s	10.0 s
C	I,II-C,IV	1.0 s	1.4 s	-
	II-L,III	1.4 s	3.0 s	-

Table 20.8: Roll-mode time constant requirements

Where, the roll-mode time constant is defined as $T_r = 1/\lambda_r$. Raven 4 at high speed has $T_r = 0.62 s$, while at low speed $T_r = 1.79 s$. This means that it is guaranteed the **Level 1** requirement for high speed and the **Level 2** requirement for low speed.



20.4.4. Spiral

It is acceptable to have an unstable spiral mode, but from *MIL-F-8785C par. 3.3.1.3* the effects of spiral stability shall be such that, following a disturbance in bank of up to 20° , the time for the bank angle to double must be greater than the values of Table 20.9

Flight Phase Category	Level 1	Level 2	Level 3
A and C	12 s	8 s	4 s
B	20 s	8 s	4 s

Table 20.9: Spiral mode time to double requirements

Where, the time to double is defined as $T_{2s} = \frac{\ln(2)}{\lambda_s}$. At high speed $T_{2s} = 114.9\text{ s}$, while at low speed $T_{2s} = 30.2\text{ s}$. Hence, **Level 1** is reached for both high and low speed in all Flight Phases.

20.4.5. Dutch roll

The frequency (ω_d) and damping ratio (ζ_d) of the dutch roll following a yaw disturbance input shall be higher than the minimum values in Table 20.11.

Level	Flight Phase Category	$\min(\zeta_d)$	$\min(\zeta_d\omega_d)\text{ rad/s}$	$\min(\omega_d)\text{ rad/s}$
1	A	0.19	0.35	0.40
	B	0.08	0.15	0.40
	C	0.08	0.10	0.40
2	All	0.02	0.05	0.40
3	All	0	-	0.40

Table 20.10: Dutch roll requirements just for a Class II aircraft

From Section 20.3.2, at high speed $\omega_d = 0.88\text{ rad/s}$ and $\zeta_d = 0.092$, while at low speed $\omega_d = 0.42\text{ rad/s}$ and $\zeta_d = 0.112$. Hence, unfortunately only **Level 2** can be satisfied for all Flight Phases.

As already predicted and anticipated in Chapter 12, lateral-directional behaviors are the most critical one. This is mainly due to the V-tail, which is very susceptible to lateral-directional oscillations (or dutch-roll). Some typical approach to improve lateral-directional dynamic stability are the increasing of vertical tail volume or the changing of the tail moment arm. However, keep in mind that the determination of stability derivatives by mid-fidelity methods (i.e., VLM on OpenVSP) is not reliable for detailed analysis. In addition, this report aims to present a preliminary design of Raven 4, so the previous discussion on flying qualities may be acceptable.

Mode	F.Q. Level in cruise	F.Q. Level in conversion
Phugoid	1	1
Short period	1	1
Roll	1	2
Spiral	1	1
Dutch roll	2	2

Table 20.11: Summary of flying qualities for Raven 4 (Class II-L aircraft)



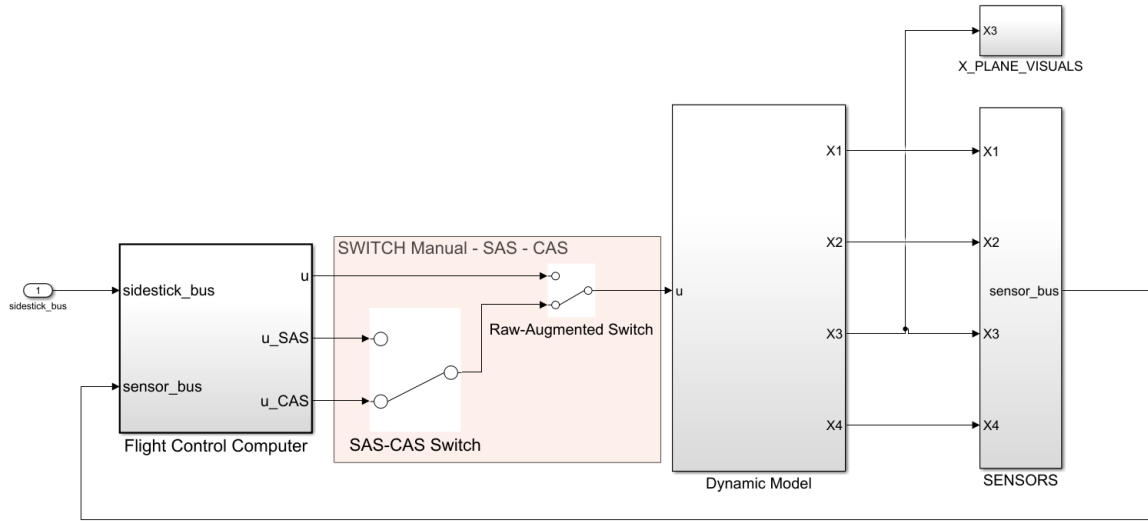
21 | Simulation and flight control laws development, handling qualities

21.1. Simulation framework

The team decided to implement a simulator on *Simulink*, taking inspiration from the open source software of *Unifier19* (Reference [33]), i.e., using *X-Plane11* only as a graphical interface of the simulator.

More specifically, in Figure 21.1 you can see the operating scheme:

- The "STICK_INPUT" block allows the joystick to communicate with the simulator. Thanks to the "sfun_joyinfoex" function up to 16 commands can be defined.
- The "FCC" block contains both the flight control model and the augmented systems for stability and control (see next Section 21.2).
- The "Dynamic Model" block is actually the most important one of the simulator since it contains the aerodynamic model of the aircraft and thus allows the forces and moments acting on the aircraft to be derived.
- Finally, the "X_PLANE_VISUALS" block allows Simulink to interact with X-Plane via UDP protocol.

Figure 21.1: *Simulink* simulator structure

The aerodynamic model implemented in the "Aero" block (see Figure 21.2) consists of computing the coefficients of forces and moments in body axes by multiplying the stability and control derivatives of the aircraft by the control inputs and flight parameters. The flight parameters are first initialized by running the Matlab file called "ProjectXPlane_LOAD.m" and then recalculated for each flight phase in the "EOMandEnviroment" block of Simulink. In equation 21.1 is described the aerodynamic model used for helicopter mode, while for the airplane model has been used a linear model.

$$\begin{pmatrix} \frac{F_X}{M} \\ \frac{M_Y}{I_Y} \\ \frac{F_Z}{M} \end{pmatrix} = \begin{bmatrix} X_u & X_q & X_w \\ M_u & M_q & M_w \\ Z_u & Z_q & Z_w \end{bmatrix} \begin{pmatrix} \dot{x}_F \\ \dot{\theta}_F \\ \dot{z}_F \end{pmatrix} + \begin{bmatrix} X_\theta & X_{\theta_0} \\ M_\theta & M_{\theta_0} \\ Z_\theta & Z_{\theta_0} \end{bmatrix} \begin{pmatrix} \theta_S \\ \theta_0 \end{pmatrix} \quad (21.1)$$

$$\begin{pmatrix} \frac{F_Y}{M} \\ \frac{M_X}{I_X} \\ \frac{M_Z}{I_Z} \end{pmatrix} = \begin{bmatrix} Y_v & Y_p & Y_r \\ L_v & L_p & L_r \\ N_v & N_p & N_r \end{bmatrix} \begin{pmatrix} \dot{y}_F \\ \dot{\phi}_F \\ \dot{\psi}_F \end{pmatrix} + \begin{bmatrix} Y_\theta & Y_{\theta_p} \\ L_\theta & L_{\theta_p} \\ N_\theta & N_{\theta_p} \end{bmatrix} \begin{pmatrix} \theta_c \\ \theta_p \end{pmatrix}$$

In addition, through the "Scopes" block it is possible for the pilot to see the flight parameters, such as artificial horizon, airspeed, altitude, AoA, and so on.



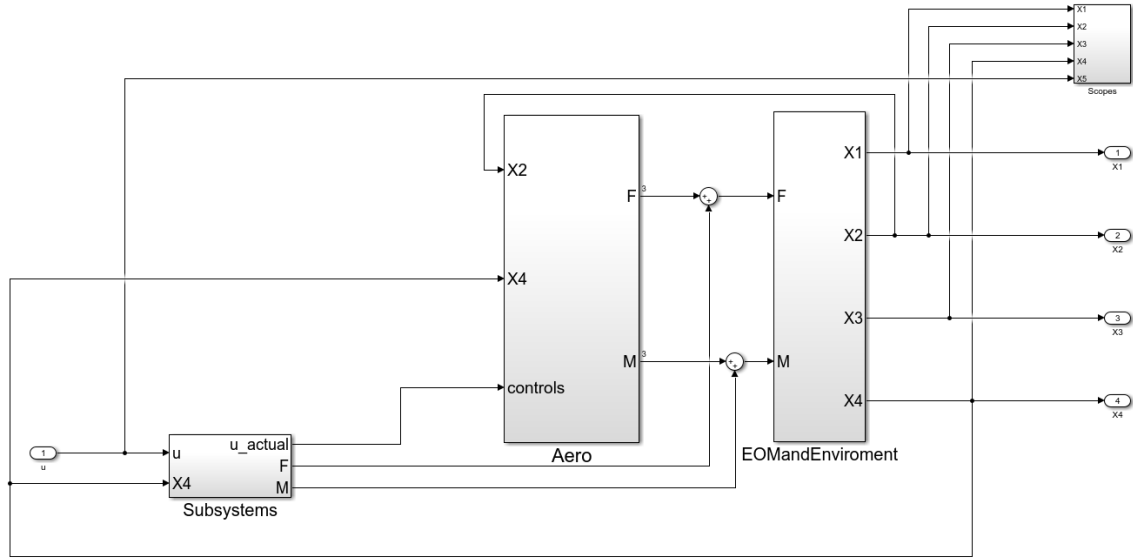


Figure 21.2: Dynamic model

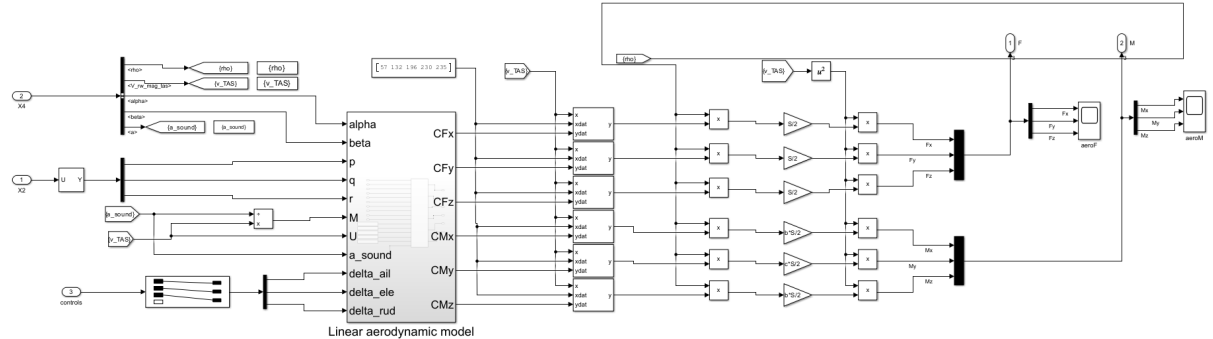


Figure 21.3: Aerodynamic model

The strength of this technology is the direct control of the designers over the aircraft model and stability derivatives. This allowed the team to implement stability and control augmented systems, which can be easily disabled by the pilot during simulated flight. Furthermore, with this model it is possible to analyze with much more precision than with X-Plane the static and dynamic stability thanks to the graphs of the angular rates of the aircraft.

Stability and control derivative are defined in section 20.2. In addition, fitting curves of aerodynamic coefficients are created in the aerodynamic model so that the appropriate stability derivatives can be recovered based on the flight speed during a simulation.

21.2. SAS, CAS, Autopilot

21.2.1. General considerations

Although the aircraft is stable, the team decided to implement both a SAS and a CAS so as to improve flying and handling qualities. Specifically:

- SAS (Stability Augmentation System) consists in conditioning the free response of the system in order to obtain better flying qualities and stabilize the unstable modes; it can be done with a simple state feedback: for a proper number of tunable parameters in the feedback line it is possible to perform the placement of each pole.
- CAS (Control Augmentation System) consists in transferring control from displacement of control surfaces to something else (i.e., pitch, roll and yaw rate). Since it performs a tracking of an input it is necessary to have an integral action to nullify the error at ended transient.
- AP (Autopilot) consists in a system designed to take or keep the aircraft to an assigned measurement set point.

Figure 21.4 shows the general structure of the control system.

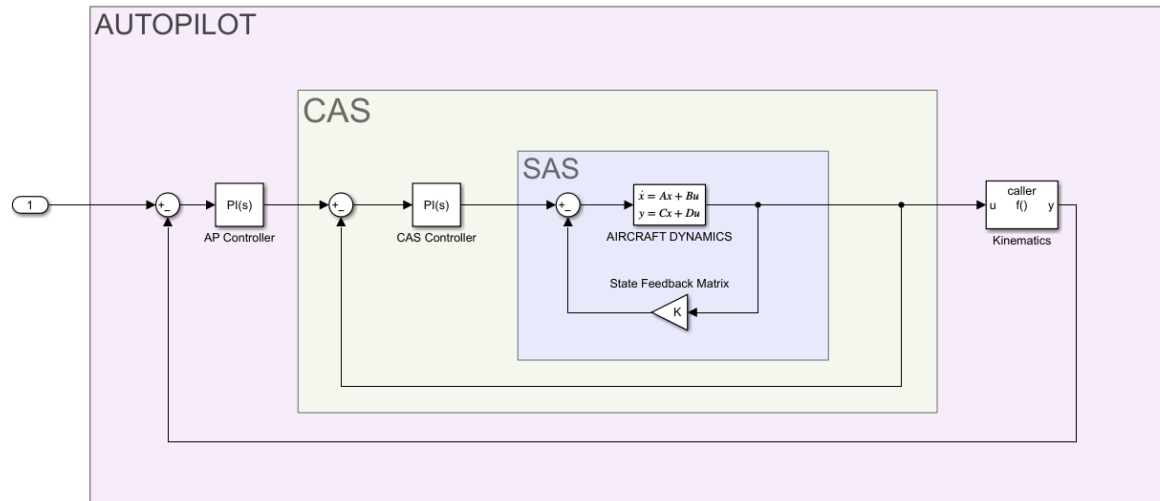


Figure 21.4: Control system architecture



21.2.2. SAS and CAS implementation

Figure 21.5 and 21.6 shows the implementation of SAS and CAS for the jet-mode. A Stability augmentation system was also implemented for the rotorcraft-mode, but due to lack of space it was not shown in the report.

In addition, a high-pass filter was added on each SAS feedback line so that only pilot commands are not considered as undesirable disturbances (considering pilot inputs between 2 and 4 Hz).

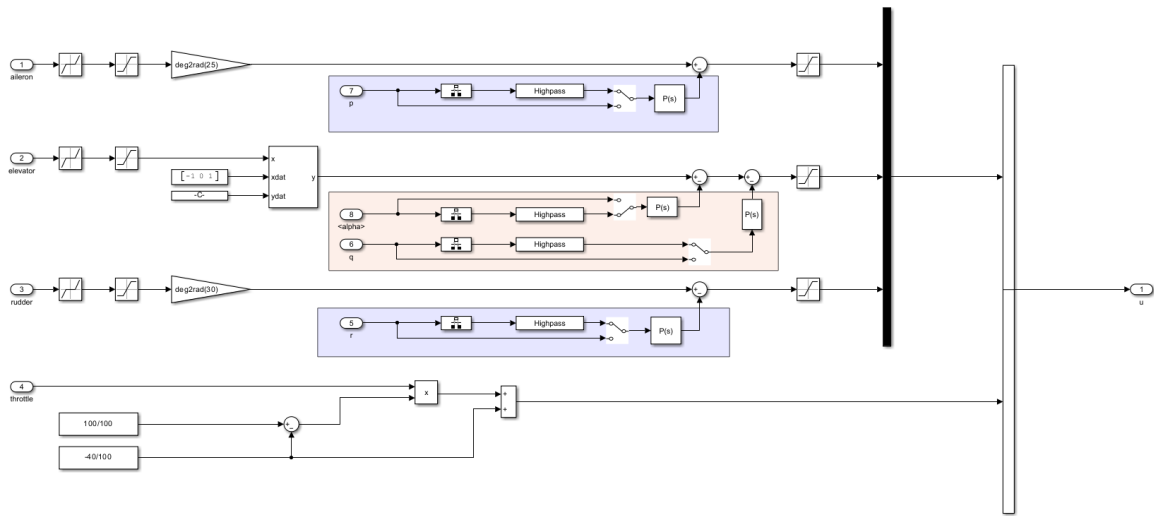


Figure 21.5: SAS implementation

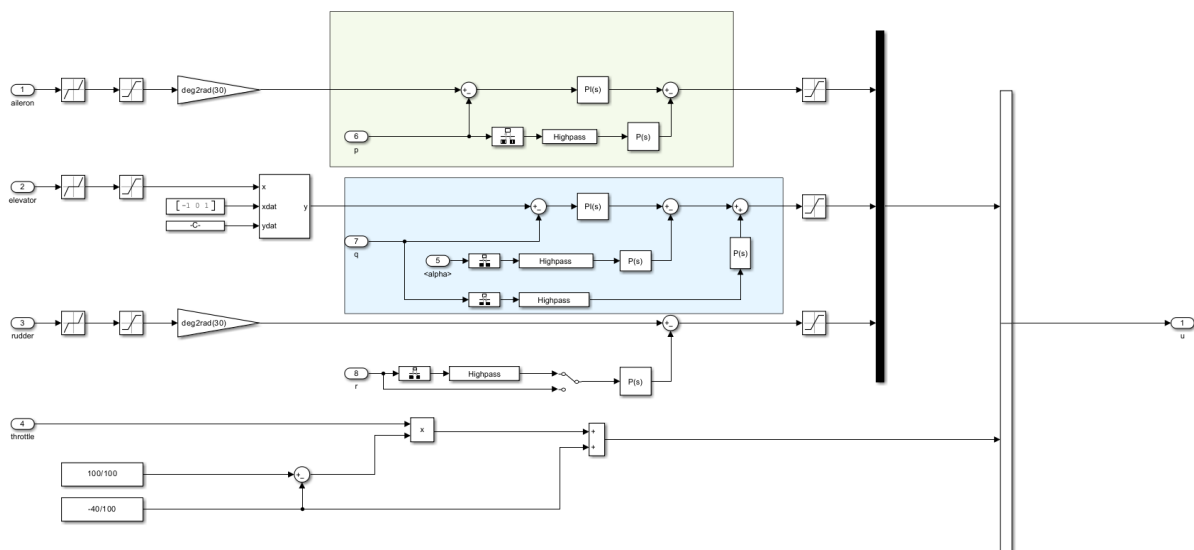


Figure 21.6: CAS+SAS implementation

In particular the SAS, figure 21.5:

- Implement a full pitch-axis scheme, with feedback of α and q to respectively stabilizing the system acting on $C_{M_{CG}|\alpha}$ and damping the short period.
- Implement a full yaw-damper scheme, with feedback of roll and yaw rate (p, r).

While the SAS+CAS architecture, figure 21.6:

- Track the pitch rate (q) for longitudinal control.
- Track the roll rate (p) for lateral-directional control.

21.3. Visual interface

Simulink sends a UDP packet to a network address identified by the remote IP address and remote IP port parameters, such as *X-Plane11*.

Then, once the proper Remote IP address and port are set (such as '127.0.0.1' and 49000) it's possible to fly an aircraft on X-Plane by running the simulator on Simulink.

In addition, as an aesthetic matter, an object model similar to the designed aircraft was also imported on X-Plane. However, since the aircraft dynamic is simulated by Simulink and X-Plane is only a graphical user interface, any aircraft from those available in the catalog can be selected.

Finally, the team performed a test of the typical mission (Figure 21.7).

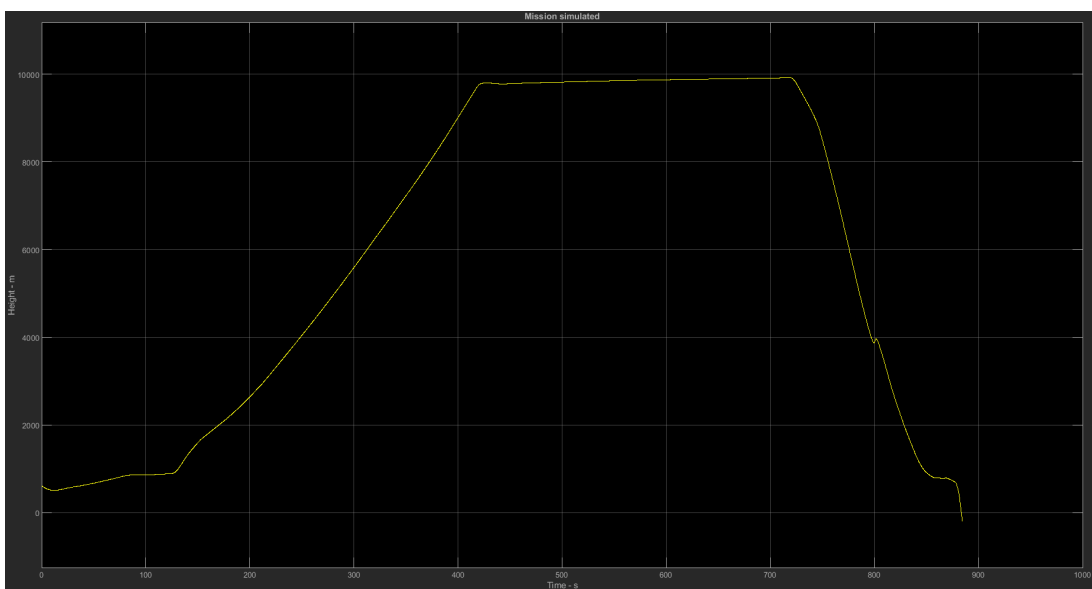


Figure 21.7: Simulation of a typical mission



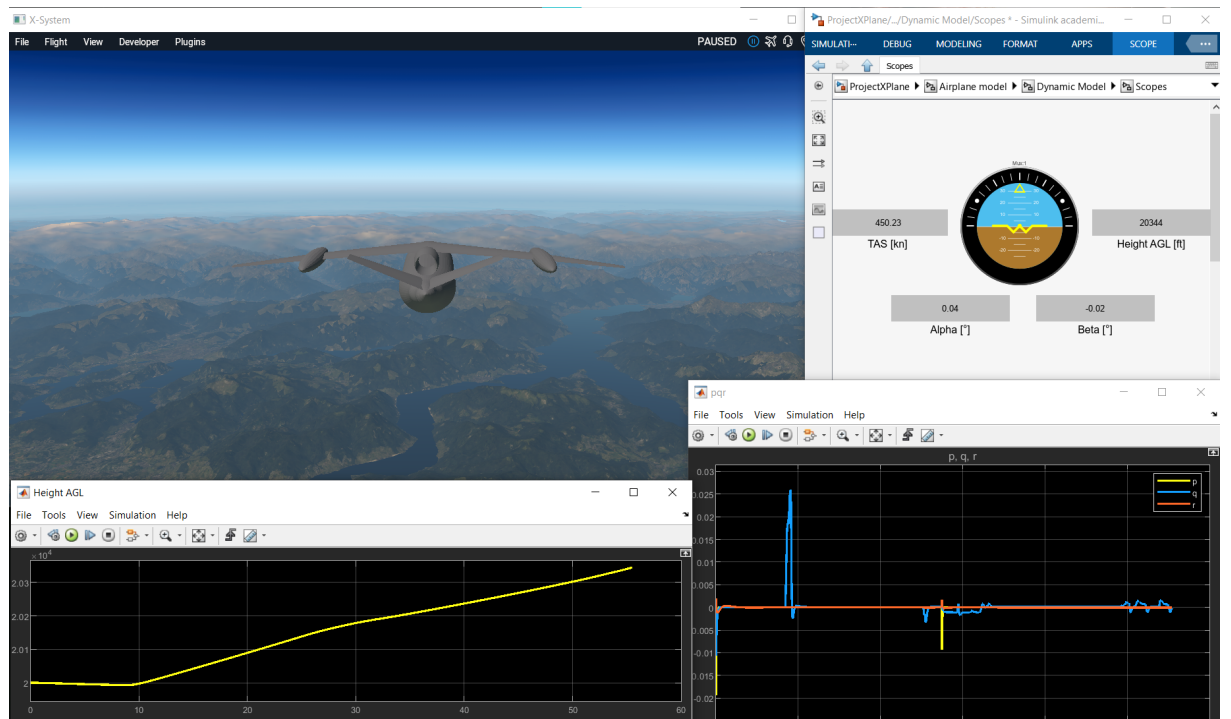


Figure 21.8: Example of visual interface of the simulator

22 | Manufacturing and cost analysis

This chapter focuses on the cost analysis associated with the aircraft. Cost analysis is a fundamental component in evaluating a project, its development costs, production costs, and operational costs throughout the aircraft's life-cycle.

In the aeronautical context, including the military one, it is crucial to understand the factors that influence the costs of an aircraft in order to make informed decisions regarding the allocation of financial resources and maintaining a balance between operational capabilities and economic sustainability. This chapter aims to examine the key components of military aircraft costs, including development, production, quality control, testing, maintenance, and upkeep costs. Additionally, factors that can influence these costs, such as technological innovation and operational requirements, will be discussed.

Various methodologies and tools used for cost analysis will be presented, along with the specific case, to provide an in-depth overview and practical application of the key financial considerations associated with the military aircraft. Through this cost analysis, the objective is to provide a comprehensive and transparent framework for the financial factors that need to be taken into account in the decision-making process regarding the military aircraft, thereby contributing to prudent financial resource management and an accurate assessment of the aircraft's effectiveness and efficiency.

22.1. Market analysis

Before delving into the costs related to the development and production of the aircraft, it was important to explore the current market in relation to the existing competitors. Table 22.1 lists some of the competitors, already mentioned in Chapter 5, along with the quantities of aircraft produced and their selling prices. Furthermore, their prices were also evaluated using the cost analysis methodology employed in this study to verify its effectiveness and accuracy.

Competitor	Quantity	Selling Price	Evaluated Price
V-280	-	\$ 43 million	\$ 42.8 million
V-22 Osprey	479	\$ 59 million	\$ 53.1 million
AW609	-	\$ 24 million	\$ 27.9 million
CH-47 Chinook	1200	\$ 30 million	\$ 33.9 million
C130	2500	\$ 48 million	\$ 51.3 million
C-27J	117	\$ 50 million	\$ 52.3 million

Table 22.1: Cost comparison of competitors

By analyzing the market data and evaluating the competitors' costs, it is possible to gain insights into pricing trends and make informed decisions regarding aircraft's cost structure. Moreover, this analysis allows to be aware that the methodology employed in our case has an accuracy rate of 8.5%.

In the Table 22.1, you can also find the production start year for each aircraft. These data are useful because they can indicate an average service life required by customers. Additionally, in the military domain, there is an increasing trend to extend the lifespan of existing aircraft rather than purchasing new ones. In terms of competitiveness and design, it was kept in mind that the aircraft should have a minimum service life of 30 years, considering the complexity of the project.

Moreover, the information regarding the production start dates serves as an indicator of the generation of transport vehicles currently in service and likely to be replaced in the coming years. For this reason, they can provide insights into future market demands. These observations were taken into consideration when determining the quantity of aircraft to be produced.

22.2. Aircraft Development and Procurement Cost

For a comprehensive cost estimation of a new aircraft, the entire life-cycle cost as depicted in the figure 22.1 needs to be considered.



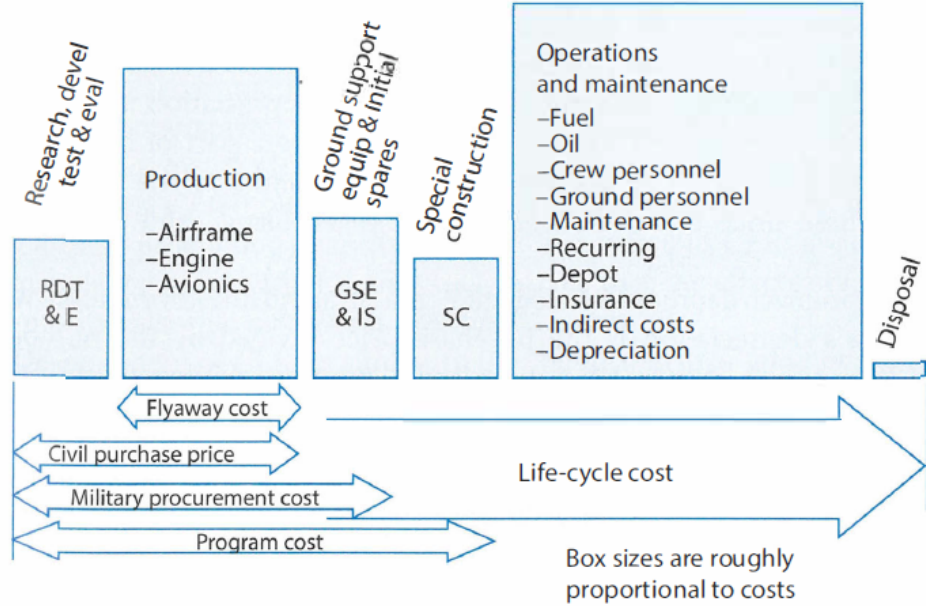


Figure 22.1: Elements of life-cycle cost. [19]

For military aircraft, RDT&E includes all of the technology research, design engineering, prototype fabrication, flight and ground testing, evaluation for operation suitability and compliance with Mil-Specs. RDT&E costs are essentially fixed and it is approximately 10% of the total cost. On the other hand, the aircraft flyaway cost which cover labor, material and tooling, it is approximately about half of LCC for military aircraft.

For civil aircraft, the selling price takes into consideration Research, Development, Test, and Evaluation (RDT&E) costs as well as production costs. However, in the case of military aircraft, it is necessary to consider additional factors such as "procurement costs" and "Program cost". The first one encompass the expenses associated with acquiring the necessary ground support equipment, including flight simulators and testing equipment, as well as the cost of initial spare parts required during operational deployment. Whereas the second one covers the total cost to develop and deploy a new aircraft into military environment.

A significant part of the aircraft's life cycle costs is attributed to operations and maintenance, which includes expenses related to operating and maintaining the aircraft throughout its service life. For this reason, the entire life cycle of the aircraft will be explored based on fuel cost, crew cost, and maintenance cost after the delivery from the manufacturer.

22.2.1. Analytical approach and Database

To approach the estimation of costs related to the design, development, and production of the aircraft here presented, a parametric estimation has been employed, typical for a general type of estimation in the early stages of the project. In fact, a more accurate cost estimation of the consumptive or Work Type Group Code type is still far from the objective of this work.

This type of estimation allows for the estimation of development and production costs of aeronautical structures through the use of generalized equations, one for each phase: engineering, tooling, manufacturing labor, manufacturing material, development support, flight test, and quality control. The relationships are expressed in the form of exponential equations and are obtained through a multiple regression technique using least squares. The adopted methodology is based on a research study initially carried out by the RAND Corporation as part of the Air Force project study entitled "Cost Analysis Methods for Air Force Systems" presented in [18] [10] [17]. These models are designed for use in situations where limited information is available about an aircraft design. The aim is to generate estimates that encompass the costs associated with program delays, engineering changes, data requirements, and various inefficiencies that typically arise in a standard program.

Although the set of Cost Estimating Relationships (CERs) developed by the RAND Corporation, known as the "DAPCA IV model" as described in Raymer [19], may not be the most up-to-date set for estimating aircraft costs, it still serves as an excellent starting point that is available to everyone for preliminary cost estimation for most classes of aircraft. With appropriate adjustments, even the specific aircraft in question can be estimated by DAPCA.

In this analysis, general assumptions will be made in terms of material procurement cost, hourly salary rates, cost of avionics, fuel and crew cost, etc. to ensure a fair comparison with respect to other designs.

22.2.2. Cost estimation

Engineering (H_{eng}), tooling (H_{tool}) and manufacturing hours (H_{mfg}) are a measure of the effort required for the airframe design and analyst, test engineering, configuration control, system, preparation of the production and the labor to fabricate the aircraft. As it can be seen in the following equations, the estimated quantity of aircraft to be produced (Q)



will be an influence on the final price of the aircraft. Designed speed (V) will have an influence on the complexity of the aircraft, whereas the empty weight mass (We) will be related to the size and amount of parts to be designed, produced and tested.

$$H_{eng} = 5.18 We^{0.777} V^{0.894} Q^{0.163} \quad (22.1)$$

$$H_{tool} = 7.22 We^{0.777} V^{0.696} Q^{0.263} \quad (22.2)$$

$$H_{mfg} = 10.5 We^{0.820} V^{0.484} Q^{0.641} \quad (22.3)$$

The quality control phase (H_{qc}), on the other hand, will account for 15% of the manufacturing effort in hours because it is part of manufacturing but it is estimated separately:

$$H_{qc} = 0.15 H_{mfg} \quad (22.4)$$

The Development Support Cost (C_{dev}) covers expenses related to procurement cost and program cost. It includes costs for ground support equipment, flight simulator, test equipment, and the development and deployment of a new aircraft into the military inventory. This may also include costs for special ground facilities required for operational deployment of certain aircraft.

$$C_{dev} = 67.4 We^{0.63} V^{1.3} \quad (22.5)$$

Flight test costs (C_{FT}) depend on the size and complexity of the aircraft, as well as the number of flight test aircraft (FTA) needed to perform the necessary verifications, certifications, and handling qualities evaluations.

$$C_{FT} = 1947 We^{0.325} V^{0.822} FTA^{1.21} \quad (22.6)$$

The Manufacturing Cost (C_{mat}) refers to all expenses associated with materials, hardware, and equipment used in the assembly of the aircraft.

$$C_{mat} = 31.2 We^{0.921} V^{0.621} Q^{0.799} \quad (22.7)$$

It is now possible to add the cost related to engines and avionics. For the engines, the market prices of the selected engines and the number of engines installed on the aircraft are known. As for the avionics, a standard price of 16,000 €/kg is used, which aligns with the estimation provided by Raymer [19].

Finally, hourly rates need to be defined in order to evaluate the engineering, tooling, manufacturing, and quality control phases. It is important to note that employee salary costs can vary significantly depending on various factors such as the country. However, for the purpose of estimation, values reported in the 2012 edition of Raymer have been chosen.

Sector	Rate
Engineering (Re)	115 USD
Tooling (Rt)	118 USD
Manufacturing (Rm)	98 USD
Quality Control (Rq)	108 USD

Table 22.2: Hourly rates in 2012 U.S. dollars

Henceforth, the total research, development, testing, and engineering cost for the entire program is calculated. The engine-related items are divided into 1 and 2 due to the presence of a turbofan engine and two turboshaft engines.

$$C_{RDTE} = H_{eng}Re + H_{tool}Rt + H_{mfg}Rm + H_{Qc}Rq + C_{dev} + C_{FT} + C_{mat} + (C_{eng_1}N_{eng_1} + C_{eng_2}N_{eng_2} + C_{avionics})Q \quad (22.8)$$

22.2.3. Correction to the model and influence of material

The formulas and references for cost evaluation are based on the assessment of the US dollar in 2012. Therefore, it is necessary to adjust the final cost with an inflation factor.

$$f_{inf} = 1.29 \quad (22.9)$$

Furthermore, to convert the costs obtained from U.S. dollars (USD) to euro (EUR), an average conversion factor based on the exchange rate in May 2023 has been applied.

$$f_{USD-EUR} = 0.93 \quad (22.10)$$



We must also take into consideration the technological evolution of materials, which has a significant impact on the manufacturing cost. This impact is not only due to the cost of the materials themselves but also to the different processes required for engineering, production, testing, and quality control for each material. In fact, all the formulas used refer to aluminum aircraft. Therefore, a correction factor will be applied to account for the higher cost to all the development-related hours (H_{eng} , H_{tool} , H_{mfg} and H_{Qc}).

Material	%	$f_{matref.}$	$f_{matpartial}$	$f_{mattotal}$
Aluminium	78%	1	0.78	
Carbon-Epoxy	10%	1.45	0.145	
Fiberglass	5%	1.15	0.058	1.1
Steel	5%	1.75	0.088	
Titanium	2%	1.5	0.03	

Table 22.3: Material factor

As the airframe consist of different materials, the final material factor (f_{mat}) will be the summation of the partial cost factor for each material as in Table 22.3.

22.2.4. Price estimation

To establish the final selling price of each aircraft, the costs related to the interiors need to be added, along with a sales margin of 10% (f_{invest}). Additionally, the cost of additional spare parts and other services included in the aircraft's final price should be considered, which, although varying from contract to contract, can be assumed to be around 15% (f_{spares}).

$$C_{aircraft} = C_{RDTE}/Q + C_{interior} \quad (22.11)$$

The final price of the aircraft will be then evaluated as:

$$P_{aircraft} = C_{aircraft} * f_{invest} * f_{spares} \quad (22.12)$$

	Quantity	Rate	Total cost	Cost Per Unit
Engineering	9,706,963 hr	115 (\$/hr)	1,163,007,375 \$	3,721,002 \$
Tooling	6,319,973 hr	118 (\$/hr)	745,756,810 \$	2,485,856 \$
Manufacturing	28,911,333 hr	98 (\$/hr)	2,833,310,637 \$	9,444,368 \$
Quality control	3,905,129 hr	108 (\$/hr)	421,754,026 \$	1,405,847 \$
Development support			180,469,152 \$	601,564 \$
Flight test			178,060,559 \$	593,535 \$
Material			1,379,420,840 \$	4,598,069 \$
Turboshaft			2,400,000,000 \$	8,000,000 \$
Turbofan			900,000,000 \$	3,000,000 \$
Avionics	1,000 kg	16,000 \$/kg	4,322,324,253 \$	14,407,748 \$
Inflation	1.29 %			
Total cost to produce			14,477,397,006 \$	48,257,990 \$
Interior				50,000 \$
Spare parts	15 %			
Profit	10 %			
Aircraft Price				61,109,607 \$

Table 22.4: Project cost analysis

The total costs reported in Table 22.4 are derived from a conservative choice regarding the production of 300 units, excluding the aircraft intended for flight tests. This choice was determined based on a sensitivity study on the quantity of aircraft to be produced and to ensure a Break Even Point for 230 units sold.

22.2.5. Sensitivity analysis

For completeness, the sensitivity studies performed on the model built to find the cost difference depending on the chosen variables of quantity of aircraft produced, Empty Weight, flight test aircraft and material factor are now reported here.



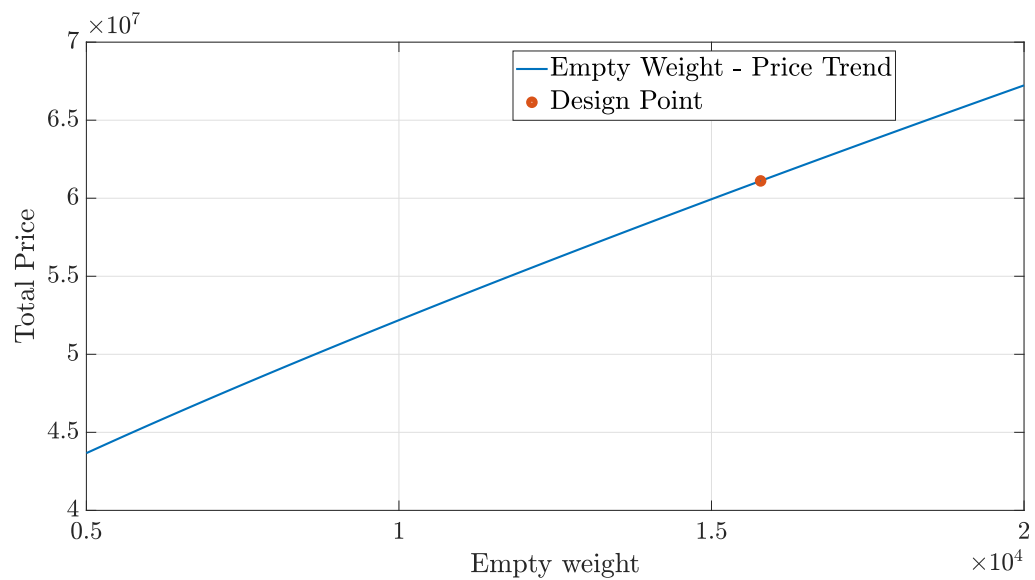


Figure 22.2: sensitivity empty weight

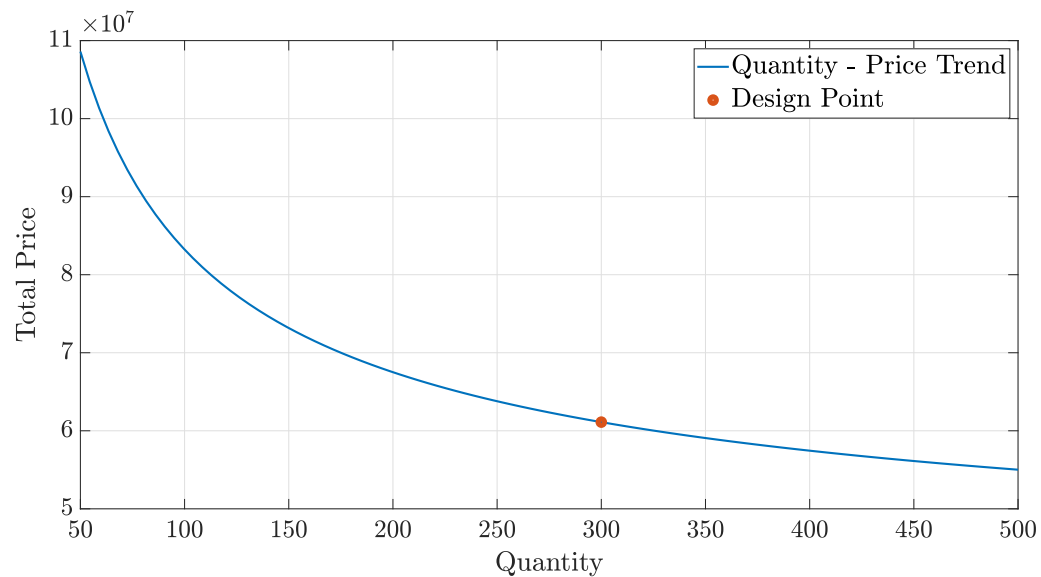


Figure 22.3: sensitivity quantity

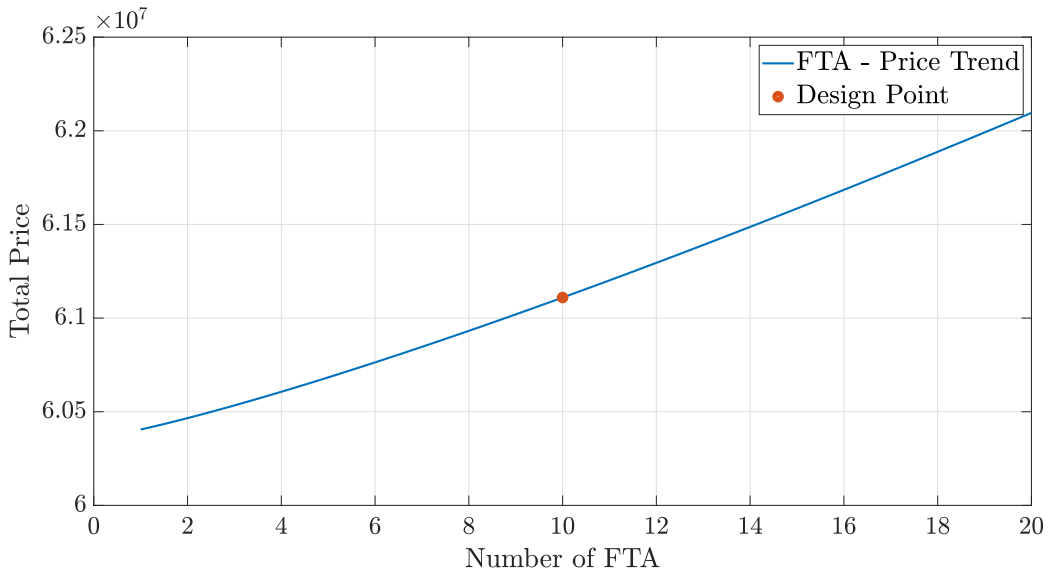


Figure 22.4: sensitivity FTA

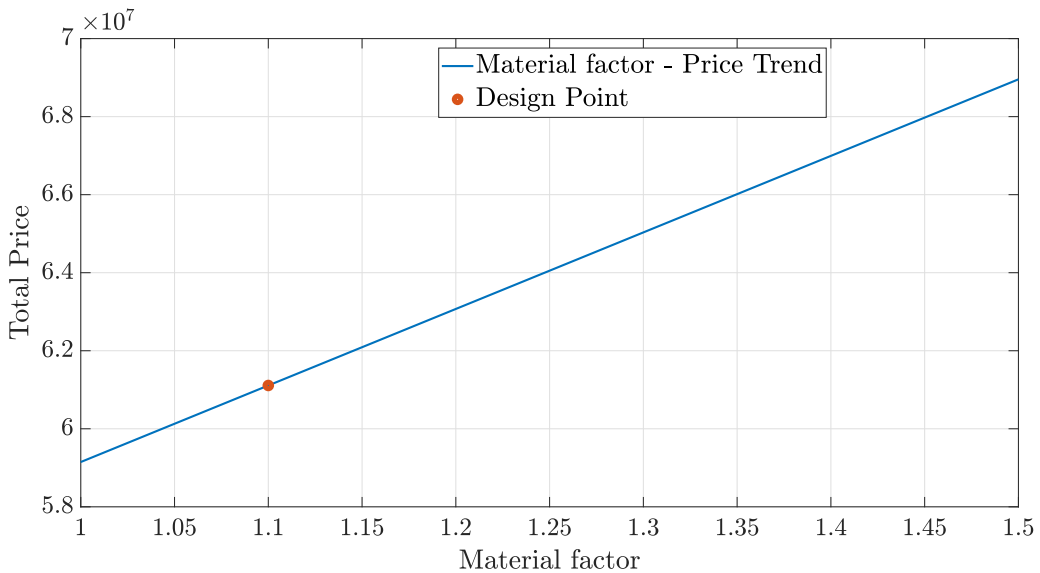


Figure 22.5: Sensitivity material factor

Particular attention was paid to the study shown in Figure 22.3 together with the data reported in Table 22.1 for the choice of the benchmark of aircraft produced. In this regard, it was chosen to set a conservative preliminary production schedule that envisioned the production of 300 aircraft. This choice leads to the preliminary estimate of program costs and revenues shown in Table 22.10.



Total program cost	14.5 Billions
Total revenues	18.4 Billions
Profit	3.9 Billions

Table 22.5: Total program cost and revenues

In conclusion, an analysis was also conducted to validate also in economic terms the initial choice to move toward an aircraft with a traditional aluminum structure.

Percentage of composite material	50 %
New material factor	1.32
Weight saving	20 %
Price of composite aircraft	60,020,191
Savings	1.8 %

Table 22.6: Cost for a more composite aircraft

From the data shown in Table 22.6 it is possible to observe that the cost savings associated with a Raven 4 more composite would be on the order of 1.8%. This estimate, even though it is very preliminary and not properly verified due to the low data availability of primarily composite aircraft, nonetheless suggests to us that the engineering choice to remain on a predominantly aluminum configuration remains a comparable choice in terms of cost to the possibility of a lighter composite aircraft.

22.2.6. Operating cost

From a perspective of competitiveness, even in the military sector, operating costs have become increasingly important over the years. In fact, the costs associated with the maintenance and utilization of a complex military asset can become compromising for a military program in terms of government funding.

In this section, some key factors that determine operational deployment within the same military service will be explored.

The program operating costs of military airplanes can be broken down as follows:

- Fuel, oil and lubricants cost

- Direct personnel cost (aircrew and maintenance)
- Indirect personnel
- Consumable material use in conjunction with maintenance
- Spares cost
- Depots
- Miscellaneous cost

Depreciation will be not taken into account in military case because obsolete military aircraft are flown one last time to reach some dedicated area where they can be collect and storage. Just as there are available models for estimating costs, there are also some models available for estimating direct operating costs. For this study, a cost estimation model presented in Roskam's "Airplane Cost Estimation" [22] was utilized, which provides a dedicated model for military aircraft. The estimation procedure described in Raymer [19] was also used to compare and verify estimates related to fuel cost, crew cost, and aircraft maintenance.

The typical mission flight and the yearly utilisation of the aircraft was established according to the parameter shown in Table 22.7.

Block time (T_{block})	220 min
utilisation Rate (U)	800 hr/year
Mission fuel	12,760 lb (5788 kg)

Table 22.7: Utilization of the aircraft.

Based on the data presented in Table 22.7, it is possible to estimate the costs related to fuel, oil, and lubricant using an equation that takes into account the years of service of the aircraft and the number of aircraft in actual service. In particular, an average service life of 30 years and a fleet of 50 aircraft were considered. For the cost of the crew and the maintenance labor rate, reference data from the tables presented in Roskam's work were used. An overhead rate factor was also applied to provide a more accurate representation of the actual pay for military personnel.

Crew Member	169 \$/hr
maintenance Labor rate	90 \$/hr

Table 22.8: Cost of direct personnel cost



Regarding the costs related to the material used for maintenance, it is challenging to estimate with precision. However, taking into account the data presented in Roskam Part VIII, a cost of 13 \$/hr for consumable materials used in maintenance has been considered.

Finally, for the costs related to indirect personnel, spares, depots, and miscellaneous expenses, typical values were assigned as percentages of the total operating costs, as shown in Table 22.9.

Cost	%
Indirect Personnel	0.2
Spares	0.15
Depots	0.18
Miscellaneous	0.04

Table 22.9: Percentage of costs related to indirect personnel, spares, depots, and miscellaneous in relation to the total operating cost.

In conclusion, we can summarize the operational costs as shown in the table 22.10.

Item	Cost	Percentage %
Fuel, Oil and Lubricant	1,340,589,097 \$	9.7 %
Direct Personnel	4,152,323,250 \$	30 %
Indirect Personnel	2,772,517,371	20 %
Consumable Materials use in maintenance	468,000,000 \$	3.4 %
Spares	2,079,388,028 \$	15 %
Depots	2,495,265,634 \$	18 %
Miscellaneous	554,503,474 \$	4 %
Total program cost	13,862,586,854 \$	
Program operating cost per flight hour	11,552 \$	

Table 22.10: Total program operating cost

23 | Aircraft drawings

This section is dedicated to 3D views of the aircraft in three different configurations:

- Jet: Figure 23.1, Figure 23.2, Figure 23.3 and Figure 23.4
- Rotorcraft: Figure 23.5, Figure 23.6, Figure 23.7 and Figure 23.8
- Conversion: Figure 23.9, Figure 23.11, Figure 23.12 and Figure 23.10

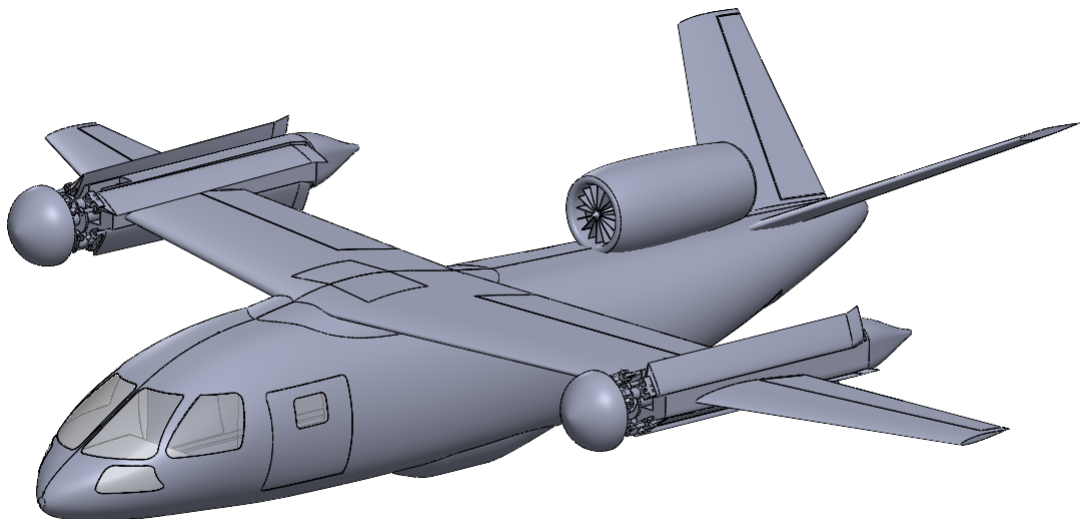


Figure 23.1: Jet configuration

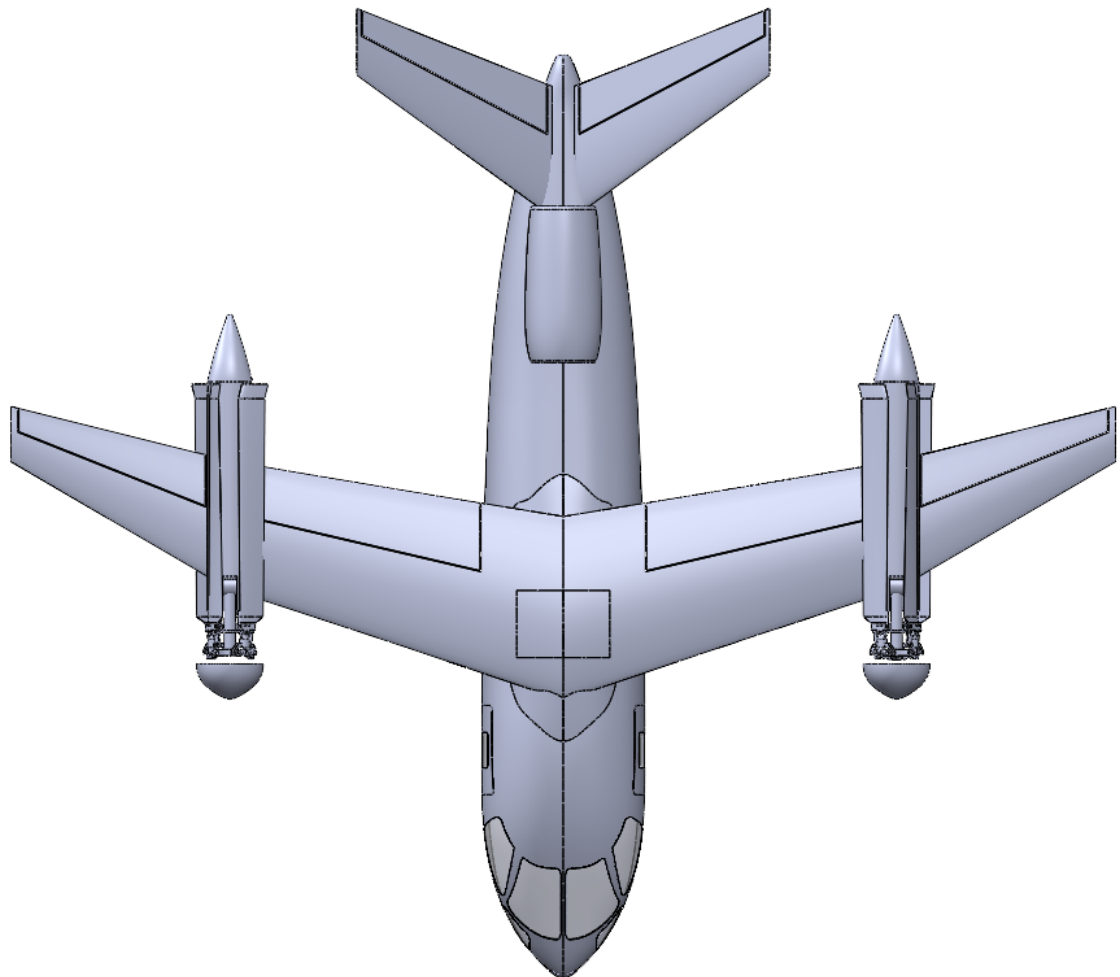


Figure 23.2: Top view - jet configuration



Figure 23.3: Front view - jet configuration



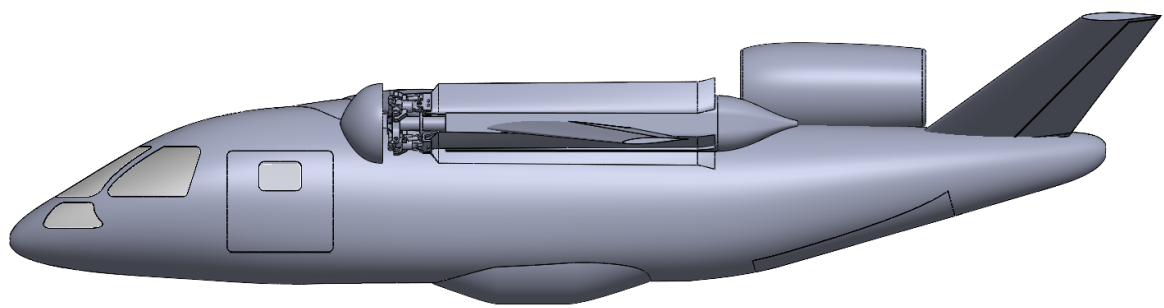


Figure 23.4: Lateral view - jet configuration

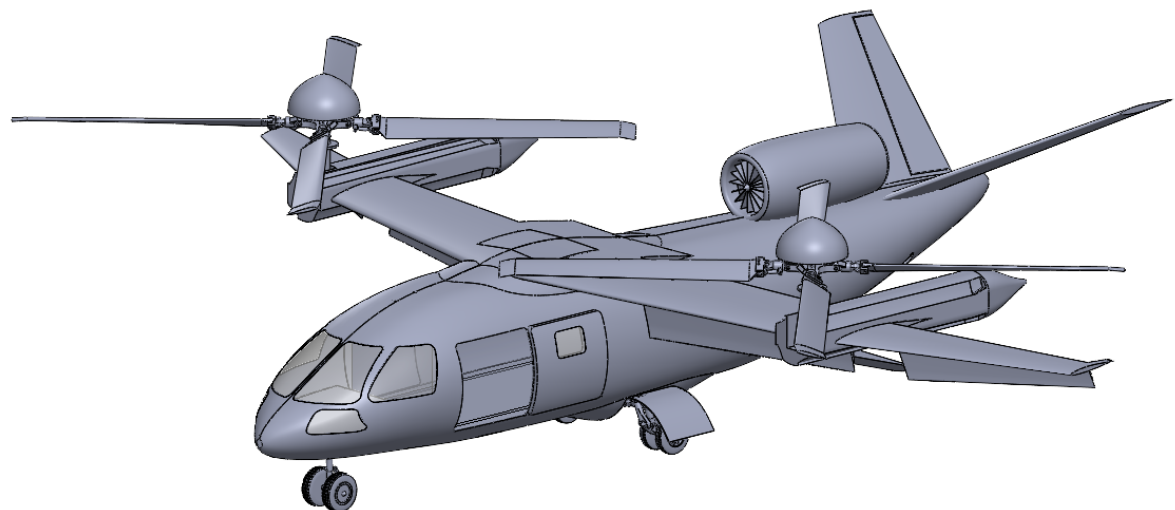


Figure 23.5: Rotorcraft configuration

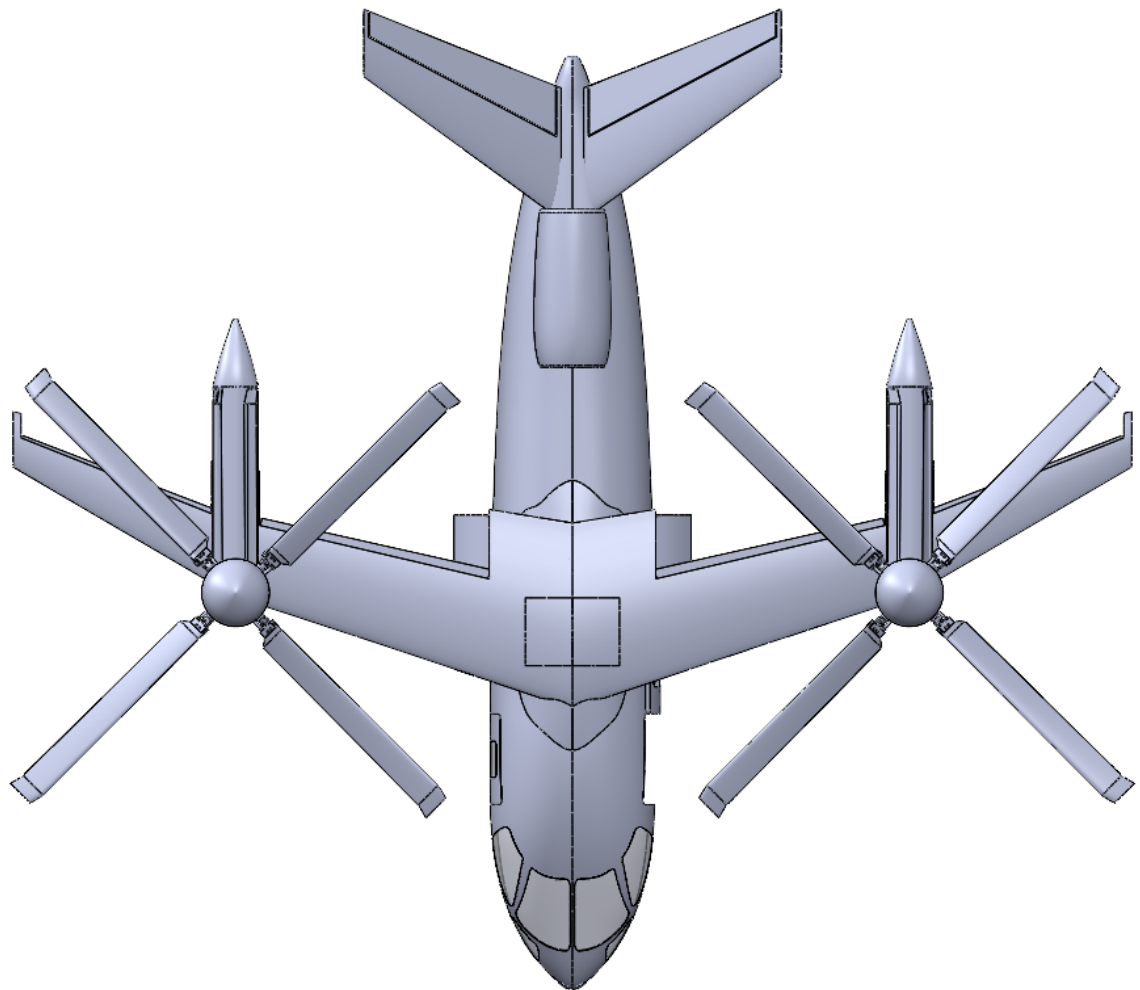


Figure 23.6: Top view - rotorcraft configuration



Figure 23.7: Front view - rotorcraft configuration



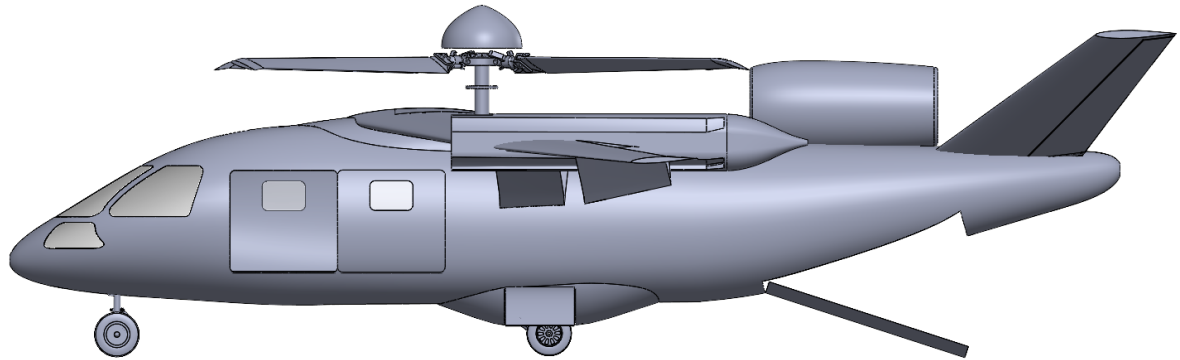


Figure 23.8: Lateral view - rotorcraft configuration

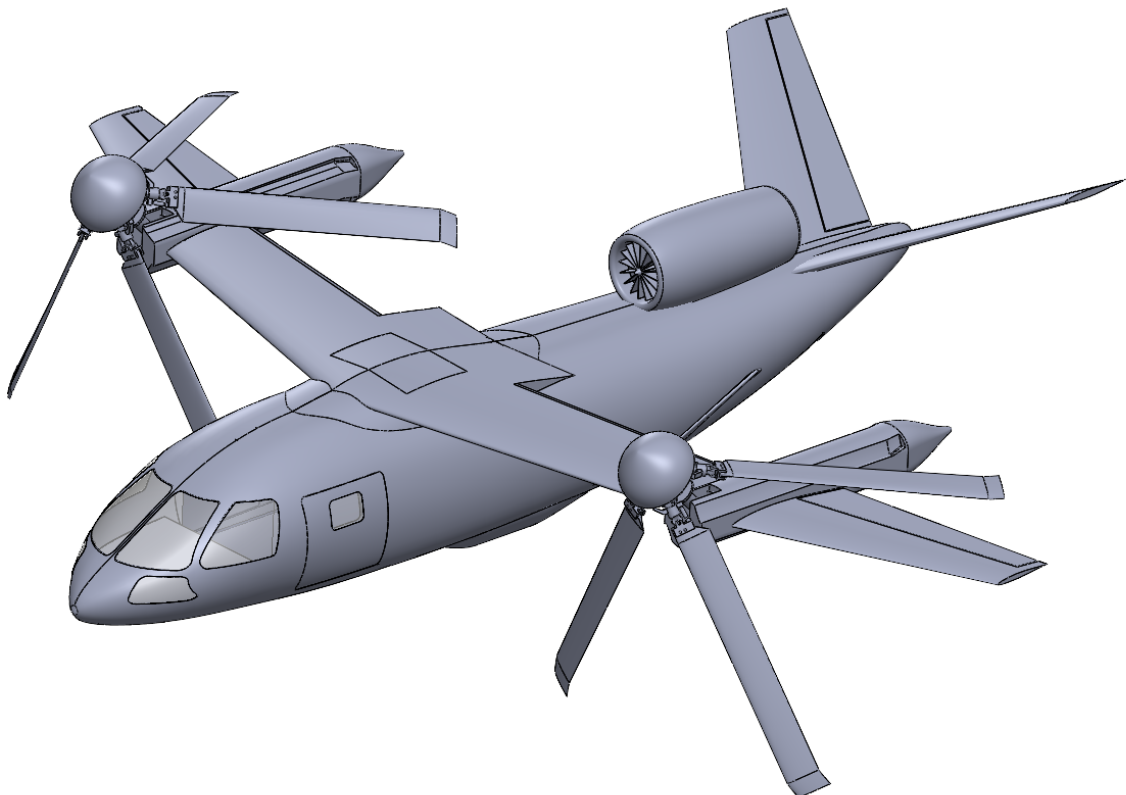


Figure 23.9: Conversion

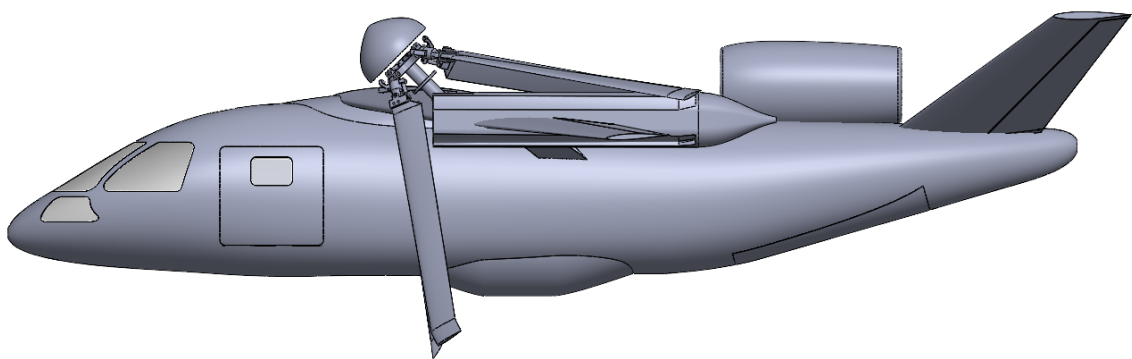


Figure 23.10: Lateral view - conversion

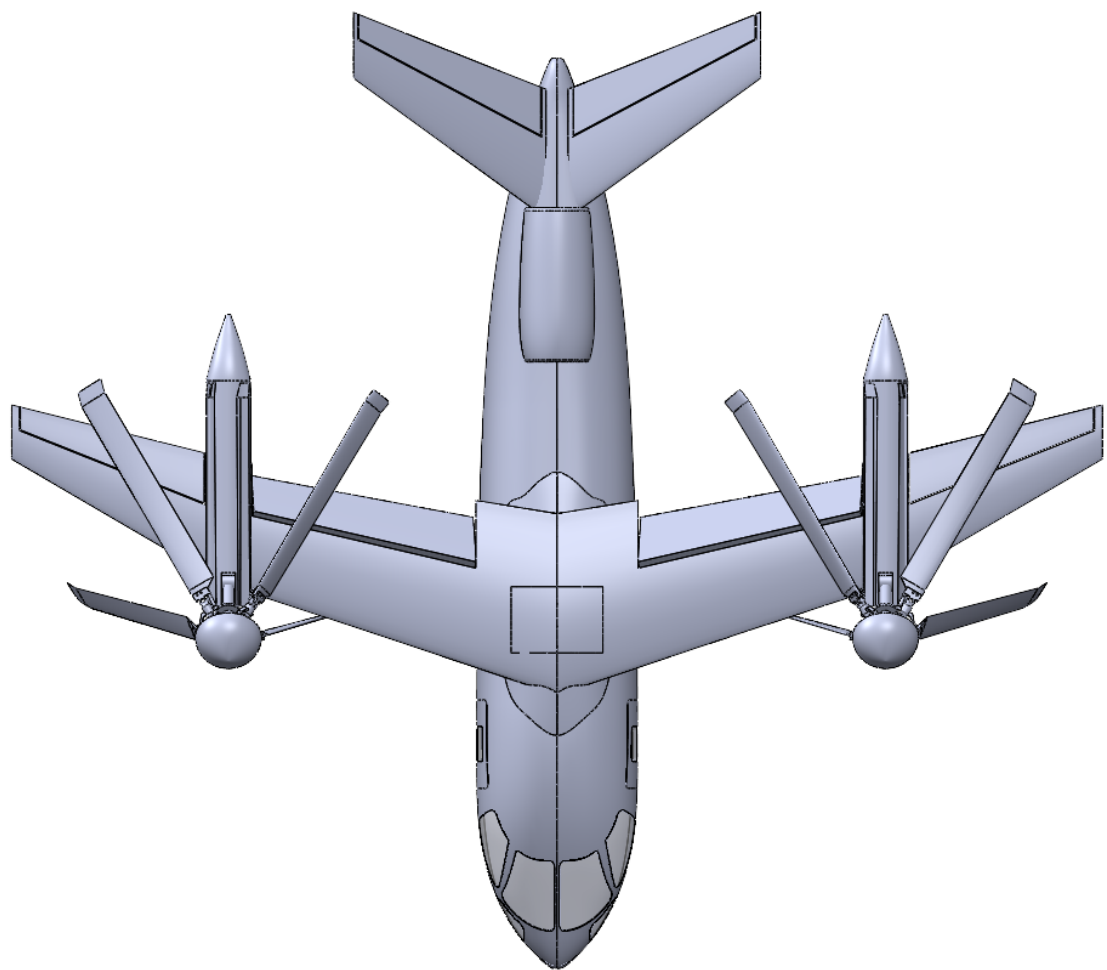


Figure 23.11: Top view - conversion





Figure 23.12: Front view - conversion

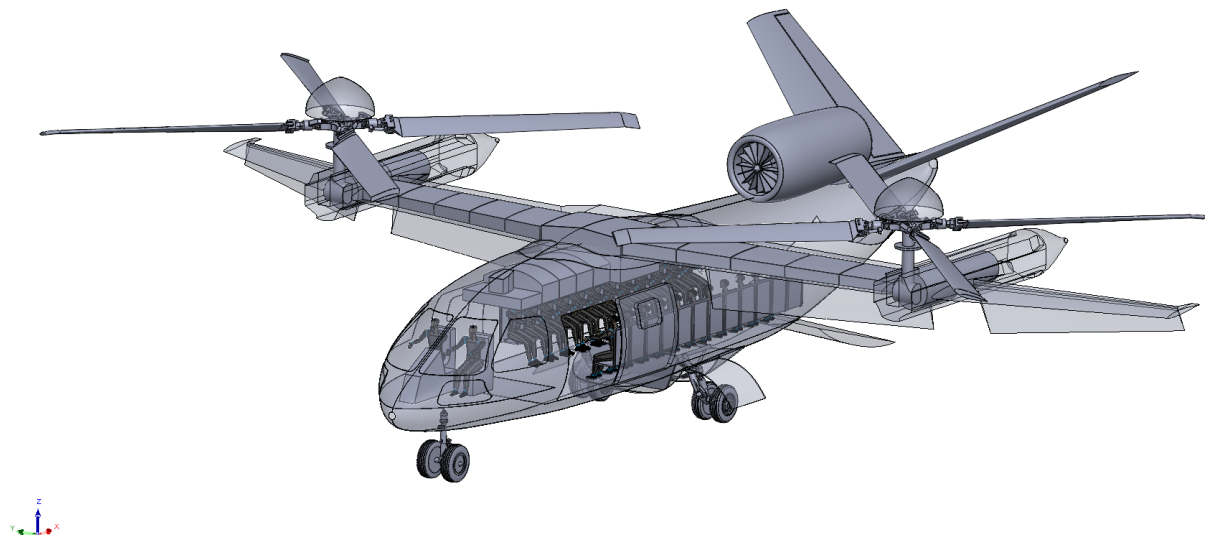
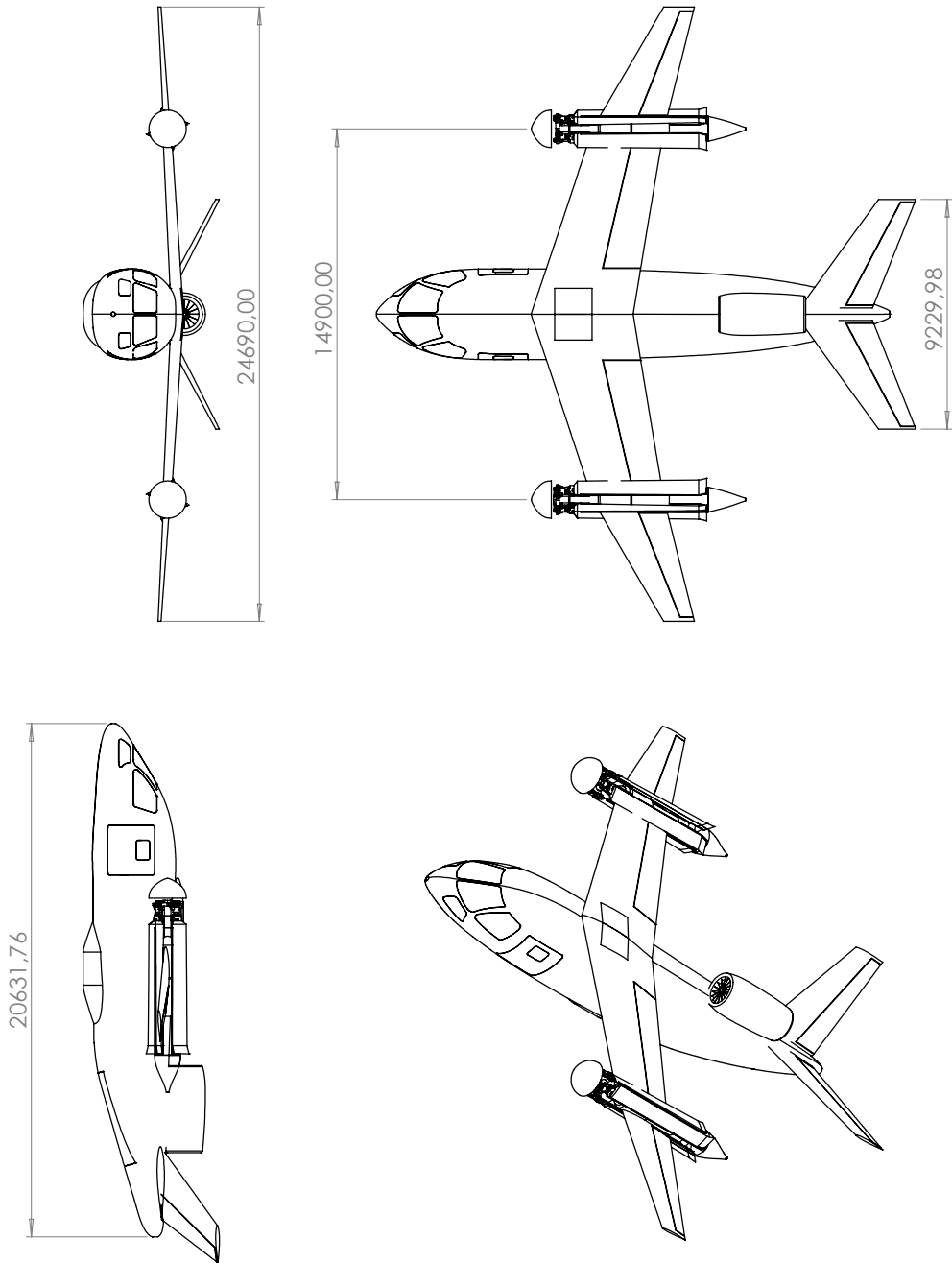


Figure 23.13: Internal details

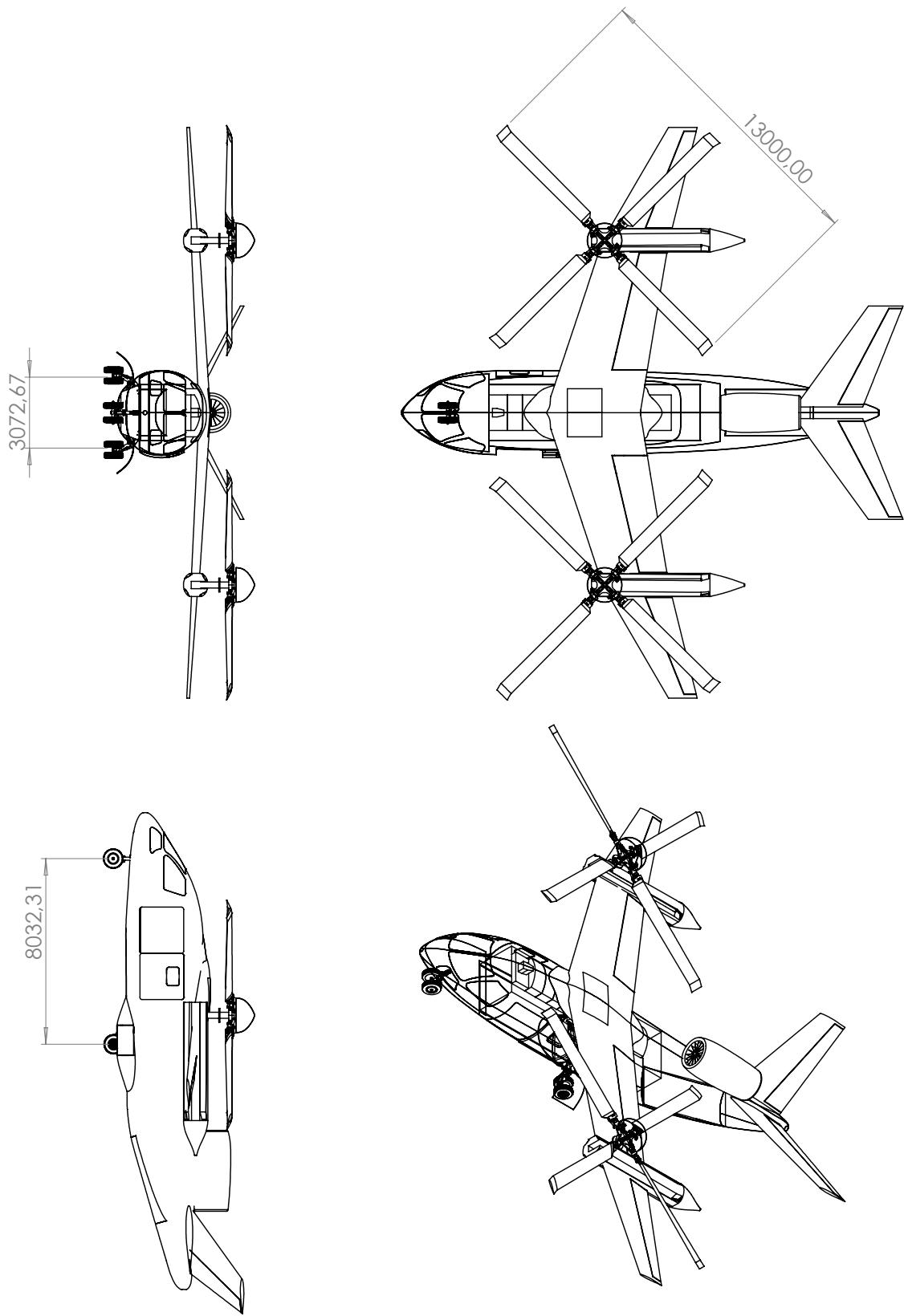
2D drawings of the airplane (scale of 1:150) with principal dimensions (expressed in mm) both in jet and rotorcraft mode are reported in Figure 23.14 and Figure 23.15.



SOLIDWORKS Educational Product. Solo per uso didattico.

Figure 23.14: 2D drawings - jet configuration





SOLIDWORKS Educational Product. Solo per uso didattico.

Figure 23.15: 2D drawings - rotorcraft configuration

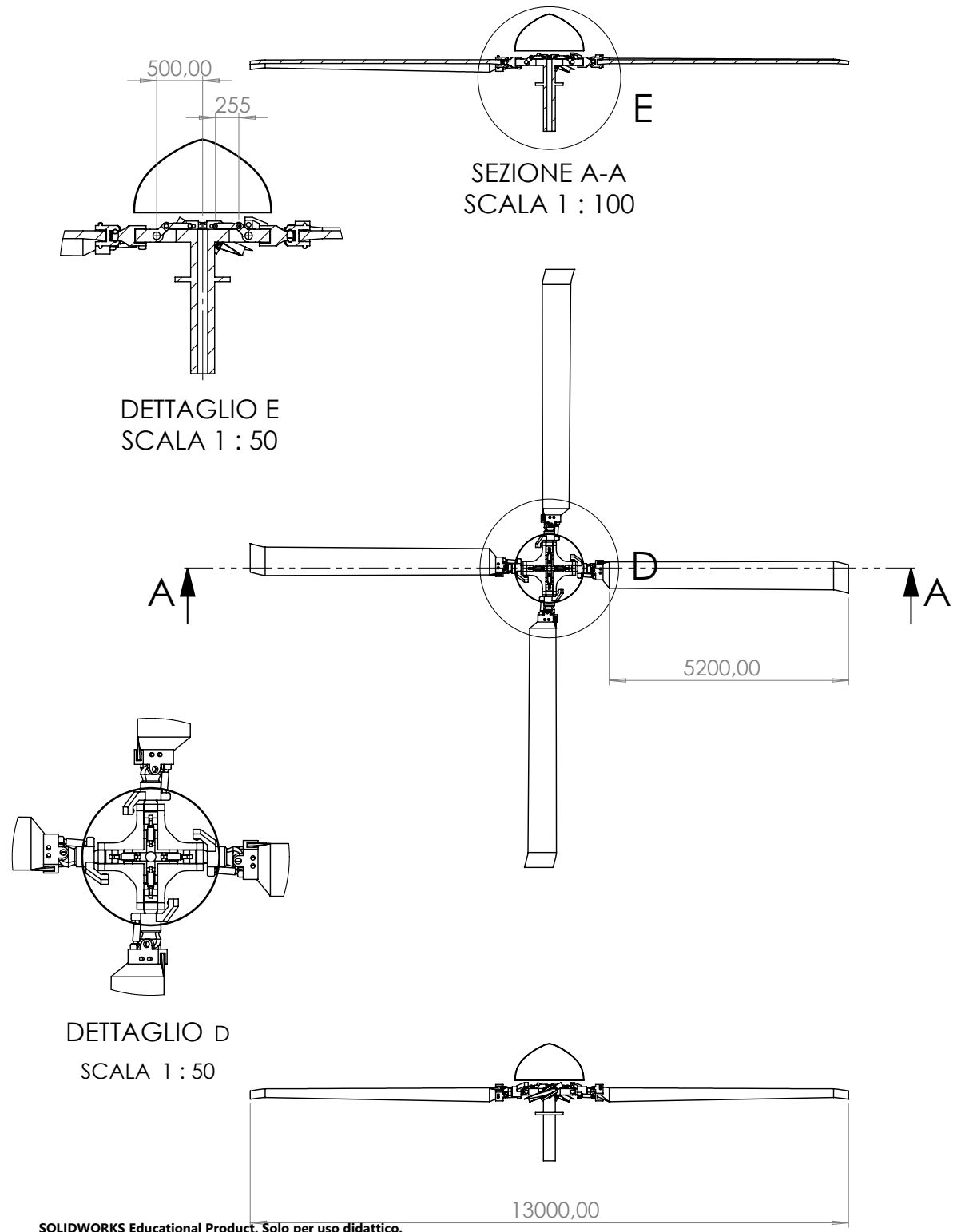


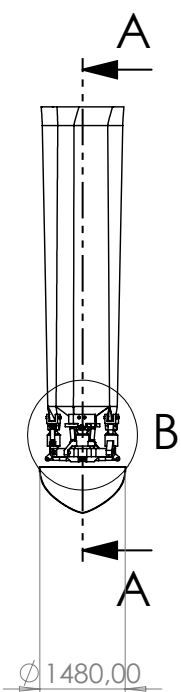
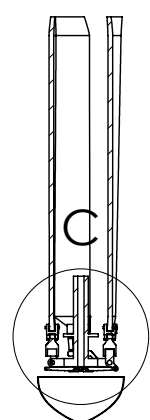
Figure 23.16: 2D drawings - Open rotor



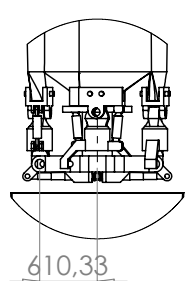


DETTAGLIO C

SCALA 1 : 50



SEZIONE A-A



DETTAGLIO B

SCALA 1 : 50

SOLIDWORKS Educational Product. Solo per uso didattico.

Figure 23.17: 2D drawings - Closed rotor

24 | Risk assessment

In this chapter it is intended to explore a preliminary analysis of the major risks associated with Raven 4 flight to observe the major safety concerns and where the greatest attention and depth would need to be given in future development and design.

In performing this analysis, reference was made to the use of an ICAO standard risk matrix as shown in Figure 24.1.

		PROBABILITY				
		Extremely Improbable 1	Improbable 2	Remote 3	Occasional 4	Frequent 5
SEVERITY	Catastrophic A	1A	2A	3A	4A	5A
	Hazardous B	1B	2B	3B	4B	5B
	Major C	1C	2C	3C	4C	5C
	Minor D	1D	2D	3D	4D	5D
	Negligible E	1E	2E	3E	4E	5E

Figure 24.1: ICAO Risk Matrix

ICAO's matrix presents 5 levels of risk probability and 5 levels of risk severity, which combined together allow a risk to be identified as acceptable without further analysis, acceptable with appropriate reasons and conditions of acceptability, or in the worst case not acceptable under any circumstances.

Definitions referring to the levels of severity and probability considered are given below:

Severity:

- *Catastrophic*: loss of human lives and destruction of materials and environment.
- *Hazardous*: serious injuries and lifelong disabilities, prolonged negative impacts on the environment and structures.

- *Major*: wounded with recoverable disabilities, relevant but recoverable impacts on structures and environment.
- *Minor*: minor injuries and minimal impact on structures and environment.
- *Negligible*: absence of wounded or minor damages and negligible impacts on both structures and environment.

Probability:

- *Frequent*: likely to occur often in the life of an item, with a likelihood of occurrence greater than 10^{-2} in any one mission.
- *Occasional*: will occur several times in the life of an item, with a likelihood of occurrence less than 10^{-2} but greater than 10^{-3} in any one mission.
- *Remote*: likely to occur sometime in the life of an item, with a likelihood of occurrence less than 10^{-3} but greater than 10^{-5} in any one mission.
- *Improbable*: unlikely but possible to occur in the life of an item, with a likelihood of occurrence less than 10^{-5} but greater than 10^{-6} in any one mission.
- *Extremely improbable*: so unlikely, it can be assumed occurrence may not be experienced, with a likelihood of occurrence less than 10^{-6} in any one mission.

For each phase of rotorcraft, conversion and jet flight, a number of critical issues assessed for their consequences and mitigation as well as their likelihood and severity are reported below in Figure 24.2.



RISK	CONSEQUENCE	MITIGATION	PROBABILITY / SEVERITY
Jet engine ingestion of debrief	Loss of the engine and inability to sustain flight in aircraft or rotorcraft mode at high speed	Attention by the crew of the areas in which to perform take-offs, landings, and hover operations	C4
Turboshaft failure	Inability to continue flight in rotorcraft mode	Drive shaft between the two turboshaft motors to ensure symmetrical thrust. Sustained flight in jet mode if at high enough speeds. Instant landing with the possibility of autorotation	C2
Jet-engine failure	Inability to maintain flight in aircraft mode	Ability to continue flight in rotorcraft mode at low speeds. If failure occurs while jet-mode is in use, there is the possibility of reopening the rotors by taking advantage of available altitude to maintain necessary speed or emergency glide	C2
Failure of rotor and drive-shaft tilting	Inability to perform rotorcraft-mode to jet-mode conversion and vice versa	Ability to continue jet-mode flight at low speeds for an emergency landing in airplane mode. If necessary, some small explosive charges allow separation from the locked rotors in order to sustain flight in jet-mode	A2
Multirail technology failure	Inability to perform rotorcraft-mode to jet-mode conversion and vice versa	Ability to continue jet-mode flight at low speeds for an emergency landing in airplane mode. If necessary, some small explosive charges allow separation from the locked rotors in order to sustain flight in jet-mode	A2
Flight Control System failure	Total loss of aircraft control	High redundancy of on-board computers and sensors	A2
Firearm damage	Possible loss of engines or control on the aircraft	Protection of the most sensitive areas with higher aluminum thicknesses to resist enemy fire	D4

Figure 24.2: Risk Matrix with mitigation items and procedures

One of the most important things inside the risk and mitigation matrix is to reduce risk probability and severity by downgrading red boxes into yellow or green boxes after the mitigation.

From the table 24.2 we can observe how the main technologies aboard Raven 4 that allow it to particularly distinguish itself are also the aspects found to be most critical to its safety and mission success. In particular we observe how a complex and safe flight control system is of paramount importance of any mission success. In fact, a loss of it would lead to a total loss of control of the aircraft, which would no longer be recoverable.

25 | Conclusions and critical evaluation

This project represents a push towards the possibility of achieving much more flexible operational capabilities in terms of speed, long-range travel, mission versatility and flexibility and can be considered more than just an alternative to aircraft already on the market, being able to outperform current competitors in the market, such as the tiltrotors used by the USAF.

Raven 4 is able to deliver all the requirements stated in chapter 8, both for rotorcraft and jet-mode, and sometimes exceed them:

- It is possible to perform cruising at the airspeed of 450 kn (as required by the RFP), extendable up to a maximum of 550 kn.
- The operational range of 1000 nm is guaranteed, and in ferry-range *Raven 4* can reach destinations up to 4200 nm, thus allowing the aircraft to be transported from the U.S. to Europe without using ships
- As for the payload, Sikorsky required 2268 kg, however the Team decided to extend it up to 3300 kg, in order to be able to take advantage of the large cabin dimensions to transport even light military vehicles and supplies for troops in hostile environments.
- All rotorcraft-mode performances far exceeds almost all requirements; this is also to maintain a wide growth margin for future development of the aircraft, a feature highly valued by the armed forces worldwide.

Finally, the preliminary price of the aircraft will be \$60 M, to be considered highly competitive in this phase of spending review even in the military context.

Raven 4 aligns with existing competitors, such as the V-22 Osprey and V-280 Valor, but adds the ability to perform high-speed cruising and exploit wider operating ranges.

Regarding future competitors, the *Arion* concept, winner of the 1-st prize of VFS graduate student HSVTOL competition 2022-2023, should be considered as a benchmark: preliminary data suggest that *Arion* will be capable of cruising at 450 kn, but with a maximum payload of 2270 kg, a ferry range of 2600 nm, and a cost of \$116.5 M. Thus, *Raven 4* proves to be more competitive in these parameters. On the other hand, avoiding rotor folding, *Arion* seems to be claiming a more mature level of technology, as well as being exempt from the major criticisms of *Raven 4*, derived from the folding mechanism. However, the choice to fly at such high speeds without folding the rotor leaves the Team at least doubtful.

Moreover, some critical points of the concept have been identified to be thoroughly analyzed in the future:

- Blade size plays a crucial role both in the drag they feel once stationary and in the space they occupy on the nacelle once stored. In this sense, a reduction in chord could be worthwhile. This reduction could be done by slightly increasing the rotational speed of the rotor, a parameter that was chosen in a conservative way.
- Each blade is closed by a dedicated actuator. In total, the aircraft has eight blades. It is clear that failure of even one of these actuators would prevent the conversion. This cannot be acceptable. It is reasonable to think of double redundancy on the actuators for each blade.
- Even with double redundancy, it is reasonable to consider the possibility of folding mechanism failure. As such, a way to get rid of the blades and be able to return home in jet-mode might be desirable. One possibility might be the use of explosive charges to force the blades apart. This hypothesis is, however, all to be analyzed.
- Operationally, the aircraft appears very vulnerable to enemy threats during the conversion phase, when its maneuverability is extremely reduced. In this sense, it is desired that the conversion time be reduced as much as possible and that countermeasures be equipped to protect the aircraft during this critical phase.
- Another definitely unfavorable aspect is the need to keep all three engines on for the duration of the flight. This need arises from the fact that, the great variation in weather conditions during the mission profile would not guarantee the ability of the engines to be turned on only when needed. This results in an inevitable waste of fuel.
- The problem of ingestion of foreign bodies lifted from the rotor wake when close to



the ground should also be carefully considered in real-life testing. Some implementations for preserving the safety and wear of the jet-engine may be needed to limit maintenance that may be more expensive than expected.

- Another problem the aircraft presents is that it can take-off in the same configuration with which it landed, because the blades would touch the ground by being too long. Hence, a future development to consider might be to design the blades to be telescopic so that they can be shortened once the aircraft has landed. This would make the *Raven 4* even more versatile.

As was reasonable to expect, the major concerns arise from the rotor folding system, in fact the only real major innovation in this design. The need for wind tunnel testing of the folding mechanism is a given.

Furthermore, this preliminary project also identifies several areas for potential future development, such as:

- Evaluate the possibility of ad hoc development of a single integrated propulsion system capable of supporting both jet-mode and rotorcraft-mode, avoiding the waste associated with not being able to shut down engines even when not in operation and the increased weight of three separate propulsion systems.
- Increasing the payload capacity in the cargo compartment.
- Exploit the growth margin associated with the available power to achieve higher performance in rotorcraft-mode.
- Evaluate whether it is appropriate to decrease the conversion speed and thus the stall speed, perhaps by implementing an enhanced flaps system.

Joining the Vertical Flight Society's request for proposal the Team is aware of how such an aircraft may still prove to be too premature for its TRL and MRL. Despite this, conducting an in-depth preliminary study in the direction of a HSVTOL allowed to delve deeper and take an extra step toward this future, being able to bring a contribution to the analysis of how such an outcome could be achieved by aviation industries.

Bibliography

- [1] M. Borri and L. Trainelli. Basic airplane equilibrium and stability revisited, 2007.
- [2] T. G. T. . R. Company. Global aviation tires. 200 Innovation Way Akron Ohio 44316, 2022.
- [3] T. G. Corporation. General electric t408, 2020.
- [4] N. S. Currey. *Aircraft Landing Gear Design:Principles and Practices*. American Institute of Aeronautics and Astronautics, Inc., 1988.
- [5] J. S. David T. Orletsky, Anthony D. Rosello. Intratheater airlift functional area analysis. Technical report, RAND corporation, 2011.
- [6] R. Healy, J. McCauley, F. Gandhi, and O. Sahni. A computational investigation of side-by-side rotors in ground effect. Technical report, Center for Mobility with Vertical Lift (MOVE), Rensselaer Polytechnic Institute, New York, USA, May 10 2021.
- [7] T. J. *Jane's All The World Aircraft's*. Jane's, London, 1976.
- [8] A. D. R. John Stillion, David T. Orletsky. Intratheater airlift functional needs analysis. Technical report, RAND corporation, 2011.
- [9] W. Johnson. *Rotorcraft Aeromechanics*. Cambridge, 32 Avenue of the Americas, New York, NY 10013-2473, USA, 2013.
- [10] D. C. Joseph P. Large, Harry G. Campbell. *Parametric Equations for Estimating Aircraft Airframe Costs*. Rand corporation, 1976.
- [11] T. C. . J. Katz. Induced drag of high-aspect ratio wings, 2004.
- [12] D. C. Martin D.Maisel, Demo J. Giulianetti. *The History of the XV-15 Tilt Rotor Research Aircraft*. National Aeronautics and space administration, 2000.
- [13] F. Nicolosi. Caratteristiche propulsive, modulo di prestazioni,corso di laurea in ingegneria aerospaziale, 2023.

- [14] U. S. D. of Defense. Mil-s-8698 (usaf), 1993.
- [15] U. S. D. of Defense. Mil-std-1472g (usaf), 2012.
- [16] Preston, Troutman, Keen, Silva, Calvert, Cardamone, Moulton, and Ferguson. Rotorwash operational footprint modeling. Technical Report RDMR-AF-14-02, U.S. Army RDECOM, 7 2014.
- [17] H. P. R. R. W. Hess. *Aircraft Airframe Cost Estimating Eelationships, Study Approach and Conlusions*. Rand corporation, 1987.
- [18] H. P. R. R. W. Hess. *Aircraft Airframe Cost Estimating Relationships: All Mission Types*. Rand corporation, 1987.
- [19] D. P. Raymer. *Aircraft Design: A Conceptual Approach*. American Institute of Aeronautics and Astronautics, Inc., 2018.
- [20] T. ROGOWAY. We talk v-280 valor versus v-22 osprey with bell's head of tiltrotor systems, 2019.
- [21] H. Rosenstein and R. Clark. Aerodynamic development of the v-22 tilt rotor. Technical report, AIAA'86, Boeing Vertol Company, Philadelphia, PA, 1986.
- [22] J. Roskam. *Airplane Design part VIII: Airplane Cost estimation: Design, Development, Manufacturing and Operating*. DARcorporation, 1990.
- [23] J. Roskam. *Airplane Design part I: Preliminary sizing of Airplanes*. DARcorporation, 1997.
- [24] J. Roskam. *Airplane Design part II: Preliminary Configuration Design and Integration of the Propulsion System*. DARcorporation, 1997.
- [25] J. Roskam. *Airplane Design part V: Component Weight Estimation*. DARcorporation, 1997.
- [26] J. Roskam. *Airplane Design part VI: Preliminary Calculation of Aerodynamic Thrust and Power Characteristics*. DARcorporation, 1997.
- [27] J. Roskam. *Airplane Design part VII: Determination of Stability, Control and Performance Characteristics Far and Military Requirements*. DARcorporation, 1997.
- [28] R. S. Basic course on neocass. Technical report, Politecnico di Milano, 2018.
- [29] M. H. Sadraey. *Aircraft Design: A Systems Engineering Approach*. John Wiley & Sons, Ltd., 2013.



- [30] L. Sala, G. Alitta, D. Berbenni, C. Capocchiano, A. Fugazza, S. Rojas, S. Sangalli, A. Scaringello, P. Waffo, and L. Trainelli. Project caururs "nibbio" - a novel tilt rotor concept for very high speed. Technical report, Politecnico di Milano, Italy, 2015.
- [31] V. F. Society. 40th annual student design competition 2022-2023 request for proposals, 2022.
- [32] V. F. Society. The v/stol wheel, 2023.
- [33] Soikkeli. Unifier19 c7a-harw flight dynamics simulator, 2022.
- [34] E. Torenbeek. *Synthesis of Subsonic Aitplane Design*. Delft University Press, Martinus Nijhoff Publishers,, 1982.
- [35] Élodie Roux. *Turbofan and Turbojet Engines, Database Handbook*. Éditions Élodie Roux, 2007.

List of Figures

2.1	Primary mission profile given by the RFP of the Vertical Flight Society	5
3.1	Work breakdown structure	8
3.2	Gantt chart and work organization	9
5.1	U.S. military operations country	16
5.2	Tiltrotors	18
5.3	Dornier Do 31	18
5.4	Tactical airlifters	19
6.1	Illustration of vertical and short take-off and landing [32].	23
6.2	Dependence on disk loading of hover efficiency	24
6.3	XV-3	25
6.4	The Bell stop/fold tilt rotor in the wind tunnel [12].	25
6.5	Slice cutting through side-by-side H/D = 0.5 2.5R separation IGE rotor hubs colored by vorticity magnitude	27
6.6	Relative thrust difference between six IGE rotor cases and an isolated OGE rotor (IGE minus OGE)	28
6.7	Nibbio	29
6.8	<i>Ragno</i>	29
6.9	<i>Ragno</i> folding steps	30
6.10	Two different tilting mechanism	31
7.1	Engine tail integration	40
7.2	Two engines at the tail	40
7.3	Tail configurations	41
7.4	Top view of the preliminary aircraft	42
9.1	Different polar estimation methods	47
9.2	Graphical solution of the implicit equation (9.5)	48
9.3	Legend of Figure 9.2	49

9.4	Preliminary weight breakdown	49
9.5	Jet-mode sizing matrix plot	50
9.6	Legend Figure 9.5 and Figure 9.7	51
9.7	Jet-mode sizing matrix plot decluttered	51
9.8	Stall speed sensitivity analysis	52
9.9	Downwash/outwash effect of single and twin rotors [16]	53
9.10	Onset of surface failure [31]	54
9.11	Momentum theory model	55
9.12	Momentum theory results	57
9.13	Sizing procedure breakdown	59
9.14	Wing root bending moment	60
9.15	Blade tip deflection, varying EJ	61
9.16	Blade tip deflection, varying blade pitch	61
9.17	Disk loading vs radius sensitivity analysis	62
9.18	Blade deflection for the chosen radius	62
9.19	Tip speed analysis	63
9.20	Induced velocity results	65
9.21	Blade element theory reference system	66
9.22	Notable angles results	66
9.23	Blade lift distribution	67
9.24	Blade twist	67
9.25	Sizing Matrix Plot (MTOW)	68
9.26	Legend of sizing Matrix Plot (MTOW)	69
9.27	Sizing Matrix Plot (MMGW)	69
9.28	Legend of sizing Matrix Plot (MMGW)	70
9.29	$C_T\sigma$	72
9.30	$DL\sigma$	73
9.31	$MTOM\sigma$	73
9.32	Validation by means of EH101	74
10.1	Different hinge order configurations	76
10.2	Right Hub detail, rotation counterclockwise from top view	77
10.3	Flap motion with hinge offset	77
10.4	Section of the blade structure	79
10.5	Position of CG	80
10.6	Property of the blade	81
10.7	Bending modes of the blade	81



10.8 Torsion modes of the blade	82
10.9 Fan Plot	83
10.10Pin rails (two for each actuator)	84
10.11Rotor in operative phase	85
10.12Figure 10.11 middle plane slice	85
10.13Rotor in cruise phase	86
10.14Figure 10.13 middle plane slice	87
10.15Open position	88
10.16Closed position	88
10.17Transition screenshot	89
10.18Actuator force	91
10.19Bending moment in O	91
10.20Actuator power for fixed actuator speed	92
10.21 $\dot{\phi}$ for fixed actuator speed	93
10.22Actuator power for fixed $\dot{\phi}$	93
10.23Actuator linear speed for fixed $\dot{\phi}$	94
10.24Critical areas of the rotor in forward flight at 100 kn	95
10.25Aerodynamic curves estimated with XFLR5 ($Re = 4*10^6$, $M = 0.4$)	97
10.26Pressure distribution for outboard blade airfoil sections	97
11.1 Project point for wing airfoil (from Reference [29])	101
11.2 $C_d - C_l$ in conversion phase	102
11.3 $C_l - \alpha$ in conversion phase	103
11.4 $C_m - \alpha$ in conversion phase	103
11.5 $C_d - C_l$ in cruise phase	104
11.6 $C_l - \alpha$ in cruise phase	104
11.7 $C_m - \alpha$ in cruise phase	105
11.8 Airfoil sections along the wingspan	108
11.9 Pressure distribution over wing airfoil (NACA 65(1)-212)	111
11.10Top view of the wing	112
11.11Typical variation of lift distribution over the wing due to sweep angle	112
11.12Twist angle along the wingspan	114
11.13Lift Distribution	115
11.14Load Distribution	116
11.15 $C_L - \alpha$ curve with slotted flap (at Mach = 0.15)	117
12.1 Tail design framework	122
12.2 Horizontal tail volume statistics collection from different literature	123

12.3 Vertical tail volume statistics collection from different literature	123
12.4 The variation of wetted area with respect to tail arm	125
12.5 Definition of butterfly angle	125
12.6 NACA 63A010 results	127
12.7 Polar curve (from viscous simulation on XFLR5)	130
12.8 $C_L - \alpha$ (XFLR5)	130
12.9 Front view of wing and tail (XFLR5)	131
12.10 Top view of wing and tail (XFLR5)	131
12.11 Top view of the preliminary aircraft	132
13.1 Flight deck lateral view	135
13.2 Flight deck front view	135
13.3 Preliminary volume of fuel tanks	136
13.4 Radius link to rotate wheel 90 deg.	140
13.5 Retraction system of BAe-146 main gear.	140
13.6 Design requirements and external shape of the fuselage	141
13.7 Relation between C_{d0} and L/D	142
13.8 Troops configuration	143
13.9 Troops and cargo configuration	144
13.10 Cargo configuration	144
14.1 F118-GE-100	147
14.2 Pratt & Whitney F135-PW-600	148
14.3 Jet-engine position	149
14.4 Turboshaft engine T408-GE-400	151
14.5 Drive system	153
14.6 Fuel tanks	154
14.7 Volume of fuel tanks	155
14.8 Cockpit view	158
15.1 Neocass architecture [28]	162
15.2 V-n diagram	163
15.3 Aerodynamic model of NeoCASS	164
15.4 Structural model of NeoCASS	164
15.5 V-tail torque bending	165
15.6 V-tail torque shear	166
15.7 V-tail bending shear	166
15.8 V-tail bending	167



15.9 V-tail torque	167
15.10V-tail shear	167
15.11V-tail max shear	167
15.12V-tail maxbernding	167
15.13V-tail max torque	168
15.14Mass distribution along the fuselage	168
15.15Deformed model for trim analysis in cruise at 40,000 ft. A scale factor equal to 10 is been chosen to better observe structural deflection.	169
15.16Mode 7	170
15.17Mode 8	170
15.18Flutter 1 st mass configuration	171
15.19Flutter 2 nd mass configuration	172
15.20Flutter 3 rd mass configuration	172
15.21Mass breakdown pie chart	175
15.22CG envelope	178
15.23Longitudinal CG position travel during Primary Mission	179
15.24Fuel distribution in the forward tanks	180
15.25Caption	180
16.1 Positive sign convention for primary airplane controls (back view of the aircraft)	184
16.2 Aileron performance for phase B and C	186
16.3 Aileron performance for phase A	186
16.4 Aileron performance for phase B and C	187
16.5 Aileron performance for phase A	187
16.6 Rudder performance	189
16.7 Controls during all configurations	192
16.8 Conversion phase	193
17.1 Graphical solution of wing wave drag coefficient	198
17.2 Build-up of transonic fuselage zero-lift drag coefficient from reference [26] . .	199
17.3 Graphical solution of empennage wave drag coefficient	205
17.4 Polar curve predicted with Class II method of Roskam in clean configuration	209
17.5 Contribution of each component on the drag polar	210
17.6 Polar curve predicted in conversion phase (with flap and unfold rotors) . .	210
17.7 Polar curve predicted in cruise phase	211
18.1 Thrust available trends	213

18.2 Conversion phase with $\delta_f = 30^\circ$	214
18.3 Conversion phase with $\delta_f = 40^\circ$ (only on the inboard wing)	215
18.4 Conversion phase with $\delta_f = 20^\circ$ all over the wing	215
18.5 Cruise phase	216
18.6 Best range altitude for constant speed and weight	217
18.7 Best range cruise at 450 kn	217
18.8 Penetration phase	218
18.9 Definition of military take-off distance	219
18.10 Take-off distance for different thrust	220
18.11 Take-off distance for different flap deflections	221
18.12 Take-off distance for different runway elevation	222
18.13 Definition of military landing distance	223
18.14 Landing distance for different weight	224
18.15 Landing distance for different flap deflections	225
18.16 Landing distance for different runway elevation	226
18.17 Major US and NATO air force facilities	227
18.18 Rate of climb at sea level (and MTOW)	228
18.19 Best rate of climb with respect to altitude	229
18.20 Airspeed of BROc with respect to altitude	229
18.21 Time to Climb	230
18.22 Effect of altitude and mach number on turbofan SFC	230
18.23 Payload range diagram	231
18.24 Ferry range capability	232
18.25 Operational Flight Envelope	232
18.26 Hover polar	233
18.27 FM vs gross weight	234
18.28 FM vs blade loading coefficient	235
18.29 Equivalent single rotor download effect	236
18.30 Equivalent single rotor download effect, V22 Osprey validation	237
18.31 Statistical hub drag	238
18.32 Edgewise forward flight (MTOW vs MCP)	239
18.33 Edgewise forward flight (MTOW vs MRP)	240
18.34 Edgewise forward flight (MMGW vs MCP)	240
18.35 Edgewise forward flight (MMGW vs MRP)	241
18.36 Rotor lift-to-equivalent drag	242
18.37 Required vs available jet thrust in conversion	243
18.38 Typical mission profile	245



18.39 Fuel consumed during primary mission profile	245
19.2 Static Margin for different position of center of gravity	250
19.3 Angle of attack in level flight	252
19.4 Elevator deflection angle in level flight	252
19.5 Example of Crocco's diagram	253
19.6 Crocco's diagram in cruise configuration	256
19.7 Crocco's diagram in conversion configuration	256
19.8 Crocco's diagram in landing configuration	257
19.9 Crocco's diagram in take-off configuration	257
19.10 Borri's parameters in coordinated turn	259
19.11 Static margins of coordinated turn	259
19.12 Trimmed lift in cruise configuration	260
19.13 Trimmed polar in cruise configuration	261
19.14 Trimmed lift in conversion configuration	262
19.15 Trimmed polar in conversion configuration	262
19.16 Trimmed lift in take-off configuration	263
19.17 Trimmed polar in take-off configuration	263
19.18 Trimmed lift in landing configuration	264
19.19 Trimmed polar in landing configuration	264
19.20 Hover trim non-linear model	266
19.21 Hover trim condition	266
19.22 Helicopter force equilibrium	267
19.23 Helicopter moment equilibrium	268
20.1 Aircraft model in OpenVSP	274
20.2 Stability and control derivatives for the conversion phase	275
20.3 Stability and control derivatives in cruise	275
20.4 Longitudinal input	276
20.5 Longitudinal mode eigenvalues (conversion configuration)	276
20.6 Longitudinal response (conversion configuration)	277
20.7 Longitudinal mode eigenvalues (cruise configuration)	277
20.8 Longitudinal response (cruise configuration)	278
20.9 Lateral-directional inputs	279
20.10 Lateral-directional mode eigenvalues (conversion configuration)	279
20.11 Lateral-directional response (conversion configuration)	280
20.12 Lateral-directional mode eigenvalues (cruise configuration)	281
20.13 Lateral-directional response (cruise configuration)	281



21.1 <i>Simulink</i> simulator structure	288
21.2 Dynamic model	289
21.3 Aerodynamic model	289
21.4 Control system architecture	290
21.5 SAS implementation	291
21.6 CAS+SAS implementation	291
21.7 Simulation of a typical mission	292
21.8 Example of visual interface of the simulator	293
22.1 Elements of life-cycle cost. [19]	297
22.2 sensitivity empty weight	303
22.3 sensitivity quantity	303
22.4 sensitivity FTA	304
22.5 Sensitivity material factor	304
23.1 Jet configuration	309
23.2 Top view - jet configuration	310
23.3 Front view - jet configuration	310
23.4 Lateral view - jet configuration	311
23.5 Rotorcraft configuration	311
23.6 Top view - rotorcraft configuration	312
23.7 Front view - rotorcraft configuration	312
23.8 Lateral view - rotorcraft configuration	313
23.9 Conversion	313
23.10 Lateral view - conversion	314
23.11 Top view - conversion	314
23.12 Front view - conversion	315
23.13 Internal details	315
23.14 2D drawings - jet configuration	316
23.15 2D drawings - rotorcraft configuration	317
23.16 2D drawings - Open rotor	318
23.17 2D drawings - Closed rotor	319
24.1 ICAO Risk Matrix	321
24.2 Risk Matrix with mitigation items and procedures	323



List of Tables

4.1	Table of correspondence between report chapters and contents (continuation on next page)	11
4.2	Continuation of table of correspondence between report chapters and contents	12
5.1	Characteristics of the competitors	20
7.1	Criteria order for the configuration choice	36
7.2	Configuration weights	38
8.1	Emission of jet-mode requirements	43
8.2	Emission of rotorcraft-mode requirements	44
9.1	Fuel fraction for each part of the mission.	46
9.2	Aerodynamics parameters	48
9.3	Weight fractions obtained at the initial iteration	49
9.4	Single rotor parameters	71
9.5	MTOW results (equivalent single rotor)	71
9.6	MMGW results (equivalent single rotor)	71
10.1	Material of the blade	79
10.2	Blade geometry and distance from hub center of rotor hinges	80
10.3	Actuator preliminary required characteristics	94
10.4	Features of rotor blade airfoil obtained from XFLR5 ($Re=4\cdot10^6$, $M=0.4$) . .	98
10.5	Cost function for features of rotor blade airfoil	98
10.6	Cost function of rotor blade airfoil normalized with respect the sum	98
11.1	Parameters of wing airfoil	105
11.2	Cost functions of wing airfoil	106
11.3	Normalized cost functions of wing airfoil	107
11.4	Taper ratio and wing chords	110
11.5	Sweep angle and wing chords	113
11.6	Aerodynamic results for the wing isolated @ $Ma = 0$	117

12.1 NACA 63A010 characteristics	127
12.2 V-tail parameters	129
12.3 Aerodynamic results @ $Ma = 0$	129
13.1 Dimensions of the flight deck	134
13.2 Preliminary volume of fuel tanks	135
13.3 Values for statistical tire sizing in inches	138
13.4 Tires preliminary sizing	138
13.5 Loads sizing	138
13.6 Tires sizing (considering 25% of margin for loads)	139
13.7 Tire sizing (considering 25% margin for loads)	139
13.8 Length and maximum diameter	143
14.1 Jet Engines Comparison	146
14.2 Specifications F118-GE-100	147
14.3 Specifications T408-GE-400	152
14.4 Volume of fuel tanks	154
15.1 Aluminium alloys properties	160
15.2 Composite material properties	161
15.3 Components material	161
15.4 Sizing maneuvers	163
15.5 Reference equivalent airspeed for sizing maneuvers	164
15.6 Mass configurations	164
15.7 First 20 structural modes	170
15.8 Dynamic pressure for divergence instability	173
15.9 Mass breakdown at MTOM	174
15.10CG positions	175
15.11CG range rotorcraft mode	176
15.12Longitudinal position of CG in rotorcraft mode	177
15.13CG range jet mode	177
15.14Longitudinal position of CG in jet mode	178
16.1 Aircraft flight control system modes	184
16.2 Outboard aileron parameters	188
16.3 Inboard aileron parameters	188
16.4 Rudder parameters	189
16.5 Elevator parameters	190
16.6 VTOL flight control system modes	191



17.1 Parameters for wing zero-lift friction drag	197
17.2 Parameters for wing drag coefficient due to lift	198
17.3 Parameters for fuselage drag coefficient due to lift	200
17.4 Parameters for jet engine parasite (zero-lift) drag	201
17.5 Parameters for the jet engine-fuselage interference drag	202
17.6 Parameters for jet engine drag due to the windmilling	202
17.7 Parameters for the nacelle parasite (zero-lift) drag	203
17.8 Parameters for the nacelle-wing interference drag	204
17.9 Parameters for empennage drag coefficient due to friction	205
17.10 Parameters for empennage drag coefficient due to lift	206
17.11 Parameters for parasite trim drag	208
17.12 Parameters for landing gear drag	208
18.1 Take-off distance for different thrust	220
18.2 Take-off distance for different flap deflections	221
18.3 Take-off distance for different runway elevation	222
18.4 Landing distance for different weight	224
18.5 Landing distance for different flap deflections	224
18.6 Landing distance for different runway elevation	225
18.7 Take-off distance for some competitor (Reference [7])	226
18.8 Runway length of some strategic air base located on NATO countries	227
18.9 Taper ratio and wing chords	231
18.10 Summary of rotorcraft performance obtained	242
18.11 Mission profile parameters	244
20.1 Longitudinal modes (conversion configuration)	277
20.2 Longitudinal modes (cruise configuration)	278
20.3 Lateral-directional modes (conversion configuration)	280
20.4 Lateral-directional modes (cruise configuration)	282
20.5 Phugoid damping ratio requirements	283
20.6 Short period damping ratio requirements	283
20.7 Short period natural frequency requirements	284
20.8 Roll-mode time constant requirements	284
20.9 Spiral mode time to double requirements	285
20.10 Dutch roll requirements just for a Class II aircraft	285
20.11 Summary of flying qualities for Raven 4 (Class II-L aircraft)	286
22.1 Cost comparison of competitors	296

22.2 Hourly rates in 2012 U.S. dollars	300
22.3 Material factor	301
22.4 Project cost analysis	302
22.5 Total program cost and revenues	305
22.6 Cost for a more composite aircraft	305
22.7 Utilization of the aircraft.	306
22.8 Cost of direct personnel cost	306
22.9 Percentage of costs related to indirect personnel, spares, depots, and mis- cellaneous in relation to the total operating cost.	307
22.10 Total program operating cost	307



List of Tools

- MATLAB: <https://it.mathworks.com/products/matlab.html>
- Simulink: <https://it.mathworks.com/products/simulink.html>
- XFLR5: <http://www.xflr5.tech/xflr5.htm>
- OpenVSP: <https://openvsp.org/>
- NeoCASS: <https://www.neocass.org/>
- SOLIDWORKS: <https://www.solidworks.com/it>
- X-Plane 11: <https://www.x-plane.com/>

Acronyms

AHP Analytic Hierarchy Process. 35

AR Aspect Ratio. 99

BEM combined Blade Element and Momentum theory. 65

BROC Best Rate of Climb. 229, 338

CAS Control Augmentation System. 250

CG Center of Gravity. 137, 164

CSAR Combat Search and Rescue. 16

FCL Fuselage Center Line. 177

FMS Flight Management System. 270

FOD Foreign Object Debris. 3

HIGE Hover In Ground Effect. 5, 70, 150

HOGE Hover Out of Ground Effect. 4, 5, 56, 150

HSVTOL High-Speed Vertical Takeoff and Landing Aircraft. 21, 326, 327

ISA International Standard Atmosphere. 4, 5, 56

LCC Life cycle cost. 297

LQR Linear Quadratic Regulator. 271

LZ Landing Zone. 5, 150

MCP Maximum Continuous Power. 4, 52, 228, 231, 239

MCT Maximum Continuous Thrust. 50, 51

MEP Mission Equipment Package. 4, 174

MMGW Mid-Mission Gross Weight. 5, 68, 150, 239

MRP Maximum Rated Power. 150

MRT Maximum Rated Thrust. 239

MSL mean sea level. 3–5, 150

MTOW Maximum Take-Off Weight. 45, 59, 68, 71, 76, 185, 189, 223, 232, 239

RDT&E Research, Development, Test and Evaluation. 297

RFP Request Of Proposal. 3, 4, 17, 19, 21, 33, 34, 36, 37, 44, 51, 54, 56, 70, 110, 134, 150, 173, 216, 231, 243, 325

ROA Radius Of Action. 4, 5

SAS Stability Augmentation System. 250

SDGW Structural Design Weight Gross. 4, 59

SFC specific Fuel Consumption. 230, 338

SMP Sizing Matrix Plot. 100

STOVL Short TakeOff Vertical Landing. 148

TOGW Takeoff Gross Weight. 4

USAF United States Air Force. 325

VFS Vertical Flight Society. 326

VLM Vortex Lattice Method. 109, 115–117, 209, 286

VNE Velocity Not Exceed. 173

VTOL Vertical Take-Off and Landing. 18, 33



Acknowledgements

On behalf of the entire team, we would like to express our gratitude to those who have offered their assistance and made themselves available to help us both in the analysis of the decisions we could make and in the technical analyses during this year. In particular, our thanks are extended to Professor Lorenzo Trainelli and Professor Carlo E. D. Riboldi, as well as to the PhD Yasir Mahmood Khan, who accompanied us throughout the year. Sincere thanks also go to Professor Giuseppe Quaranta, Professor Pierangelo Masarati, Professor Giuseppe Sala and PhD Luca Marchetti for their technical support. Finally, we extend our thanks to Eng. Luca Sala for his expertise in evaluating the request for proposal and for his support in guiding us through the organization of our work.

